NASA Conference Publication 3238

FIRE Cirrus Science Results 1993

(NASA-CP-3238) THE FIRE CIRRUS SCIENCE RESULTS 1993 (NASA) 222 p
N94-22292
--THRU--
N94-22344
Unclas
H1/47 0197500

Proceedings of a conference held in Breckenridge, Colorado June 14–17, 1993

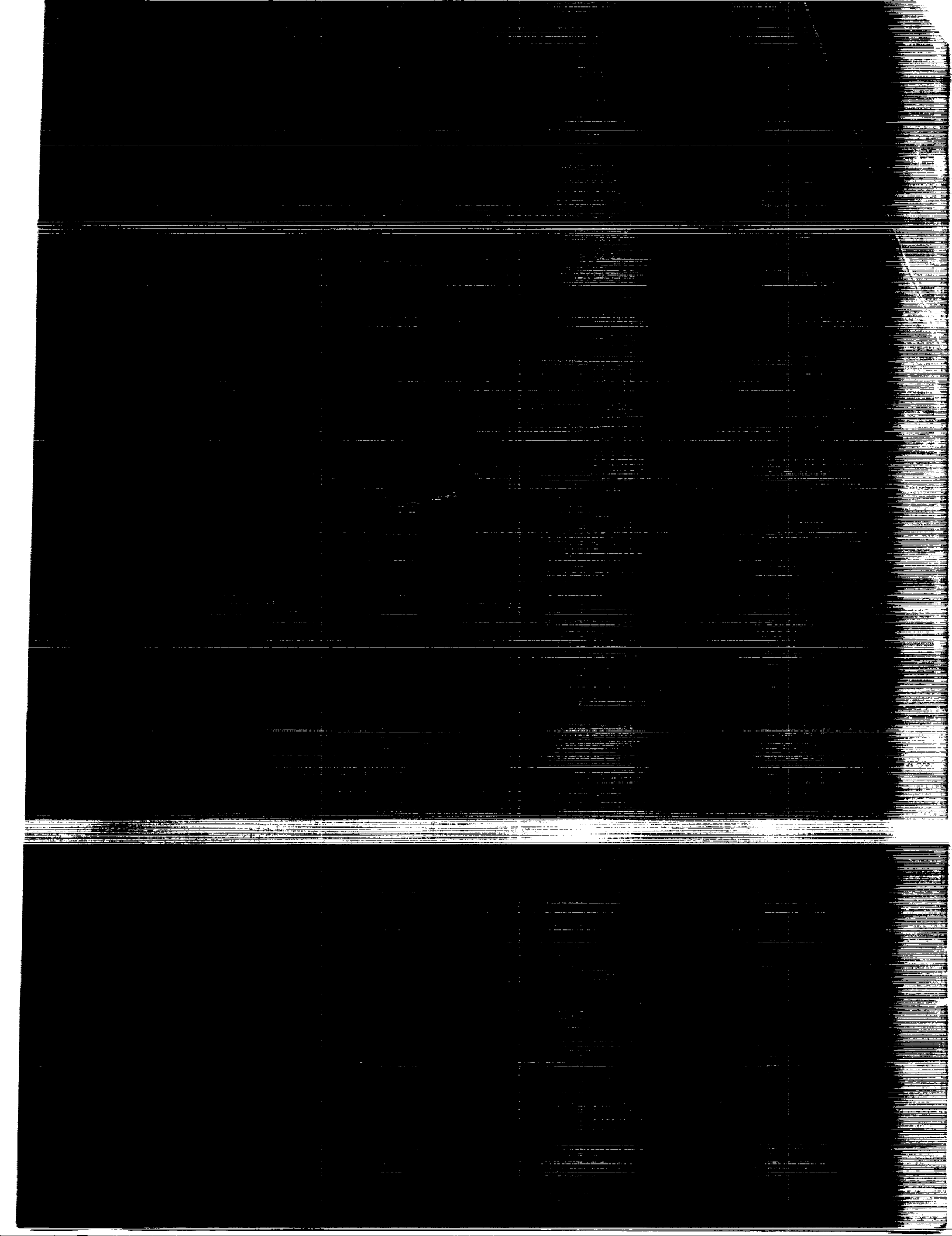

NASA Conference Publication 3238

FIRE Cirrus Science Results 1993

Edited by
David S. McDougal
NASA Langley Research Center
Hampton, Virginia

Proceedings of a conference cosponsored by the National Aeronautics and Space Administration, the National Science Foundation, the National Oceanic and Atmospheric Administration, the Department of Energy, and the Office of Naval Research and held in Breckenridge, Colorado
June 14–17, 1993

National Aeronautics and Space Administration
Office of Management
Scientific and Technical Information Program
1993

FOREWORD

The FIRE Cirrus Science Conference was held in Breckenridge, Colorado, June 14-17, 1993. The meeting featured presentations of results representing 4 years of FIRE Phase II research focusing on cirrus cloud systems. An additional outcome of this and other meetings was expected to be the definition of candidate research goals and priorities for the next FIRE Phase III.

This conference proceedings contains the text of short papers, and in some cases short abstracts, of papers presented at the conference.

This was an exciting and worthwhile conference. It is apparent that the FIRE cirrus science community has made significant progress in the analyses of data collected during the FIRE Cirrus Intensive Field Observations - II, conducted in Kansas, November 13 - December 7, 1991. It was especially exciting to see the number of collaborative efforts involving multiple authors from different organizations. There was also a session to discuss candidate cirrus cloud systems for possible FIRE Phase III studies.

The program managers of the sponsoring agencies wish to express their gratitude and appreciation to the FIRE researchers for their contributions to this important science conference as well as for their conscientiousness, teamwork, and scientific excellence demonstrated throughout FIRE Phase II. In particular, we would like to highlight the outstanding leadership of Dr. David O'C. Starr, Goddard Space Flight Center, who did a magnificent job as Lead Mission Scientist for the cirrus experiment.

We would like to thank Ms. Lisa Pearson, SAIC, for her talents and dedication in planning, preparing, and conducting the meeting. We would also like to express our appreciation to Ms. Debbie Coccimiglio, SAIC, for her excellent secretarial support in the preparation of the conference preprint and this document.

PRECEDING PAGE BLANK NOT FILMED

INTENTIONALLY BLANK

TABLE OF CONTENTS

PRECEDING PAGE BLANK NOT FILMED

PAGE IV INTENTIONALLY BLANK

51-47
197561
N94-22293

OVERVIEW OF MICROPHYSICAL AND STATE PARAMETER MEASUREMENTS FROM FIRE II

Andrew J. Heymsfield and Larry M. Miloshevich

National Center for Atmospheric Research
Boulder, Colorado 80307

1. INTRODUCTION

In this article we present data collected by the NCAR King Air and Sabreliner aircraft in the FIRE II cirrus project over southeastern Kansas and northeastern Oklahoma in November and December of 1991. We present state parameter and microphysical measurements in summary form for the cases which have been selected by the FIRE Science Team for intensive analysis, 25 and 26 November and 5 and 6 December. We will also evaluate the performance of "key" aircraft instrumentation.

2. STATE PARAMETER MEASUREMENTS

The data sets for both aircraft include temperature information from a Rosemount temperature probe, water vapor density and relative humidity from a Lyman–alpha probe and an NCAR–designed cryogenic hygrometer, and indication of the presence of liquid water from a Rosemount icing detector. The accuracy of the cryogenic hygrometer is estimated conservatively to be better than 10% based on measurements in wave clouds (Heymsfield and Miloshevich, 1993). The Lyman–Alpha probe detects changes in the water vapor density with a rapid response (10 Hz), and these measurements show that the time response of the cryogenic hygrometer (time constant of ~3 seconds) was adequate for our needs. The Rosemount icing probe can detect concentrations of liquid water less than 0.005 g m^{-3} (Heymsfield and Miloshevich 1989).

In–cloud penetration–averaged temperature and relative humidity measurements from the King Air and Sabreliner aircraft on the four case study days are shown in Fig 1; the standard deviations of the measurements are too small be be resolved in the figure. Also indicated in the figures are rawinsonde soundings released from the Coffeyville hub site, along with cloud base and cloud top heights as determined from calibration of our balloon–borne ice crystal replicators (Miloshevich et al. 1993), although the geographical locations and timing of the rawinsonde and aircraft measurements are different. Cloud base and cloud top as determined from the replicator measurements roughly match the cloud altitudes shown by the aircraft data plotted in the figure. Temperatures and temperature structure (e.g. isothermal regions, inversions, and lapse rate) as determined from the aircraft and rawinsonde measurements are unexpectedly similar. When combined with the cloud altitude information, this similarity suggests that the measurements from all platforms are accurate and that the temperature structure of the atmosphere was similar over the region of study and relatively constant in time.

Relative humidities from the in–cloud rawinsonde data are systematically below ice–saturation and are therefore unrealistically low, generally by about 20%. Conversely,

the aircraft measurements are much more realistic when compared to the ice–saturation curve, and liquid water was detected only when the relative humidity exceeded 100%. Furthermore, the aircraft data also indicate that the in–cloud regions were consistently ice–supersaturated, especially when the aircraft encountered liquid water.

3. MICROPHYSICAL DATA

Representative 2D probe measurements from the King Air on 26 November 1991 at -44^C are shown in Fig. 2, upper two panels. The larger particles in the second panel have well defined "bullet-rosette" shapes. The smaller particles in the upper panel appear to have a compact, denser shape. Their shapes are similar to the larger particles measured with our replicator sonde (lower panel, Fig. 2.) about one hour later. Note that few particles below about 100 microns are imaged with the 2D probe yet many such particles are noted in the replicator data. Data from the 2D probes and video ice particle sampler (VIPS) onboard the NCAR Sabreliner will be available in the future, as will vertical profiles of ice particle size spectra and ice crystal habits from the replicators.

4. CONCLUSIONS

A data set was acquired that contains measurements which can be used to further our understanding of cirrus microphysical processes and microphysics–radiation interaction. The goals will best be achieved by coordinated case studies which make use of the diverse data sets collected both *in–situ* and remotely. Temperature measurements from both aircraft and from the rawinsondes appear to be highly accurate and amenable to coordination. The aircraft relative humidity measurements are accurate at least to within 10%; however, the rawinsonde relative humidity measurements are unrealistically low.

REFERENCES

Heymsfield, A. J., and L. M. Miloshevich, 1993: Homogeneous ice nucleation and supercooled liquid water in orographic wave clouds. *J. Atmos. Sci.*, June 1993.

——, and L. M. Miloshevich, 1989: Evaluation of liquid water measuring instruments in cold clouds sampled during FIRE. *J. Atmos. Oceanic Technol.*, **6**, 378–388.

Miloshevich, L. M., A. J. Heymsfield, and P. M. Norris, 1992: Microphysical measurements in cirrus clouds from ice crystal replicator sondes launched during FIRE II. Presented at the 11th International Conference on Clouds and Precipitation, Montreal, Quebec, Canada, August 17–21, 1992.

Aircraft and Radiosonde: T and RH

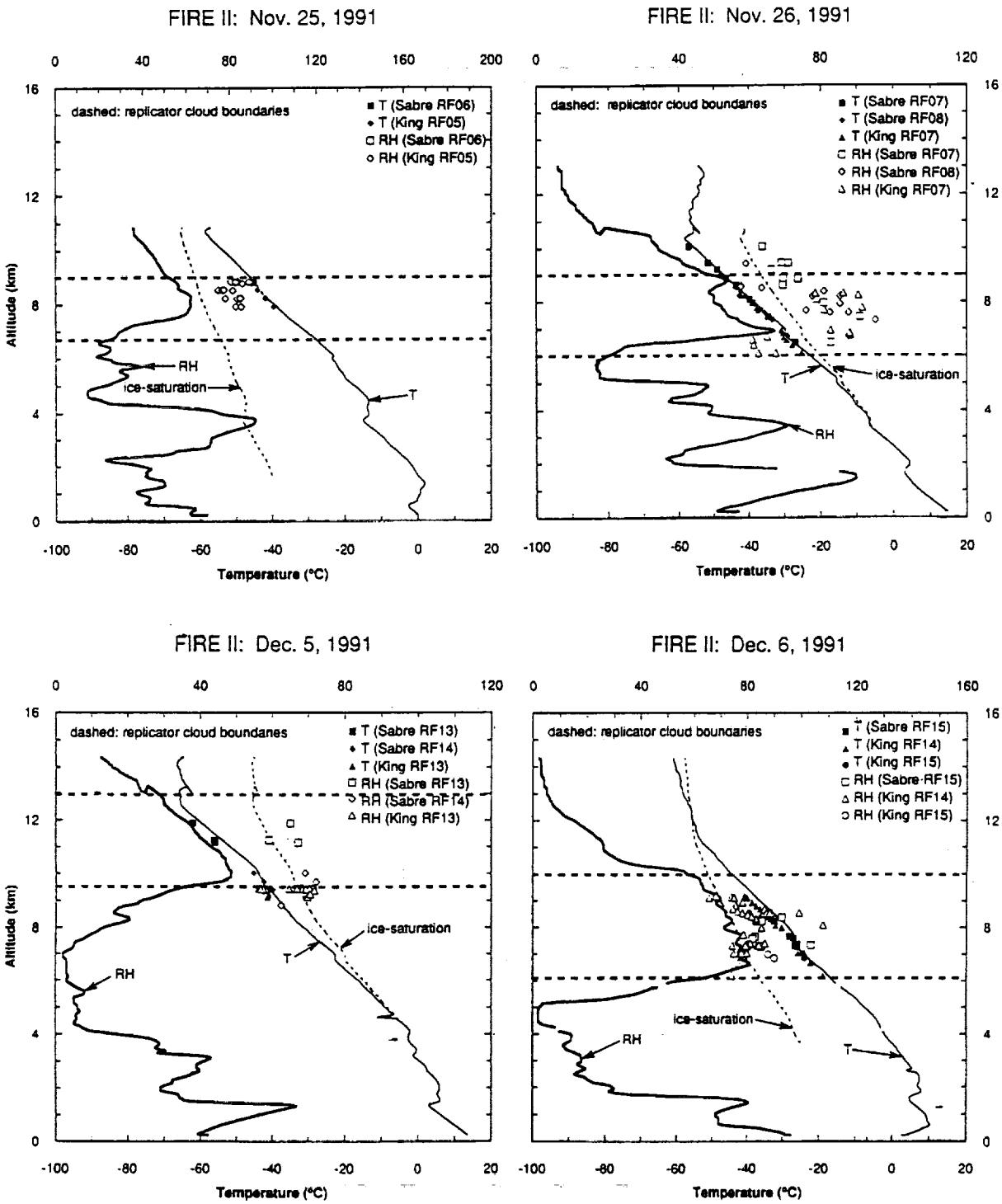

Fig. 1. Rawinsonde and penetration–averaged aircraft measurements of temperature (lower abscissa) and relative humidity (upper abscissa), on the case study days Darkened symbols show temperature measurements, and open symbols show relative humidity measurements.

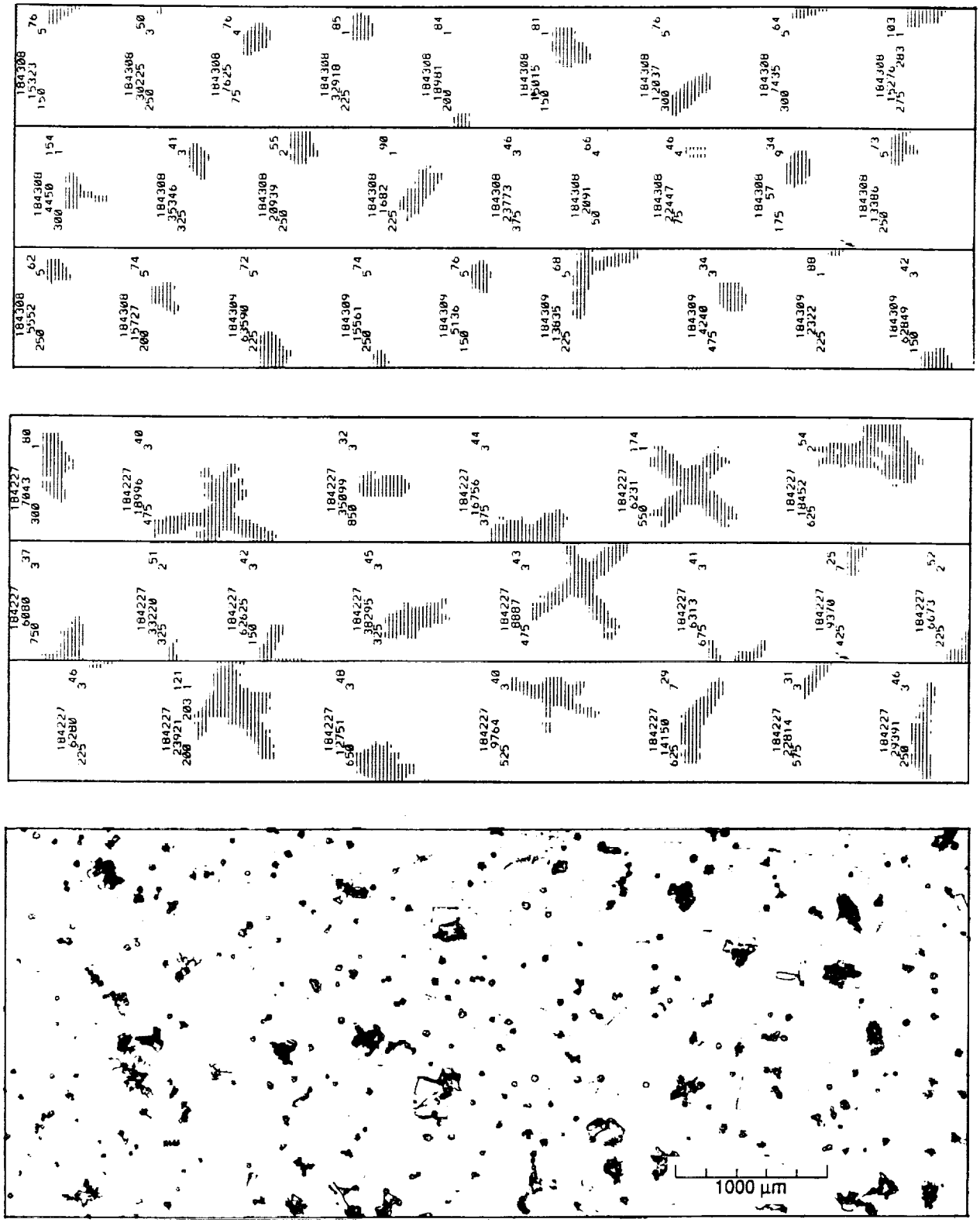

Fig. 2. King Air 2D–C measurements (upper two panels) and ice crystal replicator measurements (lower panel) on 26 November 1991.

52-47
197502
N94-22294

CIRRUS MICROPHYSICS OBSERVATIONS MADE DURING FIRE II: SMALL PARTICLES, HIGH CONCENTRATIONS, AND PROBE COMPARISONS

W P Arnott, Y Y Dong and J Hallett (All at: Desert Research Institute, PO Box 60220, Reno, NV 89506; 702-677-3123) M R Poellot (Dept of Atmospheric Sciences, Univ. N. Dakota, Box 8216, Univ. Station, Grand Forks, ND 58202; 701-777-2791)

Abstract

Aircraft observations of cirrus cloud microphysics were made near Coffeyville, Kansas during November and December 1991. Cloud microphysics measurements were made using both a PMS 2DC probe and an ice particle replicator, both mounted on the UND Citation aircraft. Intercomparison is made of the size, area, and ice mass spectra determined from these probes. The PMS 2DC undercounts particles with D < 70 μm and the replicator oversizes particles with D > 150 μm, at least when column rosettes are encountered. High concentrations of particles with D < 50 μm are noted in selected portions of the 22Nov91 replicator data set. Relations between the maximum dimension of a crystal and its shadow area (known as area dimensional relationships) are computed from the PMS data. Area and mass dimensional relationships are used to give a simple analytical expression for computing the wavelength dependent absorption coefficient averaged over a size bin. Calculations based upon the replicator data show that crystals with D < 50 μm contribute significantly to the solar extinction and infrared absorption coefficients during some time intervals.

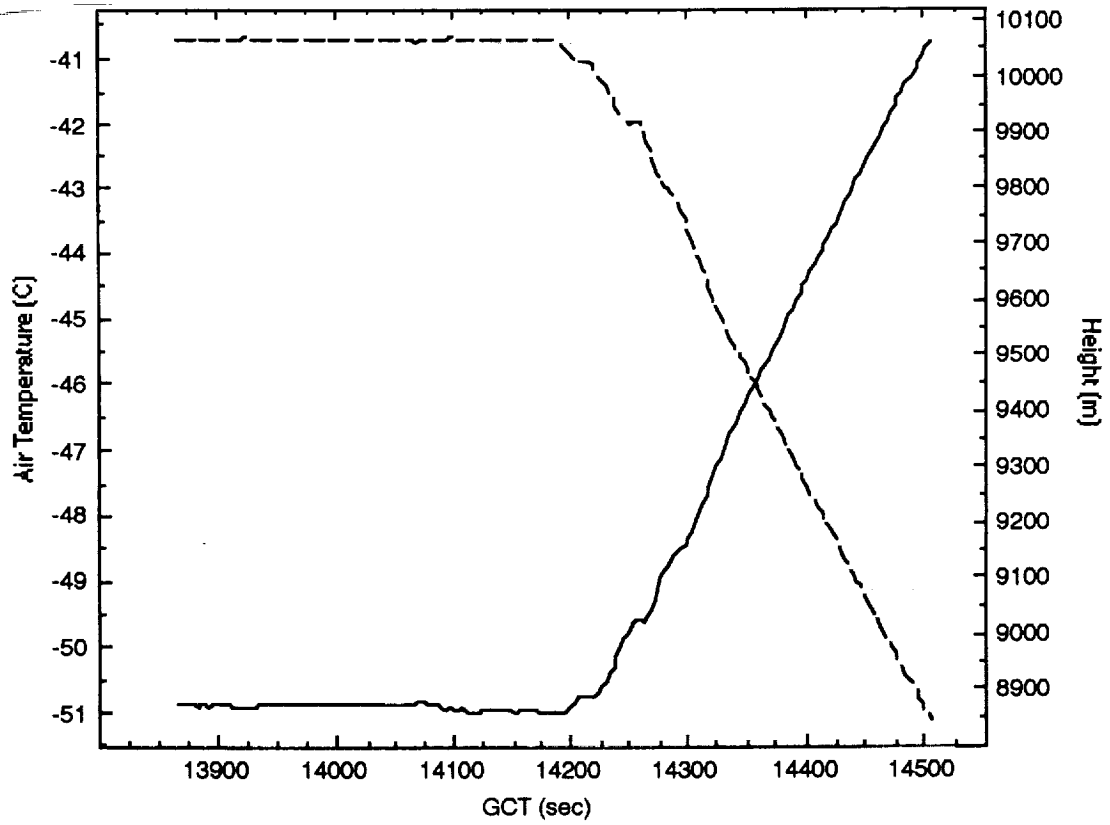

Figure. 1 Air temperature (solid) and aircraft height (broken).

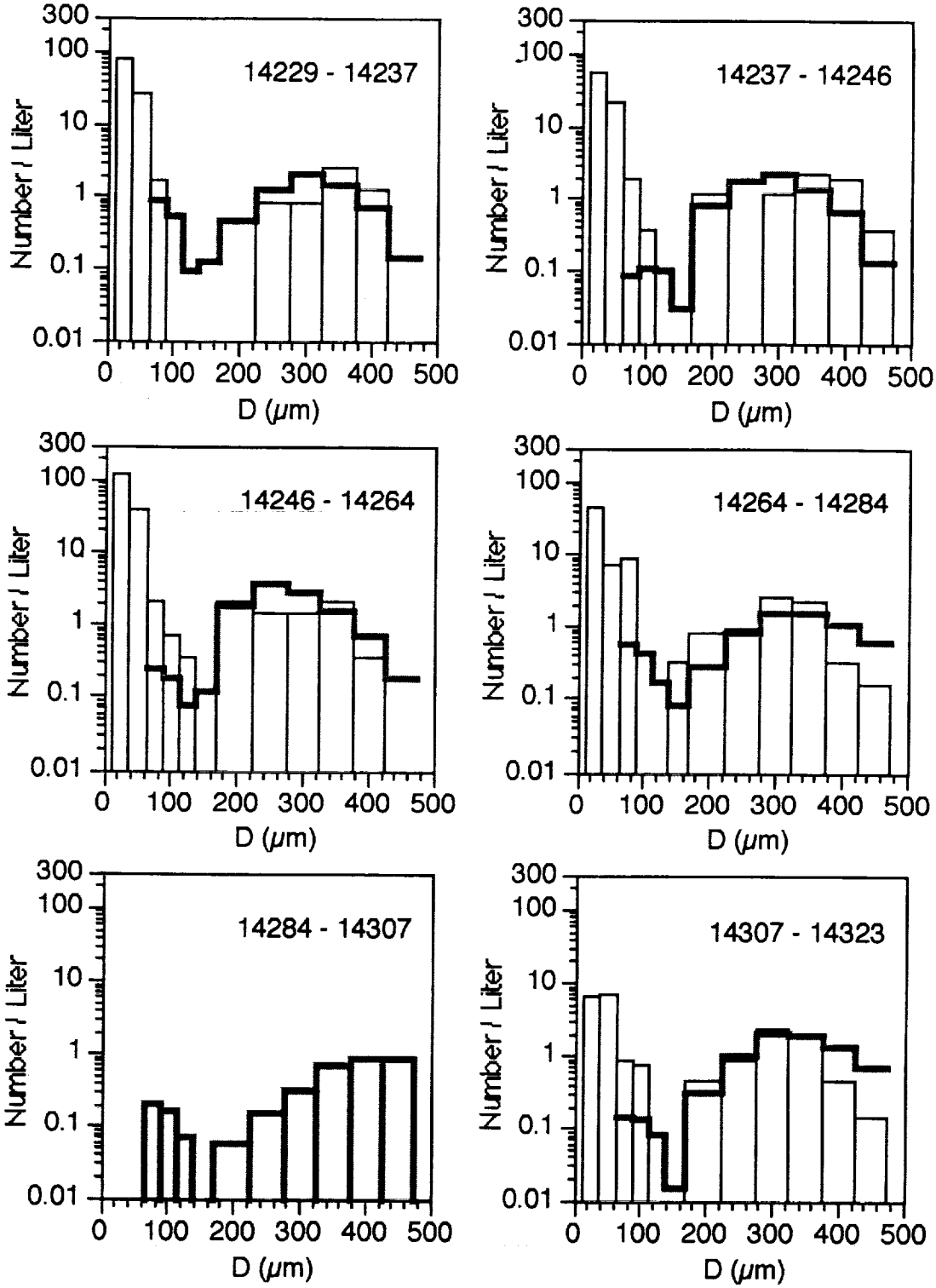

Figure 2. Representative ice crystal size distribution for the replicator (solid line) and PMS 2DC (shadowed line) as a function of time. The time interval in seconds is indicated in each graph.

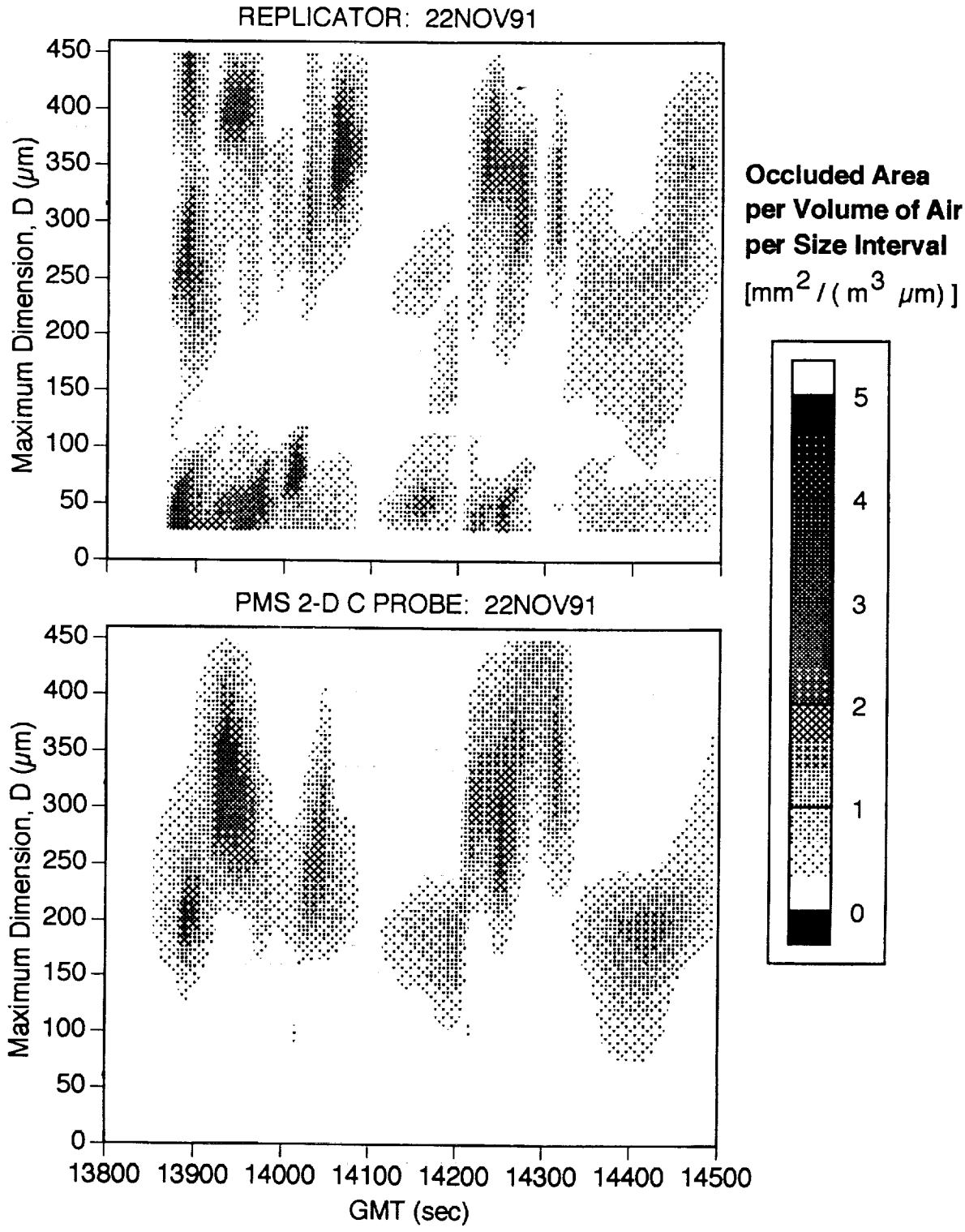

Figure 3. Area distribution of the cloud for replicator and PMS 2DC data. The replicator data shows the contribution of small ice crystals during some time intervals, especially before 13900 GMT.

Small ice crystals can influence the appearance of cirrus clouds from satellites and can be an important component of solar and IR radiative transfer. Small ice crystals have maximum dimensions less than about 60 μm and can affect cloud radiative properties if they occur in sufficient abundance compared with larger crystals. Our calculations for quantifying the radiative importance of small ice crystals used in situ aircraft microphysics data of a particular portion of a cirrus cloud obtained with a probe capable of recording the small particles (the ice crystal replicator). Calculations show that solar extinction and IR absorption coefficients can be predominately due to small ice crystals during some time intervals and in some portions of the cloud. The broader implications and generality of these results are not clear at present.

Cirrus observations were made using the University of North Dakota Citation research aircraft. Figure 1 shows the air temperature (-51 C to -40 C) and aircraft altitude (10100 m to 8850 m). Raman lidar indicated cirrus between 8 km and about 10 km. This portion of the flight occurred during the evening of 21 Nov 1991 from 21:51 to 22:02 local time, or 22 Nov 1991 3:51 to 4:02 Greenwich Mean Time (GMT). The horizontal position of the aircraft had a section of level flight followed by a spiral descent that following the prevailing wind (i.e. Lagrangian descent) to the base. The air speed of the aircraft was usually 120 m/s. The aircraft was equipped with an ice particle replicator manufactured at the DRI and a PMS 2DC optical probe for measuring cloud particle concentrations and sizes. The volume of air sampled per second by the replicator and PMS 2DC are nominally 2 liters per second and 7 liters per second, respectively, though exact numbers depend on the aircraft speed and particle size. The PMS 2DC probe was capable of sizing particles in the range of 66-1056 μm with a 33 μm resolution. Generally we find that the PMS 2DC does not record all of the small particles present. The replicator gives an over estimate by roughly 4/3 of the crystals maximum dimension due to flattening of the crystal on impact with the formvar coated film for crystals with $D > 100$ μm.

The extinction coefficient of the cloud for the solar wavelengths is essentially twice the geometric shadow of all crystals in a unit volume of air. Therefore a quick estimate of the relative importance of small ice crystals for the overall solar extinction can be made. The maximum area ratio of 25 μm and 250 μm is 1/100, so the number of 25 μm crystals must be on the order 100 times as great as the number of 250 μm crystals for the 25 μm crystals to contribute significantly to the overall solar extinction coefficient. The replicator data in Figure 2 shows definite time periods when the concentration of small crystals is sufficient that they contribute significantly to the solar extinction coefficient. Figure 3 shows the distribution of crystal area against time and maximum dimension of the crystal for the replicator and PMS data sets. The most important observation of the data set is that during the time interval (13885 - 14000), small (< 75 μm) crystals contribute very significantly to the total area.

Selected time intervals exist where there can be significant numbers of small particles ($D < 60$ μm), and very few larger particles in cirrus. Most of the projected cloud area and IR absorption cross section per volume of cloud is due to the small particles during these intervals. Though small crystals can be expected at cloud margins where they might form from evaporation of larger crystals, or at cloud top, the totality of all possible regions and situations where one might expect large numbers of small crystals is not well investigated.

Acknowledgement We acknowledge financial support by NASA contract NAG-1-1113.

53 47
197503
N94-22295

Cirrus Properties Deduced from CO_2 Lidar Observations of Zenith-enhanced Backscatter from Oriented Crystals

Wynn L. Eberhard
NOAA Wave Propagation Laboratory
US Department of Commerce
325 Broadway
Boulder, Colorado 80303

I. Introduction

Many lidar researchers have occasionally observed zenith-enhanced backscatter (ZEB) from middle and high clouds. The ZEB signature consists of strong backscatter when the lidar is pointed directly at zenith and a dramatic decline in backscatter as the zenith angle dips slightly off zenith. Mirror-like reflection from horizontal facets of oriented crystals (especially plates) is generally accepted as the cause. Thomas et al. (1990) found during a 3-year observation program that approximately 50% of ice clouds had ZEB, regardless of cloud height.

The orientation of crystals and the ZEB they cause are important to study and understand for several reasons. First, radiative transfer in clouds with oriented crystals is different than if the same particles were randomly oriented. Second, crystal growth depends partly on the orientation of the particles. Third, ZEB measurements may provide useful information about cirrus microphysical and radiative properties (e.g., Platt et al. 1978 and Eberhard, 1993). And fourth, the remarkable effect of ZEB on lidar signals should be understood in order to properly interpret lidar data.

Laboratory measurements with circular plates (Willmarth et al. 1964) and light pillar data on actual crystals (Sassen 1980), show that ice plates with Reynolds numbers $1 \leq N_{Re} \leq 100$ (or diameters ranging from ≈ 150 to ≈ 2000 μm) orient with the face in the horizontal plane. However, slight angular perturbations of orientation up to a maximum of 0.5-3° have been observed (Platt et al. 1978, Sassen 1980, and Thomas et al. 1990), with minimum perturbations at $N_{Re} \sim 10$ (Sassen 1980).

Circular cylinders in the laboratory (Jayaweera and Mason 1965) oriented with the long axis horizontal when $0.1 \leq N_{Re} \leq N_{Re,max}$, where $N_{Re,max}$ increases as the length-to-diameter ratio increases. Figure 1 shows the range of ice columns that are expected to orient expressed in terms of longest dimension (i.e., axis length) L. It is not known whether hexagonal cylinders show any tendency to orient in the roll direction such that one

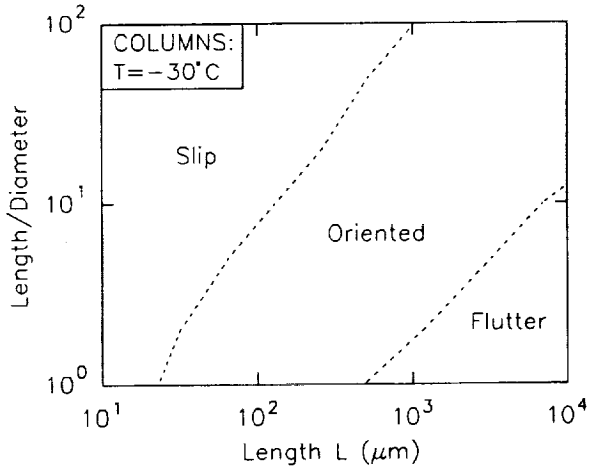

Fig. 1. Domain of sizes of hexagonal columns expected to orient with the long axis horizontal based on Reynolds-number-scaled laboratory measurements of circular cylinders.

of the six faces around the hexagon remains in the horizontal plane.

The 10.6-μm-wavelength CO_2 lidar that operated during FIRE II frequently scanned about the zenith to study the ZEB phenomenon. A companion paper (Eberhard, 1993) describes the scattering models developed for interpreting the measurements, and this paper describes some interpretations of the data using those models.

II. ZEB for CO_2 lidar

The lidar scanned in elevation angle in a plane aligned with the wind direction at cloud height. Averages were made for several scans, typically over a 500-s period, to smooth out most of the variations in cloud density. Clouds were divided into vertical layers within which the elevation-angle-dependent shape of the average ZEB signal was consistent. Average backscatter as a function of lidar elevation angle was calculated for each layer. Figure 2 shows some typical signatures from 26 November 1991 that illustrate different kinds of ZEB signatures, which depend on several factors that are explained in this section.

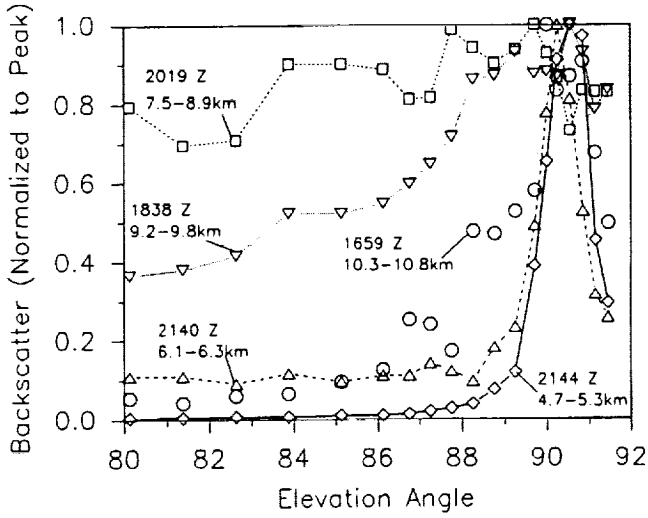

Fig. 2. Typical ZEB observations as a function of CO_2 lidar elevation angle. Times are GMT on 26 November 1991, and heights are ASL.

Clouds composed only of plates have very strong backscatter at zenith with very little backscatter in the wings far from the peak (see curve A in Fig. 1 of Eberhard 1993). Therefore, the curve for 2144 Z in Fig. 2 suggests the presence of oriented plates. According to the model in Eberhard (1993), the zenith enhancement from plates is so strong that even the small signal in the wing of the curve indicates that only 12% of the cloud (as weighted by the cross sectional area of the particles) is composed of oriented plates. In comparison, we infer that 3.5% of the particles at 1659 Z are oriented plates.

Clouds containing only perfectly shaped and horizontally oriented columns, but with random roll orientation, have less zenith enhancement and much more backscatter in the wings (curve C in Fig. 1 of Eberhard 1993) than plates have. The curve at 2140 Z in Fig. 2 might be a mixture of 30% oriented columns and 70% randomly oriented particles, but it also could be a mixture of 0.2% oriented plates and 98.8 randomly oriented particles. The data from 2144 and 1659 Z have larger peak-to-shoulder ratios than permitted by the cylinder model, but an ambiguity exists for oriented crystal type in the data at 2140 Z.

The data at 2019 Z are an example of data that decline so little with zenith angle that we infer negligible ZEB and 100% randomly oriented particles for the layer.

The width of the peak for perfectly oriented plates with truly flat faces depends on diffraction, with peak width proportional to wavelength and inversely proportional to plate diameter. The same is true, except for a numerical factor, for perfectly oriented columns with random roll orientation. In either case, the width of the peak reveals the size of the longest dimension of oriented particles. However, the peak can be additionally widened by nondiffraction factors, such as slight fluttering motions, optical imperfections, and shape imperfections that alter the stable orientation slightly from one particle to the next. Therefore, an estimate of the size of oriented particles using the width of the peak gives only a lower bound on the long dimension. Diffraction and nondiffraction factors can both be significant at 10.6-μm wavelength, whereas the nondiffraction factors dominate the width of the ZEB peak for lidars with a wavelength $\leq$ 1.5 μm. If plates are assumed for the curves at 2144 and 2140 Z in Fig. 2, the lower bound on diameters are 197 and 246 μm, respectively. If the oriented particles at 1659 and 1838 Z were plates, there must have been significant nondiffractive spreading, because the inferred lower bounds on plate diameters are only 93 and 42 μm, respectively, which are smaller than the limit for orientation discussed in the introduction. If the oriented particles for these two cases were columns, it is not clear whether nondiffractive spreading was a factor.

III. Statistics from 26 November 1991

Statistics on ZEB parameters for the period 1657-2151 Z on 26 November 1991 are compiled in Figs.

3-5. The scanning data from this period were divided vertically and temporally as described in Section II into 72 cases.

The distribution of the peak-to-shoulder ratio is shown in Fig. 3, where the peak value is the maximum

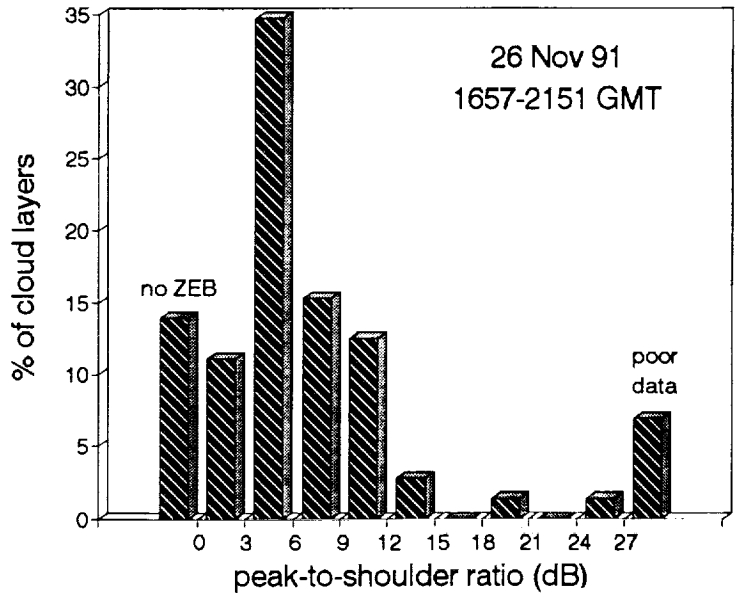

Fig. 3. Probability distribution of the strength of the ZEB signature for height- and time-averaged cloud segments.

backscatter near zenith, and the shoulder value is that at the lowest elevation angle (usually 80°). Poor data (optically thick intervening cloud or extreme patchiness) prevented analysis in five of the cases. ZEB was observed in 57 (or 85%) of the remaining cases. However, the peak-to-shoulder ratio was less than 6 dB in more than half the cases.

Assuming plates in the 57 cases with ZEB, Fig. 4 shows the distribution of the inferred lower bound on

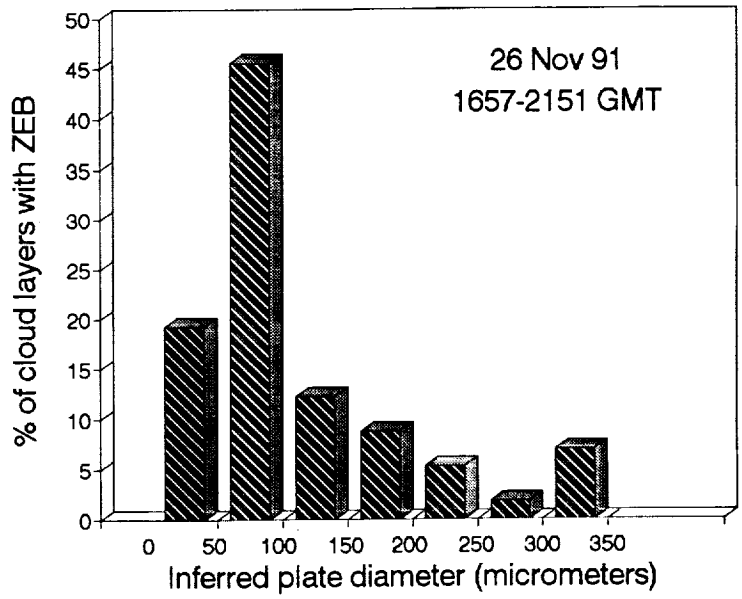

Fig. 4. Inferred lower bound of the largest dimension of oriented particles (assuming plates) for the 57 cases with ZEB.

plate diameter. More than half of the inferred diameters are less than 100 μm, i.e., less than the lower Reynolds-number limit for plate orientation. We infer nondiffractive spreading of the ZEB peak from plates or the presence of short columns rather than plates for these cases.

Figure 5 gives the statistics on the fraction of cloud, weighted by particles' cross-sectional area, composed of oriented particles. The results depend dramatically on whether plates or columns are in the cloud. Thirteen (or 18%) of the cases have ZEB strong enough that plates must be dominating the ZEB. However, the

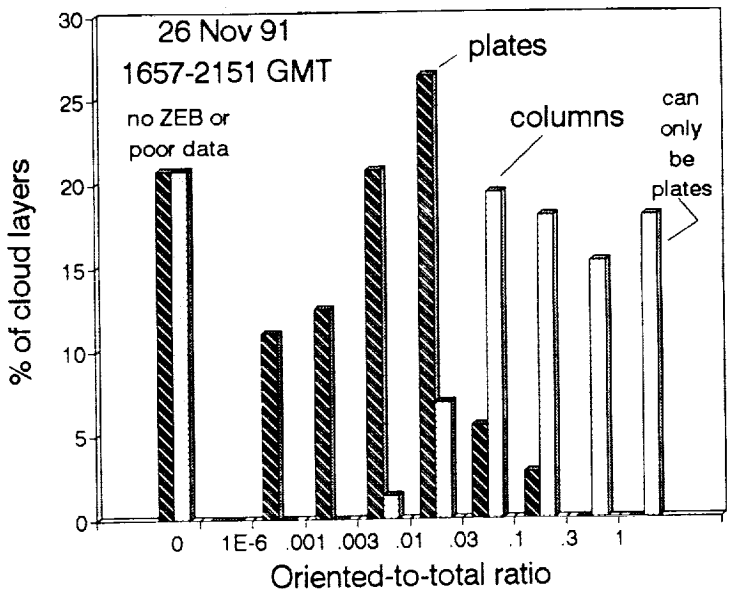

Fig. 5. Fraction of cloud composed of oriented particles (weighted according to cross sectional area) according to whether plates or columns are assumed.

model (Eberhard 1993) indicates that no more than 13% of the particles are oriented plates in any of the cases. Forty-four (or 61%) of the cases could consist partly of columns comprising cloud fraction ranging from nearly 100% to less than 1%.

IV. Discussion

The CO_2 lidar data from a 5-h period on 26 November 1991 frequently had ZEB, even more often than the more comprehensive data set of Thomas et al. (1990). The enhancement was small for most cases during the 5-h period, so adjusted lidar backscatter cross sections (Eberhard 1993) can be used with confidence for this portion of the data. The inferred diameters of the oriented particles (assuming plates) are often smaller than the range predicted from laboratory simulations, which is consistent with the expectation that nondiffractive spreading will often bias results to smaller diameters. The nondiffractive spreading of the peak and the ambiguities between different mixtures of plates, columns, and randomly oriented particles pose major problems in intrepreting ZEB data.

Future research will examine ZEB for the entire FIRE II data set and investigate whether temperature data can be used to infer the growth habit of oriented crystals to remove the plate-column ambiguity. Lidar ZEB results will be compared with simultaneous replicator and 2-D image measurements in an attempt to confirm and refine the interpretation of the ZEB signatures.

Acknowledgments. My thanks go to coworkers in Wave Propagation Laboratory for assistance in data acquisition and to B. Gordon, M. Jung and J. Bevilacqua for data processing and graphics.

V. References

Eberhard, W.L., 1993: Progress in interpreting CO_2 lidar signatures to obtain cirrus microphysical and optical properties. (this volume).

Jayaweera, K.O.L.F., and B.J. Mason, 1965: The behaviour of freely falling cylinders and cones in a viscous fluid. *J. Fluid Mech.*, **22**, 709-720.

Platt, C.M.R., N.L. Abshire, and G.T. McNice, 1978: Some microphysical properties of an ice cloud from lidar observation of horizontally oriented crystals. *J. Appl. Meteor.*, **17**, 1220-1224.

Sassen, K., 1980: Remote sensing of planar ice crystal fall attitudes. *J. Meteor. Soc. Japan*, **58**, 422-429.

Thomas, L., J.C. Cartwright, and D.P. Wareing, 1990: Lidar observations of the horizontal orientation of ice crystals in cirrus clouds. *Tellus*, **42B**, 211-216.

Willmarth, W.W., N.E. Hawk, and R.L. Harvey, 1964: Steady and unsteady motions and wakes of freely falling disks. *Phys. Fluids*, **7**, 197-208.

N94-22296

Bi-directional Reflectance and Other Radiation Parameters of Cirrus from ER-2 Observations

54-47
197504
P-4

James Spinhirne,
Dennis Hlavka and William Hart
NASA Goddard Space Flight Center/917
Greenbelt, MD 20771

Passive and active remote sensing of cirrus were acquired from the ER-2 high altitude aircraft in the 1991 Cirrus Experiment. The observations include direct measurements of cirrus bi-directional reflectance from a new translinear scanning radiometer and also the previously employed measurements by lidar and visible-infrared imaging radiometers. For any cirrus radiative transfer application it is necessary to know the appropriate model for visible reflectance in relation to angle and also the optical thickness and infrared emissivity of the clouds. At a more complicated level, for remote sensing and overall cloud effects it is ultimately required to understand effects from multiple cloud layers, broken clouds and variable microphysics. Our overall data set from the scanning radiometers and lidar is intended to provide the necessary observations to investigate these problems.

Observations

The Electro-Optic Camera instrument is based on a commercially available silicon CCD array imager (Kodak KAF-1400). The device includes a six-position filter wheel which can be fitted with a combination of spectral filters and/or polarizing elements. The camera is mounted in the nose of the ER-2 and can tilt forward or aft up to 50 degrees. Radiometric images are acquired by the 1280x1025 array detector. With the nominal f/2.8 lens in place the total angular field of view for a singe scene is 14.2 by 17.6 degrees. At full resolution the pixel size at ground altitude is about 5 m. When data is acquired the camera tilts at a steady linear rate to track a scene at a preset altitude. For the cirrus experiment the observation altitude was typically 9 km. During a scan images at the six filter positions are obtained at about a 10 degree angular separation.

The use of lidar and visible/infrared cross track scanning radiometric imagers in cloud experiments has been previously described (Spinhirne and Hart, 1990). For the cirrus experiment the ER-2 lidar incorporated an updated data system which permitted twice the previous pulse repetition rate and allowed operation over a full six hour flight. The visible/infrared

imager was an improved version of a Deadalus instrument as had been flown in the previous FIRE missions.

Analysis

The major difficulty in analyzing the cirrus bi-directional reflectance data is the inhomogeneity of the cirrus layers and underlying surfaces. In the initial attempt to analyze results we searched for scenes where observations were acquired over water for a dark uniform background and where cirrus existed as a single uniform layer. The lidar data defines the layered structure and height of the clouds. Since most of the cirrus experiment flights were over land and since most clouds are multi-layered no idealized case as given above were found. Several examples of cirrus over broken stratus with a water background were available. For these cases it was possible to determine the relation of the cloud reflectance as a function of view angle if individual cirrus parcels were identified and tracked from one image to subsequent images at other angles. Cirrus parcels were selected which were not contaminated by reflectance from the underlying broken stratus.

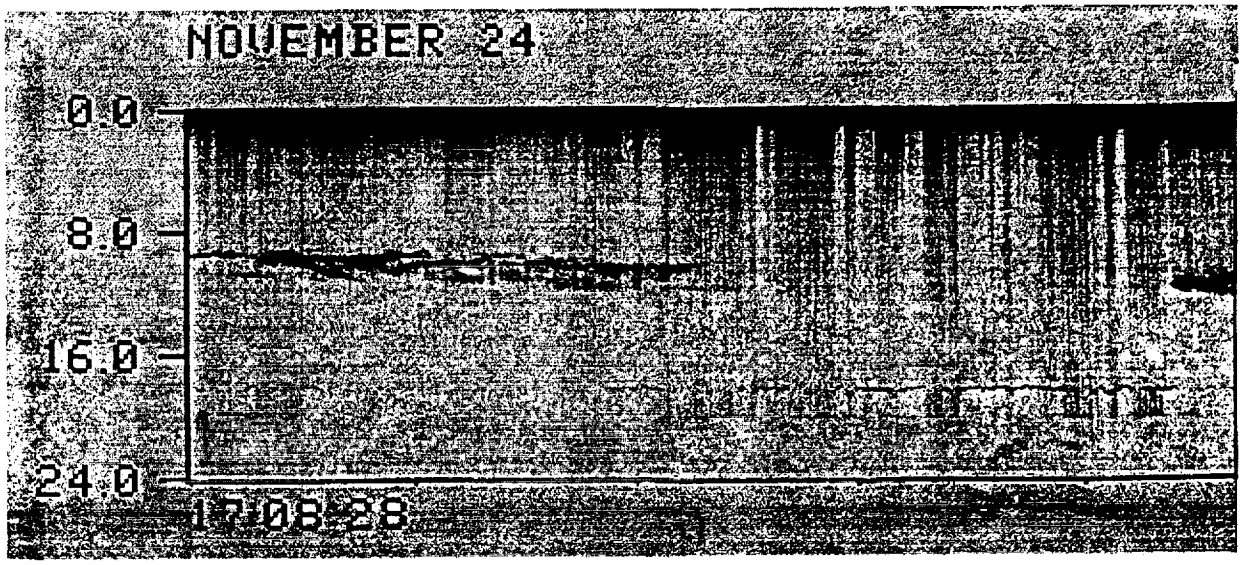

Fig. 1 Lidar data image corresponding to the EOC data for Fig 2. The vertical scale is height in kilometers from the aircraft altitude. Each horizontal tick is 2 minutes or about 24 km distance.

A case that was analyzed is from a flight on November 24, 1991 over the Gulf of Mexico. The lidar cloud structure cross section for the case is shown in Fig. 1. The two lower linear features are signals from a broken stratus deck and ocean surface. Fig. 2 gives the result for the bi-directional reflectance of the cirrus formation shown near the beginning of the data in Fig. 1. Result are shown for three small cloud areas and the overall image.

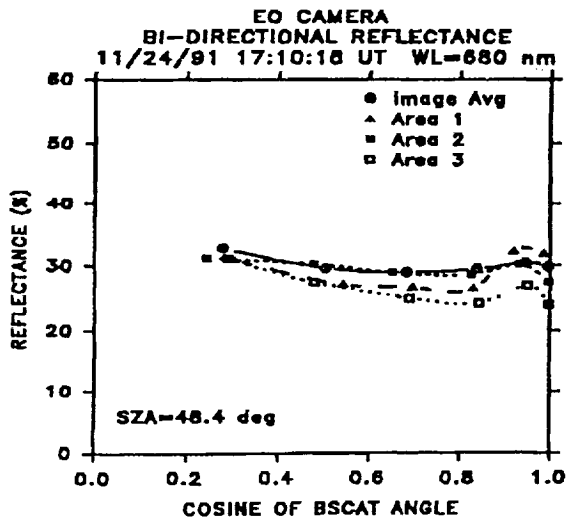

Fig. 2 Observed values of the angular dependence of a cloud scene during the 1991 cirrus experiment.

For a comparison, modeled cloud reflection curves are given in Fig. 3. The values were modeled by discrete ordinate calculations (Nakajima,1988). Phase functions for water and ice model cloud particle distributions were used. The water distribution assumed 10 um spheres and the ice phase function was that of Takano and Liu (1989).

Area 1 of Fig. 2 is the region with the least probability to be contaminated by reflectance of the underlying stratus clouds. The measured reflectance function agrees with the modeled ice cloud better than for the functions calculated for water. However even for area 1 the reflectance as a function of angle is flatter than for the calculated ice cloud curve. It is of interest to note that the scene image average with cirrus over broken status gives a much flatter function of reflectance versus angle than for either the water or ice models. For comparison, another measured angular reflection function is shown in Fig. 4. The scene of Fig. 4 is a marine stratus cloud acquired during an ASTEX flight. The measured function agrees well with the reflectance

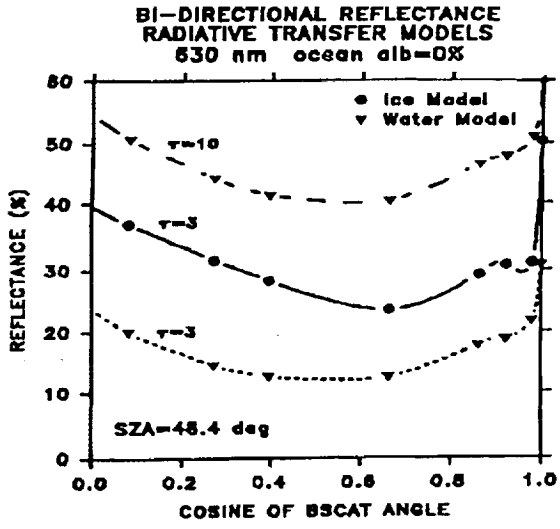

Fig. 3 Calculations of the angular reflection function for various cloud types.

function calculated for a water cloud of an optical thickness of approximately eight.

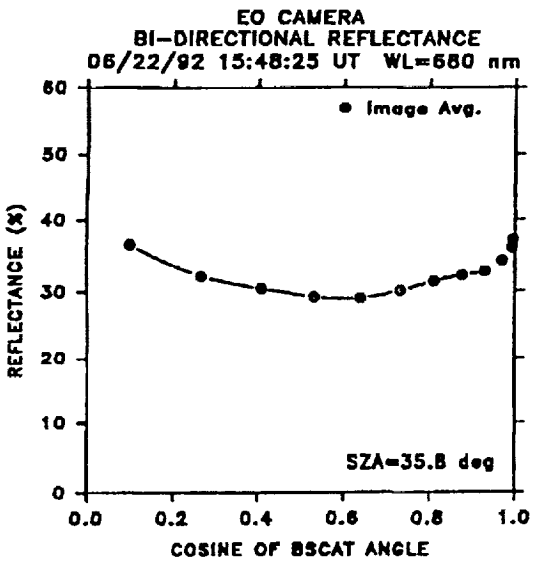

Fig. 4 Observation of the angular reflection function for a homogeneous marine stratus cloud.

The initial measurements from the EOC instrument indicate valid results. At present analysis algorithms are being automated in order that a large variety of cloud types may be investigated. In addition to data from the cirrus and ASTEX experiments, we now have a large set of measurements for tropical cirrus from the TOGA/COARE experiment. From lidar, spectral visible and infrared radiometer and flux measurements from the ER-2, it is thus possible to characterize cloud particle type and size, cloud optical thickness and emissivity. When combined with the results from the new translinear scanning radiometer instrument, a comprehensive characterization of the dependence of angular reflection function and other radiation paramters on cloud type should be possible.

References

J.D. Spinhirne, W.D. Hart, Mon. Wea. Rev., 2329-2343, 1990.

Y. Takano and K-N. Liou, J. Atmos. Sci., 46, 3-19, 1989.

T. Nakajima and M. Tanaka, J. Quant. Spectrosc. Radiat. Transfer, 40, 51-69, 1988.

55-47
197505
N94-22297

Optical Properties of Cirrus Derived from Airborne Measurements During FIRE IFO II

Francisco PJ Valero, Peter Pilewskie, Anthony Bucholtz, and Steven Platnick

NASA Ames Research Center, Moffett Field, CA

1. Introduction

The Radiation Measurement System (RAMS) on board the NASA ER–2 was used to acquire several optical parameters of interest during the FIRE Cirrus IFO II. In this abstract we present results from the November 26 IFO when the ER–2 flew over the Coffeyville airport hub site. We show retrieved optical thickness and cloud temperature, along with optical thickness obtained from RAMS instruments on the NCAR Sabreliner and at the surface site B. Independent retrieval of optical thickness, from the ER–2 and at the surface, are in agreement during the overpasses. Cirrus optical depths, derived from each platform, ranged between 1 and 2.

2. Instrumentation

RAMS was comprised of several broad and narrow–band, hemispheric and narrow–field–of–view, solar, near–infrared, and thermal infrared radiometric sensors during the FIRE IFO II. The following instruments were used to acquire the data described in this paper. Another paper will discuss the comparison of model calculations with measured broadband flux.

a) Narrow–Field–of–View IR Radiometer (NFOV): The NFOV is a dual channel infrared radiance measuring device, using a liquid nitrogen cooled blackbody reference. The two channels have 1 μm bandwidths, with band–centers at 6.7 μm and 10.5 μm. The NFOV was mounted off to the side of the ER–2 fuselage and was nadir–looking. Another NFOV was deployed at the Coffeyville airport hub, site B.

b) Total–Direct–Diffuse Radiometer (TDDR): The TDDR is a seven channel visible and near–infrared radiometer with a rotating shadow band capable of separating the direct and diffuse components of the solar flux. The bandwidths are narrow (10 nm) and are located outside atmospheric absorption bands, isolating the optical effects due to aerosol. The TDDR was pointed in the zenith direction on the ER–2, and Sabreliner, and at the surface in Coffeyville.

3. Optical Thickness and Temperature

Cirrus optical depth was measured from three platforms: ER–2, using the 2–channel infrared NFOV; Sabreliner, using the 7–channel visible and near–infrared TDDR; and surface (site B at the Coffeyville airport), also using the TDDR.

a) ER–2

The 6.7 and 10.5 μm NFOV channels are used to determine remotely cirrus visible (0.55 μm) optical thickness and cloud temperature, following the method described in Liou, et al.(1990). Clear–sky radiance at cloud base must first be determined, and fortunately, for the November 26 case study, the ER–2 was on site over Kansas before cirrus had moved in. The Planck black body radiance at both wavelengths is computed using Newton's iteration, from which cloud temperature is determined. The cloud emmissivity is found from the ratio (at either wavelength, since ϵ is only very weakly dependent on λ) of the cloud–top upwelling radiance to the blackbody radiance. Cirrus optical thickness,

τ, then, is found using the parameterization

$$\epsilon = 1 - \exp(a\tau^b),$$

where a is –0.468 and b is 0.988.

b) Sabreliner

Using the TDDR on the Sabreliner affords the advantage that an absolute calibration is unnecessary, and the derived optical thickness pertains to shallow layers, eliminating both Rayleigh extinction and extinction due to aerosols between cloud top and the top of the atmosphere. The TDDR separates the direct and diffuse components of the downwelling flux at each Sabreliner flight level. Direct flux at one level (in arbitrary units) is related to that at any other level through Beer's Law, determining the layer extinction.

c) Surface

The surface TDDR measurement also separates direct and diffuse flux but unlike the Sabreliner measurements, direct flux must be compared to exoatmospheric values derived from independent calibrations. Resultant optical thickness refers to the entire column above the detector. Rayleigh extinction is simply removed; to isolate cirrus optical depth, however, clear–sky measurements are used to determine aerosol extinction.

On November 26, between 1730 and 2000 GMT, the ER–2 flew nearly east–west racetracks with the western pivot point over Coffeyville (figure 1). In figure 2, the ER–2 NFOV retrieved cloud optical depth is shown as a function of time, along with the simultaneous ground–based measured optical depth. Keep in mind that the data includes the entire ER–2 racetrack, only a small portion of which is over Coffeyville. Furthermore, the surface–derived TDDR optical thickness pertains to that section of cloud toward the solar direction, not the zenith point where the ER–2 retrievals were made. Small arrows indicate when the ER–2 was nearly overhead at Coffeyville. At those times, agreement between the two datasets (and independent retrieval methods) is outstanding. Furthermore, the same general trend appears in both data sets, i.e., the gradual increase in cloud thickness as time progresses.

Figure 3 shows the ER–2 retrieved cloud temperature, together with the 6.7 μm and 10.5 μm brightness temperature. All three curves converge as the cloud becomes thicker (blacker). In figure 4, the background stratospheric aerosol optical depth is plotted as a function of wavelength. This spectrum was compiled from averages of spectra acquired from the ER–2 TDDR during the racetracks. Note that these relatively high levels of "background" extinction indicate the strong influence of the Pinatubo volcanic cloud at that time.

Optical depths from the Sabreliner are shown in figure 5. The Sabreliner flew twice during the November 26 IFO, in the morning (local time) and afternoon. We felt it more appropriate to show the morning flight data here for the following reasons: Although this flight occurred prior to the ER–2 overflight, it was in an region northwest of Coffeyville, the same direction from which the cirrus deck later approached. The afternoon flight, while directly above the hub site, occurred as the largest mass of highest cirrus was moving to the east. Consequently, the afternoon flight legs between 7 and 9 km show very thin cirrus, not directly comparable to that shown in figure 2.

4. Conclusions

Broad intercomparison between the multiple–platform derived optical depths for the November 26 IFO shows the general features of the cloud structure over southeastern Kansas. Several overpasses of the ER–2 at Coffeyville allow for comparison of two independent methods of determining cirrus optical depth; results show outstanding agreement between the 2–channel infrared method and the TDDR derived optical thickness. Comparison of results with in situ microphysical measurements, in particular the Sabreliner derived vertical profiles of optical depth, will be vital to relating the derived optical properties to various broadband radiation measurements.

5. Reference

Liou, KN, SC Ou, Y Takano, FPJ Valero, and TP Ackerman, *J. Appl. Meteor.*, 29, 716–726, 1990.

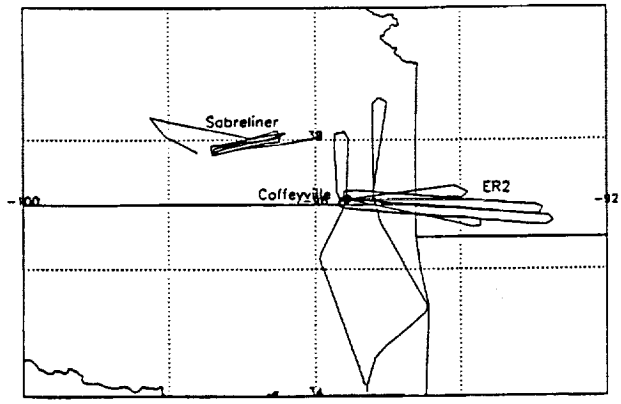

Figure 1. ER–2 Sabreliner (am) flight tracks on November 26, 1991.

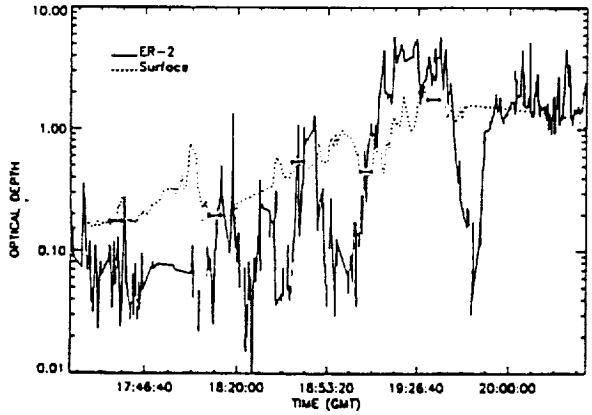

Figure 2. ER–2 2–channel IR retrieval (solid curve) and surface TDDR measurement (dotted) of mid–visible (0.5 μm) optical depth.

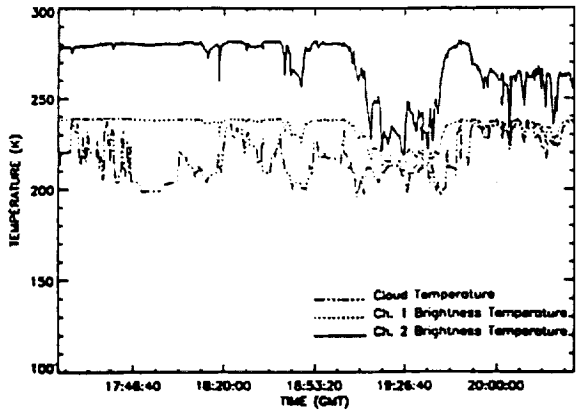

←Figure 3. 6.7 μm (dotted curve) and 10.5 μm (solid) cloud brightness temperature, with retrieved cloud temperature (dot–dash).

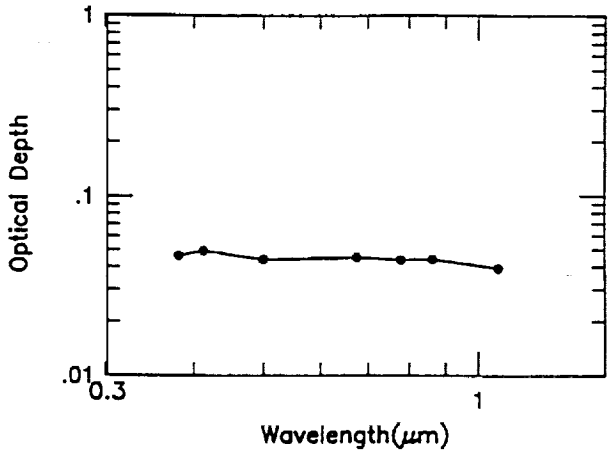

Figure 4. Stratospheric aerosol extinction measured from the ER–2 (TDDR).

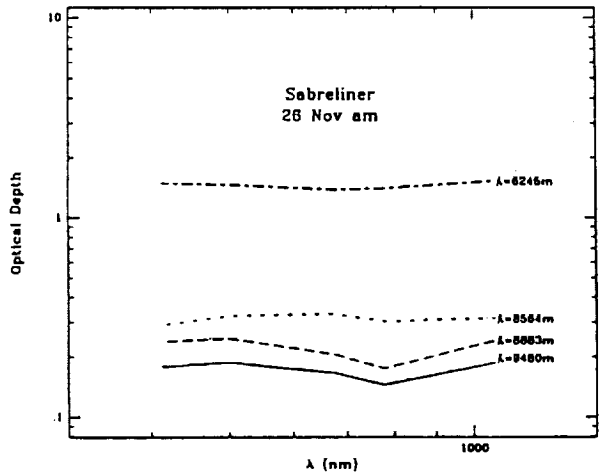

Figure 5. Sabreliner TDDR measurements of cirrus optical thickness. Leg altitudes are indicated on the right.

56-47
197506
p. 3

N94-22298

INTERCOMPARISON OF MAS, AVIRIS, AND HIS DATA FROM FIRE CIRRUS II

Liam E. Gumley[1], Michael D. King[2], Si-Chee Tsay[3], Bo-Cai Gao[3], G. Thomas Arnold[4]

(1) Research and Data Systems Corporation, 7855 Walker Drive, Greenbelt MD 20770
(2) Earth Sciences Directorate, NASA Goddard Space Flight Center, Greenbelt MD 20771
(3) Universities Space Research Association, NASA Goddard Space Flight Center, Greenbelt MD 20771
(4) Applied Research Corporation, 8201 Corporate Drive, Landover MD 20785

Introduction

The NASA ER-2 flight on December 5th, 1991 is unique among the FIRE Cirrus II missions in that data were acquired simultaneously by the MODIS Airborne Simulator (MAS), the Airborne Visible/Infrared Imaging Spectrometer (AVIRIS), and the High Resolution Interferometer Sounder (HIS). These data represent a unique source of information about the spatial and spectral properties of cirrus clouds. The MAS is a new instrument which will aid in defining algorithms and building an understanding of the ability of the Moderate Resolution Imaging Spectroradiometer (MODIS) to remotely sense atmospheric conditions for assessing global change. In order to establish confidence in the absolute calibration accuracy of the MAS radiances, an inter-comparison of MAS radiances with AVIRIS and HIS has been undertaken.

The MAS is a scanning spectrometer with 50 spectral channels in the wavelength range 0.55 to 14.3 microns. During FIRE Cirrus II a set of 11 of these spectral channels was recorded in flight at 8 bits per channel (visible/near-IR) and 10 bits per channel (IR). The scanner views a swath of approximately 38 kilometers across track, and records 716 earth view pixels per scan (6.25 scans per second) with a 2.5 milliradian instantaneous field of view. Gyroscopic roll correction is used to stabilize the viewing geometry. Calibration of the visible/near-IR channels is done using integrating sphere sources on the ground before and after flight missions. Calibration of the IR channels is done using two onboard blackbody sources. A key reason for comparing MAS data to AVIRIS and HIS data is the determination of the radiometric accuracy of the MAS visible/near-IR and IR channels.

The AVIRIS is an imaging spectrometer with 224 spectral channels in the wavelength range 0.4 to 2.5 microns. The scanner views a swath of approximately 11 kilometers across track, and records 614 pixels per scan (12 scans per second) with a 1.0 milliradian instantaneous field of view. Data are digitized at 10 bits per pixel. Calibration is done using an integrating sphere on the ground, and is monitored inflight by a reference lamp source. Absolute calibration accuracy is better than 7%, and relative calibration accuracy is better than 2%.

The HIS is a nadir viewing IR interferometer with $\approx$ 2000 spectral channels in the wavelength range 3.7 to 16.7 microns and a 100 milliradian field of view. Radiance spectra are produced using calibration information from 2 onboard blackbody sources. Absolute calibration accuracy is better than 1 K and relative calibration accuracy is on the order of 0.1 K.

MAS and AVIRIS intercomparison

At the time of the FIRE Cirrus 1991 deployment, the MAS had 5 channels in the visible/near-IR region with central wavelengths at 0.681, 1.617, 1.933, 2.088, and 2.139 microns. At this time the AVIRIS was experiencing noise problems in some of the longer wavelength channels, and thus only the data from MAS channels 2 (0.681 microns) and 3 (1.617 microns) could be used in the comparison. The MAS and AVIRIS scenes were examined to find areas of overlap, since the AVIRIS does not record continuously

during flight. Within regions of overlapping imagery, the MAS scenes were examined to find small areas of uniform brightness. Once such areas were located, a 10x10 pixel box was fitted over the region and the average radiance was computed in channels 2 and 3. The corresponding area was then located on the AVIRIS imagery, and a box of AVIRIS pixels was marked off to cover the same region as the MAS 10x10 pixel box. An average AVIRIS spectrum was then computed over the box. This average spectrum was convolved with the MAS spectral response curves for channels 2 and 3, and the corresponding radiances were computed. It should be noted that while a laboratory measured spectral response was available for MAS channel 2, none was available for channel 3. Thus using the predicted central wavelength and bandwidth at 50% response, a Gaussian spectral response was computed. A table of the radiance comparisons for 6 cases is presented below. All of these were cloud features over the Gulf of Mexico within $\pm$ 10 minutes of 1600Z. ER-2 takeoff was at 1430Z.

Case number, Cloud type	Channel 2 (0.681 micron) radiance ($W\ m^{-2}\ sr^{-1}\ \mu m^{-1}$)			Channel 3 (1.617 micron) radiance ($W\ m^{-2}\ sr^{-1}\ \mu m^{-1}$)		
	MAS	AVIRIS	Δ%	MAS	AVIRIS	Δ%
1, thick cirrus	152.56	148.92	2.4	11.77	12.97	-10.2
2, thin cirrus	35.74	33.30	7.3	2.90	2.74	5.8
3, thin cirrus	25.52	26.68	-4.3	2.14	2.43	-13.5
4, thin cirrus	25.01	25.41	-1.6	2.20	2.18	0.9
5, convective	153.66	149.93	2.5	17.72	20.30	-14.5
6, thin cirrus	20.73	20.39	1.7	1.31	1.28	2.3

While 6 cases is not a large sample, it can be seen that the MAS is providing radiances which are in general agreement with the AVIRIS. The MAS is calibrated on the ground using an integrating sphere, and does not have an in-flight visible/near-IR calibration capability. Thus the demonstration that MAS radiances are close to AVIRIS radiances gives some measure of confidence in the MAS in-flight calibration. However, some calibration uncertainties are still under investigation. Cold chamber testing of the MAS in February 1992 showed decreasing sensitivity with decreasing temperature in channels 3, 4, 5, and 6. For example in channel 3, an approximately linear decrease in instrument sensitivity of 30% was observed when the chamber was cooled from 20° C to -35° C. It is not yet clear whether this effect occurred during flight of the MAS. Temperature sensors attached to the MAS during the FIRE deployment showed a gradual decrease in head temperature over the course of the flight to a minimum of -30 to -35° C. However this minimum temperature is not reached until the end of a flight, which may be 4 to 5 hours long. The comparisons presented here are at 1.5 hours after ER-2 takeoff, and therefore do not represent the coldest instrument temperature. In future work, MAS and AVIRIS radiances will be compared over the course of the complete ER-2 flight on December 5th, to determine whether the sensitivity decrease observed in the cold chamber is observed in flight. It should be noted that after modifications to the MAS, cold chamber tests in May and August 1992 showed a reduction in temperature sensitivity, however this has not been verified in-flight. Data from future MAS and AVIRIS co-flights (SCAR-A July 1993) will be used to further investigate the calibration of the MAS visible/near-IR channels.

MAS and HIS comparison

At the time of the FIRE Cirrus 1991 deployment, the MAS had 6 channels in the IR region with central wavelengths at 3.75, 4.54, 4.70, 8.80, 10.95, and 11.95 microns. The HIS acquired data in all these spectral regions except 3.75 microns. Therefore to examine the calibration of the MAS, co-located MAS and HIS radiances were compared. The HIS data used were apodized radiance spectra, averaged over two scan directions. This gives a footprint of approximately 3.2 km along track and 2 km across track. This corresponds to a MAS scan region of approximately 91 pixels along track and 43 pixels across track. Due

to an offset between the MAS and HIS clocks, it was necessary to manually match the HIS along track data to the MAS data. It is estimated that this was done to around $\pm$ 5 seconds, which corresponds to $\pm$ 31 MAS scanlines. Thus some offset may still remain between the HIS footprints and the averaged MAS footprints. Once the co-located footprints were found, the HIS radiance spectrum was convolved with the spectral response curve for each MAS IR channel to produce an equivalent radiance, which was then converted to brightness temperature. Average radiances and brightness temperatures were computed over the corresponding 91x43 pixel MAS footprints. It should be noted that while a laboratory measured spectral response was available for MAS channel 11, none was available for channels 8, 9, 10, and 12. Thus using the predicted central wavelength and bandwidth at 50% response, Gaussian spectral responses were computed. A table of comparison results is shown below. The 76 co-located footprints were over land on a transit leg from the Gulf of Mexico to Coffeyville KS. Most of the flight track was over clear skies, however patchy cirrus was present in places.

MAS IR Absolute Accuracy (Compared to co-located HIS fields of view) 76 mostly clear sky 91x43 MAS pixel averages over land, 1651Z to 1721Z, 5-DEC-91			
Channel	Wavelength (microns)	MAS-HIS Average (K)	MAS-HIS RMS (K)
9	4.54	0.77	0.58
8	4.70	-1.68	0.75
10	8.80	0.37	1.07
11	10.95	0.51	0.91
12	11.95	0.27	1.01

Plots of the along track comparison of MAS and HIS footprints are shown overleaf. Although the RMS of the average difference is quite large with respect to the average difference itself, it is clear that reasonable brightness temperatures are derived from the MAS. Several sources of noise cause the RMS to be large with respect to the mean. First, the previously mentioned collocation error of $\pm$ 5 seconds means that over rapidly varying scenes, the HIS and MAS may view significantly different average temperatures. Second, the MAS data contain noise introduced by the detector electronics, and the aircraft power system. An estimate of the noise in the MAS IR imagery was obtained by computing the average and RMS values of a block of 50x50 pixels over a region of cloud-free ocean. From the RMS radiance values, the noise equivalent delta temperature was computed. The results for all IR channels are shown below.

MAS IR Relative Accuracy (Noise Equivalent Delta Temperature) Clear sky 50x50 MAS pixel average over water, scanline 47951, 1634Z, 5-DEC-91				
Channel	Wavelength (microns)	Bits recorded	Average Temperature (K)	NEDT (K)
7	3.75	8	289.19	1.62
9	4.54	10	274.25	0.99
8	4.70	8	284.88	0.70
10	8.80	10	290.06	0.32
11	10.95	10	291.12	0.43
12	11.95	10	289.89	0.82

The relatively large negative bias (MAS colder than HIS) in channel 8 suggests that the spectral response may not be accurately approximated by a Gaussian, or that its position is slightly different than the estimated central wavelength. It is possible that the center of the spectral response may shift during flight. The comparisons shown above were all within the space of 30 minutes, so variation throughout the flight has not been sampled. It is possible that the biases shown above drift with time over the course of a flight, as the instrument temperature changes. This will be examined in future work.

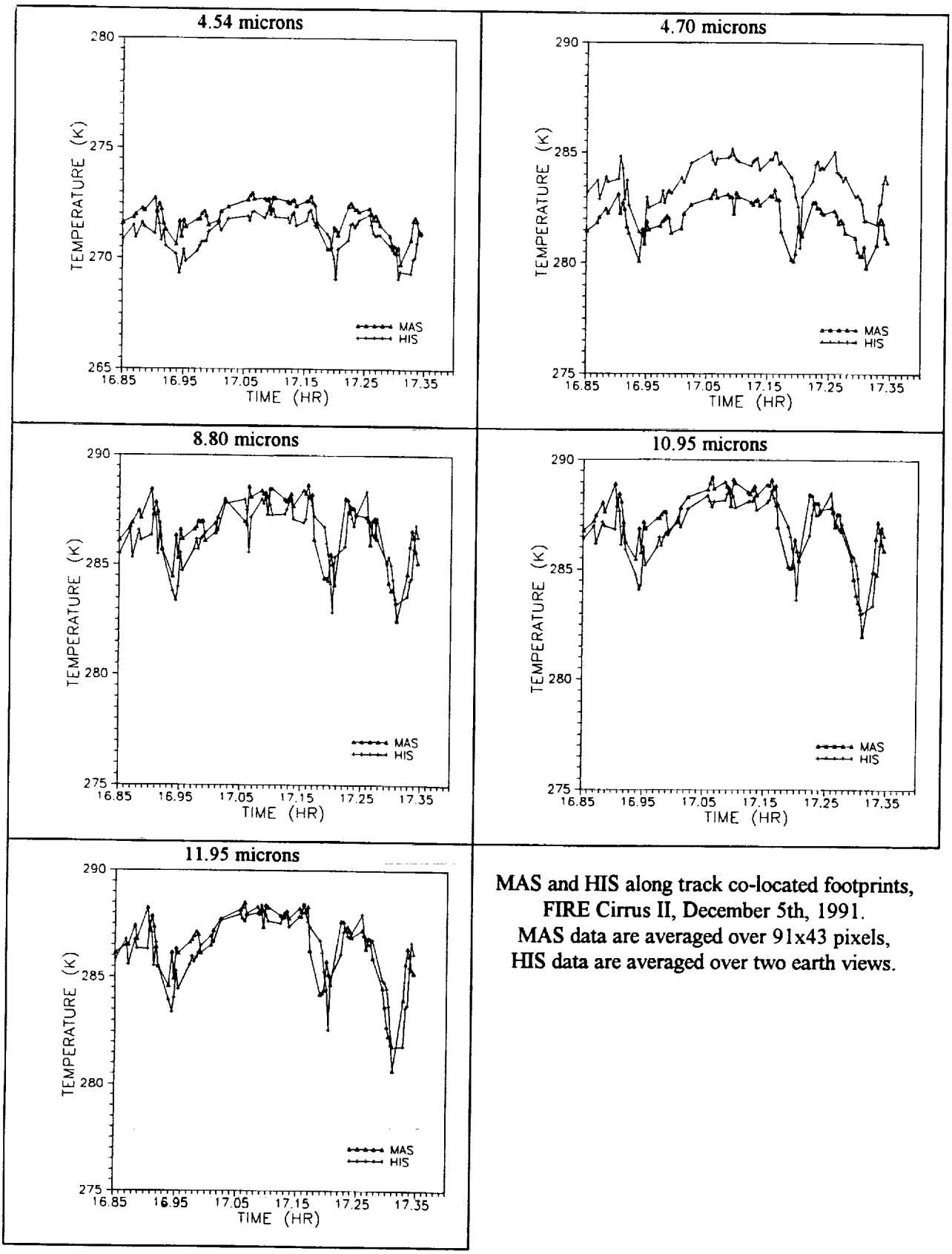

MAS and HIS along track co-located footprints, FIRE Cirrus II, December 5th, 1991. MAS data are averaged over 91x43 pixels, HIS data are averaged over two earth views.

S7-47
197507
p. 4

N94-22299

COMPARISON OF RADIATION AND CLOUD PARAMETERS DERIVED FROM SATELLITE AND AIRCRAFT MEASUREMENTS DURING FIRE-II CIRRUS IFO

Patrick W. Heck, Shalini Mayor, and David F. Young, Lockheed Engineering and Sciences Company, Hampton, VA 23666

Patrick Minnis, Atmospheric Sciences Division, NASA Langley Research Center, Hampton, VA 23681

Yoshihide Takano and Kuo-Nan Liou, Department of Meteorology, University of Utah, Salt Lake City, UT 80101

James D. Spinhirne, NASA Goddard Space Flight Center, Greenbelt, MD 20771

INTRODUCTION

Meteorological satellite instrument pixel sizes are often much greater than the individual cloud elements in a given scene. Partially cloud-filled pixels can be misinterpreted in many analysis schemes because the techniques usually assume that all of the cloudy pixels are cloud filled. Coincident Landsat and Geostationary Operational Environmental Satellite (GOES) data (Minnis and Wielicki, 1988) and degraded-resolution Landsat data (Wielicki and Parker, 1992) have been used to study the effects of both sensor resolution and analysis techniques on satellite-derived cloud parameters. While extremely valuable for advancing the understanding of these effects, these previous studies were relatively limited in the number of cloud conditions that were observed and by the limited viewing and illumination conditions. During the First ISCCP Regional Experiment (FIRE) Phase II (November 13 - December 7, 1991), the NASA ER-2 made several flights over a wide range of cloud fields and backgrounds with several high resolution sensors useful for a variety of purposes including serving as ground truth for satellite-based cloud retrievals. This paper takes a first look at utilizing the ER-2 for validating cloud parameters derived from GOES and NOAA-11 Advanced Very High Resolution Radiometer (AVHRR) data.

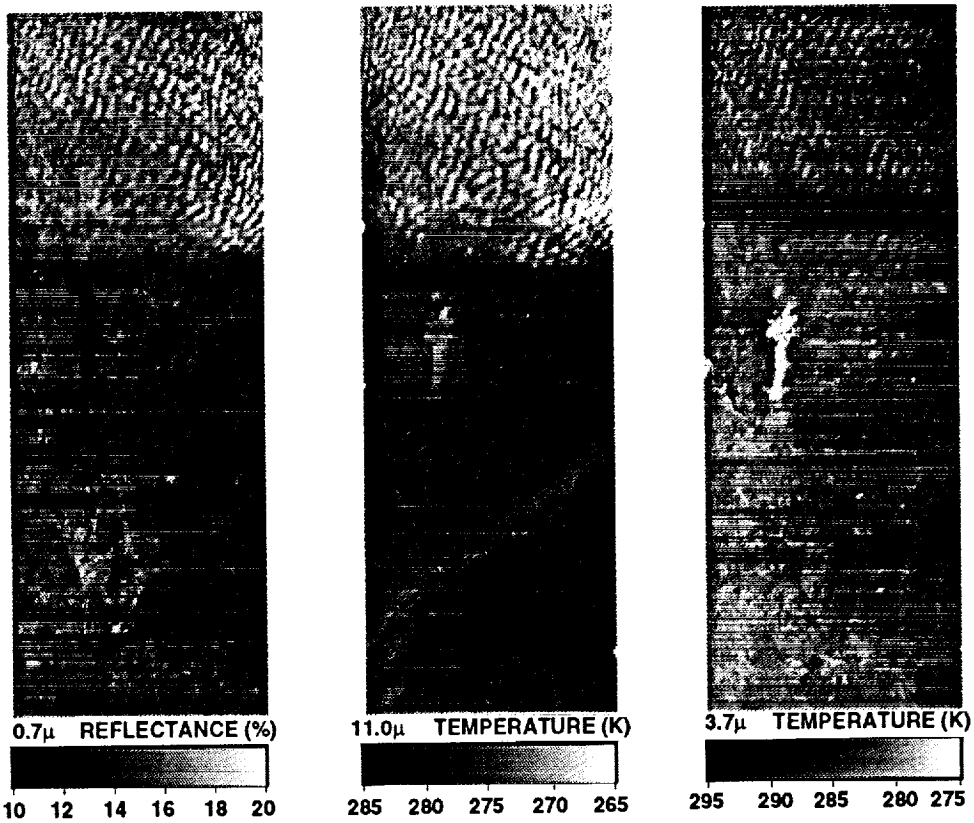

Fig. 1. MAS imagery for November 25, 1991, 1802 to 1810 UTC.

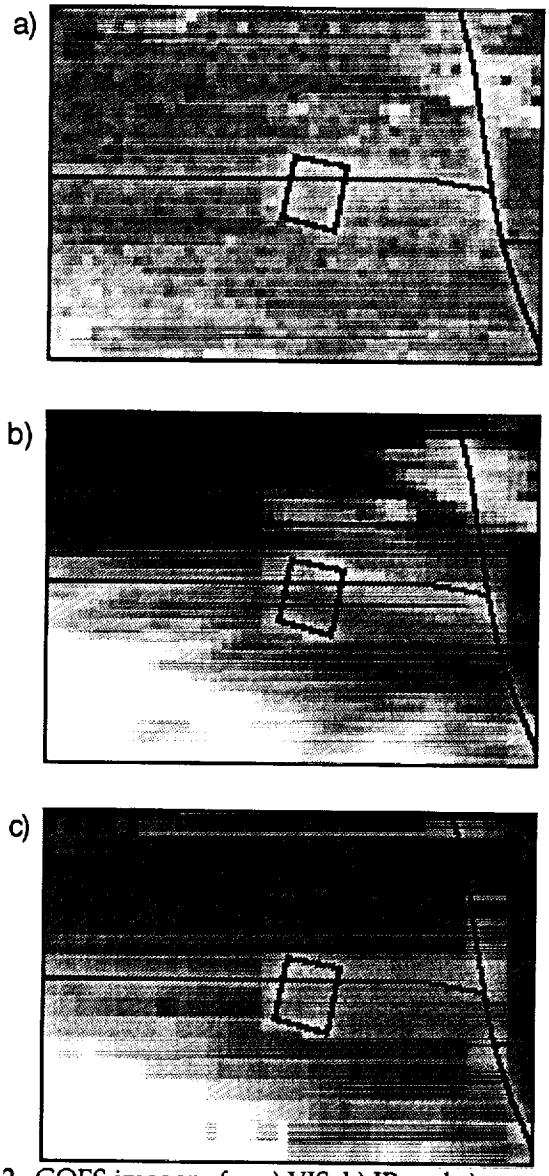

Fig. 2. GOES imagery for a) VIS, b) IR and c) NIR for November 25, 1991, 1820 UTC.

DATA AND METHODOLOGY

The MODIS Airborne Simulator (MAS; Gumley, 1993) on the ER-2 is a 12-channel crosstrack scanning radiometer that has a nominal footprint of 20 m at nadir yielding a swath width of 40 km. Channels 2, 7, and 11, corresponding to wavelengths 0.7, 3.7, and 11.0 μm, respectively, are used here. Viewing zenith angle varies continuously with each pixel along the swath from 0° at nadir to 40° at the edges of the swath. The nadir viewing 0.63-μm lidar (Spinhirne et al., 1989) provides returns of cloud top height and, in thin cloud cases, cloud base height. Visible (~0.65 μm, VIS), infrared (~11.0 μm, IR), and near-infrared (~3.8 μm, NIR) radiances from the NOAA Advanced Very High Resolution Radiometer (AVHRR) and the Geostationary Operational Environmental Satellite (GOES) were matched as well as possible to the flight path of the ER-2 and the area viewed by the MAS. The AVHRR data were taken at a 1-km resolution near 2030 UTC, while the GOES data resolutions varied from 4 to 16 km depending on the wavelength. GOES VIS and IR data were taken every half hour, while the three-channel combination was available at 20 minutes after the UTC hour every third hour. Rawinsonde data taken nearest in space and time to the particular flight segment were used to relate temperatures to altitude. Cloud amount was determined using 5K IR temperature and 2% VIS thresholds.

Cloud amount, height, optical depth τ, and effective water droplet radius r_e were derived from the MAS and satellite data using the methodology described by Young et al. (1993). For the initial analyses, the MAS pixels were spatially degraded to ~4km resolution to avoid the extreme spatial variability in the clear-sky background seen in the high resolution data. Clear-sky reflectance and temperature were derived for each leg of the MAS data by normalizing the data to nadir using empirical limb-darkening and bidirectional reflectance models. A portion of the lowest reflectances and warmest temperatures were averaged to estimate the clear-sky conditions.

RESULTS

Figure 1 shows the MAS imagery for a flight segment over Coffeyville between 1802 and 1810 UTC, December 5, 1991. An altocumulus deck covers the northern third of the segment which includes Coffeyville. An apparently clear area in the center of the leg includes an elongated lake. A thin cirrus veil evident in the lower third of the imagery covers Bartlesville, Oklahoma. The ER-2 lidar reveals that the altocumulus deck along the center of flight path is located at ~ 3.8 km above mean sea level. While the cirrus is only evident in Fig. 1 over the southern third of the area, the ER-2 indicates that cirrus is over the center line of the entire flight leg. The thickest part of the cirrus corresponds to the clouds visible in Fig. 1. The top of the cirrus varies from about 8.7 km over the altocumulus to 10.1 km in the southern part of the leg. The respective cirrus base heights range from 8.5 km to 6.8 km. Additional contrast enhancement of the MAS imagery failed to reveal the thin cirrus over the central portion of the imagery.

The corresponding GOES imagery for 1820 UTC is given in Fig. 2. The area covered by the MAS swath is indicated by the box. The solar zenith, viewing zenith, and relative azimuth angles are 57°, 43°,

and 172°, respectively. There is minimal variation in the GOES VIS reflectances (Fig. 2a) with little indication of clouds. The IR data (Fig. 2b) reveal the altocumulus deck and suggest some cirrus in the lower half of the flight box. There is only slight variability in the NIR brightness temperatures in Fig. 2c. The altocumulus clouds appear much darker north and northeast of the MAS area.

A 2-dimensional histogram of the MAS 11.0 - 3.7 μm brightness temperature differences (BTD) is plotted in Fig. 3 for the MAS data. The multispectral analysis of the northern half of the box yielded a cloud temperature of 261K and a mean $\tau = 2.1$. The cloud top is at ~ 3.8 km. According to the MAS retrieval, the altocumulus clouds cover 34% of the entire scene. The multispectral analysis could derive a value of r_e for only 40 of the 60 cloudy pixels in the northern part of the scene. The remaining 20 were too dark for the analysis to distinguish from the background. Those pixels are seen on the southwestern side of the altocumulus deck and may include part of the lake which is as cold as some of the altocumulus pixels. The optical depth for the dark pixels is likely to be much less than the mean for the brighter pixels. The mean value of r_e retrieved from the brighter altocumulus pixels is 11.9 μm. The effective radii varied from only 10 to 12 μm across the entire swath.

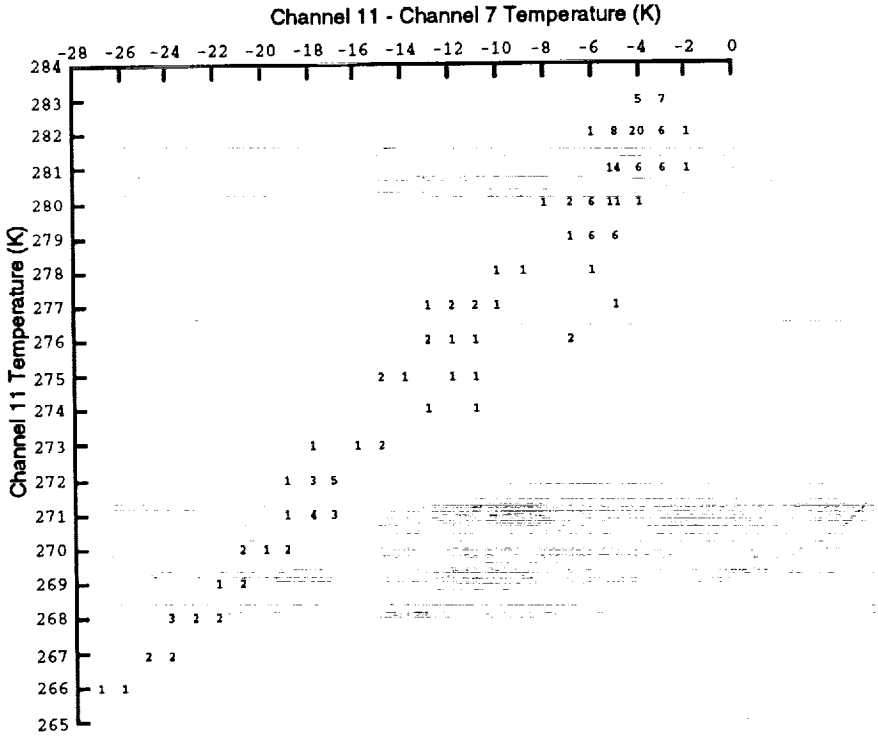

Fig. 3. 2-dimensional histogram of MAS Channel 11 (11.0μ) and Channel 11-Channel 7 (3.7μ) temperature differences.

The corresponding GOES data were analyzed with the VIS-IR technique yielding a midlevel deck with a radiating center at 3.7 km. The midlevel cloud cover was 31% and the optical depth was 1.05. The GOES VIS-IR analysis also yielded high level clouds covering 15% of the scene with a center at 9.9 km. The high cloud pixels were mostly darker than the clear scene so they were given the center altitude by default. The retrieved cirrus optical depth was 0.41. The 2-D GOES BTD histogram in Fig. 4 shows the bifurcation between the cirrus and the altocumulus clouds. This difference is not evident in Fig. 3. The extreme variation in the MAS viewing and relative azimuth angles tends to smear the angular dependencies of the BTDs in Fig. 3. Over the altocumulus area, the initial GOES multispectral analysis could only retrieve r_e for 6 of the 12 cloudy pixels yielding a mean value of 16 μm. Overall, the GOES pixels were too dark to provide reasonable solutions to the models.

Considering the differences in the datasets, the GOES and MAS retrievals yield very similar results for the thin altocumulus field. Both analyses placed the retrieved cloud deck within the uncertainty limits of the lidar data. Cloud fraction and optical depth, if the darker MAS pixels are

included, are also very close for both datasets. Additional analysis is needed for the cirrus portions of the scene.

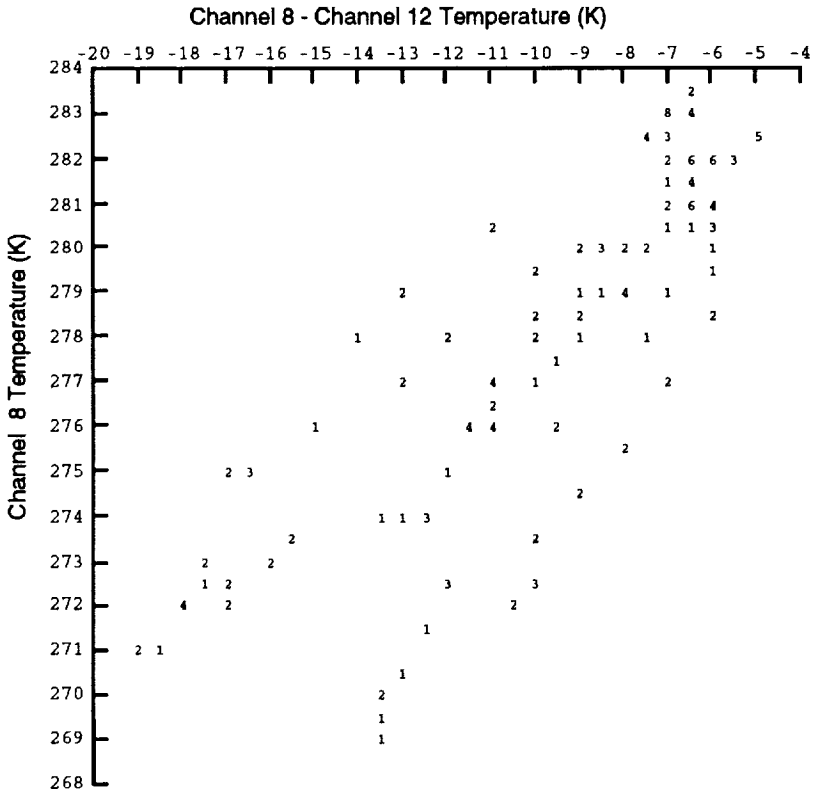

Fig. 4. 2-dimensional histogram of GOES Channel 8 (11.0μ) and Channel 8-Channel 12 (3.8μ) temperature differences.

CONCLUDING REMARKS

Preliminary analysis of the first matched GOES and ER-2 imagery shows that the aircraft data are very useful for validating the satellite cloud retrievals. This analysis has also demonstrated that, despite some limitations due to dim pixels, the multispectral analysis appears to be robust over a variety of viewing angles, at least, for water droplet clouds. While there was good agreement between the GOES and MAS results, neither imager was able to detect the subvisual cirrus seen by the lidar over the entire flight segment. It remains to be seen if the other channels on the MAS can distinguish the thin cirrus in this scene. There are many other ER-2 flight legs over a wide variety of clouds that will be examined during the continuation of this study.

REFERENCES

Gumley, L. E., 1993: MODIS Airborne Simulator Level-1B Data User's Guide, Version 1.0. Draft Technical Memorandum. NASA Goddard Space Flight Center, Greenbelt, MD 20771, February.

Minnis, P. and B. A. Wielicki, 1988: Comparison of cloud amounts derived using GOES and Landsat data. *J. Geophys. Res.*, 93, 9385-9403.

Spinhirne, J. D., R. Boers, and W. D. Hart, 1989: Cloud top liquid water from lidar observations of marine stratocumulus. *J. Appl. Meteorol.*, **28**, 81-90.

Wielicki, B. A. and L. Parker, 1992: On the determination of cloud cover from satellite sensors: The effect of sensor spatial resolution. *J. Geophys. Res.*, 97, 12799-12823.

Young, D. F., P. Minnis, J. Snider, T. Uttal, J. M. Intrieri, and S. Matrosov, 1993: Comparison of cloud microphysical parameters derived from surface and satellite measurements during FIRE Phase II. *FIRE Science Conf.*, Breckenridge, CO, June 14-17.

58-47
197508
p. 4

N94-22300

Cloud Properties from the Analysis of AVHRR Observations for FIRE II

Xijian Lin and James A. Coakley, Jr.

College of Oceanic and Atmospheric Sciences
Oregon State University
Corvallis, OR 97331–2209

1. Introduction

Preliminary results are presented for cloud properties from the analysis of AVHRR observations for FIRE II. The properties were obtained from a combination of the spatial coherence method (Coakley and Bretherton, 1982) and a multispectral retrieval scheme (Lin and Coakley, 1993). Geographically gridded fields for the number of cloud layers were produced. For single-layered cloud systems, fractional cloud cover, cloud emission temperature, cloud emissivity and particle size were retrieved. Statistics on the properties of upper-level clouds and the Coffeeville cloud conditions are presented.

2. Method

The processing of AVHRR data obtained during FIRE II involved two steps. The first step used the spatial coherence method to distinguish between single and multilayered cloud systems and to obtain cloud-free radiances. Each satellite overpass was divided into subframes which, in this study, were arrays of 32 by 32 4–km pixels and were equivalent to $\sim$ 100−km scale regions. Cloud layer structure and cloud-free radiances were obtained for each subframe. The second step used a multispectral retrieval scheme to obtain cloud properties for those systems found to be single-layered within the $\sim$ 100−km scale subframes.

The multispectral retrieval scheme used an automated procedure for fitting two-wavelength radiance pairs obtained from radiative transfer calculations to those observed by satellite. In the radiative transfer calculations, the cloud was assumed to be single-layered and homogeneous in emission temperature and particle size throughout the 100–km scale region. The cloud particles were assumed to be ice spheres at one effective radius. Radiances observed in IR windows were taken to be given by:

$$I_i = (1 - A_c)I_{si} + A_c(e_i I_{ci} + t_i I_{si}) \tag{1}$$

where the subscript i represents the instrument channel number; A_c is the fractional cloud cover within the field of view (FOV); I_{si} is the cloud-free radiance; I_{ci} is taken to be given by the Planck function at the cloud emitting temperature; e_i and t_i are the mean emissivity and transmissivity for the cloud. Mie theory was used to calculate the single particle extinction efficiency, single

scattering albedo and asymmetry given the effective radius, R_{eff}. The Eddington approximation was used to calculate the cloud emissivity and transmissivity given the ice water path length.

Lin and Coakley (1993) describe the method of fitting (1) to observed satellite radiances. Figure 1 shows 11 and 12–μm radiance pairs calculated on the basis of (1). Figure 2 shows a typical fit to observations obtained during FIRE II. The observations are for a $\sim$ 100–km scale subframe. Each point in the figure gives radiances for a 4–km pixel. In this case the cloud emission temperature was 240°K and the effective radius was 4.0 μm. Based on the best fit, pixel-scale cloud emissivity and fractional cloud cover are obtained from the pixel's position in the radiance domain as given by the radiative transfer calculations. The 100–km scale cloud emissivity and fractional cloud cover are obtained by averaging the pixel-scale results.

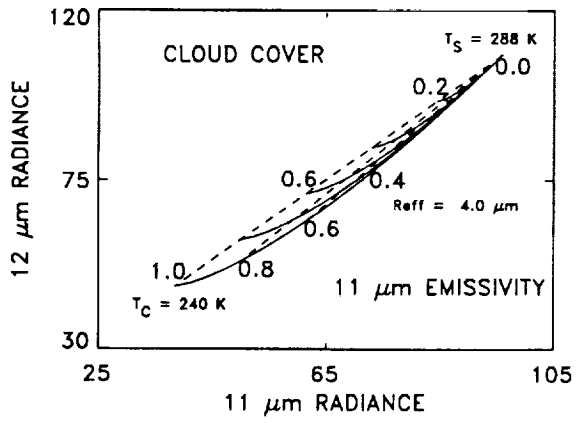

Figure 1 Theoretical relationships for 11 and–12 μm radiances ($mWm^{-2}sr^{-1}cm$) for single layered cloud system.

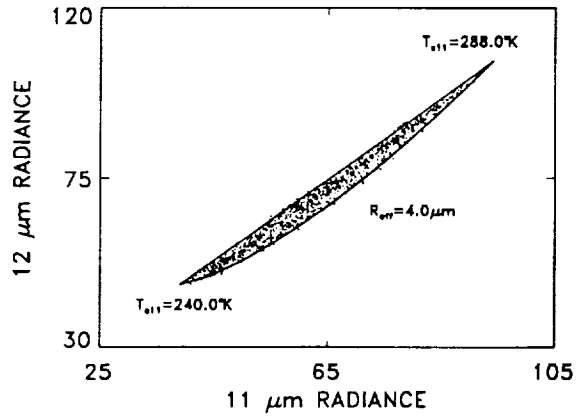

Figure 2 Fit of model results in Fig. 1 to satellite radiances obtained during FIRE II

3. Results

Based on the method described above, NOAA-11 daytime data have been processed. 44 overpasses were processed spanning November 13 — December 7. Statistics on the cloud systems obtained from the 44 overpasses are displayed in Figure 3. The Y-axis is the number of subframes. On the X-axis, CLR represents cloud—free subframes (100–km scale region); SGL: single-layered cloud system for which cloud properties were retrieved; XXX: single-layered cloud system for which properties were not retrieved because the clouds were either opaque or contained large particles; MLT: multi-layered cloud system, no retrievals; YYY: analysis failed for six overpasses because of missing scan lines and missing pixels, or other technique problems. It seems that cloud-free, single-layered and multi-layered cloud systems were equally common on the 100–km scale.

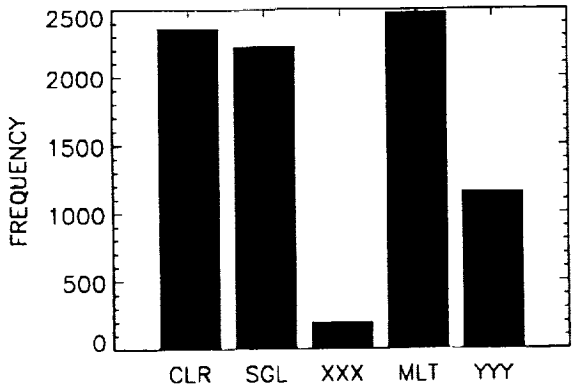

Figure 3 Cloud layer statistics.

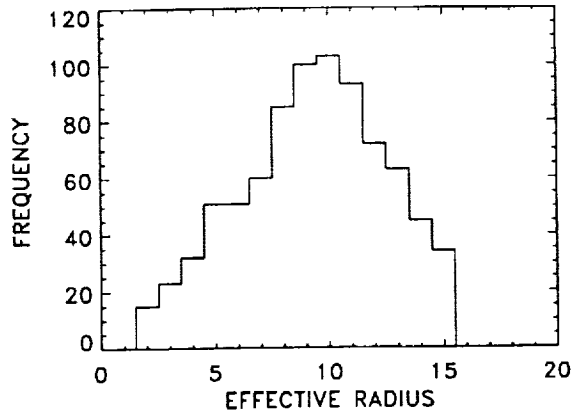

Figure 4 Upper-level cloud particle sizes. The X-axis is the effective radius and the Y-axis is the number of subframes.

Clouds with emission temperatures < 245°K were taken to be upper-level clouds, presumably cirrus. Figure 4 displays the distribution of retrieved particle sizes for upper-level clouds. Because of the simple radiative transfer model, the effective radius should be interpreted only as a size index. In addition, there were no retrievals for opaque clouds and for clouds with particles larger than 15 μm because there is no way to distinguish between opaque clouds and clouds having large particles on the basis of emission at 11 and 12 μm. Fortunately, only a small fraction of the subframes showed this ambiguity, as indicated in Fig. 3 by the results for XXX. In addition, for the upper-level single layered clouds the 100–km average 11–μm emissivities were found to be positively correlated with the regional scale cloud cover.

Satellite observed cloud properties over Coffeeville, Kansas were obtained for comparison with *in-situ* observations during the FIRE II experiment. Table 2 gives the cloud conditions over Coffeeville, Kansas. The results were obtained for the $\sim$ 100—km subframe which was nearest Coffeeville for each NOAA-11 overpass and for which the center longitude and latitude deviated from Coffeeville's by less than 2 degrees. In the table, ST is the start time of the overpass (HHMMSS, GMT); (X,Y): subframe center latitude, west longitude;Tc: cloud emission temperature if single-layered semitransparent clouds were observed.

4. Future Work

Based on the preliminary results, the following is under consideration for future work:

1. Process all of the AVHRR data obtained during the FIRE II experiment.
2. Obtain lidar and radar observations to compare retrieved cloud heights and to verify the retrieved results.
3. Carry on retrievals simultaneously using different combinations of 3.7–12 μm and 0.63–12 μm
4. Improve the radiative transfer model used in the retrieval.

Table 1 Cloud conditions over Coffeeville on indicated days in November and December.

10 /	11 /	12 /	13 / SGL ST=200300 (36.9, 95.2) Tc=233.1	14 / MLT ST=195200 (37.1, 95.0)	15 / SGL ST=212800 (36.4, 96.8) Tc=253.7	16 / SGL ST=211600 (36.3, 97.2) Tc=243.8
17 / CLR ST=210500 (36.3, 96.8)	18 / CLR ST=205200 (36.6, 96.0)	19 / MLT ST=203500 (36.8, 96.1)	20 / NO-data	21 / CLR ST=201000 (36.8, 95.2)	22 / MLT ST=195800 (36.7, 96.3)	23 / No-data
24 / SGL ST=212400 (36.9, 96.0) Tc=255.2	25 / SGL ST=211200 (36.7, 95.8) Tc=258.4	26 / SGL ST=210000 (36.5, 95.5) Tc=214.3	27 / No-data	28 / No-data	29 / No-data	30 / No-data
1 / No-data	2 / SGL ST=213000 (36.8, 97.4) Tc=238.7	3 / MLT ST=211800 (36.9, 94.4)	4 / CLR ST=210600 (36.7, 94.6)	5 / MLT ST=205500 (36.8, 96.0)	6 / CLR ST=203700 (37.0, 96.1)	7 / CLR ST=202400 (36.2, 96.0)

5. Acknowledgment

We thank Fu-lung Chang and Guy Boulanger for their help in data processing. This work was supported by NASA Grant NAG-1–1234.

6. References

Coakley, J.A., Jr. and F.P. Bretherton, 1982: "Cloud cover from high-resolution scanner data: Detecting and allowing for partially filled fields of view", *J. Geophys. Res.*, **87**, 4917–4932, 1982.

Lin, X. and J.A. Coakley, Jr., 1993: "Retrieval of properties for semitransparent clouds from multispectral infrared imagery data", *J. Geophys. Res.* (in press).

59-47
197509
8-4

N94-22301

DEVELOPMENT OF METHODS FOR INFERRING CLOUD THICKNESS AND CLOUD-BASE HEIGHT FROM SATELLITE RADIANCE DATA

William L. Smith, Jr., Lockheed Engineering and Sciences Co., Hampton, VA 23666

Patrick Minnis and Joseph M. Alvarez, Atmospheric Sciences Division, NASA Langley Research Center, Hampton, VA 23681-0001

Taneil Uttal, NOAA Wave Propagation Laboratory, Boulder, CO 80302

Janet M. Intrieri, Cooperative Institute for Research in the Environmental Sciences, University of Colorado, Boulder, CO 80309

Thomas P. Ackerman and Eugene Clothiaux, Department of Meteorology, Pennsylvania State University, University Park, PA 16802

INTRODUCTION

Cloud-top height is a major factor determining the outgoing longwave flux at the top of the atmosphere. The downwelling radiation from the cloud strongly affects the cooling rate within the atmosphere and the longwave radiation incident at the surface. Thus, determination of cloud-base temperature is important for proper calculation of fluxes below the cloud. Cloud-base altitude is also an important factor in aircraft operations. Cloud-top height or temperature can be derived in a straightforward manner using satellite-based infrared data. Cloud-base temperature, however, is not observable from the satellite, but is related to the height, phase, and optical depth of the cloud in addition to other variables. This study uses surface and satellite data taken during the First ISCCP Regional Experiment (FIRE) Phase-II Intensive Field Observation (IFO) period (November 13 - December 7, 1991) to improve techniques for deriving cloud-base height from conventional satellite data.

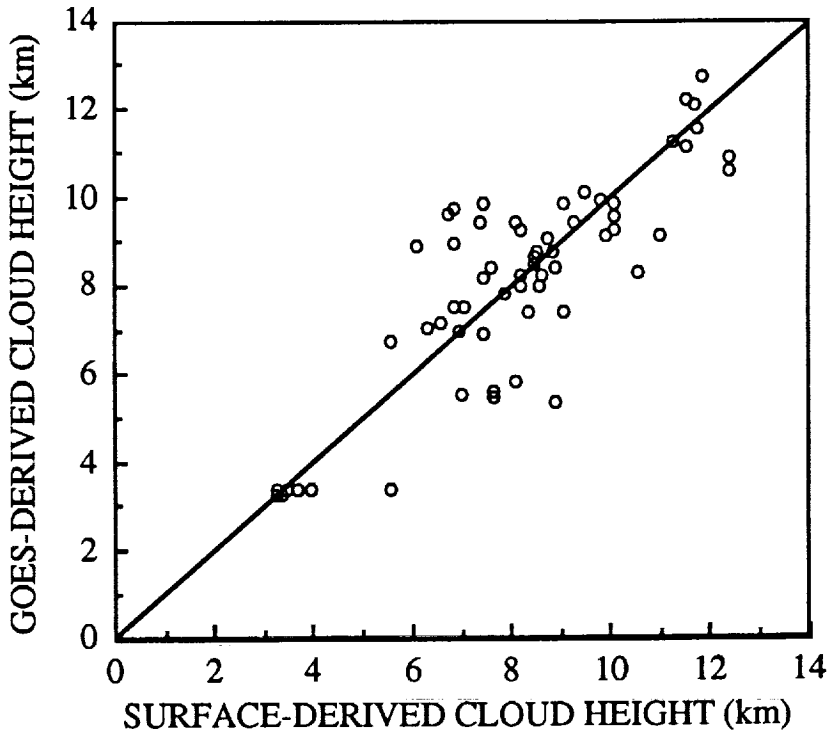

Fig. 1. Comparison of GOES-derived cloud center heights and surface-derived mean cloud heights.

DATA AND METHODOLOGY

Cloud base and cloud top altitudes were derived from several active remote sensor datasets taken during the FIRE-II IFO. The NASA Langley 8-inch visible wavelength lidar was operated on a regular basis throughout the experiment from Parsons, Kansas east of the hub at Coffeyville. The NOAA WPL 8.66-mm radar was located at the hub and operated from November 13 - 28. Both the NOAA WPL infrared lidar and Penn State University 95 GHz radar took data at the hub from November 11 to datasets whenever the cloud top could be clearly defined. Typically, the lidars were only used for cirrus clouds with visible optical depths $\tau < 4$. The Parsons lidar data were analyzed manually from graphical data. An automated digital threshold method was used to determine cloud boundaries from the radar and the infrared lidar data (Uttal et al., 1993). Cloud thickness is $\Delta z = z_t - z_b$.

The initial analysis uses data for a 0.3° region containing Coffeyville. Collocated 8-km visible and infrared radiances from the Geostationary Operational Environmental Satellite (GOES) were analyzed with the method of Minnis et al. (1993) to determine cloud optical depth and cloud-top height for the region. A bidirectional reflectance model having an effective radius of 10 μm was used to derive optical depth for clouds with a derived top temperature $T_c > 253$K. A cirrostratus ice crystal model was used for clouds having $T_c \leq 253$K. The cloud-top height is found from T_c and the Coffeyville sounding.

RESULTS

The mean cloud center heights derived from the surface and satellite data are shown in Fig. 1. The mean difference of 0.1 km and the rms difference of 1.3 km are almost identical to the same quantities found by Minnis et al. (1993) for FIRE-I data taken only for cirrus clouds. This dataset contains both cirrus and liquid water clouds. Cloud thicknesses Δz from the surface-based sensors were correlated

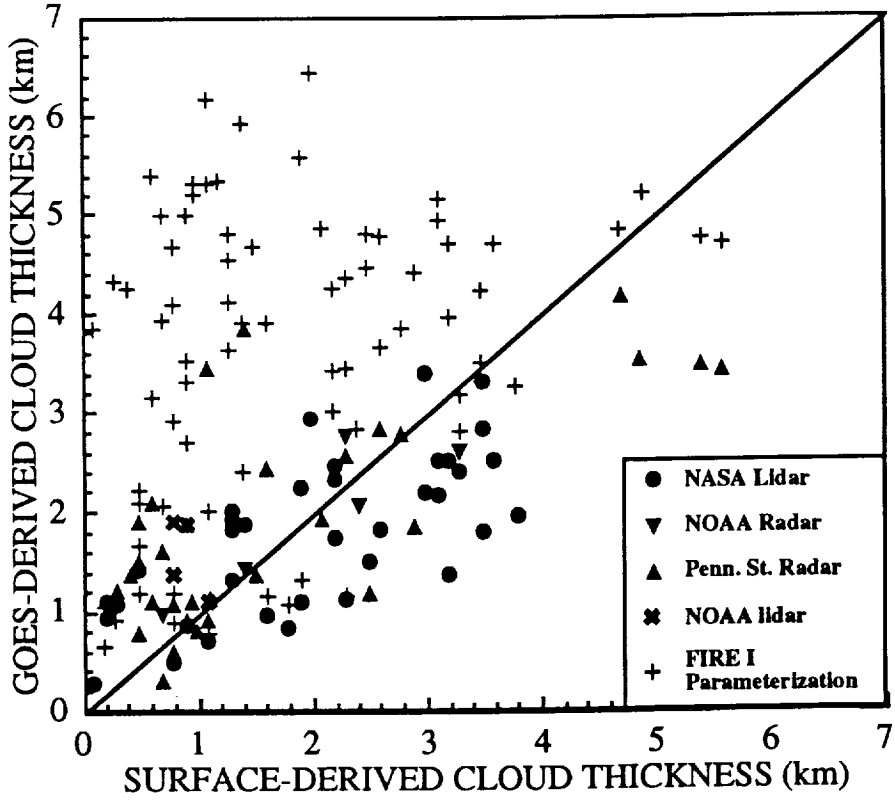

Fig.2. Comparison of GOES-derived and surface-derived cloud thickness.

with the GOES optical depths τ and cloud-center temperatures T_c to obtain the following parameterization.

$$\Delta z = 7.5 - 0.026\, T_c + 0.85 \ln \tau. \qquad (1)$$

The thicknesses computed with this parameterization are compared with the corresponding surface-based values in Fig. 2. The line of agreement in Fig. 2 indicates that (1) tends to underestimate thicker clouds and overestimate the thinner ones. The rms difference is 0.92 km. The parameterization derived by Minnis et al. (1990) from the FIRE-I cirrus data results in an overestimation of cloud thickness for almost all of the FIRE-II data. These differences between the FIRE-I and FIRE-II results are not unexpected. The FIRE-I analysis included only cirrus clouds but multiple layer cirrus were included. In the present analysis, only single layer clouds are used. Both liquid and ice water clouds are used here. Water droplet clouds tend to be more compact than cirrus so there should be less thickness for a given optical depth for liquid water clouds than for ice crystal clouds. Some of that effect may be causing some of scatter in the data plotted in Fig. 2.

Cloud base heights derived using the difference between cloud-top height and cloud thickness are shown in Fig. 3. The mean and rms differences are 0.3 and 1.3 km, respectively. These statistics reflect the errors in cloud-top height (Fig. 1). If the thickness parameterization errors and the cloud-top height errors were independent, the rms difference in cloud base altitude should be ~1.6 km. The derived rms difference is lower suggesting that some compensating effects are occurring in the techniques for deriving cloud-top height and cloud thickness. The slight bias in cloud base would translate to a 3% underestimate of the downwelling radiative flux for a cloud base at 253K. The rms uncertainty would be ~ ± 10%.

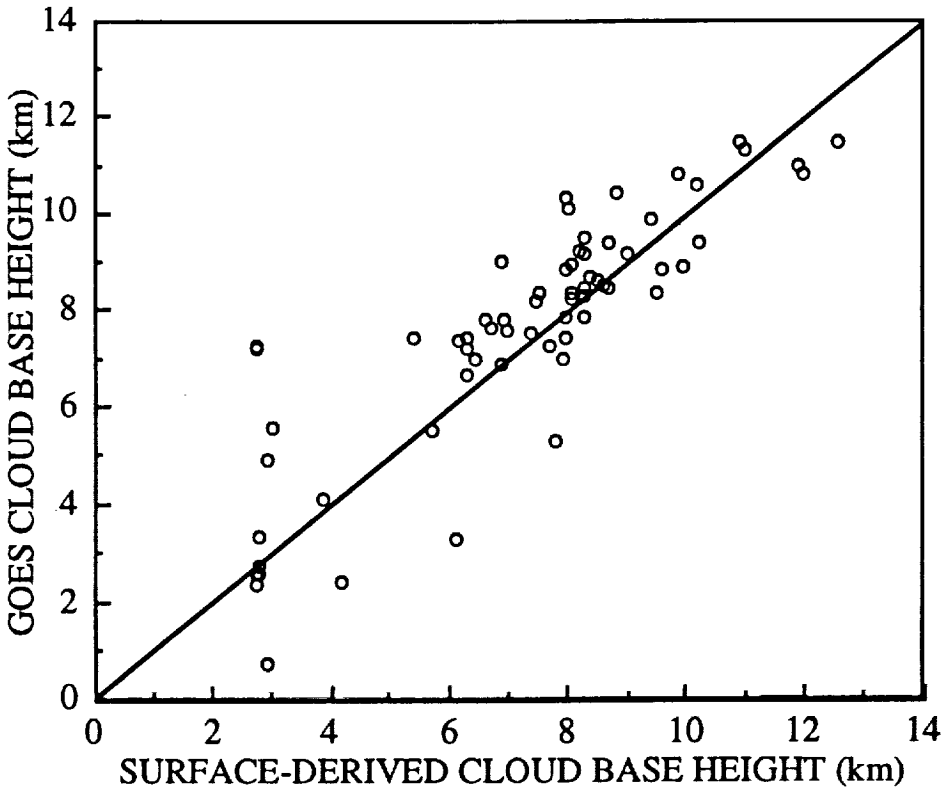

Fig. 3. Comparison of GOES-derived and surface-derived cloud base.

DISCUSSION AND CONCLUDING REMARKS

The uncertainties in the derived values due to the satellite data were noted above. Some additional uncertainty may be introduced by mixing the different surface datasets. Because of differences in the characteristics of the lidars and radars, Uttal et al. (1993) found some systematic differences between the cloud boundaries observed using the NOAA lidar and radar and the Penn State radar. These differences are not apparent in Fig. 2. The data points do not appear to line up according to the sensor. The greatest outliers in this dataset, however, are from the PSU radar indicating that the sensor effect needs to be examined more closely.

The results from this preliminary study and others are encouraging for the development of parameterizations of cloud thickness based on cloud optical depth, temperature, and, perhaps, the phase of the clouds. These parameterizations may have applications to mesoscale and larger scale climate models in addition to the remote sensing applications. Future analyses of the combined satellite-lidar-radar datasets need to examine the effects of phase and cloud layering. Additional data from the ER-2 would also help expand the number of samples for developing the cloud thickness parameterizations.

REFERENCES

Minnis, P., P. W. Heck, and E. F. Harrison, 1990: The 27-28 October 1986 FIRE IFO Cirrus Case Study: Cloud parameter fields derived from satellite data. *Mon. Wea. Rev.*, **118**, 2426-2446.

Minnis, P., P. W. Heck, and D. F. Young, 1993: Inference of cirrus cloud properties from satellite-observed visible and infrared radiances. Part II: Verification of theoretical radiative properties. *J. Atmos. Sci.*, **50**, 1305-1322.

Uttal, T., T. P. Ackerman, and J. M. Intrieri, 1993: Cloud boundaries during FIRE II. *26th Intl. Conf. Radar Meteorol.*, Norman, OK, May 24-28.

510-47
197510
P-4

N94-22302

CLOUD FIELDS DERIVED FROM SATELLITE AND SURFACE DATA DURING FIRE CIRRUS PHASE II

Patrick Minnis, Atmospheric Sciences Division, NASA Langley Research Center, Hampton, VA 23681

William L. Smith, Jr., David F. Young, and Patrick W. Heck, Lockheed Engineering and Sciences Company, Hampton, VA 23666

INTRODUCTION

The interpretation of surface and aircraft measurements of cloud properties taken during field programs must take into account the large-scale cloud and meteorological conditions. Cloud properties are also required at scales beyond the point and line data taken from ground and aircraft platforms. Satellite data can provide a quantitative description of these large-scale cloud properties. When derived from geostationary satellite data, the cloud fields constitute a unique source for evaluating the development and demise of a cloud system. Satellites, however, can only see the tops of clouds, so that cloud layers below the uppermost cloud deck may remain undetected resulting in a incomplete depiction of the cloud system. Some multilayer clouds are amenable to detection from satellites. Many, especially in midlatitude cyclonic systems, can only be observed from the surface. A combination of surface and satellite cloud observations should be the most complete quantification of large-scale cloudiness if there are sufficient surface measurements.

During the First International Satellite Cloud Climatology Project (ISCCP) Regional Experiment Phase II (FIRE-II) Cirrus Intensive Field Observation (IFO) period (November 13 - December 7, 1991) conducted at Coffeyville, Kansas, cirrus observations were taken in a variety of conditions. The IFO area was selected for a variety of reasons including the relatively dense network of surface weather stations and special surface instrumentation sites. Thus, the FIRE-II IFO presents an excellent opportunity to combine cloud observations from surface and satellite observations. This paper presents an analysis of cloud properties on a mesoscale grid using satellite cloud property retrievals, surface observer data, and rawinsonde temperature and humidity profiles.

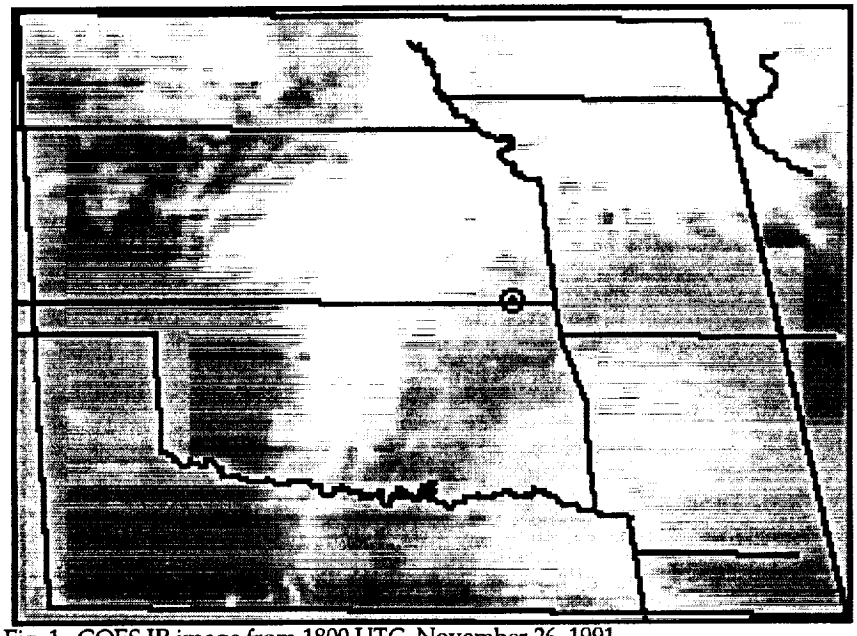

Fig. 1. GOES IR image from 1800 UTC, November 26, 1991.

DATA AND METHODOLOGY

Half-hourly, visible (0.65-μm, VIS) data from the Geostationary Operational Environmental Satellite (GOES-7) were averaged to a resolution of 8 km and matched with 8-km infrared (11.2 μm, IR) data to form two-dimensional histograms of pixel radiances for a 0.5° latitude-longitude grid bounded by 32°N and 42°N latitudes and 92°W and 102°W longitudes. The VIS-IR histograms were analyzed with the methodology of Minnis et al. (1993) to produce a three-level cloud dataset. At each level, low (below 2 km), middle (between 2 and 6 km), and high (above 6 km), the analysis produces cloud fractional coverage C_{si}, cloud-top height z_{si}, and cloud optical depth τ_i, where the subscripts s and i refer to satellite and cloud layer (low = 1), respectively. The total cloud amount C_s is the sum of the three layers, while the average cloud height and total optical depths are the cloud-amount weighted sums of the three layer values. Clear-sky temperatures used in the analysis are derived using the

technique of Minnis et al. (1987) with some supplementary data provided from the surface observations. National Meteorological Center (NMC) gridded meteorological analyses were used to relate cloud IR temperature to cloud altitude. The VIS data were converted to reflectance using a calibration based on surface measurements at White Sands, New Mexico (Charles Whitlock, NASA Langley Research Center, personal communication).

Hourly surface observations were acquired from the University of Wisconsin Man-computer Data Analysis System (McIDAS) for 43 stations within the domain. The observations include cloud base height (in feet above ground) and nominal coverage (scattered, broken, or overcast) for up to 3 levels. Surface temperature was also recorded for each station. Six-hourly rawinsonde data were available for selected stations. Scattered, broken, and, overcast were assigned cloud fractions of 33, 67, and 100%, respectively, for each level. The clouds were assigned to the low, middle, and high layers by the recorded cloud-base height. If two surface-observed cloud layers were located in the same height layer, the sum of the two amounts were assigned to that height category. The resulting layer cloud amounts for a given station were assigned to the 0.5° region in which the station was located. If two or more stations were in the same region, averages of the station values were assigned to each height category for that region. Total surface cloudiness C_g is the sum of the individual layer cloud amounts unless that sum is greater than or equal to 100%. In that case, $C_g = 100\%$.

Because of reporting methods, some stations recorded clear skies and missing values in the same manner preventing a unambiguous determination of clear sky stations. For that reason and because of the sparse spatial sampling by the surface observers, the surface observations were prepared in the following manner before combination with the satellite data. Regions deemed clear ($C_s < 1\%$) by the satellite analysis were added to the surface regional dataset. A Gaussian interpolation scheme was then applied to the combined clear satellite-cloudy surface regional dataset to estimate a cloud amount value at each height category for every region. The final cloud amount value for each region was determined using the following logic.

For high clouds:
If $C_{s3} > 0$, then $C_3 = C_{s3}$.
Otherwise, $C_3 = C_{g3}$.

For low clouds:
If $C_{s2} + C_{s3} = 100$, $C_1 = C_{g1}$.
If $|C_{s1} - C_{g1}| > 15$, C_1 = greater of C_{g1} and C_{s1}.
If $|C_{s1} - C_{g1}| < 15$ and $C_{g1} < 100$, $C_1 = C_{s1}$.

For midlevel clouds:
If $C_{s3} = 100$ and $C_{g1} = 100$, C_2 = undefined.
If $C_{s3} = 100$ and $C_{g1} < 100$, $C_2 = C_{g2}$.
If $C_{s3} < 100$ and $C_{g1} = 100$, $C_2 = C_{s2}$.
If $C_{s3} < 100$ and $C_{g1} < 100$, $C_2 = C_{s2}$ if $|C_{s2} - C_{g2}| < 15\%$ or $C_{s2} > C_{g2}$, otherwise $C_2 = C_{g2}$.

All undefined values are filled by interpolation.

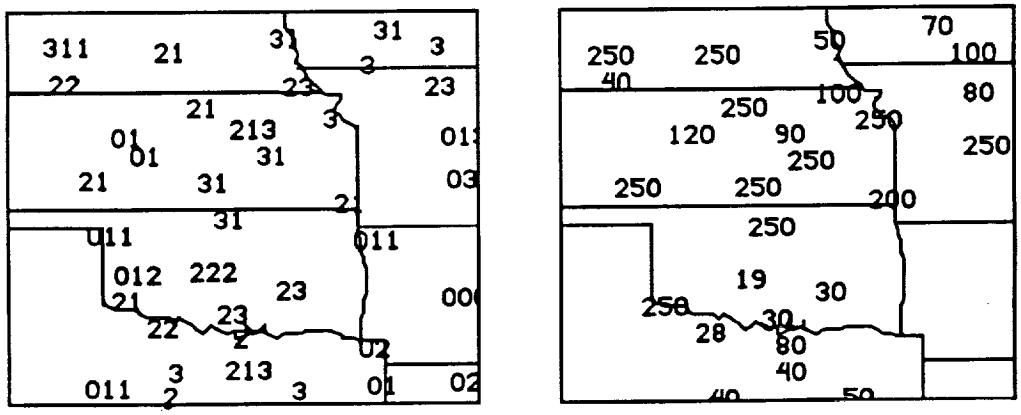

Fig. 2. Cloud data from surface reports, 1800 UTC, November 26, 1991. First panel indicates ceiling, first non-ceiling, and second non-ceiling (0=clear, 1 = scattered, 2 = broken, 3= overcast). Second panel indicates height in x 100 ft.

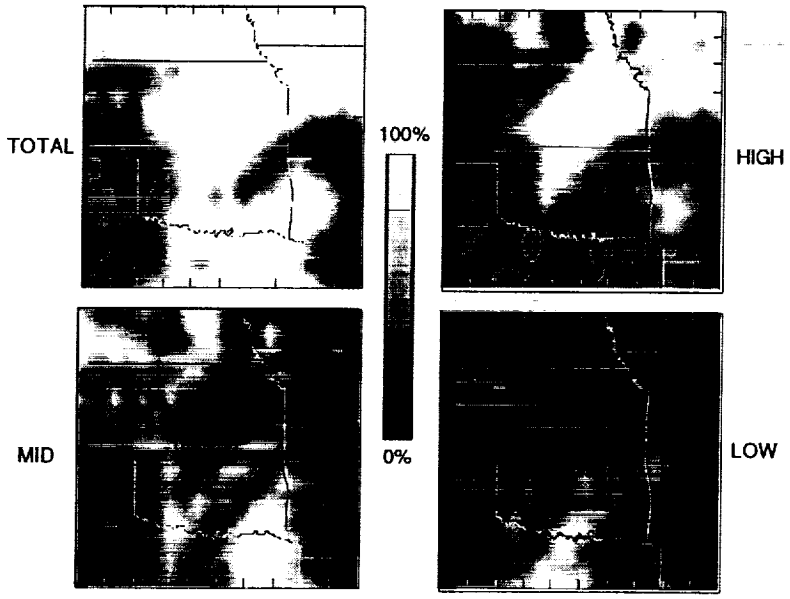

Fig. 3. Cloud Fraction derived from GOES data at 1800 UTC on November 26, 1991. The black areas indicate cloud fractions less than 1%.

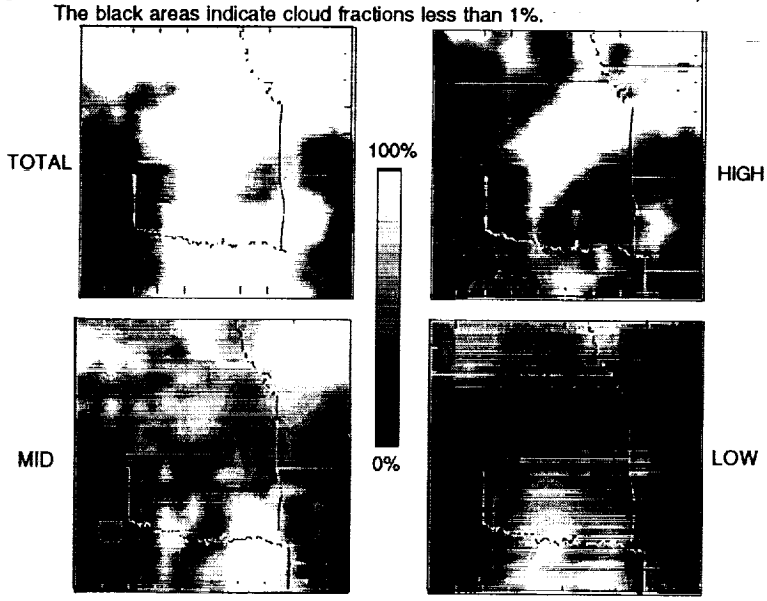

Fig. 4. Combined Satellite and surface derived cloud fraction for November 26, 1991 at 1800 UTC The black areas denote cloud fractions less than 1%.

RESULTS

Figure 1 shows the GOES IR imagery for 1800 UTC, November 26, 1991. Examples of the surface-observed cloud conditions in Fig. 2 indicate overcast conditions over much of Nebraska, Iowa, central and eastern Kansas, and central Texas and Oklahoma. The lowest cloud ceilings observed from the surface (Fig. 2b) vary from 2000 ft to 25,000 ft (the maximum reported value is 25,000 ft regardless of true height). Low clouds are the lowest clouds seen over northern Texas, central Oklahoma, and southern Nebraska and Iowa. Midlevel clouds are the lowest observed decks over much of Kansas, while high clouds are the only clouds reported over central Arkansas, the Texas panhandle, and the area just north of Coffeyville, Kansas. A somewhat similar picture is seen in the satellite analyses (Fig. 3) with some notable exceptions. No low clouds were detected over Nebraska and Iowa. Midlevel clouds were found over northeastern Texas. High clouds are the only type retrieved over most of eastern Kansas, Iowa, and northern Missouri. Combining the two datasets yields the contours in Fig. 4 that show midlevel clouds extending as far south as central Missouri and covering much of Kansas. Low clouds are also found over much of Nebraska and Iowa.

DISCUSSION

These results have important ramifications for using satellite data to verify cloud-process model results and to determine the radiative properties of clouds. The western and northern portions of the large area of satellite-derived high cloudiness (Fig. 3) where midlevel clouds were observed from the surface (Fig. 2) have very high optical depths (Fig. 5). The optical depths for the high-cloud-only regions are all less than 4. Thus, it appears that the larger high-cloud optical depths are caused by thick cloud layers underneath the highest layer. The satellite misinterprets this as a very thick high cloud. For example, the sounding over Omaha (Fig. 6) indicates thin clouds with tops at ~250 and 420 mb over a very thick cloud with a top near 510 mb. A low deck is apparent at ~ 910 mb. The average satellite-

derived cloud height over Omaha is 350 mb. The optical depth is assigned to the high cloud since that is the only cloud type seen over Omaha from the satellite. Most of the optical depth belongs in the midlevel clouds. Using the combined dataset (Fig. 4), we can estimate cloud cover over Omaha as being overcast high clouds, 50% midlevel, and 80% low. While the sounding suggests that this result is not complete, it is much closer than the satellite alone. To improve the analysis further, it is necessary to use the available soundings and cloud thickness-optical-depth relationships (e.g., Smith et al., 1993) to flesh out the middle levels and to estimate the optical depths for clouds not seen by the satellites. Such an approach is probably feasible only over areas of dense surface networks.

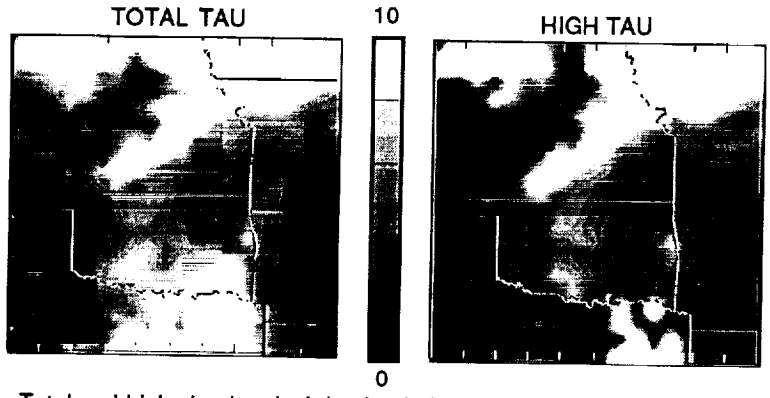

Fig. 5. Total and high cloud optical depths derived from GOES data at 1800 UTC on November 26, 1991. The black areas denote cloud fractions less than 1%.

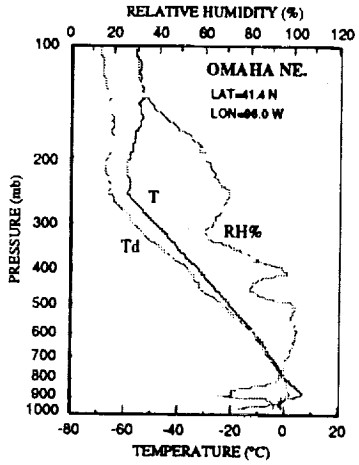

FIG. 6. Rawinsonde temperature and moisture profiles for Omaha, Nebraska at 1800 UTC on November 26, 1991.

CONCLUDING REMARKS

This paper has presented a preliminary combined surface-satellite cloud analysis for the FIRE-II region. Because cirrus clouds occur over lower clouds during much of the experiment and at any given time, it is important to account for the underlying clouds that cannot be detected from the satellite. The use of statistical relationships between cloud thickness and derived optical depth and other techniques such textural methods may improve the detection of multilevel clouds. When the higher clouds become optically black, however, there is little information to be derived from the satellite about the lower levels. For now, the only source for the lower-level information is in the surface or sounding data. The blending of surface and satellite data is a challenge requiring much additional research.

REFERENCES

Minnis, P., E. F. Harrison, and G. G. Gibson, 1987: Cloud cover over the eastern equatorial Pacific derived from July 1983 ISCCP data using a hybrid bispectral threshold method. *J. Geophys. Res.*, **92**, 4051-4073.

Minnis, P., P. W. Heck, and D. F. Young, 1993: Inference of cirrus cloud properties from satellite-observed visible and infrared radiances. Part II: Verification of theoretical radiative properties. *J. Atmos. Sci.*, **50**, 1305-1322.

Smith, W. L., Jr., P. Minnis, J. M. Alvarez, T. Uttal, J. M. Intrieri, T. P. Ackerman, and E. Clothiaux, 1993: Development of methods for inferring cloud thickness and cloud base-height from satellite radiance data. *Proc. FIRE Science Conf.*, Breckenridge, CO, June 14-17.

511-43
197511
P-4

N94-22303

Remote Sensing of Multilevel Clouds During FIRE IFO II

Bryan A. Baum[1], J. Titlow[2], V. Tovinkere[2],
M. Poellot[3], T. P. Ackerman[4], J. Alvarez[1], T. Uttal[5], and J. Intrieri[6]

[1]NASA Langley Research Center, Hampton, VA 23681-0001
[2] Lockheed Engineering and Sciences Co., Hampton, VA 23666
[3]University of North Dakota, Grand Forks, ND 58202
[4]Pennsylvania State University, University Park, PA 16802
[5]NOAA Wave Propagation Lab, 325 Broadway, Boulder, CO 80302
[6]CIRES, University of Colorado, Boulder, CO 80309

1. Introduction

An unresolved difficulty in the remote sensing of clouds concerns the inability of the cloud retrieval algorithms to adequately recognize and analyze scenes containing overlapping cloud layers. Most cloud retrieval schemes, such as that used by the International Satellite Cloud Climatology Project (ISCCP) (Schiffer and Rossow, 1983), assume that each picture element (pixel) contains a single cloud layer. The current study begins to address the complexities of multilayered cloud property retrieval through the application of a modified multispectral, multiresolution (MSMR) method , first detailed in Baum et al. (1992), which merges 1.1-km (at nadir) spectral data from the Advanced Very High Resolution Radiometer (AVHRR) with 17.4-km (at nadir) High Resolution Infrared Radiometer Sounder (HIRS/2, henceforth HIRS). Both instruments are flown aboard the National Oceanic and Atmospheric Administration (NOAA) polar-orbiting platforms. An ideal case study for this investigation is provided by the NOAA-11 overpass at 20:48 UTC on November 28, 1991. At this time, a large-scale cirrostratus veil overlaid a low-level stratus deck over much of the IFO region. There were both surface lidar and radar observations of the clouds as well as University of North Dakota (UND) Citation aircraft measurements. The presence of overlapping cloud layers within a HIRS FOV is determined from colocated AVHRR spectral data through the use of a fuzzy logic expert system (Tovinkere et al., 1993). Conventional algorithms such as spatial coherence (Coakley, 1983) and CO_2 slicing (McCleese and Wilson, 1976; Smith and Platt, 1978) are used to retrieve cloud pressure and height for each identified cloud layer. The results from the satellite cloud retrieval analysis are compared to results from both surface- and aircraft-based measurements.

2. Data

Further details on the AVHRR and HIRS instruments, spectral channels, and sampling may be found in Kidwell (1991). The raw counts for the AVHRR infrared channels (10.8- and 12-mm) are converted to radiances using the nominal calibration (Kidwell, 1991) and to brightness temperature using the nonlinearity corrections of Weinreb et al. (1990). The MSMR cloud retrieval method uses temperature and relative humidity data collected during the FIRE IFO II by NWS (National Weather Service) and CLASS (Cross Chain Loran Atmospheric Sounding System) sondes and the European Center for Medium Range Weather Forecasting (ECMWF). Cloud heights and cloud bases are compared to a variety of surface observations recorded at Parsons and Coffeyville in addition to cloud heights recorded by the UND Citation. Coffeyville surface observations include the NOAA 8.6-mm radar and NOAA lidar, and the Pennsylvania State University (PSU) 3-mm radar. The Langley Research Center (LaRC) lidar took observations at Parsons.

3. Methodology

The MSMR method incorporates techniques such as CO_2 slicing (e.g. McCleese and Wilson, 1976; Smith and Platt, 1978) to estimate cloud height, threshold methods to calculate fractional coverage, and radiative transfer theory to infer bulk optical properties. Details of the MSMR scheme may be found in

Baum et al. (1992). The MSMR cloud pressure retrieval schematic shown in Figure 1 has since been modified to include the spatial coherence technique (Coakley, 1983), a scheme for analyzing temperature profile data to infer tropopause height, and a surface elevation map. In addition, the MSMR scheme uses a hybrid relative humidity profile that incorporates both the relative humidity of water and ice (Starr and Wylie, 1990). To determine whether more than one cloud-layer is present, we employ an artificial intelligence method to automatically classify a subset of AVHRR spectral data colocated with a HIRS field of view (FOV). A variety of classificiation techniques have been discussed in the literature over the past 30 years, but only until recently have these techniques been applied to satellite data (e.g. Garand, 1988; Ebert, 1987; Welch et. al., 1992). However, one drawback to many of these techniques is that a given data sample may contain mixed classes of cloud, such as cirrus over stratus. In such a case, a classifier using a clustering technique is able to provide information on only the most prevalent cloud class. Fuzzy logic classification has the ability to assign multiple classes to a given data sample. For example, a given array of AVHRR data may be assigned membership values for both cirrus and stratus, or cirrus, land, and water. A fuzzy logic expert system (Tovinkere et al., 1993) is prepared for use in the MSMR methodology in order to attempt classification of subgrid cloud layering through analysis of the AVHRR data collocated with each HIRS FOV. The fuzzy logic approach uses both textural and spectral features calculated from a 32x32 pixel array of AVHRR data collocated with each HIRS FOV to determine whether the following five classes are present, either singly or in combination: (1) land; (2) water; (3) unbroken stratiform cloud; (4) broken stratiform cloud; and (5) cirroform cloud. These classes are broad in scope and may contain a number of representative subclasses. For instance, land covers all surface not covered by water, unbroken stratiform includes both stratus and altostratus cloud types, broken stratiform includes both stratus and altostratus cloud types in which some amount of surface is uncovered by cloud in the data array, and cirroform includes cirrostratus, cirrus uncinus, and other cirrus types. If the classification shows that any low cloud is present, the assumption is made that the HIRS pixel has a lower cloud layer effective cloud amount of 1 ($\varepsilon A_c=1$, where ε is emittance and A_c is cloud fraction). The HIRS radiometric data are then reanalyzed with the surface defined to be the lower cloud top pressure instead of the ground. When a low cloud is used as the lower surface instead of the ground, the end result is to increase the cloud height from the value obtained using a single cloud layer assumption. When the cirrus becomes very thin (i.e, $\varepsilon < 0.2$), the cloud signal tends to become small in the HIRS 15-μm channels with the result that the retrieved cloud pressures may be dependent on the choice of channels. When cloud pressures vary widely with channel choice, the most likely cloud pressure is assumbed to be the one that corresponds with a maximum in the relative humidity of ice .

4. Results

Results from the November 28, 1991 NOAA-11 overpass at approximately 20:48 UTC are shown in Figure 2 for the MSMR-derived cloud heights. In Figure 2, the ellipses refer to HIRS pixels (not drawn to actual size) and contain the MSMR-derived cloud height in kilometer (km). There is some uncertainty for very thin cirrus as to whether the cirrus cloud heights are actually cloud top or cloud center. The lower layer cloud top height is determined from spatial coherence analysis to be 1.9 km. The classification system determined that both cirroform and broken stratiform cloud were present in each of the HIRS pixels noted in the figure. The Coffeyville and Parson sites are denoted by a solid dot. The hatched area refers to the flight region of the Citation. The small letters in parentheses below the surface site name are used as a reference to results shown in Table 1, where cloud height results are shown from the UND Citation aircraft and the surface lidars and radars. For the upper cloud layer, the cloud base to cloud top range is given. Analysis of CLASS sonde data showed two maxima in the vertical relative humidity profile, and the height in km of each peak is also provided in the table. The MSMR results agree well with both surface and aircraft cloud layer height observations, and are encouraging given the scene complexity.

Table 1: Surface and aircraft cloud height observations recorded during the November 28, 1991 NOAA-11 overpass at 20:48 UTC, where Z_{LC} refers to the lower clou-top height and Z_{UC} refers to upper cloud height (both cloud base and cloud top given where possible).

	INSTRUMENT	LOCATION	Z_{LC} (km) top	Z_{UC} (km) base-top
a	NOAA CO_2 LIDAR	Coffeyville	---	8.2-9 10.1-10.8
b	NOAA K-BAND RADAR	Coffeyville	1.8	8.1-9.2
c	PSU RADAR	Coffeyville	1.8	8-10
d	CLASS SONDE (RH/RHI)	Coffeyville	2.0	10
e	LaRC LIDAR	Parsons	---	8-11.3 (perhaps two layers)
f	UND Citation	See flight track (Figure 2)	1.8	8.3-11.2

5. References

Baum, B. A., B. A. Wielicki, P. Minnis, and L. Parker, 1992: Cloud property retrieval using merged HIRS and AVHRR data, *J. Appl. Met.*, **31**, 351-369.

Coakley, J. A., Jr., 1983: Properties of multilayered cloud systems from satellite imagery. *J. Geophys. Res.*, **88**, 10,818-10,828.

Ebert, E., 1987: A pattern recognition technique for distinguishing surface and cloud types in the polar regions. *J. Clim. Appl. Meteorol*, **26**, 1412-1427.

Garand, L., 1988: Automated recognition of oceanic cloud patterns. Part I: Methodology and application to cloud climatology. *J. Clim.*, **1**, 20-39.

Kidwell, K. B., NOAA polar orbiter data users guide. NOAA National Climatic Data Center, Satellite Data Services Division, 1991.

McCleese, D. J., and L. S. Wilson, 1976: Cloud top heights from temperature sounding instruments, *Quart. J. Roy. Met. Soc.*, **102**, 781-790.

Schiffer, R. A., and W. B. Rossow, 1983: The international satellite cloud climatology project (ISCCP): The first project of the World Climate Research Programme, *Bull. Amer. Meteor. Soc.*, **64**, 779-784.

Smith, W. L., and C. M. R. Platt, 1978: Comparison of satellite-deduced cloud heights with indications from radiosonde and ground-based laser measurements, *J. Appl. Met*, **17**, 1796-1802.

Starr, D. O'C. and D. P. Wylie, 1990: The 27-28 October 1986 FIRE IFO cirrus case study: Meteorology and clouds, *Mon. Wea. Rev.*, **118**, 2259-2287.

Tovinkere, V.R., M. Penaloza, A. Logar, J. Lee, R. C. Weger, T. A. Berendes, and R. M. Welch, 1993: An intercom parison of artificial intelligence approaches for polar scene identification, *J. Geophys. Res.*, **98**, 5001-5016.

Weinreb, M. , G. Hamilton, and S. Brown, 1990: Nonlinearity corrections in calibration of Advanced Very High Resolution Radiometer infrared channels. *J. Geophys. Res.*, **95**, 7381-7388.

Welch, R.M., S. K. Sengupta, A. K. Gorock, P. Rabindra, N. Rangaraj, and M. S. Navar, 1992: Polar cloud and surface classification using AVHRR imagery: An intercomparison of methods. *J. Appl. Met.* **31**, 405-420,.

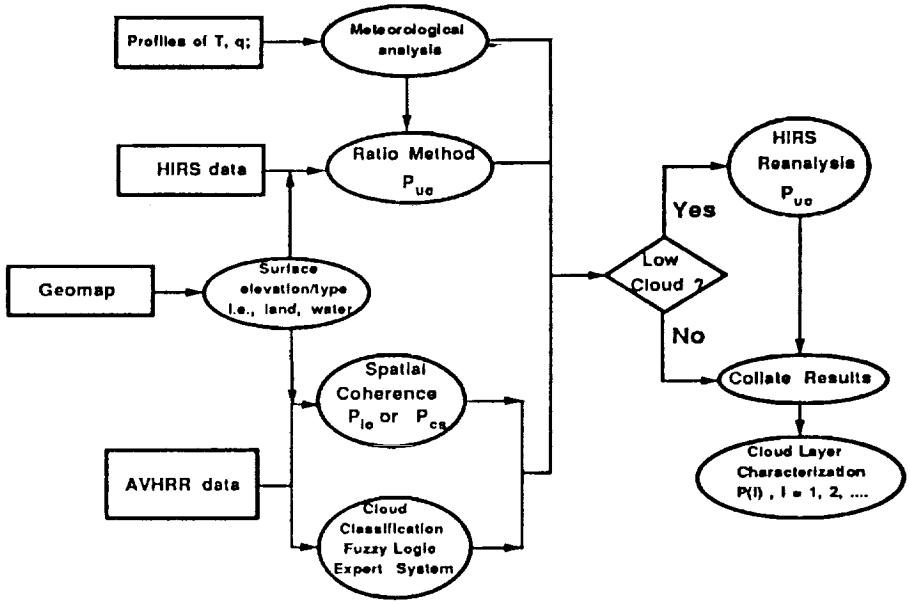

Figure 1. Schematic for merged AVHRR/HIRS data processing scheme. The subscripts lc, uc, and cs refer to lower-level cloud, upper-level cloud, and clear sky, respectively.

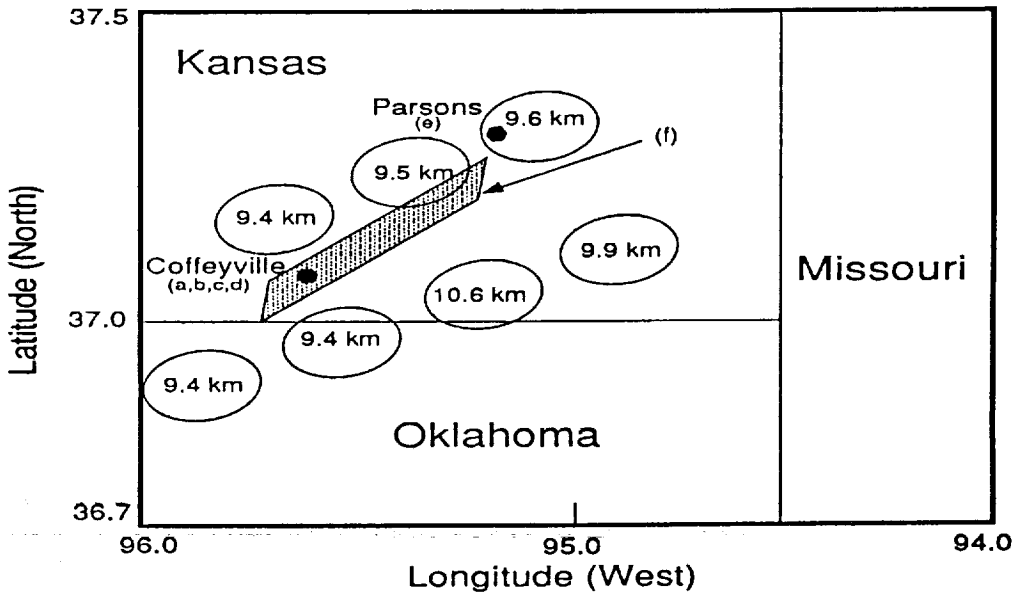

Figure 2. MSMR upper cloud height results for HIRS fields of view on November 28, 1991 at 20:48 UTC during the FIRE IFO II. The solid dots refer to locations of Coffeyville and Parsons. The cross-hatched area shows UND Citation flight track region. The small letters in parentheses under city names refer to corroborative cloud height measurements detailed in Table 2.

S12-47
197512
P. 4

N94-22304

MICROPHYSICAL PROPERTIES OF THE NOVEMBER 26 CIRRUS CLOUD RETRIEVED BY DOPPLER RADAR / IR RADIOMETER TECHNIQUE

Sergey Y. Matrosov

Cooperative Institute for Research in Environmental Sciences
University of Colorado/NOAA, Boulder, Colorado

Robert A. Kropfli, Brad W. Orr, Jack B. Snider
NOAA/Wave Propagation Laboratory, Boulder Colorado

1. INTRODUCTION

Gaining information about cirrus cloud microphysics requires development of remote sensing techniques. In an earlier paper, Matrosov et al. (1992) proposed a method to estimate ice water path (IWP)(i.e., vertically integrated ice mass content IMC) and characteristic particle size averaged through the cloud from combined ground-based measurements of radar reflectivities and IR brightness temperatures of the downwelling thermal radiation in the transparency region of 10-12 μm. For some applications, the vertically averaged characteristic particle sizes and IWP could be the appropriate information to use. However, vertical profiles of cloud microphysical parameters can provide a better understanding of cloud structure and development.

Here we describe a further development of the previous method by Matrosov et al. (1992) for retrieving vertical profiles of cirrus particle sizes and IMC rather than their vertically averaged values. In addition to measurements of radar reflectivities, the measurements of Doppler velocities are used in the new method. This provides us with two vertical profiles of measurements to infer two vertical profiles of unknowns, i.e., particle characteristic sizes and IMC. Simultaneous measurements of the IR brightness temperatures are still needed to resolve an ambiguity in particle size - fall velocity relationships.

2. THEORETICAL CONSIDERATIONS

Doppler velocities, V_m, measured with the vertically pointed radar antenna represent the sum of reflectivity-weighted particle fall velocities, V_f, and of vertical air motion, V_a:

$$V_m = V_f + V_a. \tag{1}$$

To extract values of V_f from measured quantities V_m, we used an approach based on the assumption that, over time intervals of 1 - 2 hours, the mean vertical air motion in a cloud is small compared to fall velocities of ice particles. Thus, the observed average value of Doppler velocity closely approximates V_f (Orr and Kropfli 1993). Averages were performed for 1 dB reflectivity intervals to find reflectivity- fall velocity relationships at different range gates to get estimates of V_f at the same time intervals as those of reflectivity. Our experience with Doppler velocity data processing shows that changing the averaging time from 1 hour to 2 hours usually does not cause significant variations in estimated values of fall velocities V_f, which demonstrates the soundness of this approach.

The largest dimensions of ice particles in cirrus clouds usually do not exceed $D_{max} \approx 2$ mm (Dowling and Radke 1990), which is still within the Rayleigh scattering regime for radar frequencies up to the Ka-band (Yeh et al. 1982). In this regime, backscattering cross sections of individual particles increase with the sixth power of particle characteristic size. After integrating these cross sections with the particle size distribution, we get, for the radar reflectivity with respect to ice, Z_i,

$$Z_i = f_1 C D_m^6, \tag{2}$$

where C and D_m are particle concentration and median diameters, respectively, and the coefficient f_1 depends on the particle size distribution. Hereafter, we assume that this distribution is the gamma function of the first order. This function adequately describes many experimental size spectra of cirrus cloud particles (Kosarev and Mazin 1989). For the first order gamma function, $f_1 \approx 0.486$ if Z_i is in cm^3, C is in cm^{-3}, and D_m is in cm. Equation (1) implies that particles are spherical. Effects of nonsphericity, however, can be approximately taken into account by tuning the coefficient f_1.

Integrating over the distribution, we can obtain also the expression for IMC as follows:

$$IMC = f_2 C D_m^3, \tag{3}$$

where $f_2 \approx 0.111$ if the size distribution is the first order gamma function and IMC is in g cm^{-3}.

From (2) and (3) one can see that finding vertical profiles of particle sizes and IMC is equivalent to having estimations of C and D_m at each radar range gate. Equation (2) provides one vertically resolved relationship between the measured values (i.e. Z_i) and the unknowns. A second relationship should connect these unknowns and the particle fall velocity estimates.

Particle fall velocity V_f is the reflectivity-weighted velocity of individual particles in the radar resolution volume, v_f:

$$V_f = \int_0^{D_{max}} v_f N(D) D^6 dD / Z_i, \tag{4}$$

where $N(D)$ is the size distribution function.

Experimental studies of the fall velocities of individual ice crystals demonstrate that fall velocity-size relationships can be approximated by the power law function (Pruppacher and Klett 1978):

$$v_f = AD^B, \tag{5}$$

where A and B are constant for a particular crystal shape. According to the data presented by Pruppacher and Klett (1978), the coefficient B generally varies from 0.8 to 1.3. The coefficient A shows much greater variations, up to two orders of magnitude.

Integrating according to (4) gives the following expression for V_f estimates:

$$V_f = A f_3 D_m^B. \tag{6}$$

The coefficient f_3 depends slightly on D_m, but this dependence is negligibly small. The value of f_3 depends also on B. For the first-order gamma function and B=1, $f_3 \approx 1.71$ if V_f is in cm s^{-1}.

Equation (6) provides the second vertically resolved relationship between the measurables and unknowns. Given relatively low variations of B, we can reasonably assume that $B \approx 1$. However, possible large variations of A indicate that the value of this coefficient has to be estimated from at least one additional measurement.

A measurement for estimating A is obtained from the brightness temperature of cloud downwelling thermal radiation. Matrosov et al. (1992) proposed a technique to infer cloud optical thickness due to extinction from brightness temperature measurements in the IR "window" region by a narrow-band IR radiometer. In this region, cirrus particle size factors ($\pi D/\lambda$) are large compared to the wavelength, and we can assume that particle extinction efficiency is close to 2. In this case, the cloud extinction coefficient α and the optical thickness τ can be expressed as follows:

$$\alpha = f_4 C D_m^2, \tag{7}$$

and

$$\tau = \sum_j (f_4 C D_m^2)_j \Delta h_j, \tag{8}$$

where the summation is with respect to range gates Δh_j and $f_4 \approx 0.432$ if α is in cm^{-1}.

At the first step of the retrieval cloud microphysical parameters for each radar beam, we assume some initial value for A. Then, from estimates of fall velocities V_f, we retrieve values of particle sizes D_m from (6) at each range gate. Knowing D_m allows calculations of particle concentrations C from reflectivity data using (2). After that, the value of optical thickness τ is calculated using (8) and compared with the actual value from the IR radiometer measurement for the considered radar beam. From the ratio of the calculated and measured values of optical thickness we find a corrected value of A for which the newly calculated and measured values of τ would coincide. The corrected value of A is then used to calculate final vertical profiles of particles sizes, concentrations, and IMC using (6), (1), and (3).

3. EXPERIMENTAL EXAMPLE

We use experimental data obtained during the FIRE-II experiment to illustrate the proposed method. One of the priority dates was November 26, when a slowly developing cirrus cloud was seen over a time period of several hours. Radar data were taken by the Wave Propagation Laboratory (WPL) Doppler 8.6 mm wavelength radar with the antenna pointing vertically. This radar was able to measure vertical velocities with an accuracy of about 5 cm s^{-1}. IR brightness temperatures were measured with a modified Barnes narrow angle radiometer (PRT-5), which had a wavelength band from 9.95 to 11.43 μm. Water amount was obtained from WPL's two channel microwave radiometer (working at frequencies of 31.65 GHz and 20.6 GHz) to account for the atmospheric transparency and thermal radiation when retrieving optical thickness values from IR brightness temperatures using the technique described by Matrosov et al. (1992).

Figure 1 shows a time height cross section of the retrieved particle median diameters (D_m). It can be seen that larger particles are mostly located in the lower part of the cloud. Particles are generally getting larger as the cloud becomes thicker and gradually descends. For the first order gamma function size distribution, the relationship between the median diameter and the effective radius (r_e), another widely used characteristic size of cloud particles, is the following: $r_e = 0.46 D_m$.

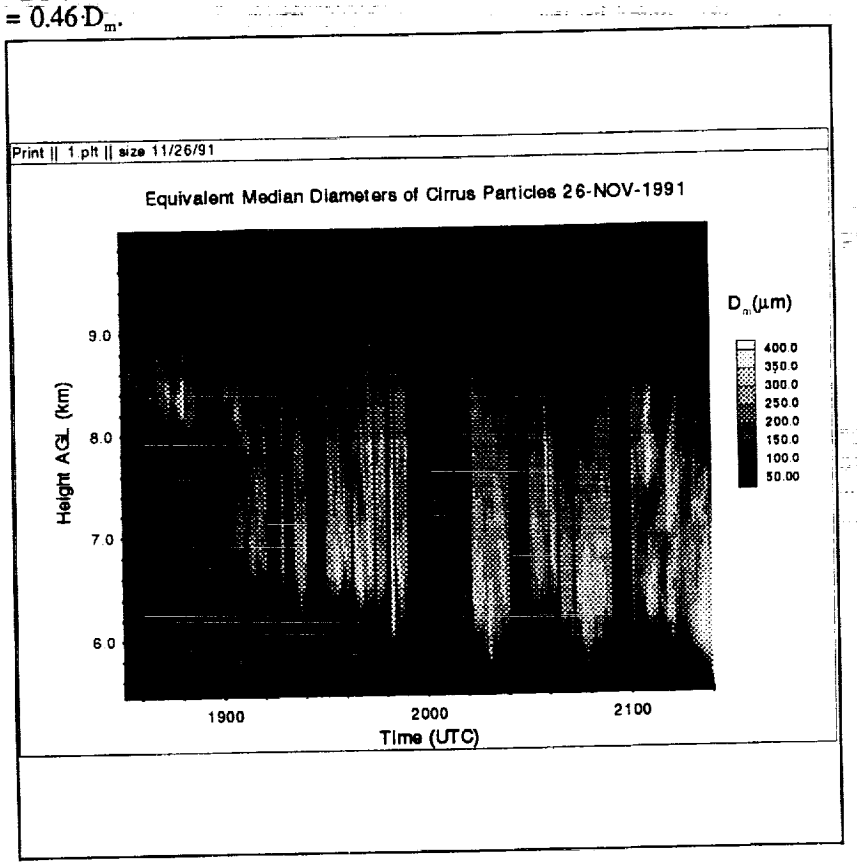

Figure 1. Time height cross section of cirrus particle median diameters observed on November 26, 1991

Figure 2 shows a time height cross section for retrieved values of particle concentrations. The highest particle number densities are in the upper part of the cloud. However, the sizes of these particles are small. As particles descend through the cloud, they grow larger and their concentrations decrease.

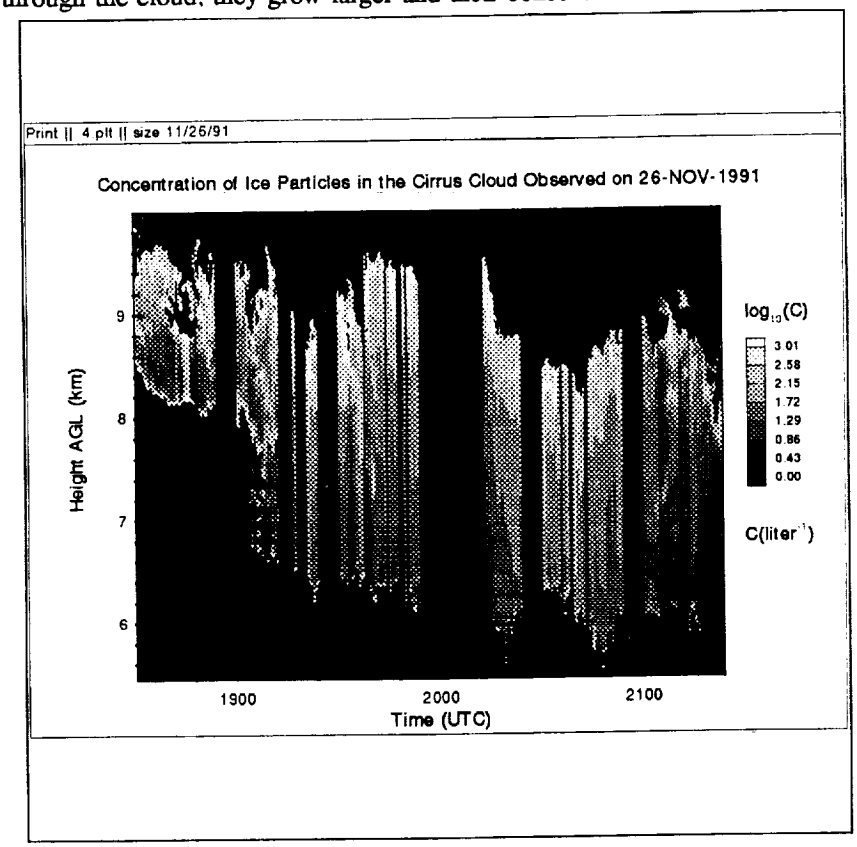

Figure 2. Time height cross section of cirrus particle concentrations observed on November 26, 1991.

The size information obtained using the radar/IR radiometer technique is in general agreement with the lidar/radar technique and data of direct measurements (Intrieri et al. 1993). Knowing characteristic sizes, concentrations and terminal velocities of particles one can easily calculate some other parameters of cloud microphysics such as vertical profiles of ice mass content and ice mass flux. Integrating vertical profiles of ice mass content provides values of ice water path which is important for longwave cloud feedback (Ebert and Curry, 1992). Our future plans include retrieving and studying information about aforementioned parameters and estimating possible retrieval errors.

REFERENCES

Dowling, D.R. and L.F. Radke, 1990: A summary of the Physical properties of cirrus clouds. *J. Appl. Meteorol.*, **29**, 970-987.

Ebert, E.E., and J.A. Curry, 1992: A parameterization of ice cloud optical properties for climate models. *J. Geophys. Res.*, **97**, 3831-3836.

Intrieri, J., K. Healy, T. Uttal, and A. Heymsfield, 1993: Combining lidar and radar measurements to derive cirrus clouds effective radii: in situ comparison and simplistic model results. In Proceedings of Conference on *Combined Optical-Microwave Earth and Atmosphere Sensing*. March 22-25, Albuquerque, NM, 119-122.

Kosarev, A.L., and I.P. Mazin, 1989: Empirical model of physical structure of the upper level clouds of the middle latitudes. In *Radiation Properties of Cirrus Clouds*, Moscow, Nauka, 29-52.

Matrosov, S.Y., T.Uttal, J.B. Snider, and R.A. Kropfli, 1992: Estimation of ice cloud parameters from ground based infrared radiometer and radar measurements. *J. Geophys. Res.*, **97**, 11567-11574.

Orr, B.W., and R.A. Kropfli, 1993: Estimation of hydrometeor fall speeds from vertically pointing Doppler radar. Prepr., *26th Conf. on Radar Meteorology*. Norman, OK, May 24-28,Boston, Amer. Meteorol. Soc.

Pruppacher, H.R., and J.D. Klett, 1978: *Microphysics of clouds and Precipitation*. D. Reidel, 714 pp.

Yeh, C., R. Woo, A. Ishimaru, and J. Armstrong, 1982: Scattering by single ice needles and plates at 30 GHz. *Radio Sci.*, **17**(6), 1503-1510.

513-47
197513
p. 4

N94-22305

Lidar and Radar derived Cirrus Microphysical Properties for the 26 November 1991 Case Study

Janet M. Intrieri and Graham Feingold

Cooperative Institute for Research in Environmental Sciences
University of Colorado/NOAA
Campus Box 449
Boulder, Colorado 80309-0449

1. Cirrus Parameters from Combined Lidar and Radar Measurements

The Wave Propagation Laboratory's CO_2 lidar ($\lambda = 10.6\ \mu m$) and Ka-band radar ($\lambda = 8.66$ mm) operate at widely separated wavelengths; the differences in how the transmitted waves interact with cloud targets can be exploited to provide information that neither sensor could provide alone. This can be as simple as overlapping the data sets to provide additional coverage on cloud geometry (see Uttal and Intrieri, 1993) or combining the measurements in a theoretical framework to provide cirrus cloud parameters of the size spectrum, i.e., characteristic particle size and number concentration. In this paper, the latter option is described and an example case study presented to illustrate the types of information available for cloud and radiation transfer models.

The wavelength-dependent difference in returned backscatter from the same-sized particle forms the theoretical basis of the lidar-radar method (Intrieri et al., 1993). This particular combination of wavelengths provides information on particle sizes as shown in Fig. 1a where the slope in the ratio of lidar to radar backscatter Kernels indicates unambiguous information throughout the spectrum of most cloud particle sizes. The predicted sizes are constrained by the lower limit sensitivity of the radar (making $\sim 30\ \mu m$ the smallest predictable characteristic size) and attenuation from particles by the lidar (usually from clouds having an optical depth greater than 2). Corrections for attenuation and specular reflection are made to the lidar signal as needed. The error in predicted size increases as the theoretical curves become flat with increasing size (see Fig. 1b, solid line). However, the effective radii inferred from our data thus far have not been larger than $\sim 225\ \mu m$, which fall well within reasonable size ranges for cirrus clouds. Because the lidar and radar produce range-resolved information, size estimates can be determined every 75 m throughout the depth of the cloud. This allows us to analyze the microphysical evolution of the cloud (i.e., growth, decay, precipitation, etc.) along with the changing radiation fields.

Once r_e is determined, the number densities (N_o) can be calculated from either the radar or lidar backscatter. A similar method was used for determining size distribution information from dual polarization radar (e.g. Feingold and Levin, 1987). In Fig. 1b the theoretical curve used to estimate the number density from the radar backscatter is also plotted (dashed line).

Using the derived r_e and N_o, the ice water content (*iwc*) of the cirrus clouds can be calculated using

$$iwc = 4/3\pi\rho \int r^3 n(r) dr = 4/3\pi\rho N_o 3/8 r_e^3, \qquad (1)$$

where $n(r)$ is the size distribution of ice particles and ρ is the density of ice, assumed to be 0.9 g cm^{-3}. Figure 2 shows the radii having the largest contributions to η (radar backscatter coefficient), β (lidar relative backscatter), and *iwc* (respectively r_η, r_β, and r_i) as a function of the mode radius of $n(r)$. Essentially, r_β, r_i, r_η are the 2nd, 3rd, and 6th moment weighted mode radii. We see that $r_\beta < r_i < r_\eta$ illustrating the added value of using the lidar data in combination with the radar data, versus using the radar information alone, to infer ice water contents in cirrus clouds because the correlation between r_β and r_i is better than that between r_η and r_i.

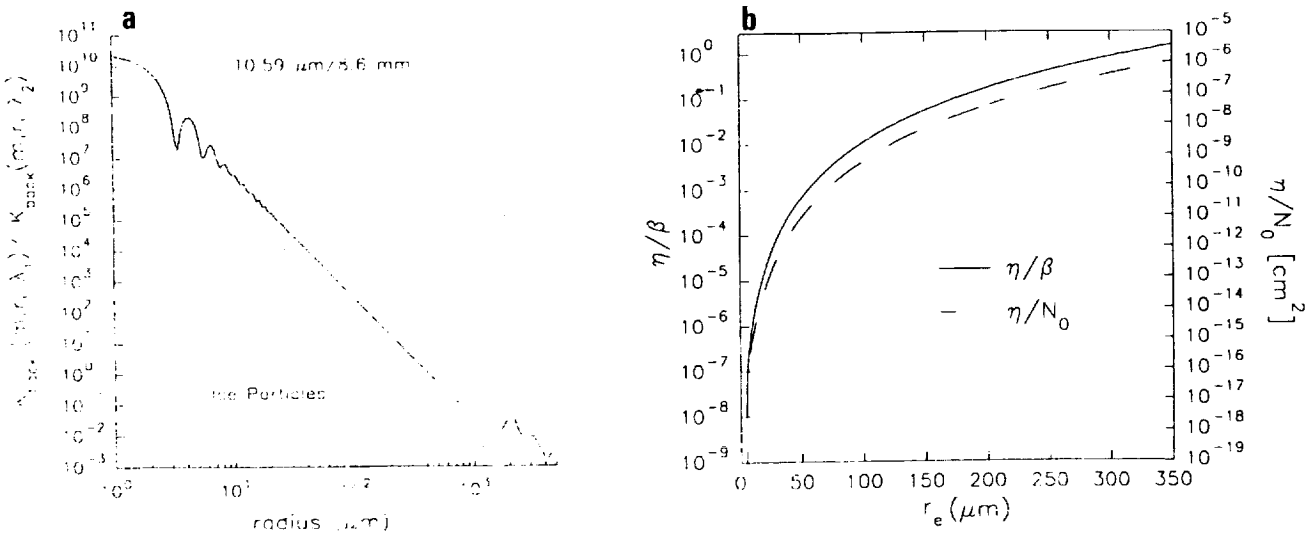

Fig. 1. a) Ratio of lidar to radar Kernels as a function of particle size. b) Theoretical curves of radar/lidar backscatter coefficients, η/β, (solid line) and radar backscatter/number density, η/N_o, (dashed line) vs. effective radius, μm.

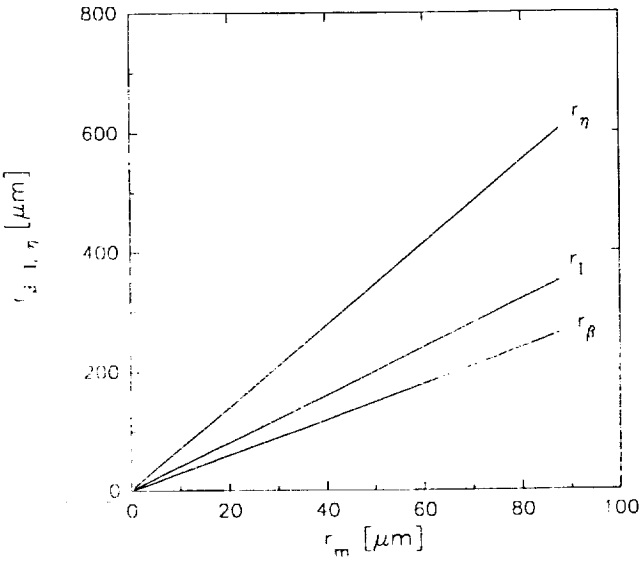

Fig. 2. The 2nd, 3rd, and 6th moment weighted mode radii (r_β, r_l, r_η, respectively) as a function of the mode radius r_m.

2. Cirrus Cloud Case Study

On 26 November 1991 a cirrus cloud system exhibiting three phases was observed passing overhead by the radar and lidar over a period of 5.5 h. During phase 1 the cirrus cloud was thin and tenuous and was detected only by the lidar (1600-1730 UTC, 9-10 km AGL). During phase 2 the cirrus cloud deepened (8-10 km AGL) and similar boundaries were detected by both the lidar and radar (1730-1900 UTC). Later, in phase 3, the cloud became optically thick enough to sporadically attenuate the lidar signal (1900-2130 UTC). The time-height cross sections of r_e, N_o, and *iwc* for the period from 1737-1855 UTC are presented in Fig. 3.

ORIGINAL PAGE IS
OF POOR QUALITY

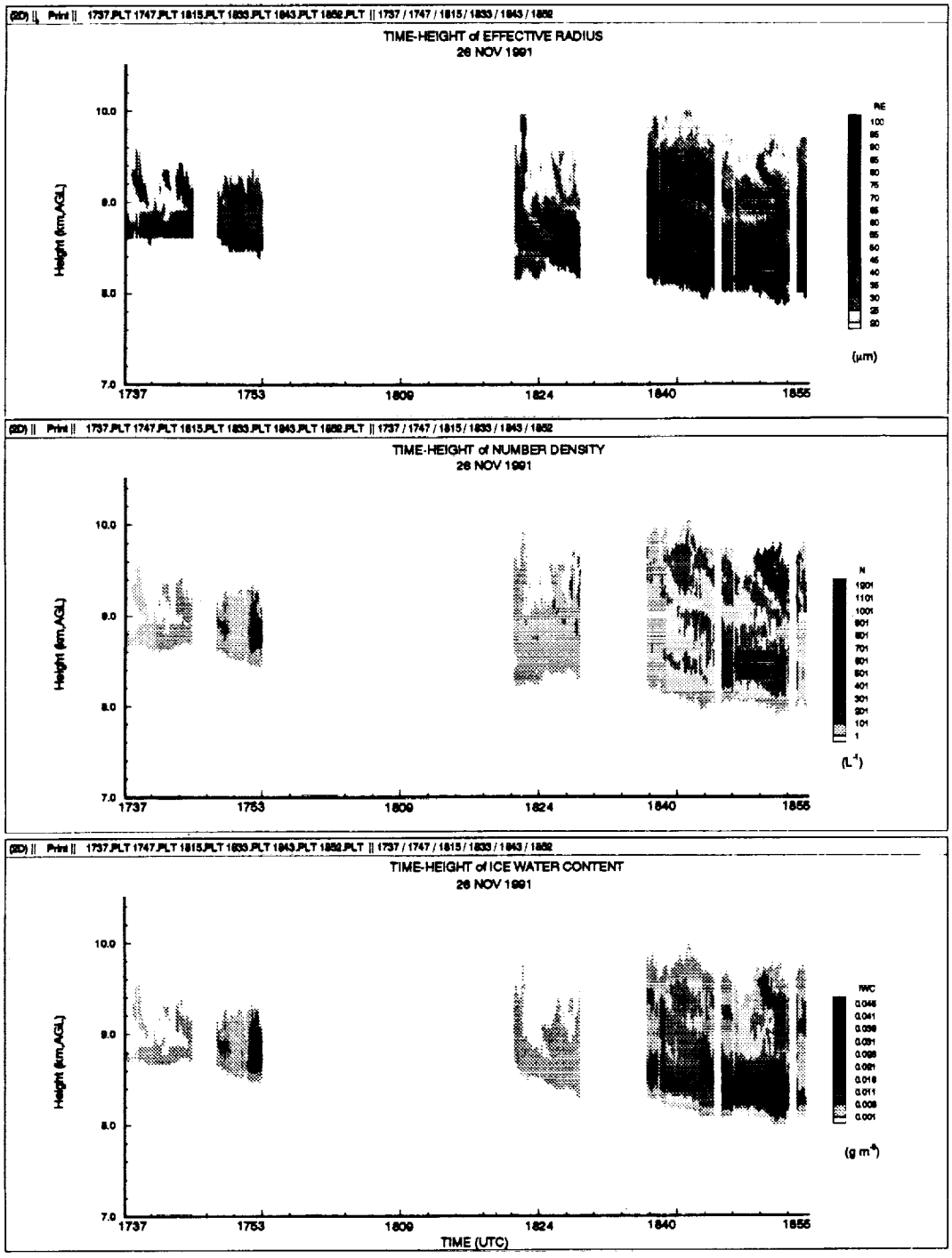

Fig. 3. Time-height series of a) effective radius (μm), b) number density (l^{-1}), and c) ice water content (g m^{-3}) from 1737 to 1855 UTC on 26 November 1991.

In Figure 3a, the effective radii, in μm, are plotted. Note that the largest effective radii are located at the cloud bottom, in banded structures within the cloud, and in the turret-like feature at 1820 UTC. Particles having the smallest r_e are located in other regions within the cloud and at the top of cloud from 1840-1855 UTC. The number densities, in l^{-1}, (Fig. 3b) tend to be a maximum in location above the maximum in

r_e and are often better correlated with the *iwc* field (Fig. 3c). For example, the large concentration of small particles in the upper regions of the cloud at 1850 UTC suggests a nucleation region. The *iwc* profiles, in g m^{-3}, indicate that the cloud from 1820 to 1830 UTC is emitting less IR radiation downward than the cloud from 1845 to 1855 UTC (Fig. 3c).

3. Summary

By utilizing multiple-sensor combinations and integrating data sets we can begin to understand how thickness, size distribution and optical properties affect cirrus cloud radiative properties. An important advantage of using the radar and lidar is that they can obtain extended periods of measurements with good spatial and temporal resolution, whereas aircraft, the primary alternative for cloud sampling, are expensive and limited to only a few hours of data sampled one point at a time. Combined lidar and radar cloud information can be obtained from 3 s which is appropriate for smaller scale cloud microphysical or radiation models.

Much needed longer term cloud statistics can be easily compiled (i.e., cloud boundaries, particle sizes, and number concentration) for larger scale models needing average bulk property parameterizations. This information can be reduced to any time increment from 3 s to as long as the data was obtained i.e. 1 month of wintertime continental cirrus.

Acknowledgements. The authors would like to thank everyone who operated and maintained the lidar and radar during the FIRE II experiment. This work was supported by a grant titled Cloud Remote Sensing in National Climate Research Programs, from NOAA's Climate and Global Change Program Office.

References

Feingold, G. and Z. Levin, 1987: Application of the lognormal raindrop distribution to differential reflectivity radar measurements (Z_{DR}). *J. Atmos. Oceanic Tech.*, **4**, 377-382.

Intrieri, J.M., G.L. Stephens, W.L. Eberhard, and T. Uttal, 1993: A method for determining cirrus cloud particle sizes using a lidar/radar backscatter technique. *J. Appl. Meteor.*, **32**, 1074-1082.

Uttal, T., and J.M. Intrieri, 1993: Comparison of cloud boundaries measured with 8.6 mm radar and 10.6 μm lidar (This volume).

S14-47
197514
P-4

N94-22306

COMPARISON OF CLOUD MICROPHYSICAL PARAMETERS DERIVED FROM SURFACE AND SATELLITE MEASUREMENTS DURING FIRE PHASE II

David F. Young, Lockheed Engineering and Sciences Company, Hampton, VA 23666

Patrick Minnis, Atmospheric Sciences Division, NASA Langley Research Center, Hampton, VA 23681

Jack Snider and Taneil Uttal, NOAA Wave Propagation Laboratory, Boulder, CO 80302

Janet M. Intrieri and Sergey Matrosov, Cooperative Institute for Research in the Environmental Sciences, University of Colorado, Boulder, CO 80309

INTRODUCTION

Cloud microphysical properties are an important component in climate model parameterizations of water transport, cloud radiative exchange, and latent heat processes. Estimation of effective cloud particle size, liquid or ice water content, and optical depth from satellite-based instrumentation is needed to develop a climatology of cloud microphysical properties and to better understand and model cloud processes in atmospheric circulation. These parameters are estimated from two different surface datasets taken at Coffeyville, Kansas, during the First ISCCP Regional Experiment (FIRE) Phase-II Intensive Field Observation (IFO) period (November 13 - December 7, 1991). Satellite data can also provide information about optical depth and effective particle size. This paper explores the combination of the FIRE-II surface and satellite data to determine each of the cloud microphysical properties.

DATA AND ANALYSIS TECHNIQUES

The NOAA WPL 8.66-mm Doppler radar and an infrared radiometer were used to estimate ice water path (*IWP*) and mean ice particle diameter, D_e, over Coffeyville using the techniques of Matrosov et al. (1992). Optical depth was derived from the surface using the NOAA WPL 10.6-μm Doppler lidar whenever the cloud was thin enough to obtain a return signal from the stratospheric aerosol layer. Liquid water path was derived from data taken by an uplooking 2-channel microwave radiometer (Hogg et al., 1983). Visible (~0.65 μm, VIS), infrared (~11.0 μm, IR), and near-infrared (~3.8 μm, NIR) radiances from the NOAA Advanced Very High Resolution Radiometer (AVHRR) and the Geostationary Operational Environmental Satellite (GOES) were used to estimate effective ice crystal and water droplet sizes, and optical depth over the surface site and other locations. The AVHRR data were taken at 1-km resolution, while the GOES data resolutions varied from 4 to 16 km.

Bidirectional reflectance and effective emittances were computed for a variety of conditions using an adding-doubling radiative transfer model. Reflectances, $\rho_{vis}(\tau, r_e, \theta_o, \theta, \psi)$ and $\rho_{nir}(\tau, r_e, \theta_o, \theta, \psi)$, were computed for VIS optical depths, τ = 0.25, 0.5, 1, 2, 3, 4, 8, 16, 32, 64, 96, 128, for effective water droplet radii r_e = 2, 4, 6, 8, 12, 16, 32 μm, for randomly oriented hexagonal ice crystals in the cirrostratus (CS) and cirrus uncinus (CU) distributions (Takano and Liou, 1989) and for a full range of solar zenith θ_o, satellite zenith θ, and relative azimuth ψ angles. The NIR optical depths are $\tau_{nir} = \tau_{vis} Q_{nir}/Q_{vis}$, where Q is the extinction efficiency for a given wavelength and particle. The reflectances were compiled in lookup tables. The albedos for r_e = 6 and CS are shown in Fig. 1 for τ =1 and 4. The CS albedo is much less than the water droplet model and is much less sensitive to changes in optical depth. Water droplet albedo decreases with increasing r_e. The same holds true for ice crystals. The CU model produces a smaller albedo than CS for the same optical depth. Optical depth is derived from a measured ρ_{vis} for a given model using the procedures of Minnis et al. (1993).

Effective emittance $\varepsilon(\tau, r_e, \theta, \Delta T)$ was computed for the same range of optical depths up to τ = 16, for the same particle size distributions, and satellite zenith angles as the reflectance calculations for the NIR and IR wavelengths. The emittances were computed for cloud temperatures T_c = 195, 220, 240, 255, 275, 285, 295K and for surface temperatures T_s = 260, 280, 300, 320K to yield a range in cloud-clear temperature differences ΔT = 5 to 125K for cirrus clouds and 5 to 80K for water clouds. The results were

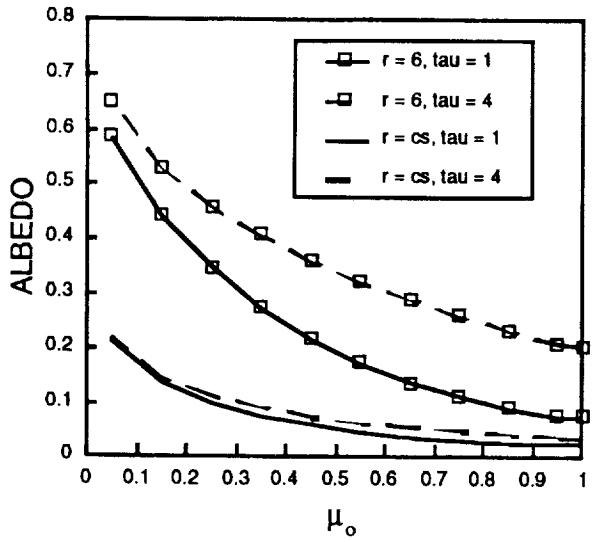

Fig. 1. Albedo for water droplet and cirrostratus ice crystal clouds at 3.73 μm from adding-doubling model computations.

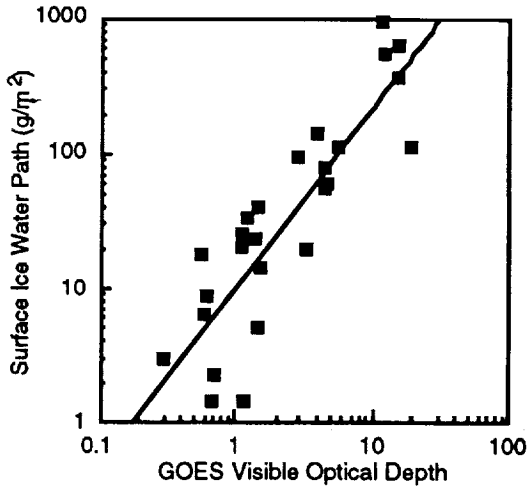

Fig. 2. Correlation of GOES-derived optical depth and surface-radar-derived ice water path for cirrus clouds over Coffeyville, Kansas during November 17 and 26, 1991.

parameterized as follows for a given wavelength λ.

$$\varepsilon(r_e) = a_0 + a_1\{1/\ln(\Delta T)\} + a_2\{1/\ln(\Delta T)^2,$$

where $\mu = \cos\theta$, $a_i = S\, b_j\, t^j$, $j = 0, 4$ and $b_j = \Sigma\, c_k\, \mu^k$, $k = 0, 6$. The model standard error is ± 5%.

When only VIS and IR data are available, cirrus cloud optical depth and cloud-top temperature are derived as in Minnis et al. (1993) using the CS model. When all three channels are used, the particle size and optical depth are determined iteratively for each cloudy pixel similar to the method of Han (1991). The VIS-IR data are first used to determine the clear-sky temperature T_s. The models are used to compute sets of reflectance and emittance for each particle size and optical depth for the given pixel. The measured NIR and IR radiances are given in equivalent blackbody temperature T_λ where

$$B_\lambda(T_\lambda) = \varepsilon_\lambda\, B(T_c) + (1 - \varepsilon_\lambda)\, B(T_s) + \rho_\lambda / \mu_o E_\lambda \qquad (1)$$

$\mu_o = \cos\theta_o$, and E_λ is the spectral solar constant which is zero for the IR channel. Effective radius, optical depth, and T_c are found simultaneously by solving (1) for the IR and NIR and matching τ to ρ_{vis} through the parameterization of Minnis et al. (1993). So far, the technique has only been used to determine r_e for water clouds and to simulate the radiances given T_c and either the CS or CU models.

RESULTS

GOES VIS and IR data were analyzed over Coffeyville to obtain the cirrus optical depth. In Fig. 2, the results for several days during November are plotted in a logarithmic scale with *IWP* derived from the radar data. This preliminary result shows that the two quantities are well correlated over the large range of IWP values. The linear logarithmic fit yields a much higher correlation than the simple linear fit. The scatter in this figure can arise from many sources including time and space mismatches between the surface and satellite, water cloud contributions to the optical depth, and variable particle sizes.

During December 5, the ER-2 flew missions over the Gulf of Mexico and over the hub. The ER-2 Gulf flight was coincident with the Landsat overpass at ~ 1030 LT. In the Gulf, scattered cirrus were observed over a layer of stratocumulus clouds. The NOAA-11 overpass occurred almost 4 hours later when cirrus cells could be seen over the stratocumulus clouds in the AVHRR imagery. A histogram of the effective radii derived using the AVHRR data over a portion of the stratocumulus field is shown in Fig. 3. The effective radii for cirrus-free scenes vary from 6 to 12 μm with an average of 10.2 μm. The mean radii ranged from 10 to 14 μm over the vicinity of the Landsat overpass. Figure 4 shows the 2-dimensional histogram of the channel 4 (10.8 μm) - channel 3 (3.7 μm) brightness temperature differences (BTD) plotted as functions of T_4. The VIS-IR analysis for this area showed that the lower and upper cloud layer had cloud-top temperatures of 275K and 247K, respectively. The curve corresponding to r_e = 12 μm plotted for the lower cloud shows that the data and the theoretical parameterizations are in

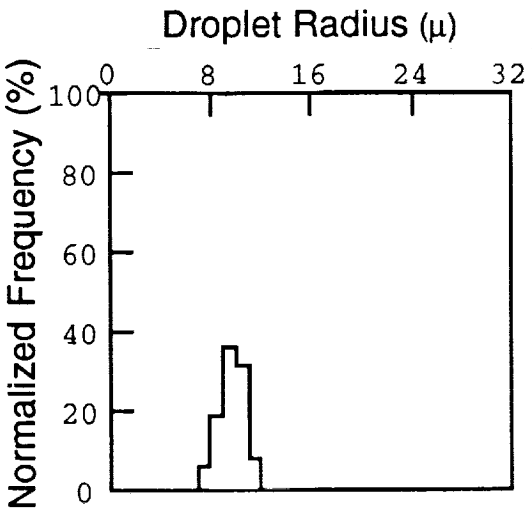

Fig. 3. Histogram of GOES-derived stratocumulus water droplet radius over the Gulf of Mexico from December 5, 1991.

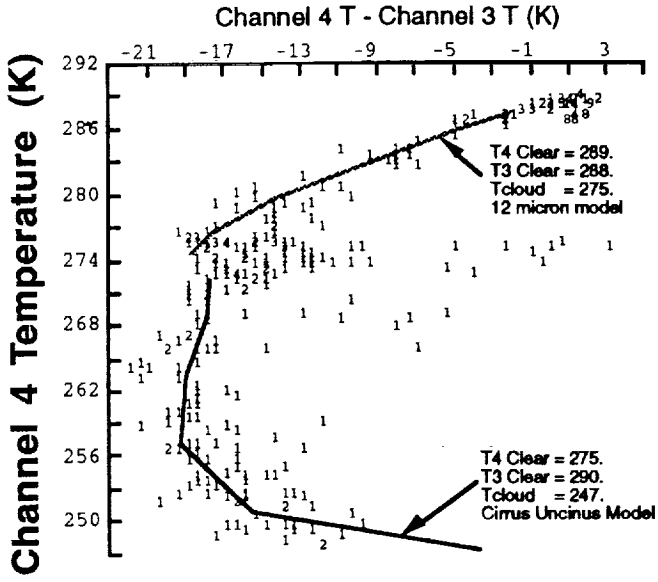

Fig. 4. IR BTD histogram of cirrus uncinus over a stratocumulus layer.

excellent agreement. Since the high cloud is over the lower cloud and not over clear ocean, $T_S = 275K$ in (1) for the high cloud. The cirrus uncinus model produces an excellent fit to the data for the colder cloud. In the imagery, the high cloud shows the gross characteristics of cirrus uncinus, a dense head with streamers from the bottom. The pixels with $T_4 = 275K$ and BTD > -5K are apparently low clouds shadowed by the higher clouds. Low clouds without solar illumination typically have BTD ≥ 0. Fitting a single model to the cirrus clouds over Coffeyville met with less success as shown in Fig. 5. Surface lidar data indicate that the tops of the clouds at 2130 UTC varied from 11.3 to 12.1 km or 218 to 211K, while the bottom of the clouds ranged from 9.5 to 9.7 km or 231 to 230K. Using a single value of $T_C = 224K$ yields the curves shown in Fig. 5. The CS model appears to fit the thinner clouds quite well compared to the CU model. Thicker or higher clouds corresponding to the colder temperatures do not follow the CS model indicating that the cloud temperature was too warm or the effective crystal diameter was too large for the colder or thicker clouds. An iterative approach having a full spectrum of crystal sizes like the water droplet method is needed to fit these data.

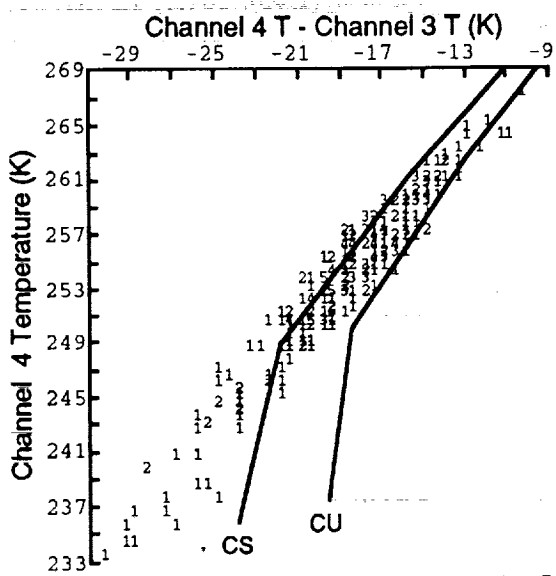

Fig. 5. IR BTD histogram over Coffeyville, December 5, 1991.

DISCUSSION

Optical depth is related to the effective particle cross-sectional area and thickness of the cloud. Ice or liquid water path is related to the mean volume of the cloud particle distribution and the cloud thickness. Since the cross-sectional area is related to volume by the geometry of the particle, IWP or LWP is related to τ via the size and shape of the particle. Given the gamma size distribution for spheres, LWP can be approximated as $2\tau r_e /3$. This formulation is the basis for deriving r_e using the surface microwave LWP and the VIS optical depth. The relationship is not likely to be as simple for ice crystals because of the wide variety of shapes and sizes of particles within cirrus clouds. The results in Fig. 2 are encouraging, especially if it is possible to include the effective ice crystal size in the formulation.

The initial retrievals of r_e using the multispectral data are also encouraging but they highlight some of the difficulties that will be encountered in any application of the methodology. Selection of ice or water droplet models is straightforward if the cloud-top temperature is warmer than 273K or colder than 233K. For the many clouds having temperatures between 233 and 273K selecting the correct set of models is more complicated. While there may be some overlap in albedos for very small ice crystals and large water droplets, it may be possible to use the marked differences between the water droplet and ice 3.7-μm albedos (e.g., Fig. 1) to select the proper model set. A greater problem for applying the multispectral technique is the selection of the background radiating temperature. If only one layer is present in the scene, the use of the clear-sky temperature is warranted for all pixels. For the frequent occurrences of multilevel and convective clouds, it is necessary to know the characteristics of the background clouds. The large range in BTD for the pixels near T = 275K indicates that background clouds, even for a single contiguous stratus, can have variable optical properties. Deciding whether a pixel contains a thin cloud over a lower layer or a thick cloud at higher layer may also produce some ambiguities. The cloud shadowing seen in Fig. 3 also presents some logic challenges for automating the analysis procedures.

CONCLUDING REMARKS

Only a small portion of the FIRE-II lidar and radar IWP datasets has been used here. Combination of the remainder with the satellite products should provide a dataset large enough for an initial parameterization of IWP in terms of τ. Effective cirrus ice-crystal sizes may also be derivable using the multispectral data. The parameterization of IWP would probably be more reliable if the ice crystal size were included in the formulation. The surface-based LWP measurements (not shown here) will be used to estimate a value of r_e that may be a better representation of the entire cloud than the multispectral value. The latter may be highly dependent on the microphysics at the top of the cloud. The surface-based LWP data will also aid in determining the contributions of the water clouds to the satellite-observed radiances in the mixed phase and multilevel cloud systems observed during the IFO. In the future, these results will be compared to the FIRE-II in situ measurements to ensure the validity of the satellite and surface-derived quantities.

REFERENCES

Han, Q., 1992: Global survey of effective particle size in liquid water clouds. Ph.D. Dissertation, Columbia University, New York, NY, 199 pp.

Hogg, D. C., F. O. Guiraud, J. B. Snider, M. T. Decker, and E. R. Westwater, 1983: A steerable dual-channel microwave radiometer for measurement of water vapor and liquid in the atmosphere. *J. Appl. Meteorol.*, **22**, 789-806.

Matrosov, S. Y., T. Uttal, J. B. Snider, and R. A. Kropfli, 1992: Estimation of ice cloud parameters from ground-based infrared radiometer and radar measurements. *J. Geophys. Res.*, **97**, 11,567-11,574.

Minnis, P., P. W. Heck, and D. F. Young, 1993: Inference of cirrus cloud properties from satellite-observed visible and infrared radiances. Part II: Verification of theoretical radiative properties. *J. Atmos. Sci.*, **50**, 1305-1322.

Takano, Y. and K. N. Liou, 1989: Radiative transfer in cirrus clouds: I. Single scattering and optical properties of oriented hexagonal ice crystals. *J. Atmos. Sci.*, **46**, 3-20.

5/5-47
197575
p. 6

N94-22307

CIMSS FIRE RESEARCH ACTIVITIES

W. L. Smith, S. A. Ackerman R. O. Knuteson, X. L. Ma, and H. E. Revercomb,
Cooperative Institute for Meteorological Satellite Studies

ABSTRACT

This paper presents an overview of the Cooperative Institute for Meteorological Satellite Studies' FIRE research activities. The paper focuses on analysis of the High-resolution Interferometer Sounder (HIS) made from the ER-2 as well as ground based measurements made by the Atmospheric Emitted Radiance Interferometer (AERI) prototype. Details are covered in companion papers.

ER-2 HIS OBSERVATIONS

The HIS aircraft instrument (Smith et al 1989) is a Michelson interferometer with a spectral resolving power ($\lambda/\Delta\lambda$) of approximately 2000 covering the spectral range from approximately 3.5-16.7 μ m. The HIS spectra have an unapodized resolution of approximately 0.35 cm^{-1} from 600-1100 cm^{-1}, and 0.7 cm^{-1} resolution from 1100-2700 cm^{-1}. A cycle of HIS interferograms consists of four cold blackbody views, four hot blackbody views and 12 earth views. The on board high emissivity, temperature controlled reference blackbody views are used for the calibration of the earth views. The HIS has a noise equivalent temperature and reproducibility of about 0.1-0.2°C over much of the spectrum (Revercomb *et al.*, 1988). Recent upgrades to the HIS have significantly improved instrument performance in the 3.5-5.0 μm spectral region.

The HIS flew aboard the NASA ER-2 during FIRE Phase I (Oct-Nov 1986). The most significant result of these observation was that cirrus clouds do not emit radiation like blackbodies, irregardless fo their optical thickness. Figure 1 has become an historical example of the FIRE I HIS finding that the spectral variation of the radiating temperature of cirrus has a large spectral variation across the climatolically important 8-12 μm "window" region of the thermal infrared.

Another very important finding from FIRE-I HIS radiance spectra was that the water phase of clouds could be diagnosed from simultaneous infraed window measurements at 8, 11 and 12 μm (Smith et al 1988, Ackerman et al 1990). Figure 2 shows a time sequence of 8.3, 11.1 and 12.0 μm HIS brightness temperature together with simultaneous Lidar cloud backscatter observations with the CALS (Spinhirne, 1990). It can be seen that for the case of ice particle cirrus (high altitude backscatter) the 8.3 μm brightness temperature is significantly larger than the 11 and 12 μm brightness temperature whereas for the case of liquid water droplet lower clouds (low altitude backscatter) both the 8 and 11 μm brightness temperature are larger than 12 μm. These results correspond to the different spectral absorption properteis of ice and water (Figure 3).

For FIRE II, HIS data analysis has focused on the determination of the radiative and microphysical properties of cirrus clouds. Table 1 below lists the days and times of available HIS data during FIRE II. Our research objectives under the FIRE Phase II program include: 1) to improve our understanding of the relationship between the microphysical and radiative properties of cirrus clouds; 2) to quantify the capabilities and limitations of various cirrus cloud satellite retrieval techniques; and 3) to improve our capabilities of describing cirrus cloud properties utilizing passive radiometric observations. Since the last FIRE team meeting, we have focused our activities on objectives 1) and 3).

A doubling/adding model has been developed to simulate high-spectral resolution measurements from ground and ER-2 aircraft. This model has been used to study the sensitivity of the spectral observations to various cloud conditions and then to develop and test cloud retrieval algorithms using such observations (Smith et al 1990,1992, 1993). A time section of cloud ice particle size and ice water content deduced from HIS spectra from the ER-2 aircraft are shown in Figure 4. The cloud altitude and thickness were set at the height levels observed by the CALS. The cloud ice water content varies between 2.3 g m^{-3} and effective radius is about 20 μm. Cloud heights are accurately determined using HIS carbon kioxide channel information even for relatively low effective cloud emissivites. Improvements in cloud properties retrieval from HIS data by incorporating the 3.7-4.0 μm window and the 4.3 CO_2 radiances are now being investigated.

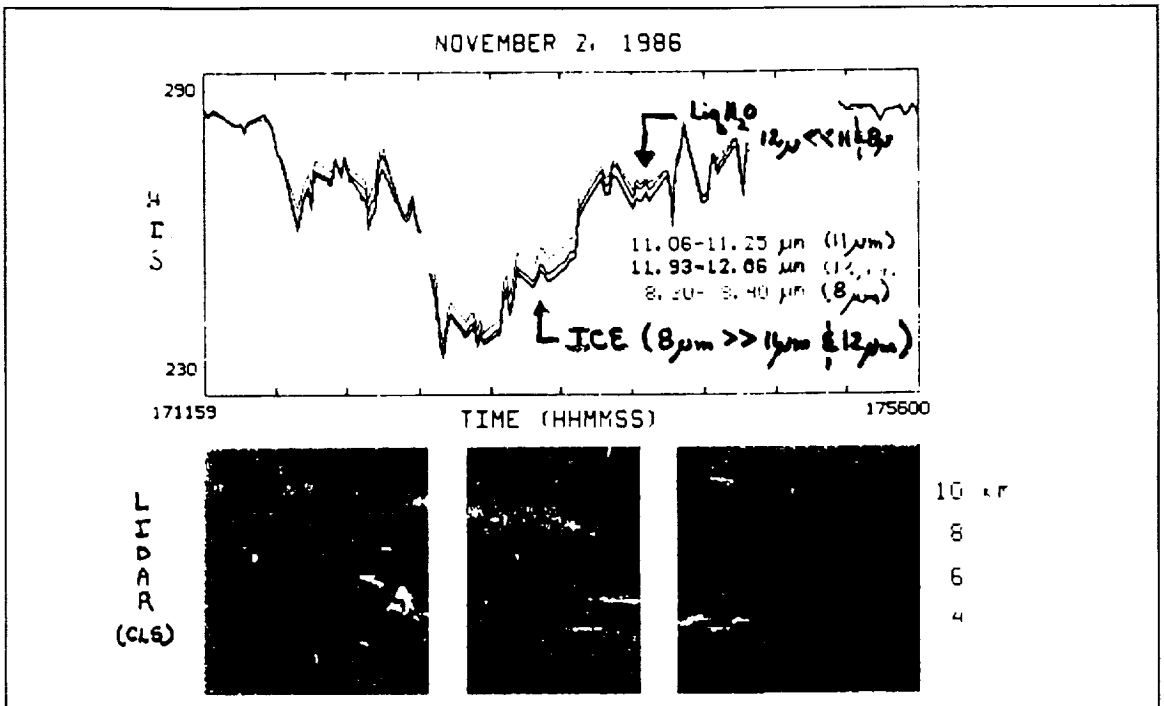

Figure 2. Time series plot of 8, 11 and 12 m brightness temperatures. CALS lidar image is displayed below.

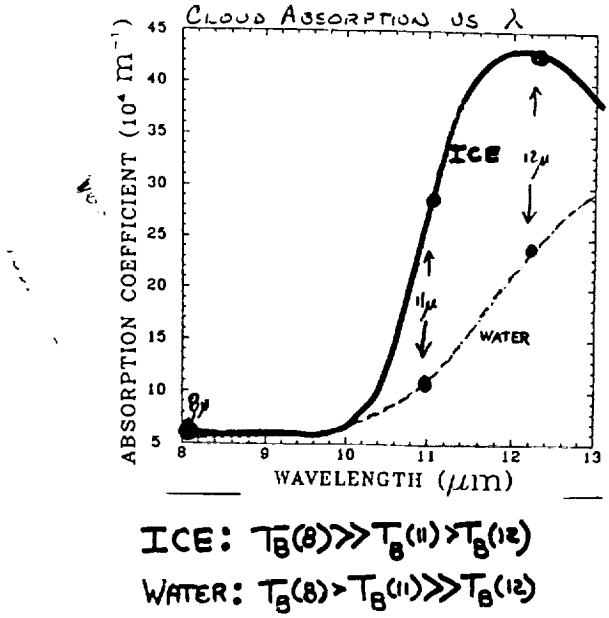

Figure 3. Absorption Coefficient as a function of wavelength

TABLE 1. SUMMARY OF HIS FLIGHT DATA

DATE	TARGET AREA	TIME (UTC)	HIS DATA STUDY OBJECTIVE
14 Nov 91	Kansas	14:01-18:00	Cirrus
18 Nov 91	Kansas	20:56-23:30	Clear sky
22 Nov 91	Kansas	18:30-20:30	Cirrus
24 Nov 91	Gulf Mex	17:00-21:10	Cirrus
25 Nov 91	Oklahoma	16:00-20:00	Cirrus
26 Nov 91	Kansas	15:00-17:50	Cirrus
3 Dec 91	Gulf Mex	15:30-18:00	Cirrus
4 Dec 91	Gulf Mex	18:30-20:30	Corpus Christi / Gulf of Mexico
5 Dec 91	Kansas	15:00-19:00	Cirrus

AERI OBSERVATIONS

The AERI instrument is a goundbased HIS system for the accurate and continuous measurement of downwelling infrared radiation from the atmosphere. The observed spectra are being used for many diverse functions, including identification and elimination of absolute errors in calculated spectra for known atmospheric states; evaluation and improvement of cloud radiation calculations; characterization of the distribution and evolution of effective cloud radiative properties; and studies of the state parameter changes associated with cloud formation, evolution, and dissipation. Table 2. is a summary of when the AERI prototype was operational during the DOE Spectral Radiance Experiment (SPECTRE) in association with FIRE II, conducted in Coffeyville, Kansas in the Fall of 1991. Observations of the atmosphere were collected approximately every 10 minutes.

Examples of cloudy brightness temperature spectra during FIRE II are shown in Figure 5. As found with HIS aircraft observations, clouds do not behave as "blackbodies" for which the brightness temperature would be constant in the regions between absorption lines in the atmospheric window between 8 and 13 μm (770-1250 cm^{-1}). The low cloud spectrum in the figure is close to that of a blackbody cloud, but the middle cloud shows major deviations from that simple behavior. The deviations from blackbody behavior are being used to estimate cloud base microphysical properties in much the same way cloud top microphysical propeties are being estimated from ER-2 HIS spectra (Smith, et al., 1993).

The AERI data have been used to assess the capabilities of radiative transfer model results, analyze the evolution of the boundary layer, and retrieve cloud properties. These applications are discussed in a companion paper.

FUTURE ACTIVITIES

Ground-based interferometer observations, at a resolution similar to the aircraft HIS, were collected at Coffeyville KS as part of FIRE II and SPECTRE. ER-2 over-flights of the site will enable assessment of the spectral infrared effects of clouds on the radiance distribution at the ground and at the top of the atmosphere. Cloud base properties will also be derived from the ground-based interferometer for comparison with the ER-2 based derived cloud top properties. This study is crucial for the characterization of the downwelling radiance of a cloud, based on satellite observations of the upwelling radiance as needed for use in global climate studies.

Upgrades to the HIS prior to the FIRE II field experiment improved instrument performance in the 2000-2700 cm^{-1} regime. This spectral region is also measured by the AERI. The 3.7 μm region has been employed in cloud retrieval techniques applicable to satellite observations. Radiance in the 3.5-4.6 μm region are sensitive to the particle size, shape and water phase of the cloud. We plan to enhance our previously developed capabilities of inferring cloud microphysical characteristics from the 8-12 μm spectral region using radiance from the 3.5-4.5 μm spectral region. Inferences of the cloud particle phase and effective size will be based on the spectral variability in the 3.5- 4 μm and 8-12 μm regions.

REFERENCES

Ackerman, S. A., W. L. Smith, J. D. Spinhirne, and H. E. Revercomb, 1990: The 27-28 October 1986 FIRE cirrus case study: spectral properties of cirrus clouds in the 8-12 μm window. *Mon. Wea. Rev.*, **118**, 2377-2388.

Revercomb, H.E., H. Buijs, H.B. Howell, D.D. LaPorte, W.L. Smith, and L.A. Sromovsky, 1988: Radiometric Calibration of IR Fourier Transform Spectrometers: Solution to a Problem with the High Resolution Interferometer Sounder. *Applied Optics*, 27, 3210-3218.

Smith W. L., H. E. Revercomb, H. B. Howell, and M. -X. Lin; 1988: Multi-spectral window radiance observations of cirrus from satellite and aircraft - November 2, 1986 "Project FIRE", FIRE Science Results 1988, Proceeding of a conference held in Vail, CO July 11-15, pp 89-93.

Smith W. L., H. E. Revercomb, D. D. LaPorte, H. M. Woolf, H. B. Howell, R. O. Knuteson, H. L. Huang, L. A. Sromovsky and S. Silverman, 1989: GHIS, the Geostationary High-resolution Interferometer Sounder. *CIMSS View*, **Vol. V**, No.1, available from the Space Science and Engineering Center, Universtiy of Wisconsin, Madison, Wisconsin, 53706.

Smith W.L., Xia Lin Ma, S.A. Ackerman, H.E. Revercomb, and R.O. Knuteson, 1993: Remote Sensing Cloud Properties from High Spectral Resolution Infrared Observations. *J. Appl. Met*, in press, 1993.

Smith, W. L. and R. Frey, 1990: On cloud altitude determinations from high resolution interferometer sounder (HIS) observations. *J. Appl. Meteor.*, **29**, 658-662.

Smith, W. L., and R. Frey, 1991: Altitude specification of cloud motion winds. Workshop on Wind Extraction from Operational Meteorological Satellite Data, Washington, D.C. September 17-19.

Table 2. WISCONSIN AERI INSTRUMENT OPERATIONS

LOCATION: COFFEYVILLE, KANSAS
YEAR: 1991
REMARKS: (1) Observations are at 10 minute intervals betweenstated START and END times. (2) The letter H indicates that the ER-2 HIS was overhead. (3) OP # refers to an AERI operating period.

OP #	DATE	TIME PERIOD	CONDITIONS FROM VISUAL OBS
1	11 NOV	17:06 - 17:30	low overcast
2	12 NOV	23:26 - 02:29	cirrus
	13 NOV	02:53 - 04:28	cirrus/clear
3	13 NOV	18:18 - 01:26	cirrus
	14 NOV	02:13 - 03:41	thin cirrus
4	17 NOV	17:58 - 21:12	mixed cirrus to clear
	18 NOV	01:29 - 24:00	clear
	19 NOV	00:00 - 05:57	clear/cirrus/low thick cloud
5	20 NOV	17:20 - 23:33	clear
	21 NOV	00:12 - 24:00	clear
	22 NOV	00:00 - 19:07	cirrus/clear/rain
6	23 NOV	16:28 - 24:00	clear/mixed/overcast
	24 NOV	00:47 - 23:29	overcast/clear
	25 NOV	00:37 - 05:48	overcast
7	25 NOV	16:19 - 23:52	alto-cumulus/scatter cirrus
	26 NOV	00:29 - 24:00	clear/cirrus/mixed
8	27 NOV	14:01 - 17:21	low cloud
9	28 NOV	14:40 - 22:35	cirrus/overcast stratus
10	29 NOV	15:00 - 24:00	overcast/clear
	30 NOV	00:00 - 17:34	clear/overcast
11	03 DEC	00:25 - 23:08	overcast/ clear/ cold
	04 DEC	23:55 - 06:41	clear
12	04 DEC	17:16 - 24:36	clear/ aerosol
	05 DEC	01:23 - 24:00	clear/cirrus
	06 DEC	00:00 - 05:31	thin cirrus
13	06 DEC	14:52 - 20:33	mixed cirrus/alto cu
	07 DEC	00:54 - 05:52	clear/ aerosol/low cloud
14	07 DEC	14:49 - 21:23	low overcast/broken low

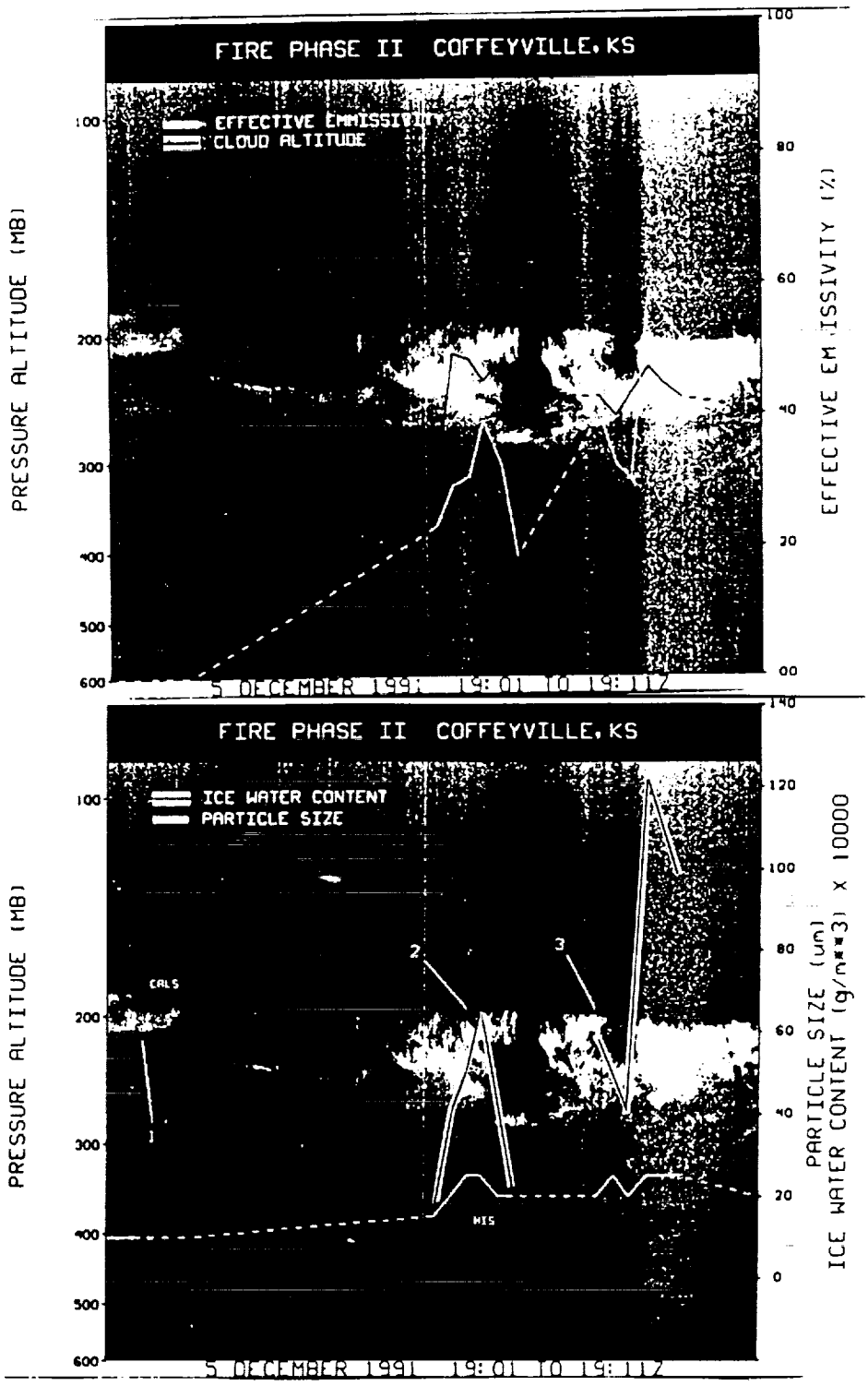

Figure 4. HIS observation near Coffeyville KS on Dec 5, 1991. (a) Cirrus ice water content and effective particle size and (b) deduced cloud altitude and effective emissivity

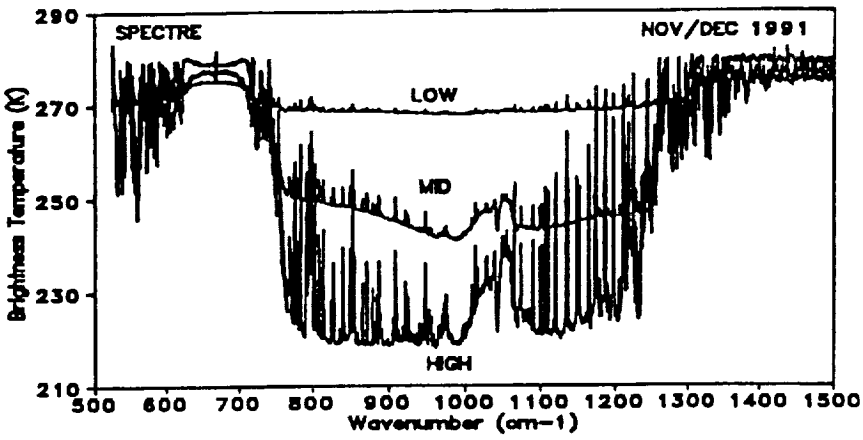

Figure 5. AERI measurements of the downwelling spectra of clouds showing deviations from black body emission.

cm.T

November 26 Case Study Utilizing Data Collected by the NOAA Wave Propagation Laboratory

Taneil Uttal, Wynn Eberhard, Jack Snider, Brad Orr, Bob Kropfli

NOAA/ERL Wave Propagation Laboratory
R/E/WP6
325 Broadway
Boulder, Colorado 80302

Janet Intrieri and Sergey Matrosov
Cooperative Institute for Research in Environmental Science
University of Colorado
Campus Box 449
Boulder, Colorado 80309

The NOAA Wave Propagation Laboratory operated a 8.66 mm radar, a 10.6 μm lidar and radiometers at the FIRE II field experiment. For the period between 1630 and 2400 GMT on November 26, we will present a pictorial times series display of the data collected by these sensors. This display will include derived products such as cloud particle sizes, concentrations, and ice water paths determined by different methods described in other papers in this conference. We will perform a preliminary case study analysis that will be basis for WPL contributions to a larger scale case study analysis that will involve other project sensors, including but not limited to satellites, aircraft and other ground-based remote sensors.

N94-22308
197516
P. 4

Progress in Interpreting CO_2 Lidar Signatures to Obtain Cirrus Microphysical and Optical Properties

Wynn L. Eberhard
NOAA Wave Propagation Laboratory
U.S. Department of Commerce
325 Broadway
Boulder, Colorado 80303

One cloud/radiation issue at FIRE II that has been addressed by the CO_2 lidar team is the zenith-enhanced backscatter (ZEB) signature from oriented crystals. A second topic is narrow-beam optical depth measurements using CO_2 lidar. This paper describes the theoretical models we have developed for these phenomena and the data-processing algorithms derived from them.

I. Reflection with diffraction from oriented crystals

When a lidar scans in elevation angle, the backscatter from ice-containing clouds often exhibits a strong enhancement at the vertical (Thomas et al., 1990). The mechanism is partial reflection of the laser's light by horizontally oriented ice crystals. Ice particles absorb strongly at the 10.6-μm wavelength of the CO_2 lidar. The propagation distance within a bulk piece of ice is only 6.9 μm before absorption reduces the intensity by e^{-1}. Therefore, reflection from the first surface dominates the backscatter from ice particles in clouds. Additional substantiation comes from calculations for spheres and infinitely long cylinders of ice, which indicate this is a useful approximation for particle size distributions with mean radii greater than about 5 μm. Diffraction effects are also important at this longer wavelength. These characteristics permit the use of geometrical optics, when diffraction effects are included, for approximate calculation of backscatter from plate-like and column-like particles.

An oriented hexagonal plate can be approximated by a circular plate of the same thickness and face area A_p. For light of collimated collimated irradiance E_i incident normal to the face, the reflected flux in the geometrical optics approximation is

$$F_p = E_i A_p R_n , \tag{1}$$

where R_n is the Fresnel reflectance from a flat surface of ice. The angular distribution of the reflected light is given approximately by Fraunhofer diffraction (Hecht and Zajac, 1974) through a circular aperture with radius $r_p = (A_p/\pi)^{1/2}$. As the lidar scans across the vertical (zenith angle $\zeta \leq 15°$ or so), F_p is nearly constant because the cross-sectional area and reflectance change little. The measured backscatter cross section $\beta_p(\zeta)$ traces out the shape of the diffraction pattern (Fig.1, Curve A). Because the incident and reflected angles are equal but on opposite sides of the normal to the face, $\zeta = \alpha/2$, where α is the off-axis angle for Fraunhofer diffraction.

We assume that hexagonal columns orient with the long dimension horizontal but with

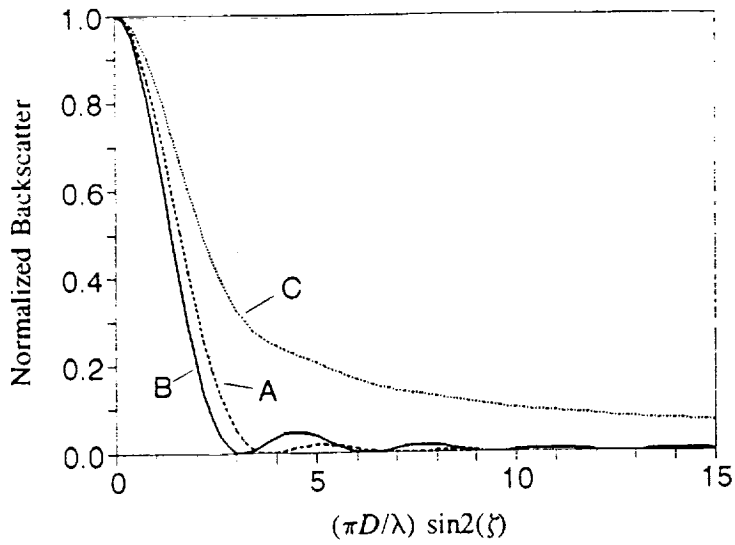

Fig. 1. Backscatter from horizontally oriented crystals as a function of lidar zenith angle (ζ), particle long dimension (D), and wavelength (λ). Curve A is Fraunhofer diffraction for plates, curve B is narrow-slit diffraction representing columns with axis aligned in the scan plane, and curve C is narrow-slit diffraction representing columns with random azimuthal orientation.

azimuth and roll orientations random. The backscatter for a collection containing many of these particles can be approximated by that from cylinders of equal length L and with radius $r_c = (a_c/\pi)^{1/2}$, where a_c is the hexagonal-shaped area across the narrow dimension of the column. The reflected flux for light at (or near) normal incidence is given approximately by

$$F_c = E_i \, (L \, r_c \, / \, 2) \, R_n \, . \tag{2}$$

The shape of the backscatter profile depends on the azimuthal orientation of the long axis relative to the vertical plane of the elevation scan. If the particles were all oriented with the long axis perpendicular to the scan plane so the lidar views the "side" of the particles, the backscatter would be independent of ζ. If the particles were aligned with the scan, the backscatter would trace out the shape (Fig. 1, Curve B) of diffraction from a long, narrow slit (Hecht and Zajac, 1974). A calculation of $\beta_c(\zeta)$ for the case in clouds of a uniform distribution in particle azimuth (i.e., a large number of random orientations) gives the zenith dependence shown in Fig. 1 (Curve C).

II. Retrieval of microphysical parameters

One parameter desired for interpreting ZEB is the backscatter cross section from a collection of particles with equal geometrical cross section but not exhibiting specular scatter. We develop here the simplest equivalence, in which we assume spherical particles with the same cross-sectional area as the oriented particles when viewed at zenith. The backscatter cross section β_{ep} for these plate-equivalent spheres is found as follows. The cross section for light reflected from the plate is

$$b_p = A_p \, R_n = F_p \, / \, E_i \tag{3}$$

is also given by

$$b_p = 4\pi \int \beta_p(\zeta) \, sin(\zeta) \, d\zeta \, , \tag{4}$$

where the limits of integration over ζ are far enough from the zenith to include most of the reflected flux F_p for an adequate approximation. The backscatter cross section for a highly absorbing ice sphere in the geometrical optics limit is (Bohren and Huffman, 1983)

$$\beta_s = r_s^2 R_n / 4 \quad , \tag{5}$$

where r_s is the radius of the sphere. By setting $\pi r_s^2 = A_p$, one obtains

$$\beta_{ep} = b_p / 4\pi = \int \beta_p(\zeta) \sin(\zeta) \, d\zeta \, . \tag{6}$$

The approximation $\sin(\zeta) = \zeta$ can also be made with little error.

Derivation of a similar relationship for horizontally oriented columns is more difficult because of the tail at large ζ in Fig. 1, which arises from particles with axis nearly perpendicular to the scan plane. However, we have developed a useful algorithm. We first consider the case of columns oriented with long axis parallel to the lidar scan plane, when

$$b_c = (r_c \, L/2) \, R_n = 8 \int \beta_c(\zeta) \, d\zeta \, . \tag{7}$$

By setting $\pi r_s^2 = 2 \, r_c \, L$ and introducing a correction factor C_b that relates the uniform-azimuth result with long-axis-parallel result, we have

$$\beta_{ec} = 2 \, (\pi \, C_b)^{-1} \int \beta_c(\zeta) \, d\zeta \, , \tag{8}$$

where $C_b \geq 1$. In our processing we have found it practical to use nomograms to determine C_b in the following manner. The value of $\beta_{c,min}$ at the largest value of ζ in the scan [or where the curve $\beta_c(\zeta)$ flattens out] is subtracted from all values of $\beta_c(\zeta)$ before the integration in (8). Then the width of the ZEB peak is used to find a final correction factor, which depends on how far down the peak the integration is terminated, to determine β_{ec}.

The values for β_{ep} and β_{ec} are used to adjust lidar data for other purposes, such as radar/lidar determination of ice particle sizes and number densities. They also comprise part of the information for estimating the fraction of particles that are oriented.

The longest dimension of the oriented particles can be estimated from the width of the ZEB peak. The ratio of area to peak

$$w_{A/p} = \int \beta_c(\zeta) \, d\zeta \; / \; \beta_{max} \tag{9}$$

is one simple measure of width, but others (e.g., standard devation) could be used. Based on the Fraunhofer diffraction approximation, the diameter of the face of a plate is given by

$$D_p = 2 \, r_p = 31.1 \, \lambda \, / \, w_{A/p} \, , \tag{10}$$

where $w_{A/p}$ is in degrees. The expression for the column length is

$$L = 28.6 \, C_w \, \lambda \, / \, w_{A/p} \, , \tag{11}$$

for which a nomogram procedure similar to that used for β_{ec} is invoked to obtain C_w (≥ 1).

Cloud parameters inferred from some of the FIRE II cirrus observations will be at the conference in a separate paper.

III. Narrow-beam optical depth

Data from the 10.6-μm wavelength CO_2 lidar can be used in two different ways to obtain the narrow-beam optical depth of cirrus in this region of the infrared.

The first method (Platt et al., 1987), called the LIRAD method, combines vertical backscatter profiles from the lidar, emission from the same cloud as measured by an infrared radiometer, and temperature profiles (e.g. from radiosonde). The technique produces the vertical profile of emissivity and the narrow-beam optical depth of the cirrus cloud. The data for this technique from FIRE II are less than ideal. An infrared radiometer, operated by another division of our laboratory at the SPECTRE site, were not collocated. An infrared radiometer located much closer and operated in conjunction with the University of Utah lidar may provide better results, but temporal coverage is much less complete. However, LIRAD with CO_2 lidar, whose wavelength is within the passband of the infrared radiometer, may give better results than lidars with wavelengths an order of magnitude shorter.

The second method uses aerosol particles injected into the stratosphere by the Pinatubo volcano as a cooperative target. The decrease in apparent backscatter from the stratosphere between clear and cloudy conditions leads directly to the cloud optical depth (Hall, et al., 1988). Unfortunately, the conditions for accurate retrieval with this method were met only during a small fraction of the time at FIRE II.

Optical depth is an important parameter for the FIRE II research objectives, so we are pursuing retrieval in spite of the limitations. Our progress and the outlook for accuracy and temporal coverage will be reported.

Acknowledgments -- The assistance of Brent Gordon, John Bevilacqua, and Kathleen Healy in preparation of figures and programming of the processing algorithms is appreciated. This research was funded through a grant from the Climate and Global Change Program of the National Oceanic and Atmospheric Administration and Grant No. DE-FG02-90ER61059 in the Department of Energy's Atmospheric Radiation Measurement program.

IV. References

Bohren, C.E., and D.R. Huffman, 1983: **Absorption and Scattering of Light by Small Particles**. Wiley, 530 pp.

Hall, F.F., Jr., R.E. Cupp and S.W. Troxel, 1988: Cirrus cloud transmittance and backscatter in the infrared measured with a CO_2 lidar. **Appl. Opt., 27**, 2510-2516.

Hecht, E. and A. Zajac, 1974: **Optics**. Addison-Wesley, 565 pp.

Platt, C.M.R., J.C. Scott and A.C. Dilley, 1987: Remote sounding of high clouds. Part VI: Optical properties of midlatitude and tropical cirrus. **J. Atmos. Sci., 44**, 729-747.

Thomas, L., J.C. Cartwright and D.P. Wareing, 1990: Lidar observations of the horizontal orientation of ice crystals in cirrus clouds. **Tellus, 42B**, 211-216.

N94-22309

A NUMERICAL TECHNIQUE FOR THE CALCULATION OF CLOUD OPTICAL EXTINCTION FROM LIDAR

J.M. Alvarez, LaRC, MS 417, Hampton, VA 23681 (804) 864-2677
M.A. Vaughan, SAIC, MS 417, Hampton, VA 23681 (804) 864-5331

ABSTRACT

A simple numerical algorithm which calculates optical extinction from cloud lidar data is presented. The method assumes a two-component atmosphere consisting of "clear air" and cloud particulates. "Clear air" may consist of either molecules only or a mix of molecules and atmospheric aerosols. For certain clouds, the method may be utilized to provide an estimate of the cloud-atmospheric parameter defined as the ratio of the cloud volume backscatter coefficient to the cloud extinction coefficient divided by the atmospheric volume backscatter coeffficient at a given altitude. The cloud-atmospheric parameter may be estimated only from cloud data from which the optical thickness may reliably be used as a constraint on the numerical solution. This constraint provides the additional information necessary to obtain the cloud-atmospheric parameter. Conversely, the method may be applied to obtain cloud extinction and optical thickness from lidar cloud soundings if an estimate of the cloud-atmospheric parameter is available.

INTRODUCTION

The equation(Liou 1980) underlying all attempts to obtain optical extinction from lidar data is given by

$$E(r) = \frac{c\tau\beta A_r}{8\pi r^2} e^{\left(-2\int_0^r \sigma(r')\,dr'\right)} P \qquad (1)$$

where E is the backscattered power received by a lidar system emitting power P equipped with a telescope of effective area A_r, c is the speed of light, τ is the laser pulse length, ß is the volume backscattering coefficient, r is the range, and σ is the extinction coefficient. Published solutions to this equation are so numerous and well developed that only very few are cited(Viezee 1969, Collis 1976, Barrett and Ben-Dov 1967, Davis 1969, Klett 1981). If atmospheric scattering and cloud aerosol scattering are to be explicitly considered, then the lidar equation contains two components and is given by

$$E(r) = D\frac{\beta_a+\beta_c}{r^2} e^{-2\int_0^r [\sigma_a(r')+\sigma_c(r')]\,dr'} \qquad (2)$$

where D is $c\tau A_r P/8\pi$ and the a and c subscripts refer to the atmospheric(air) and the cloud parts of the signal. Solutions for equation 2 are not as well developed as for equation 1 partly because there is no analytic solution for this equation as it stands. At present only iterative solutions for equation 2 have been proposed(Fernald 1972, Fernald 1983, Klett 1985).

We present a simple numerical method for the calculation of optical extinction from the two component lidar equation . This new method modifies equation 2 so that a straightforward calculation yields optical extinction.

TECHNIQUE

We start by noting that the numerical array comprising each lidar sounding is proportional to equation 2. *We assume that a "clear" atmosphere is a combination of molecules and the background atmospheric aerosol.* At altitudes above and below the cloud, equation 2 holds but $ß_c = \sigma_c = 0$. If equation 2 is divided by the lidar signal from a "clear" atmosphere as determined from a lidar sounding in a clear region below the cloud or from an atmospheric model fit to the clear air part of the lidar return, the attenuated scattering ratio, R_{sc}, is obtained. In the cloud, this ratio is given by

ORIGINAL PAGE IS
OF POOR QUALITY

$$R(r)_{sc} = \left(1 + \frac{\beta_c}{\beta_a}\right) e^{-2\int_{r_b}^{r} \sigma_c(r')_c dr'} \quad (3)$$

where r_b is cloud base altitude, and the subscripts "a" and "c" refer to "clear air" and cloud respectively. This ratio is obviously 1 below the cloud. In the region above the cloud the attenuated scattering ratio is given by

$$R_{sc} = e^{-2\int_{r_b}^{r_t} \sigma_c(r')_c dr'} \quad (4)$$

where r_t is cloud top altitude. This equation implies that in certain cases, the cloud optical thickness can be obtained directly from the lidar data via the attenuated scattering ratio .

We next assume that the atmospheric volume-backscattering coefficient is proportional to the atmospheric molecular number density N(r) for altitudes greater than some minimum altitude. This assumption is supported by the aerosol data presented by Wallace(1977) who showed that averages of aerosol number densities obtained from Aiken particle counters exhibited the same altitude distribution as the molecular number density at altitudes above about 3 or 4 kilometers. If the molecular number density for the higher altitudes is given by

$$N(r) = N_0 \rho(r) \quad (5)$$

where N_0 is the number density at altitude r_0 and ρ contains the altitude dependence of the molecular number density for altitudes greater than r_0, then the atmospheric volume backscatter coefficient $\beta(r)$ is given by

$$\beta(r) = \beta_0 \rho(r) \quad (6)$$

where β_0 is the atmospheric volume backscatter coefficient at altitude r_0. If we further assume that, for the cloud, the ratio of backscatter volume to extinction coefficients is a constant, k_c(equal to β_c/σ_c) then, equation 3 may be rewritten as

$$R_{sc} = \left(1 + \frac{k_c}{\beta_0} \frac{\sigma_c}{\rho(r)}\right) e^{-2\int_{r_0}^{r} \sigma_c(r')\, dr'} \quad (7)$$

Note that R_{sc} is a function of the cloud-atmospheric parameter(CAP), k_c/β_0 and the functions $\sigma_c(r)$ and $\rho(r)$. Since the molecular number density altitude distribution can be obtained from radiosonde data or a model, $\rho(r)$ can be considered known.

We will initially assume that the CAP(the ratio k_c/β) is known; later we will see how this ratio can itself be determined from lidar data. If we suppose that the CAP is known, then equation 7 contains only one "unknown", the extinction $\sigma_c(r)$. We translate equation 7 to a numerical equation by subdividing the cloud into layers of equal thickness in altitude. We then use the trapezoid rule to obtain

$$R_i = \left(1 + \frac{k_c}{\beta_0} \frac{\sigma_i}{\rho_i}\right) e^{(-\sigma_0 \Delta - 2\Delta(\sigma_1 + \sigma_2 + \ldots \sigma_{i-1}) - \sigma_i \Delta)} \quad (8)$$

where the "i"- corresponds to different altitudes with i=0 being the first cloud layer(stratum), and i=K being cloud top; the finite differential altitude is Δ. The one-half weighting on the first and last elements in the sum in the exponential is in accordance with the trapezoid rule.

We start our calculation at cloud bottom(i=0) where only the first extinction term, σ_0, is present. At this first point, equation 8 is a transcendental equation in σ_0 and we solve this equation numerically by Newton's method. We then consider the second point(i=1) and since we know R_1, ρ_1, σ_0, and the CAP, we again obtain σ_1 numerically. We continue in this manner until we obtain the entire extinction array. At the end of this process we sum the extinction coefficients and calculate the cloud optical thickness, thus completing the calculation.

If the CAP is unknown, the problem is more challenging. To obtain a solution under these conditions requires cloud lidar returns having adequate atmospheric signal at altitudes above and below the cloud. Equation 4 can be utilized to measure the optical thickness for such clouds. We initially set the CAP to some arbitrary value. For this, the extinction coefficient array is calculated as before and the optical thickness is estimated by summing the extinction. Then, this optical thickness estimate is compared to the lidar-measured optical thickness obtained by equation 4. If the two are not sufficiently close the CAP is changed and the entire solution process is repeated. This cycle is reiterated until the optical thickness from the inversion is substantially the same as the measured optical thickness. This analysis thus obtains the cloud optical extinction array and the CAP which can then be used to calculate the optical thickness of denser clouds.

EXAMPLE

Figure 1 below presents a simulated lidar signal function(the natural logarithm of the range-squared corrected lidar return) used to test the inversion algorithm. The lidar return is one which would be expected from a noiseless sounding of an exponential Rayleigh atmosphere having a scale height of 9 km. The atmospheric extinction for the simulated lidar return is 0.008/km at an altitude of 2 km; this extinction fixes the value of β_0 at 2 km. The cloud optical thickness is assumed to be 0.100. The extinction coefficient has the parabolic-shaped altitude distribution shown by the middle line(labeled (o) in figure 2). The same middle line in figure 2 corresponds to the inverted values of extinction if the optical thickness constraint used in the inversion is the correct one. The rest of the curves
presented in figure 2 correspond to inversions having incorrect values of cloud optical thickness, Γ, thus resulting in incorrect values for the cloud extinction coefficients and the cloud backscatter/extinction ratio, k_c, used here in place of the CAP. In actual cloud lidar returns, the measured cloud optical thickness is obtained from noisy atmospheric signals above and below the cloud. The atmospheric signal noise results in errors in the inferred optical thickness. The errors made in the input data and the consequent incorrect values for the backscatter/extinction ratio, k_c, are presented in Table 1 following Figures 1 and 2.

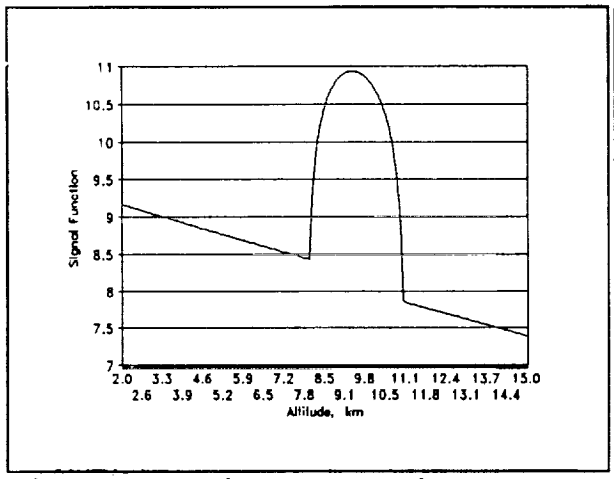

Figure 1. Simulated Lidar Return Signal Function.

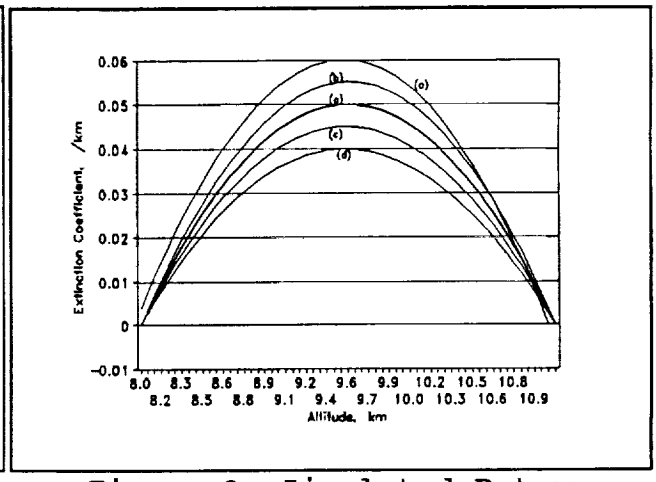

Figure 2. Simulated Return Extinction Coefficients.

Table I. Error Analysis Results

Per cent error in Γ	20.0%	10.0%	0	-10.0%	-20.0%
Per cent error in k_c	-15.2%	- 8.0%	0	9.6%	22.4%

Perusal of the two figures and the accompanying values given in Table 1 above indicate that if the optical thicknesss used to invert the k_c's are too high, the extinction coefficients are too high and the corresponding k_c's are too low and vice versa.

The accuracy of the inversion is also affected by other factors. One of these factors is the noise in the atmospheric lidar data below the cloud. The reason for this effect is that the attenuated scattering ratio in the cloud is obtained by fitting the actual lidar signal below the cloud to the expected atmospheric lidar signal. Thus, errors in the fit below the cloud produce errors in the attenuated scattering ratio which translate into errors in the CAP and the optical thickness. Another factor contributing to inversion errors is the noise present in the lidar data in the cloud itself. These errors likewise translate into errors in the final results. We are performing an extensive error analysis of the inversion. Thus far it appears that noise in the lidar data does not produce errors in the inversion which rapidly escalate or behave in an unstable fashion.

REFERENCES

Barrett, E. W., and O. Ben-Dov, 1967: Application of the Lidar to Air Pollution Measurements, J. Appl. Meteor., 6, 500-515.

Collis, R. T. H., 1966: Lidar: A new atmospheric probe, Q. J. R. Meteorol. Soc., 92, 220-230

Davis, P.A., 1969: The Analysis of Lidar Signatures of Cirrus Clouds, Appl. Opt., Vol. 8, No. 10, 2099-2102

Fernald, F. G., B. M. Herman, and J. A. Reagan, 1972: Determination of Aerosol Height Distributions by Lidar, J. Appl. Meteorol., 11, 482-489.

Fernald, Fredrick, G., 1984: Analysis of Atmospheric Lidar Observations, J. Appl. Opt., Vol. 23 No. 5, 652-653.

Klett, James D. 1981: Stable Analytical Inversion Solution for Processing Lidar Returns, J. Appl. Opt., Vol. 20 No. 2, 211-220.

Klett, James D. 1985: Lidar Inversion with Variable Backscatter/Extinction Ratios, J. Appl. Opt., Vol. 24 No. 11, 1638-1643

Liou, Kuo-Nan, 1980: Introduction to Atmospheric Radiation, Academic Press, pg. 288.

Wallace, John M. and Peter V. Hobbs, 1977: Atmospheric Science, An Introductory Survey, Academic Press, 144-149.

Viezee, W., E. E. Uthe, and R. T. H. Collis, 1969: Lidar Observations of Airfield approach Conditions: An Exploratory Study, J. Appl. Meteor., 8, 274-283.

N94-22310

As previously published in the Ninth Conference on Atmospheric and Oceanic Waves and Stability, 10–14 May 1993, San Antonio, Texas

BREAKING KELVIN-HELMHOLTZ WAVES AND CLOUD-TOP ENTRAINMENT AS REVEALED BY K-BAND DOPPLER RADAR

S18-47
197518
p. 4

Brooks E. Martner and F. Martin Ralph

Wave Propagation Laboratory, NOAA/ERL
Boulder, Colorado

1. INTRODUCTION

Radars have occasionally detected breaking Kelvin-Helmholtz (KH) waves under clear-air conditions in the atmospheric boundary layer (e.g. Gossard et al. 1970) and in the free troposphere (e.g. Browning 1971). However, very few direct measurements of such waves within clouds have previously been reported (Takahashi et al. 1992; Weckwerth and Wakimoto 1992), and those have not clearly documented wave breaking. In this article we present some of the most detailed and striking radar observations to date of breaking KH waves within clouds and at cloud top and discuss their relevance to the issue of cloud-top entrainment, which is believed to be important in convective (Reuter 1986) and stratiform clouds. Aircraft observations reported by Stith (1992) suggest that vortex-like circulations near cloud top are an entrainment mechanism in cumuliform clouds. Laboratory and modeling studies (Broadwell and Breidenthal 1982; Baker et al. 1984) have examined the possibility that KH instability may be responsible for mixing at cloud top, but direct observations have not yet been presented. Preliminary analyses shown here may help fill this gap.

The data presented in this paper were obtained during two field projects in 1991 that included observations from the NOAA Wave Propagation Laboratory's K$_a$-band Doppler radar (wavelength = 8.7 mm) and special rawinsonde ascents. The sensitivity (-30 dBZ at 10 km range), fine spatial resolution (37.5-m pulse length and 0.5° beamwidth), velocity measurement precision (5-10 cm s^{-1}), scanning capability, and relative immunity to ground clutter make it sensitive to non-precipitating and weakly precipitating clouds (Martner and Kropfli 1993), and make it an excellent instrument to study gravity waves in clouds. In particular, the narrow beam width and short pulse length create scattering volumes that are cylinders 37.5 m long and 45 m (90 m) in diameter at 5 km (10 km) range. These characteristics allow the radar to resolve the detailed structure in breaking KH waves such as have been seen in photographic cloud images (e.g. Martner 1985).

2. KH BILLOWS IN A NON-PRECIPITATING STRATIFORM CLOUD

As part of the Winter Icing and Storms Project (WISP) in early 1991, the K-band radar was operating at Erie, Colorado (1503 m above mean sea level) during the approach and passage of a strong and complex cold front. The mode of operation consisted of making east-west oriented range-height indicator (RHI) scans every 15 min. At 0500 UTC 6 March, several hours after the passage of the surface cold front, a relatively unperturbed layer of stratiform clouds was present over the radar from 2-6 km above ground level (AGL). (Henceforth altitudes will be AGL, unless otherwise stated.) However, by 0600 UTC the reflectivity pattern of the cloud layer had taken on the structure of KH billows (Fig. 1a). Comparison of the radar data with a CLASS rawinsonde ascent launched at the same time from Platteville, 27 km east of the radar, shows that the billows were located in a layer of strong vertical wind shear, but below the layer of strongest shear within the upper front (Fig. 1b). The Richardson number (Ri) profile (Fig. 1c), calculated from the rawinsonde data, also indicates that the billows were in a deep layer of low Ri in which KH instability could occur.

Further verification that the observed reflectivity pattern is a manifestation of breaking KH waves can be gained by comparing the wave parameters with well-known features of KH waves. While several of the important wave characteristics can be determined directly from the radar observations, others require calculations based on theoretical considerations. In this case study, an upper bound for the horizontal wavelength (λ) can be determined directly from the RHI of reflectivity (Fig. 1a), and is 6.1 km. From the observed reflectivity patterns at 0545 (not shown) and 0600 UTC, it is possible to track the easternmost billow cloud, yielding a zonal phase speed of 15 m s^{-1}. However, in order to determine the actual λ it is also necessary to know the wave orientation, or the ground-relative horizontal phase velocity (c). Because only east-west RHI's were performed, c must be estimated from the shear across the layer containing the wave (layer method), or from the wind velocity at the wave's critical level (center method), which is at the center of the billow. In the layer method, the propagation direction is given by the direction of the shear vector and the phase speed is given by the component of the layer mean flow in that direction. Two logical choices for the shear layer are evident in this case: 1) the layer between 2.0 and 5.8 km which contains all of the cloud, and most of the shear below the upper front, and 2) the layer between 2.7 and 4.9 km that marks the vertical range of the billow structure. These predict values of c that are 15.4 m s^{-1} from 232°, and 11.6 m s^{-1} from 222°, respectively. The center method predicts that c is 20 m s^{-1} from 272° as an average from 3.5-4.2 km, but it is very sensitive to the choice of critical level because of the strong

C-2

directional shear and speed shear in that layer (i.e., from 16-26 m s^{-1} and 280-266°). Thus, λ appears to be 5.1 ± 1.0 km, with c = 15.8 ± 4.2 m s^{-1} from 247 ± 25°. Hence, the zonal component of c calculated from theoretical considerations is 14.8 ± 4.1 m s^{-1}, which compares favorably with the observed value.

Another important wave parameter is the ratio between λ and the shear layer depth (H). Taking the vertical extent of the billow structure (i.e., 2.7-4.9 km) as the most appropriate shear layer yields H=2.2 km. Thus, the ratio λ/H=2.3±0.5 is somewhat less than the value of 3.2-3.5 observed in the atmospheric boundary layer (Gossard et al. 1970, and Hooke et al. 1973). It is also smaller than the ratios predicted for the fastest growing mode of KH instability by Drazin (1958) for a continuous model (λ/H=4.4), by Miles and Howard (1964) for a piecewise 3-layer model (λ/H=7.5), and by Holmboe (see Gossard 1990) for an alternate continuous model (λ/H=3-6, depending on Ri).

3. KH BILLOWS ATOP A DEEP, PRECIPITATING CLOUD

During November 1991 the radar was deployed in Coffeyville, Kansas (227 m MSL) as part of the FIRE-II experiment and was co-located with a rawinsonde launch site. As a weak cyclone deepened to the south of the radar site on 22 November, a frontal zone developed in the lower troposphere and helped trigger deep stratiform rain clouds. By 1800 UTC the cloud filled the layer between 2 and 8 km and produced light rain that can be seen as fall streaks extending from cloud base to the ground (Fig. 2). The radar operated in the vertically-pointing mode during this event. The waves occurred at the top of the cloud, and had the distinctive structure of KH billows as revealed in the radial velocity plot (Fig. 3a) which focuses on the time and region of interest. This plot also displays the remarkable spatial resolution of the radar, and its ability to clearly measure the wave activity. The time series of vertical velocity near the center of the billows (Fig. 3b) allows a more quantitative assessment of the waves. This data indicates the wave had a period of 68 ± 4 s and a maximum amplitude of 1.7 m s^{-1}. Although these measured Doppler velocities are actually a combination of the clear-air vertical motion and the hydrometeor fall speed, the terminal velocities are likely to be < 0.1 m s^{-1} since the region is at cloud top and the reflectivities are small (-20 dBZ), i.e., the hydrometeors are small. This conclusion is supported by the fact that the amplitude of the upward motion (1.7 m s^{-1}) is only 0.1 m s^{-1} less than that of the downward motion (-1.8 m s^{-1}).

Figure 4 shows the radial velocity in the upper half of the cloud (Fig. 4a) and the temperature and wind speed profiles (Fig. 4b) from a rawinsonde that ascended through the layer containing the waves. The rawinsonde reached the appropriate altitude 25-35 min before the waves appeared over the radar, and had drifted 25-30 km to the northeast. The waves developed in a layer of strong vertical shear (primarily speed shear) between 7.5 and 8.5

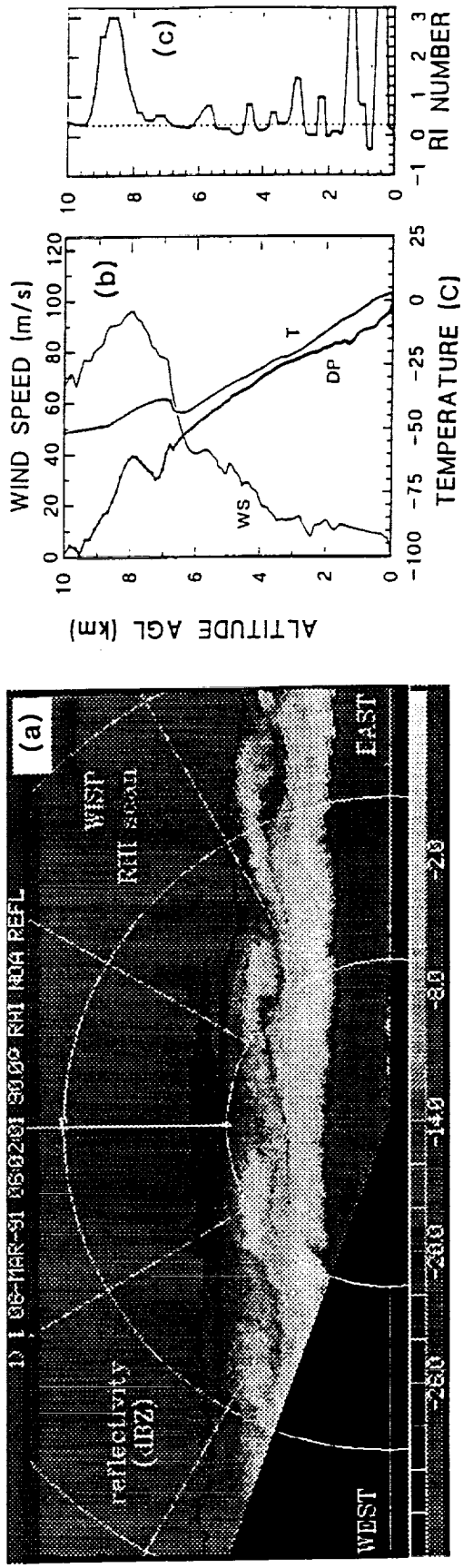

Fig. 1 a) RHI of radar reflectivity at 0600 UTC. b) Temperature, dew point temperature, and wind speed from a CLASS sounding at Platteville at 0600 UTC. c) Richardson number calculated from the sounding in (b).

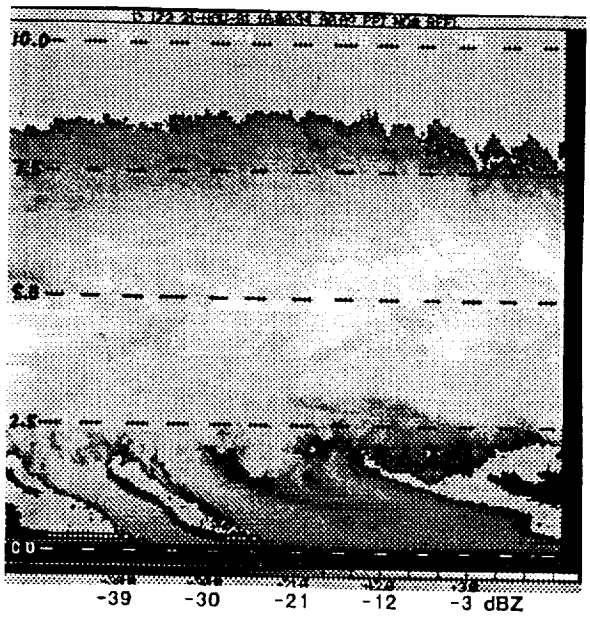

Fig. 2 Time-height cross section of radar reflectivity. Horizontal axis spans 14.5 minutes.

km that had Ri ≈ 0.25 (Fig. 4c).

As with the earlier case, it is possible to estimate λ and c from the conditions in the shear layer. In this case the wave period is also known, but there is no measurement to provide an upper bound on λ. Two plausible options for the shear layer are the layer from 7.3-8.3 km that contains most of the vertical shear, and the layer from 7.5-8.55 km that defines the vertical extent of the billow clouds. These yield values of 35.9 m s^{-1} from 209°, and 38.6 m s^{-1} from 220°, respectively. The alternative method that uses the wind vector at the center altitude of the billows yields 33.0 m s^{-1} from 229°, or 38.0 m s^{-1} from 226°, for altitudes of 7.6 and 8.0 km, respectively. Thus, c is 35.8 ± 2.8 m s^{-1} from 219 ± 10°. Combining this result with the observed wave period predicts λ = 2.4 ± 0.3 km. Taking the depth of the layer of low Ri (i.e., 650-930 m) as H yields a ratio of λ/H=3.0 ± 1.0. Based on the observed wave structure, conditions in the wave environment, and the deduced wave parameters, it is possible to conclude that the observed perturbations at cloud top are the result of KH instability.

4. RELATIONSHIP TO CLOUD-TOP ENTRAINMENT

The observations presented here provide convincing evidence that KH instability can mix relatively clear air (i.e., containing few if any hydrometeors at < -30 dBZ) at least 1-2 km down into stratiform clouds (Figs. 1a and 4a). In one case the mixing includes roughly half of the vertical extent of a 4-km deep nonprecipitating cloud, while in another case the waves developed along the top of a 6-km deep cloud and produced distinct vertical motion perturbations that extended fully 2 km below cloud top (Fig. 4a). Although the waves created large vertical displacements (at least 1 km) and mixed apparently unsaturated and saturated air, it does not appear that they triggered strong downdrafts in these clouds. This may be due in part to the stratiform nature of the clouds, which implies that the formation of downdrafts would be inhibited. Vigorous downdrafts are more likely to develop under less stable conditions.

Attention has also focused on cloud-top entrainment as a possible mechanism for the breakup of marine stratocumulus (e.g. Siems and Bretherton 1992). As with the problem of entrainment in cumuliform clouds, the exact mechanism that is active in stratiform clouds has not yet been clearly documented observationally. Because the cases shown here are primarily stratiform in nature they provide evidence that may be relevant to this issue, although it is desirable to obtain similar radar observations in shallow marine stratocumulus.

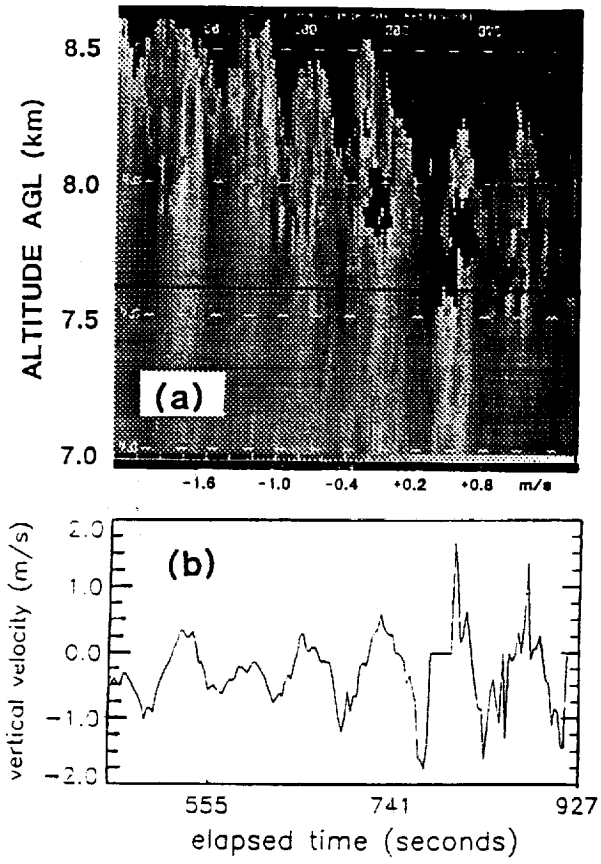

Fig. 3 a) Time-height cross-section of Doppler vertical velocity centered on the KH billows seen atop the cloud in Fig. 2. Regions where reflectivity is < -35 dBZ are shown as black. b) Time-series of Doppler vertical velocity at height shown as a black line in (a).

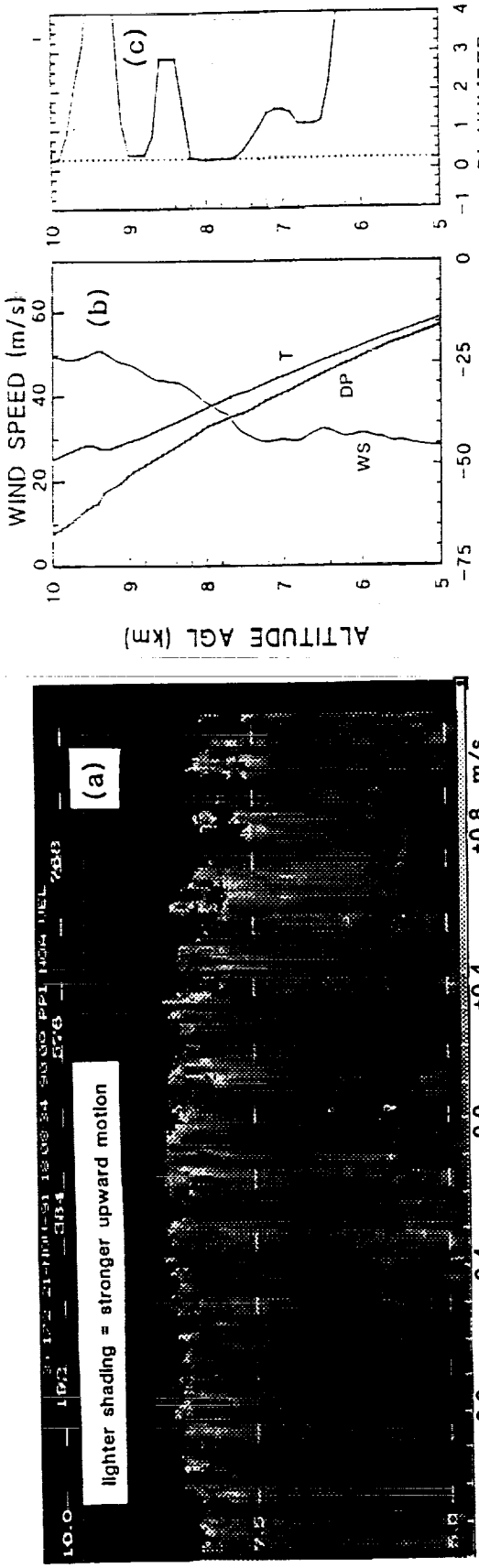

Fig. 4 a) Time-height cross section of Doppler vertical velocity in the upper half of the cloud shown in Fig. 2. b) and c) Same as Fig. 1, but from Coffeyville, KS at 1711 UTC.

5. ACKNOWLEDGEMENTS

The K_a-band radar's participation in WISP and FIRE-II was supported by the Federal Aviation Administration and the NOAA Office of Climate and Global Change, respectively.

6. REFERENCES

Baker, M. B., R. E. Breidenthal, T. W. Choularton, and J. Latham, 1984: The effects of turbulent mixing in clouds. *J. Atmos. Sci.*, **41**, 299-304.

Broadwell, J. E., and R. E. Breidenthal, 1982: A simple model of mixing and chemical reaction in a turbulent shear layer. *J. Fluid Mech.*, **125**, 397-410.

Browning, K. A., 1971: Structure of the atmosphere in the vicinity of large-amplitude Kelvin-Helmholtz billows. *Quart. J. Roy. Meteor. Soc.*, **97**, 283-299.

Drazin, P. G., 1958: The stability of a shear layer in an unbounded heterogeneous inviscid fluid. *J. Fluid Mech.*, **4**, 214-224.

Gossard, E. E., J. H. Richter, and D. Atlas, 1970: Internal waves in the atmosphere from high-resolution radar measurements. *J. Geophys. Res.*, **75**, 3523-3536.

Gossard, E. E., 1990: Radar research on the atmospheric boundary layer. Chapter 27a, *Radar in Meteorology*, D. Atlas, ed., Amer. Meteorol. Soc., Boston, 477-527.

Hooke, W. H., F. F. Hall, Jr., and E. E. Gossard, 1973: Observed generation of an atmospheric gravity wave by shear instability in the mean flow of the atmospheric boundary layer. *Bound.-Layer Meteor.*, **5**, 29-41.

Martner, B. E., 1985: Kelvin-Helmholtz billow cloud. *Reprints, 5th Conf. on Atmos. Ocean Waves and Stability*, New Orleans, Amer. Meteorol. Soc., cover and front piece.

Martner, B. E., and R. A. Kropfli, 1993: Observations of multi-layered clouds using K-band radar. *Reprints, 31st Aerospace Sci. Meet.*, Reno, Amer. Inst. Aeronautics and Astronautics, 8 pp.

Miles, J. W., and L. N. Howard, 1964: Note on a heterogeneous shear flow. *J. Fluid Mech.*, **20**, 331-336.

Reuter, G. W., 1986: A historical review of cumulus entrainment studies. *Bull. Amer. Meteor. Soc.*, **67**, 151-154.

Siems, S. T., and C. S. Bretherton, 1992: A numerical investigation of cloud-top entrainment instability and related experiments. *Quart. J. Roy. Meteor. Soc.*, **118**, 787-818.

Stith, J. L., 1992: Observations of cloud-top entrainment in cumuli. *J. Atmos. Sci.*, **49**, 1334-1347.

Takahashi, N., H. Uyeda, and K. Kikuchi, 1992: Doppler radar observations on the Kelvin-Helmholtz billows in stratiform rainfall. *Reprints, 11th Intl. Conf. on Clouds and Precip.*, Montreal. ICCP, 979-982.

Weckwerth, T. M., and R. M. Wakimoto, 1992: The initiation and organization of convective cells atop a cold-air outflow boundary. *Mon. Wea. Rev.*, **120**, 2169-2187.

N94-22311

As previously published in the

31st Aerospace Sciences Meeting, 11-14 January 1993 San Antonio, Texas

S19-47
197519
P- 8

OBSERVATIONS OF MULTI-LAYERED CLOUDS USING K-BAND RADAR

Brooks E. Martner and Robert A. Kropfli
NOAA/Wave Propagation Laboratory, Boulder, Colorado

Abstract

Rudimentary ground-based K-band radars were once used by the U.S. Air Force to monitor clouds over air bases. The NOAA Wave Propagation Laboratory has developed a significantly advanced dual-polarization Doppler K-band system that provides remarkably detailed visualizations of the structure and kinematics of non-precipitating and weakly precipitating clouds. Unlike lidar and infrared radiometer systems, K-band radar can penetrate liquid water cloud layers and obtain measurements through moderate rainfall and heavy snowfall to reveal intricate cloud features including multiple layers of cloud. This is accomplished at less cost than would be possible with traditional longer wavelength weather radars. The radar's capabilities have been demonstrated in several recent cloud research field projects. In combination with measurements by other remote sensors, the radar can help detect aircraft icing hazards and infer microphysical properties of clouds. An automated, unattended version of the radar could provide a continuous, detailed depiction of the cloud environment in the vicinity of airports.

1. Introduction

By virtue of its excellent sensitivity, spatial resolution, and velocity measurement precision, the Wave Propagation Laboratory (WPL) K_a-band (λ = 8 mm) Doppler radar is ideally suited for detailed observations of the structure and kinematics of non-precipitating clouds. Signals at this wavelength are not attenuated by liquid water as seriously as those of lidars, infrared radiometers, and shorter wavelength radars. Thus, the WPL K-band radar can penetrate liquid cloud layers and continue to obtain measurements through moderate rainfall and heavy snowfall. It provides very detailed visualizations of cloud locations and properties even in situations of multiple cloud layers. Furthermore, power in the radar antenna's side lobes is very weak, thus it is relatively immune to ground clutter contamination problems.

This paper is declared a work of the U.S. Government and is not subject to copyright protection in the United States.

The WPL radar has been used in several recent research projects ranging from studies of aircraft icing hazards to the radiative effects of cirrus and marine stratus clouds. Scans of multi-layer clouds excerpted from these projects are reproduced in this article to illustrate a few of the radar's capabilities. The potential usefulness for cloud surveillance at airports is discussed for a proposed automated version of this radar system.

2. Background

For the last three decades, radar meteorology research has been dominated by studies of severe storms; less dramatic, but important, cloud systems have been largely ignored. This very focused emphasis is now broadening with the new widespread interest in how clouds affect radiative transfer in the atmosphere and, thereby, climate and climate change. The traditional longer wavelength radars (λ = 5-11 cm), used so effectively for severe storm monitoring and research, may not be the best tools for observing the details of non-precipitating clouds.

For particles much smaller than the observing wavelength (Rayleigh scattering conditions), the backscattering cross section of a sphere is inversely proportional to the fourth power of the wavelength. Thus, longer wavelength radars have an inherent disadvantage for detecting signals backscattered from very small hydrometeors, such as cloud droplets and new ice crystals. In practice, however, long wavelength weather radar systems can compensate for this disadvantage by using very powerful transmitters, large antennas, and very sensitive receivers, all at considerable expense. Thus, the primary advantages of a short wavelength radar, are its relatively small size and cost, in addition to its excellent sensitivity, resolution, and clutter minimization.

The main disadvantage of short wavelength radar is signal attenuation from rain and cloud liquid water that becomes more severe for decreasing wavelengths. For optical and infrared systems such as ceilometers, lidars, and IR radiometers, attenuation by liquid water is so extreme that it prohibits probing beyond the first 100-200 m of a liquid cloud boundary. Low

stratus, fog, drizzle, or rain will block these instruments and prevent them from detecting all higher cloud features and layers.

K-band radar represents a reasonable compromise between the expense limitations of longer wavelength radars and the attenuation limitations of shorter wavelength systems, including shorter wavelength radars. Thus, although K-band is unsuitable for monitoring severe convective storms and weather systems with widespread moderate to heavy rain, its proper niche is for observing non-precipitating and weakly precipitating clouds. These clouds are common, often pervasive, and can be significant factors for aviation, weather modification, and climate.

3. K-band Radar Systems

In the 1960s, K-band radars were used by the U.S. Air Force as "radar ceilometers" to monitor clouds at numerous air bases[1]. These vertically pointing, non-Doppler, AN/TPQ-11 radars provided useful information on the heights and structure of overpassing clouds, but suffered from frequent hardware failures and poor displays, and were eventually abandoned. The University of Washington added Doppler capability to a surplus AN/TPQ-11 and has productively used it for cloud physics studies[2].

The WPL K-band radar is an original design with dual-polarization and full scanning and Doppler capabilities[3]. Recent extensive upgrades, including a new antenna, have significantly improved the system's capabilities[4]. The radar can transmit linear, circular, or elliptical polarizations and receive the co- and cross-polarized backscattered signals; the amount of depolarization is related to the hydrometeors' shapes, orientations, and thermodynamic phase. The beamwidth is 0.5° and the range resolution is 37.5 m. The system is capable of detecting signals as weak as -31 dBZ at a range of 10 km, and the radial velocity measurements are demonstrated to be accurate to within 0.05 m s^{-1} in typical situations. The antenna side lobes are very weak, thus ground clutter is seldom a serious problem. Table 1 summarizes the radar's characteristics; its offset Cassegrain antenna is shown in Figure 1.

4. Multi-layer Cloud Examples

The ability of the WPL K-band radar to detect weak clouds has been demonstrated in a number of recent experiments, including the Cloud Lidar and Radar Exploratory Test (CLARET-I & II) in Colorado, the Winter Icing and Storms Project (WISP) in Colorado, the First International Satellite Cloud Climatology Project Regional Experiment (FIRE-II) in Kansas, and the Atlantic Stratocumulus Transition

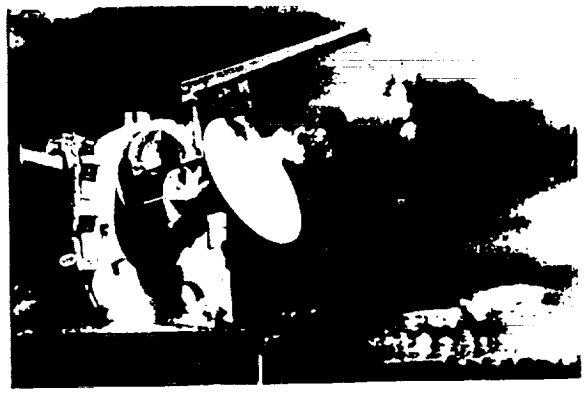

Figure 1. Offset Cassegrain antenna of the WPL K-band radar.

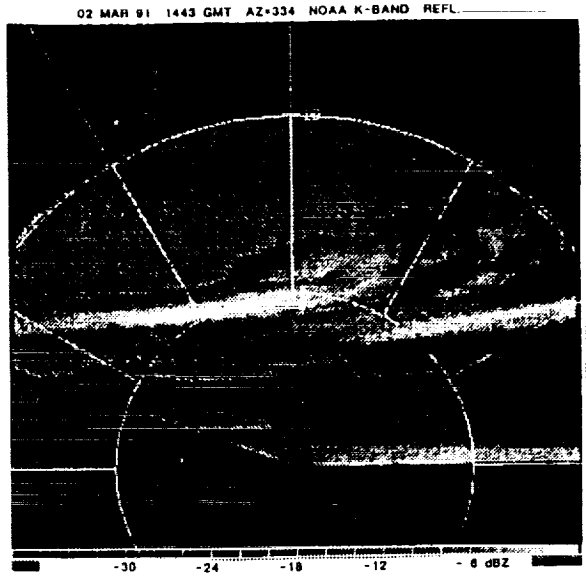

Figure 2. K-band radar reflectivity factor (dBZ) pattern for an RHI scan from the WISP project in Colorado. Cirrus (upper), altostratus (middle), and stratus (lower) cloud layers are shown. Range rings are shown at 5-km increments.

Table 1

CHARACTERISTICS OF THE NOAA/WPL K-BAND RADAR

Major capabilities: reflectivity, velocity, and depolarization for atmospheric research, including observations of non-precipitating clouds

Frequency: 34.6 GHz = 8.7 mm wavelength (K_a-band)

Peak transmitted power: 85 kW

PRF: 625 to 2500 μs

Sensitivity: approximately -30 dBZ at 10 km

Polarization: circular typical, but elliptical and linear possible by rotating quarter-wave plate

Beam Width: 0.5° circular

Antenna: Millitech offset Cassegrain with 1.2 m diameter parabolic dish; 49.5 dB gain; -30 dB sidelobes

Scan Types: PPI (incl. sector scans), RHI (incl. over the top), zenith, fixed beam

Pulse width: fixed, 0.25μs (37.5 m)

Range gate spacing: (n)*(37.5 m) where n = 1, 2, 3 ...

Number of range gates: up to 328 gates

Scan rates: 0-30 deg/s; fastest rate depends on sector size

Parameters measured: reflectivity (main- & cross-polarized), mean Doppler velocity, variance of Doppler spectrum, circular depolarization ratio (CDR), correlation of successive pulses, full Doppler spectrum in a separate recording mode

Doppler processing: pulse-pair or time-series techniques

Data system: Data General S-120 computer controls antenna operation, recording and displays through NOAA's Radar Control Program. Hundreds of pre-programmed scans can be retrieved from disk for immediate use. SUN workstation for post-processing in field.

Recording: Exabyte 8mm video cassette tape drives. VCR used for recording visual weather in direction of radar beam. PC electronic logbook for operator's comments.

Real-time displays: color monitor of Doppler velocity, reflectivity, CDR and correlation patterns; Video monitor of weather along beam; digital displays of azimuth, elevation, and time; field tapes can be played back through color monitor.

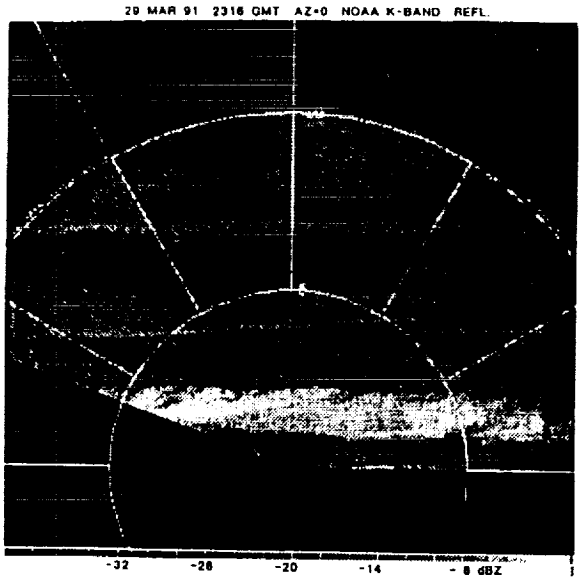

Figure 3. As in Fig. 2, except for another date.

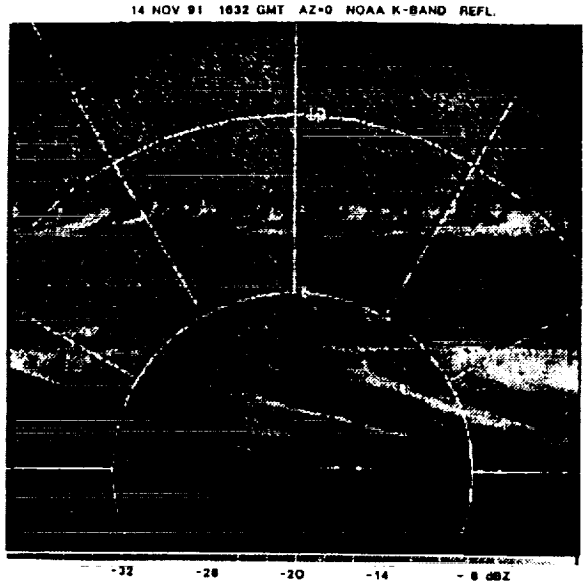

Figure 5. Reflectivity pattern for an RHI scan from the FIRE-II project in Kansas. Cirrus and precipitating altostratus layers are shown.

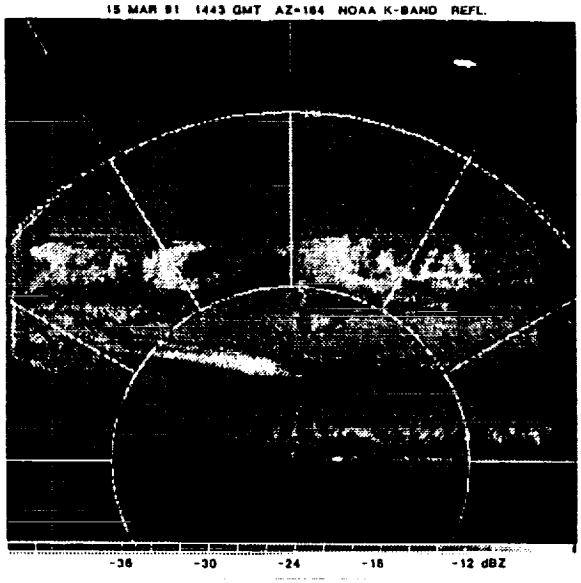

Figure 4. As in Fig. 2, except for cloud layers with more broken and cellular structure.

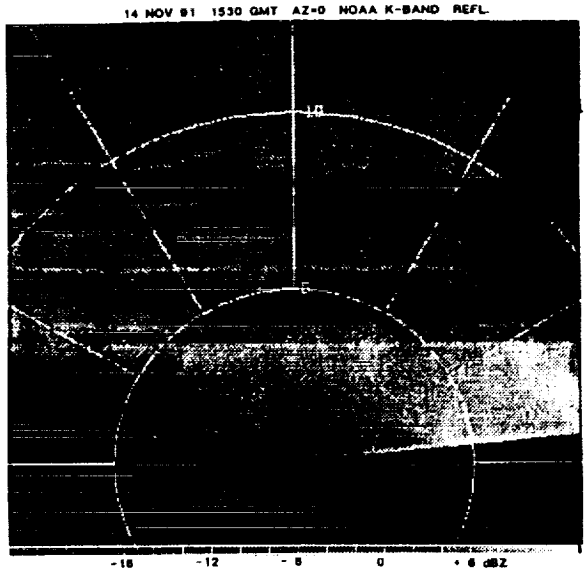

Figure 6. Reflectivity pattern of cirrus and nimbostratus from an RHI scan during the FIRE-II project. The thin horizontal line near 3.5 km AGL is the melting layer bright band.

Experiment (ASTEX) in the Madeira Islands of Portugal. A sampling of cloud reflectivity and velocity patterns from these projects are shown in Figures 2-12. These are black and white (gray scale) renditions of the color images used in data analysis, therefore some detail is lost in these reproductions. Darker shadings represent weaker reflectivities. Black speckles on some of the figures are random noise between cloud layers that has not been entirely edited from the data by thresholding schemes.

Figures 2, 3, and 4 from different days during WISP show combinations of stratus, altostratus, and cirrus layers. These are range-height indicator (RHI) displays of scans from one horizon over the top of the radar to near the opposite horizon. They are nearly instantaneous, vertical cross section "snapshots" of the cloud reflectivity structure. In Fig. 4, the stratus cloud from just above the ground to about 1.5 km AGL was penetrated by a research aircraft and found to contain only small supercooled liquid water droplets. This aircraft icing hazard cloud was not detected by other, longer wavelength radars used in WISP. Its cellular structure is apparent in the K-band data.

Figure 5 from FIRE-II shows two altostratus layers below 5 km and a cirrocumulus layer near 7.5 km. Precipitation streamers from the upper and lower layer are stretched in opposite directions by shear of the horizontal winds.

Figure 6 from FIRE-II shows an RHI scan of a cirrus layer above a deep nimbostratus cloud. The horizontal line of stronger reflectivity at 3.5 km is the radar bright band caused by melting. It marks the transition from snowfall (above) to rainfall (below) in the cloud. The radar's ability to penetrate precipitation and detect clouds beyond the precipitation is clearly illustrated.

Figure 7 from CLARET-II is a time-height reflectivity display of clouds passing over the radar while its antenna was pointed at the zenith. It shows an altostratus layer at 2-4 km and cirrus clouds above 5.5 km. A similar situation from FIRE-II is shown in Fig. 8, but the altostratus' reflectivity pattern has a more cellular appearance in this case.

Marine stratus and stratocumulus clouds from ASTEX are shown extending less than 2 km above the surface in the time-height display of Fig. 9. At such close ranges, reflectivities as weak as -50 dBZ are detectable from these liquid water clouds. Streamers of drizzle can be seen reaching the surface on the lower right side of the figure.

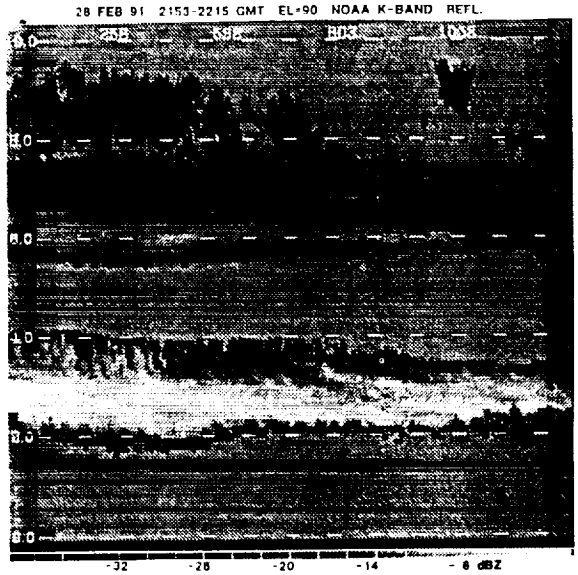

Figure 7. Reflectivity time-height display of cirrus and altostratus clouds passing over the vertically pointing radar during the CLARET-II project in Colorado. The horizontal scale spans 24 minutes (time increases toward the right), and the vertical scale spans 10 km above ground level with tick marks shown at 2-km increments.

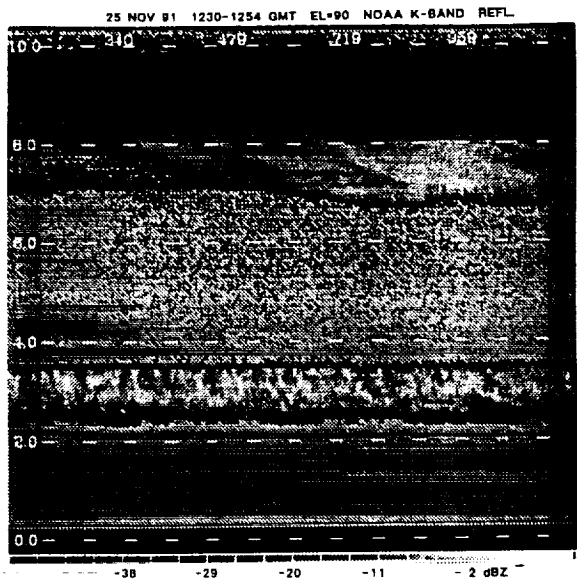

Figure 8. As in Fig. 7, but for clouds observed in the FIRE-II project.

Figure 10 is a time-height display of a deep stratiform cloud that produced drizzle during FIRE-II. Cloud base was near 2 km (+3°C) and cloud top was near 8 km (-36°C). The radar easily penetrated the drizzle streamers to reveal detailed structure in the cloud to its top. As time progressed, Kelvin-Helmholtz instability billows developed at cloud top and eventually took the shape of breaking waves in the upper right part of the figure.

Figures 11 and 12 are time-height displays of reflectivity and vertical Doppler velocity, respectively, for a pair of cirrus layers during FIRE-II. The Doppler velocity, which is the air's updraft speed minus the mean hydrometeor fallspeed, varies from about -1.25 to +0.75 m s^{-1} with a 2-min periodicity. These velocity undulations are offset in time in the two layers, as shown by the tilted pattern. This suggests the undulations were the result of either a vertically propagating wave or a slightly tilted wave front that propagated horizontally, reaching the lower layer first.

5. Cloud Detection and Boundaries

The radar's ability to detect various weak clouds has been demonstrated in these recent projects. Comparisons with measurements by a collocated WPL lidar have been made in the CLARET and FIRE-II experiments. From this experience we conclude that the radar can detect almost all clouds overhead, with the notable exception of some tenuous cirrus. This exception may be a serious shortcoming in some kinds of studies, but is probably insignificant for aviation applications, for which the radar's ability to penetrate liquid cloud layers is a much more important attribute.

How well the radar echo tops and bases agree with actual hydrometeor cloud tops and bases has not yet been established. In the WISP experiment the radar echo tops were compared with cloud top heights recorded by research aircraft flying in 21 nearby stratus and altostratus layers and the agreement was excellent. It is expected, however, that the radar echo tops will often underestimate the cloud top height of weak cirrus because the ice particles may be very small and present in low concentrations at relatively long range. The radar's usually precise measurement of cloud base height is sometimes obscured by precipitation and virga, as in Fig. 6, but it can be estimated if the streamers are intermittent, as in Fig. 10. Lidars have much narrower beamwidths that allow them to miss very sparse precipitating hydrometeors and therefore obtain a more precise measurement of cloud base. However, if the rain rate increases to light intensity, the optical beam becomes blocked near the surface and its measurements are not useful.

6. Combined Remote Sensors

Combining simultaneous data from different collocated remote sensors presents an opportunity to obtain new information on cloud microphysics and overcome the shortcomings of individual instruments. For example, the combined data from a vertically pointing microwave radiometer, Radio Acoustic Sounding System (RASS), ceilometer, and K-band radar have been used to estimate profiles of liquid water aloft and determine aircraft icing altitudes[5]. Several additional remote sensors may also be useful for detecting icing conditions[6]. In separate but related studies, the WPL K-band radar measurements have been combined with those of a lidar[7], an infrared radiometer[8], and an infrared spectrometer[9] to infer microphysical properties of clouds, such as characteristic particle sizes.

7. Aviation Applications

Knowledge of the heights and thicknesses of all cloud layers in the vicinity would be useful for vectoring aircraft near a terminal area. The sensitivity demonstrated by the WPL K-band radar is clearly sufficient to detect low reflectivity and low-level cloud layers that are not detectable by conventional longer wavelength radars available today at similar cost. In addition, the excellent ground clutter performance of this system allows detection of weakly reflecting clouds at rages within a few hundred meters.

The WPL K-band radar is designed for research. As such it generally cannot be operated unattended. However, a simplified, durable version could be designed today with the engineering sophistication necessary to allow long-term, continuous, unattended operation. Such an operational radar system could be used in a vertically pointing, fixed-beam mode or in a scanning mode to monitor the spatial distribution of clouds in the airport vicinity. By combining measurements from the radar to locate cloud boundaries, RASS to measure profiles of temperature, and a microwave radiometer to measure the total amount of liquid water along its beam, layers of supercooled liquid water that produce aircraft icing would be detected and isolated. With such a system, the airport of the future would have a much more complete depiction of the cloud environment than the rudimentary ceiling and visibility information available today. Such a system would also be very useful for climate-related field studies of how clouds modulate the atmosphere's radiation budget.

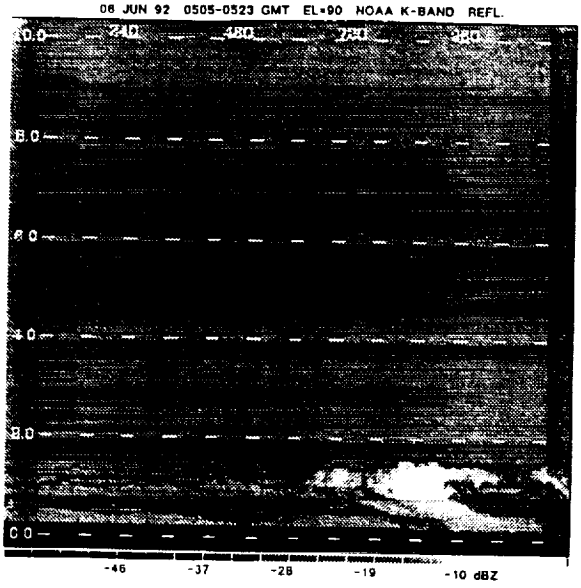

Figure 9. Time-height display of the reflectivity pattern of marine stratus and marine stratocumulus from the ASTEX project in the eastern Atlantic Ocean. The horizontal scale spans 18 minutes.

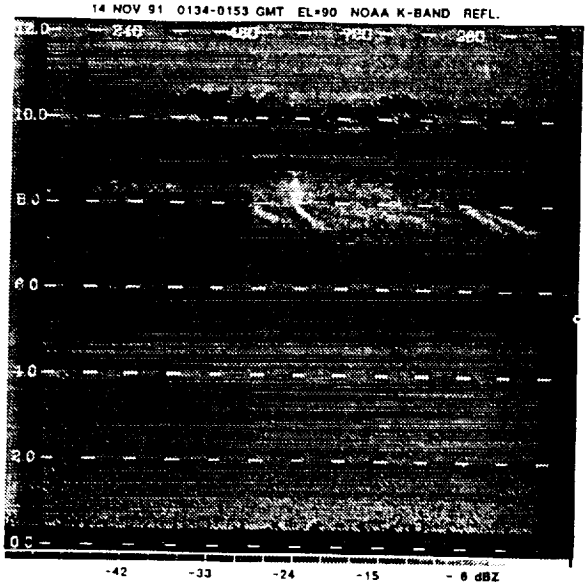

Figure 11. Time-height display of reflectivity of two cirrus layers during the FIRE-II project. The horizontal scale spans 19 minutes.

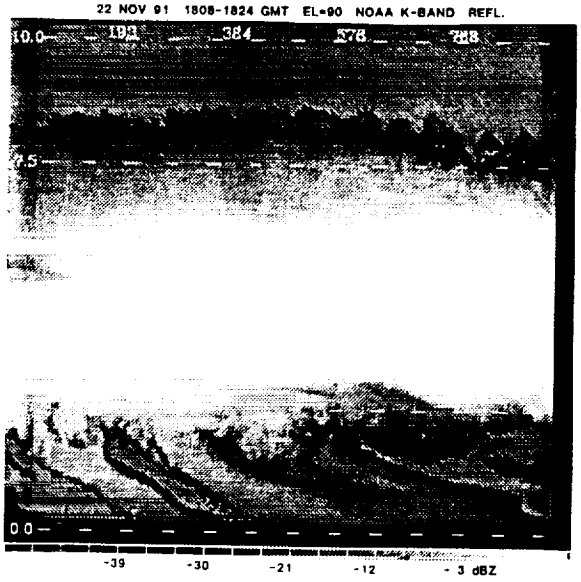

Figure 10. Time-height display of a deep stratiform cloud that produced drizzle during the FIRE-II experiment. The horizontal scale spans 14 minutes. Note the breaking waves at cloud top in the upper right corner.

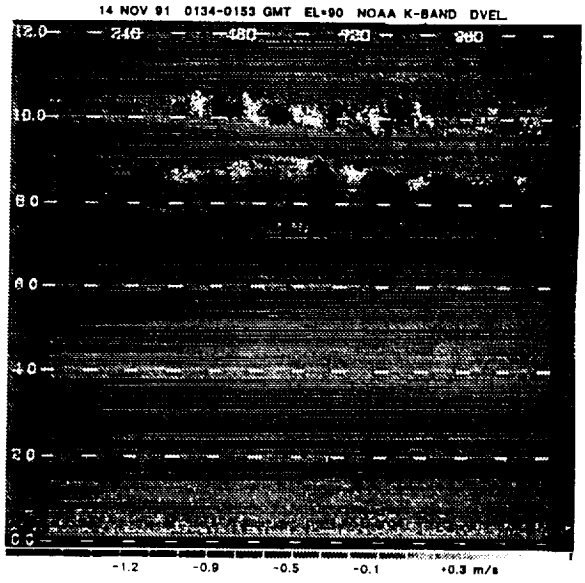

Figure 12. As in Fig. 11, except showing the vertical Doppler velocity pattern in the cirrus layers. Positive values indicate upward motion.

Acknowledgements

Participation of the WPL K-band radar in the various projects was supported by the following organizations: the Federal Aviation Administration (WISP), the Department of Energy's Atmospheric Radiation Measurement program (CLARET and ASTEX), and the NOAA Office of Climate and Global Change (FIRE-II and ASTEX).

References

1. Petrocchi, P.J., and W.H. Paulsen, 1966: Meteorological significance of vertical density profiles of clouds and precipitation obtained with the AN/TPQ-11 radar. Preprints, 12th Conf. on Radar Meteor., Norman, OK, Amer. Meteor. Soc., 467-472.

2. Hobbs, P.V., N.T. Funk, R.W. Weiss, J.D. Locatelli, and K.R. Biswas, 1985: Evaluation of the 35 Ghz radar for cloud physics research. J. Atmos. Oceanic Tech., 2, 35-47.

3. Pasqualucci, F., B.W. Bartram, R.A. Kropfli, and W.R. Moninger, 1983: A millimeter-wavelength dual-polarization Doppler radar for,cloud and precipitation studies. J. Climate and Appl. Meteor., 22, 758-765.

4. Kropfli, R.A., B.W. Bartram, and S.Y. Matrosov, 1990: The upgraded WPL dual-polarization 8.6 mm Doppler radar for microphysical and climate research. Preprints, Conf. on Cloud Physics, San Francisco, Amer. Meteor. Soc., 341-345.

5. Politovich, M.K., B.B. Stankov, and B.E. Martner, 1992: Use of combined remote sensors for determination of aircraft icing altitudes. Preprints, 11th Intl. Conf. on Clouds and Precip., Montreal, ICCP, 979-982.

6. Westwater, E.R., and R.A. Kropfli, 1989: Remote sensing techniques of the Wave Propagation Laboratory for the measurement of supercooled liquid water: Applications to aircraft icing. NOAA Tech. Memo. ERL WPL-163. NOAA Envr. Res. Labs., Boulder, CO, 28 pp.

7. Intrieri, J.M., G.L. Stephens, W.L. Eberhard, and T.A. Uttal, 1993: A method for determining cirrus cloud particle sizes using a radar/lidar backscattering technique. J. Appl. Meteor., 32 (in press).

8. Matrosov, S.Y., T. Uttal, J.B. Snider, and R.A. Kropfli, 1992: Estimation of ice cloud parameters from ground-based infrared radiometer and radar measurements. J. Geophys. Res., 97, 11567-11574.

9. Palmer, A.J., S.Y. Matrosov, B.E. Martner, T. Uttal, D.K. Lynch, M.A. Chatelain, J.A. Hackwell, and R.W. Russell, 1993: Combined infrared emission spectra and radar reflectivity studies of cirrus clouds. IEEE Trans. Geosci. Remote Sensing (in press).

N94-22312
S20-47
197526
P_4

Atmospheric Parameterization Schemes for Satellite Cloud Property Retrieval During FIRE IFO II

James Titlow[1] and Bryan A. Baum[2]

[1]Lockheed Engineering and Sciences Co., Hampton, VA 23666
[2]NASA Langley Research Center, Hampton, VA 23681-0001

1. Introduction

Satellite cloud retrieval algorithms generally require atmospheric temperature and humidity profiles to determine such cloud properties as pressure and height. For instance, the CO_2 slicing technique called the ratio method (e.g. McCleese and Wilson, 1976; Smith and Platt, 1978) requires the calculation of theoretical upwelling radiances both at the surface and a prescribed number (40) of atmospheric levels. This technique has been applied to data from, for example, the High Resolution Infrared Radiometer Sounder (HIRS/2, henceforth HIRS) flown aboard the NOAA series of polar orbiting satellites and the High Resolution Interferometer Sounder (HIS) (Smith and Frey, 1990). In this particular study, four NOAA-11 HIRS channels in the 15-μm region are used: 4 (14.22 μm), 5 (13.95 μm), 6 (13.66 μm), and 7 (13.34 μm). The ratio method may be applied to various channel combinations to estimate cloud top heights using channels in the 15–μm region. Presently, the multispectral, multiresolution (MSMR) scheme (Baum et al., 1992) uses 4 HIRS channel combination estimates, namely 4/5, 5/6, 5/7 and 6/7, for mid- to high-level cloud pressure retrieval and Advanced Very High Resolution Radiometer (AVHRR) data for low-level (>700 mb) cloud level retrieval. In order to determine theoretical upwelling radiances, atmospheric temperature and water vapor profiles must be provided as well as profiles of other radiatively important gas absorber constituents such as CO_2 , O_3, and CH_4. The assumed temperature and humidity profiles have a large effect on transmittance and radiance profiles, which in turn are used with HIRS data to calculate cloud pressure, and thus cloud height and temperature. For large spatial scale satellite data analysis, atmospheric parameterization schemes for cloud retrieval algorithms are usually based on a gridded product such as that provided by the European Center for Medium Range Weather Forecasting (ECMWF) or the National Meteorological Center (NMC). These global, gridded products prescribe temperature and humidity profiles for a limited number of pressure levels (up to 14) in a vertical atmospheric column. The FIRE IFO II experiment provides an opportunity to investigate current atmospheric profile parameterization schemes, compare satellite cloud height results using both gridded products (ECMWF) and high vertical resolution sonde data from the National Weather Service (NWS) and Cross Chain Loran Atmospheric Sounding System (CLASS), and suggest modifications in atmospheric parameterization schemes based on these results.

2. Clear Sky Temperature/Radiance

Atmospheric temperature and moisture profiles are used to determine transmittance and hence radiance profiles. Variations in atmospheric profiles and surface conditions can have a considerable effect on the radiance profiles (Menzel et al., 1992). Surface conditions, temperature in particular, have considerable importance since clear-sky radiance provides the benchmark for comparisons with measured radiance values in order to estimate cloud heights. The first atmospheric parameterization involves determining the surface temperature for use in determining the surface, or clear-sky, radiance. In order to diagnose the clear-sky radiance at a particular pixel location, some have simply employed the "closest" clear-sky radiance value from a nearby region and then interpolated to the pixel under analysis (Smith and Frey, 1990; Menzel et.al., 1992). This parameterization is most accurate when the clear-sky pixel is in close proximity to the one under analysis, but may be less accurate in cases of large-scale cloud coverage when the "closest" clear-sky pixel is a large distance from the analysis pixel. Also, one has to determine whether the closest "clear-sky" radiance is really "clear-sky".

Even in the absence of frontal situations where temperature gradients may be quite large, clear-sky radiances can vary quite significantly over a short distance. For example, cloud top heights are computed using the ratio method for all HIRS fields of view (FOV) in the 2.5 degree square ISCCP box containing Coffeyville for the NOAA-11 overpass at 0932 UTC on Dec 5th. Of the 56 feet, two are classified as "clear-sky". That is, all four combinations in the 15-μm window yielded cloud-free estimates. The 11-μm brightness temperatures (HIRS and AVHRR) for the northernmost clear FOV were approximately 270 K, while the southernmost FOV had temperatures some six degrees

warmer at 276 K. The two feet are denoted as solid ovals on figure 1. The difference may have been attributed to some frozen ground in the northern region of the ISCCP box. Nonetheless, if either of these two feet were to be used as a "box-average" clear-sky radiance value (in the absence of the other), it would be quite unrepresentative of the entire region. ECMWF surface temperature values are 275.8, 274.5, and 276.9 for the grid points on the northern edge of the box, and 277.3, 275.3, and 274.7 on the southern edge of the box. These too cannot totally account for the frozen ground, but they do provide a more coherent spatial pattern for the calculation of clear-sky radiances. Therefore, in situations when the closest clear-sky pixel is too far from the analysis pixel, surface air temperatures are employed for calculating clear-sky radiances.

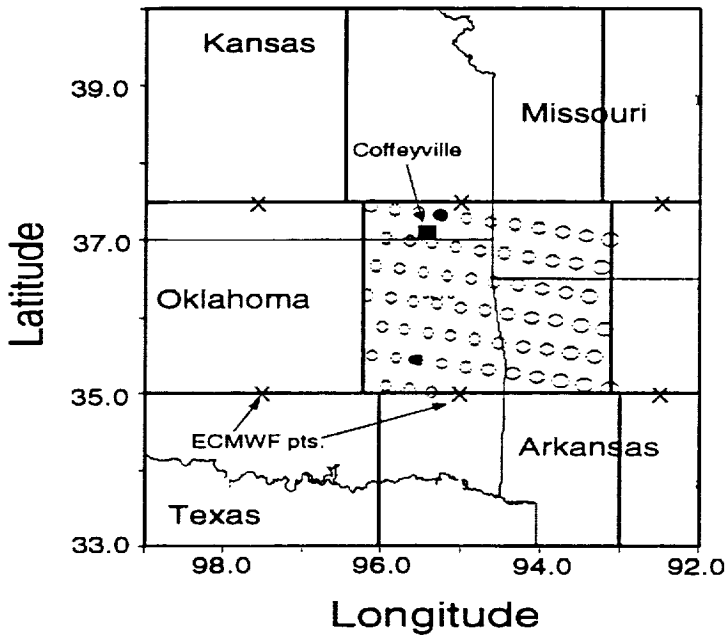

Figure 1. NOAA-11 HIRS/2 footprints within ISCCP box for Coffeyville, Kansas for Dec 5th 09UTC overpass. ECMWF dataset grid points also shown on figure. Solid pixels denote "clear-sky" conditions.

In addition, since ECMWF gridded data sets contain surface temperature and a 2-meter air temperature, adjustments are made when situations (i.e. fog, shallow nocturnal inversions, etc.) create markedly different values between the surface and 2 meter temperature value. The same adjustment is made when using high-vertical resolution rawinsonde data with data levels immediately above the surface. The exact adjustment to surface temperature is a function of the surface and above-surface air temperatures plus surface moisture conditions.

3. Tropopause

While atmospheric temperature and moisture profiles are required to compute upwelling radiances, these profiles may be used for additional purposes in cloud retrieval schemes. The ratio method allows diagnosis of cloud heights by comparing ratios of remotely-sensed radiances to clear-sky radiances of two closely spaced spectral bandsin the CO_2 band. Computationally, the technique is bounded by the surface and the portion of the free atmosphere that is assumed to be void of temperature inversions. With the definition of the tropopause based partially on temperature inversion, the logical upper bound is placed here. Physically, the tropopause often marks the upward vertical ascent of cirrus and convective clouds. Therefore, an accurate diagnosis of the tropopause is often crucial in determining cirrus cloud heights.

In the MSMR algorithm, the diagnosis of the tropopause is a 2-step process. Initially, the tropopause is set climatologically as a function of the Julian day and the latitude of the pixel under analysis. Nine default climatological profiles are set to choose from. Once an initial level is set, a looping procedure is employed starting at 2 levels below the initial tropopause level and extending to 2 levels above the initial tropopause. The lapse rate is computed for each level; if it is less than 5.0 C per kilometer, the tropopause level is re-set to that level. This allows for the tropopause to be re-set below OR above the level initially set. For example, during the NOAA-11 2108 UTC overpass over Coffeyville on Dec 5th, the tropopause is diagnosed at 200 mb over the northern region of the ISCCP box containing Coffeyville, but changes to 150 mb over the southern portion of the box. On this day, cloud top heights were measured at high altitudes approaching the tropopause. All surface-based instruments and aircraft yield cloud-top heights ranging from 12 to 12.3 km which is in accordance with the MSMR results. ECMWF relative humidity profiles reveal the peak moisture layer at the two grid points at 35 degrees north at 200 mb, whereas the peak moisture layer is lower at 250 mb along the 37 degree north parallel. This parameterization allows higher cloud height retrievals over the southern portion of the region which coincides with the higher peaks in the relative humidity profiles.

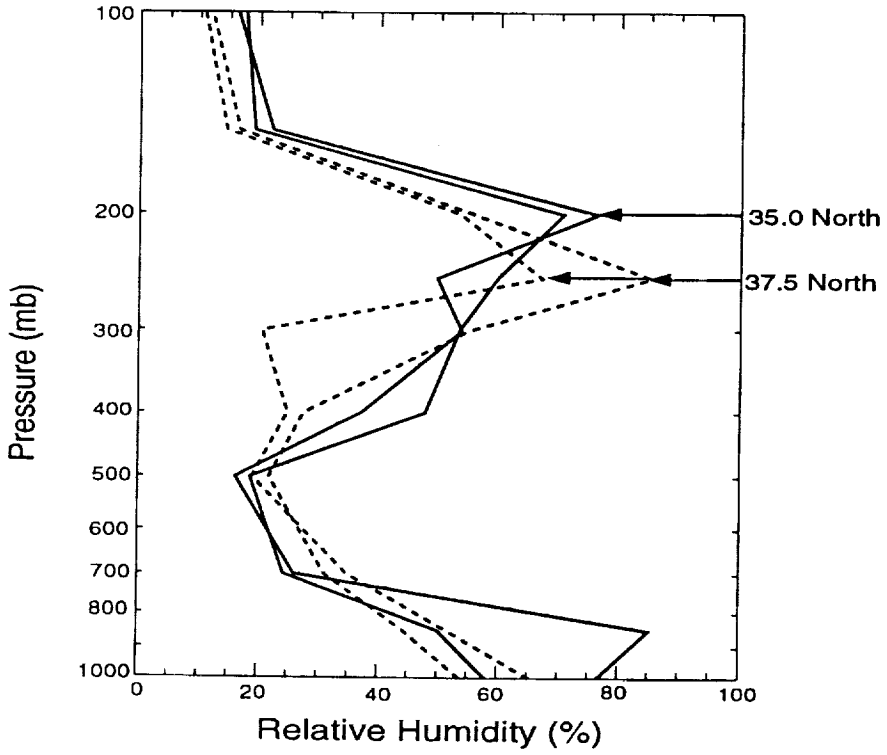

Figure 2. Dec 6th 00 UTC 1991 ECMWF relative humidity profiles for 4 grid points along 2 latitude bands: 35.0 and 37.5 degrees north. The longitude points are 95.0 and 97.5 degrees west.

4. Cloud Top Relative Humidity

Another atmospheric parameterization further reveals cloud features on this day. The four HIRS channel ratio combinations may yield markedly different cloud pressure estimates when cloud elements are thin and/or patchy in nature due to low cloud signal (the difference in upwelling radiance due to the presence of cloud). A priori knowledge of the region of the atmosphere where clouds exist may reveal the best channel combination to use. Unfortunately this knowledge rarely exists, so large differences in cloud-top pressure estimates may result. Therefore, there is a need for additional information to help choose the "correct" cloud-top estimate. Since cloud elements are often regions of increased moisture, cirrus uncinus a possible exception, a useful parameterization involves employing the input moisture profile to create a profile of relative humidity in the region of the cloud-top height estimations. A relative humidity value can then be diagnosed for each of the different cloud top heights. Heights that correspond areas with high relative humidity are treated with a greater degree of confidence than those with lower values. The relative humidity

profile is created as a function of temperature and mixing ratio using the procedure outlined in Starr and Wylie,1990.

The Dec 5th 1991 NOAA-11 2108 UTC overpass provides some excellent examples of how the addition of the relative humidity data provide the necessary information to choose the proper channel combination cloud-top estimate. In the southern portion of the "Coffeyville ISCCP box" there appear to be broken cirrus at very high altitudes. The tropopause parameterization scheme increases the possible "cloud-top placement" region to 13.85 km (150 millibars). For the HIRS foot over Fort Smith, Arkansas (on the Oklahoma/Arkansas border), the five channel combination estimates are: 8.2, 7.4, 8.0, 10.3, and 13.84 km. The relative humidity values for the same combinations are 57, 40, 52, 90, and 40%, respectively. The 90% relative humidity value corresponds to the 10.3 km cloud top height. This value is consistent with the values estimated by aircraft to the northwest of Fort Smith, and the Monett Missouri Rawinsonde humidity trace. The relative humidity profile is only a good as the input moisture profile. While all input atmosphere profiles are converted to 40 levels for use in theoretical radiance calculations, the ECMWF profiles are input at 14 levels while rawinsondes are input at about 400 levels. One can see that the resolution of the sondes will yield more representative values for the 40-level relative humidity profile. Comparisons of the ECMWF and rawinsonde derived profiles yeilded similar results over the Coffeyville region. Dense spatial coverage of rawinsondes, input in ECMWF product, are responsible for the agreement. One would expect that over oceans and in the southern hemisphere, the ECMWF relative humidity profiles will be more suspect.

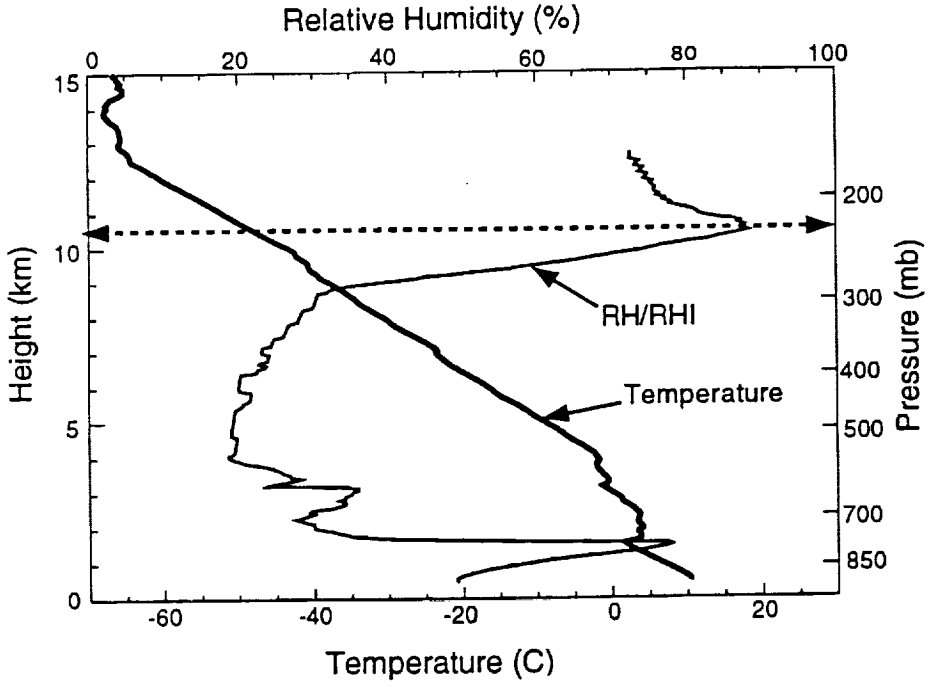

Figure 3. Rawinsonde temperature and relative humidity(liq/ice) trace for NWS Monett, Missouri Dec 6th 00UTC launch.

Baum,B.A., B.A. Wielicki, P. Minnis, and L. Parker, 1992: Cloud property retrieval using merged HIRS and AVHRR data, *J. Appl. Met.*, 31, 351-369.

McCleese, D. J., and L. S. Wilson, 1976: Cloud top heights from temperature sounding instruments, *Quart. J. Roy. Met. Soc.*, **102**, 781-790.

Menzel, P., D.P. Wylie, and K.I. Strabala, 1992: Seasonal and diurnal changes in cirrus clouds as seen in four uears of Observations with the VAS. *J. Appl. Met.*, 31, 370-385.

Smith, W.L. and R. Frey, 1990: On cloud altitude determinations from High Resolution Interferometer Sounder (HIS) observations. *J. Appl. Met.*, 29, 658-662.

Smith, W. L., and C. M. R. Platt, 1978: Comparison of satellite-deduced cloud heights with indications from radiosonde and ground-based laser measurements, *J. Appl. Met*, **17**, 1796-1802.

Starr, D.O'C. and D.P. Wylie, 1990: The 27-28 October 1986 FIRE cirrus case study: Meteorology and clouds, *Mon. Wea. Rev.* 188, 11, 2259-2287.

S21-47
197521
N94-22313

Automated Cloud Classification With A Fuzzy Logic Expert System

Vasanth Tovinkere[1] and Bryan A. Baum[2]

[1]Lockheed Engineering and Sciences Co., Hampton, VA 23666
[2]NASA Langley Research Center, Hampton, VA 23681-0001

1. Introduction

An unresolved problem in current cloud retrieval algorithms concerns the analysis of scenes containing overlapping cloud layers. Cloud parameterizations are very important both in global climate models and in studies of the Earth's radiation budget. Most cloud retrieval schemes, such as the bispectral method used by the International Satellite Cloud Climatology Project (ISCCP), have no way of determining whether overlapping cloud layers exist in any group of satellite pixels. One promising method uses fuzzy logic to determine whether mixed cloud and/or surface types exist within a group of pixels, such as cirrus, land, and water, or cirrus and stratus. When two or more class types are present, fuzzy logic uses membership values to assign the group of pixels partially to the different class types. The strength of fuzzy logic lies in its ability to work with patterns that may include more than one class, facilitating greater information extraction from satellite radiometric data. The development of the fuzzy logic rule-based expert system involves training the fuzzy classifier with spectral and textural features calculated from accurately labelled 32x32 regions of Advanced Very High Resolution Radiometer (AVHRR) 1.1-km data. The spectral data consists of AVHRR channels 1 (0.55-0.68 μm), 2 (0.725-1.1 μm), 3 (3.55-3.93 μm), 4 (10.5-11.5 μm), and 5 (11.5-12.5 μm), which include visible, near-infrared, and infrared window regions. The textural features are based on the gray level difference vector (GLDV) method. A sophisticated new interactive visual image classification system (IVICS) (Tovinkere et al., 1993) is used to label samples chosen from scenes collected during the FIRE IFO II. The training samples are chosen from predefined classes, chosen to be ocean, land, unbroken stratiform, broken stratiform, and cirrus. The November 28, 1991 NOAA overpasses contain complex multilevel cloud situations ideal for training and validating the fuzzy logic expert system.

2. Classification scheme

(i) *Features and Classes*

Both textural and spectral features were computed for each of the regions for use as features. The textural features were computed using the GLDV approach (Haralick et al, 1973; Weszka et al, 1976; Chen et al. 1989). As noted by Tovinkere et al. (1993), the set of features used by Ebert (1987), Garand (1988), and Tovinkere et al. (1993) may not necessarily compose the optimum feature vector, i.e., the best choice of features. There are alternative feature sets that may perform as well or better. For this investigation, the feature vector was determined through a sequential forward selection (SFS) procedure (Devijer and Kittler 1982), which is a simple bottom-up procedure where one measurement at a time is added to the current feature set. At each stage, the attribute to be included in the feature set is selected from the remaining available measurements, so that the new set yields a maximum value of a criterion function used. The feature selector uses the Jeffries-Matusita distance (also known as the Bhattacharya distance) as the criterion function (Welch et. al., 1992). A second level of feature selection is performed on the feature set selected by the SFS algorithm. This eliminates redundant information and comes up a minimal set required to discriminate the given classes. The measures chosen for this investigation have both textural and spectral features. The spectral features are (1) mean gray level (GL) difference of channels 2 and 3 (GL 2-GL 3) and (2) mean brightness temperature of channel 4 (Rmean 4). The textural features include entropy (ENT) of channels 1 and 3, homogeneity (HOM) of channel 3 and the angular second moment (ASM) of

channel 1. Details for computing these textural measures can be found in Welch et al. (1992). Each of these features uniquely describes at least one class and are chosen for daytime classification analysis.

The spectral feature GL 2-GL 3 is computed by scaling the reflectance of channel 2 to lie between 0 and 255. The range of values between 0- 255 represent the reflectivities between 0%-100%. Similarly, channel 3 brightness temperature is scaled to lie between 0-255 which represents temperatures between 200-327.5 K in half degree increments. The mean gray level for channels 2 (GL 2) and channels 3 (GL 3) are obtained by computing the mean of the gray levels of all pixels in the 32x32 region for the respective channels. The feature Rmean 4 is mean brightness temperature of channel 4 for the 32x32 pixel region.

A number of scenes from the IFO were used to derive training and testing samples. The mean (μ) and the standard deviations (σ) are calculated for the complete training data set. The graphs in Figure 1 show the extent of each feature for each class, i.e., (μ - σ) to (μ + σ). These graphs depict the separability of the classes for each feature. The data from the NOAA-11 and NOAA-12 overpasses on November 28, 1991, are classified into the following classes: (1) water, (2) land, (3) unbroken stratiform,(4) broken stratiform, and (5) cirroform. These classes are broad in scope and may contain a number of representative subclasses. For instance, land covers all surface not covered by water, unbroken stratiform includes both stratus and altostratus cloud types, broken stratiform includes both stratus and altostratus cloud types in which some surface is visible in the 32 by 32 pixel sample, and cirroform includes cirrostratus, cirrus uncinus, and other cirrus types.

(ii) Training of the fuzzy classifier

The fuzzy logic classifier is trained and tested using the 1.1-km AVHRR data. A number of scenes from the FIRE IFO II time period were used to derive numerous 32 by 32 pixel subregions of "pure" classes for classification purposes. Region labeling was performed using the IVICS system (Tovinkere et al., 1993). Details of the fuzzy logic-based expert system can be found in Tovinkere et al. (1993). The number of classes is limited for this initial study to ease interpretation of the classification results for mixed cloud and/or surface types.

3. Results

(i) Classification of pure samples

Two thirds of the data set from the spectral and textural database, with replacement, is used to train the classifier and the remainder is used as the test data to determine the accuracy. Replacement of the sample allows each sample to be selected more than once to generate the training data. This insures an unbiased estimate of classification accuracy. Table 1 shows the misclassification chart for the classifier.

Table 1: Misclassification chart for the fuzzy classifier.

CLASSES	1	2	3	4	5	Percentage Accuracy
Ocean/Water	57	2	0	0	0	96.61
Land	2	62	0	0	0	96.88
Unbroken Stratiform	0	0	71	2	0	97.26
Broken Stratiform	0	0	3	80	0	96.39
Cirroform	0	0	1	0	130	99.24
Overall Accuracy						**97.56**

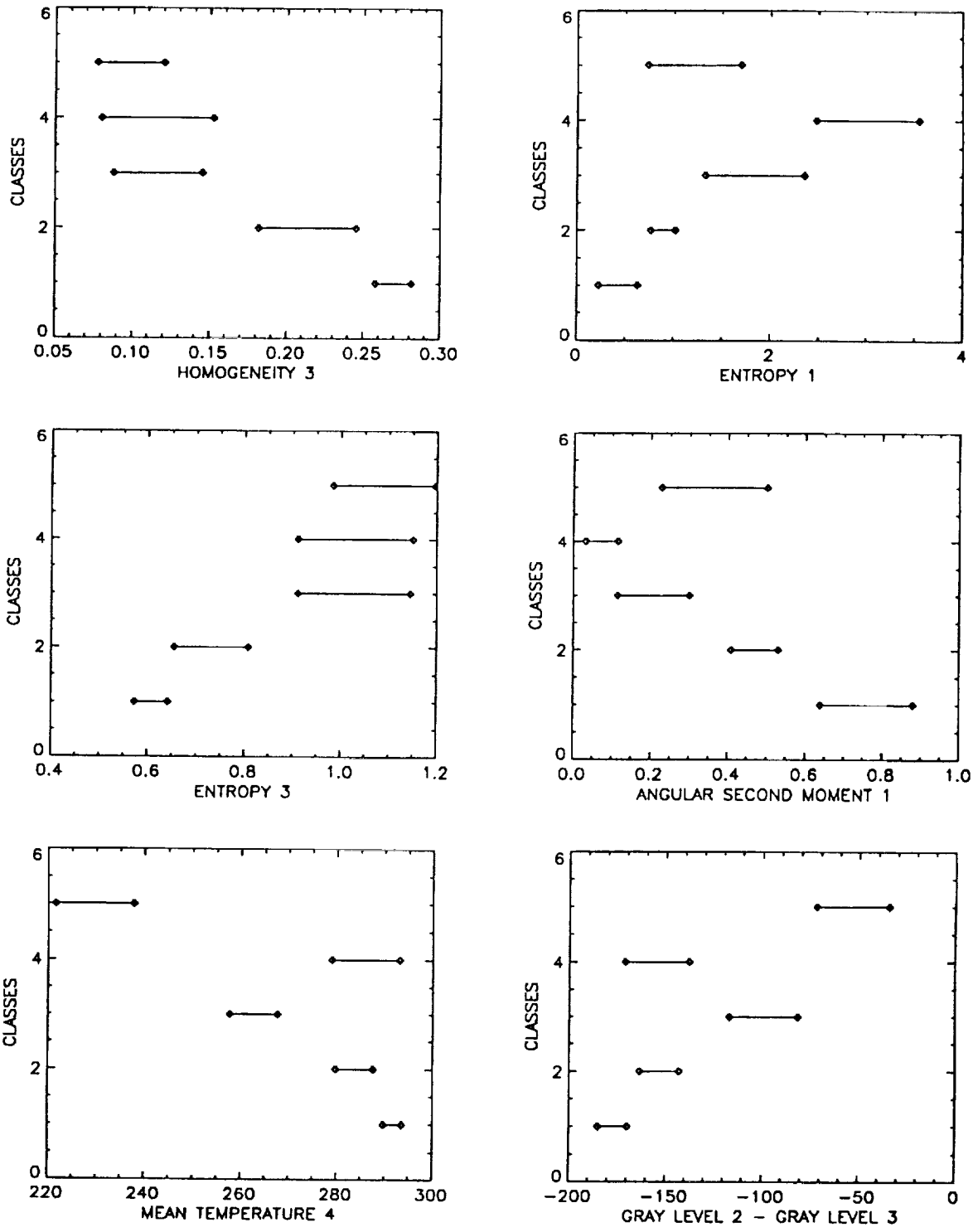

Figure 1. Class means and standard deviations for all the features used in the fuzzy classifier. The classes considered in the above case are: 1. Ocean/Water, 2. Land, 3. Unbroken Stratiform, 4. Broken Stratiform, and 5. Cirroform. The feature set under consideration is for daytime analysis only as they rely on the visible channels.

(ii) Classification of mixed scenes

The classifier was tested for 100-200 samples consisting of multilayer clouds. The classifier was able to determine the various classes present in regions of patchy cirrus and when thin cirrus completely covered the stratiform clouds indicating a multilayer situation. However, it failed when optically thick cirroform clouds enveloped the region. The classifier was also tested on regions that contained mixed surface types. In most cases the classifier was able to identify the different surface types present in the region. More detailed results will be presented regarding the ability of the classifier to identify regions of mixed cloud types.

REFERENCES

Chen, D. W., S. K. Sengupta, and R. M. Welch, Cloud field classification based upon high spatial resolution textural features, Part 2, Simplified vector approaches, *J. Geophys. Res., 94*, 14,749-14,765, 1989.

Devijer, P. A., and J. Kittler, *Pattern Recognition: A Statistical Approach*, 448 pp, Prentice Hall, Englewood Cliffs, N. J., 1982.

Ebert, E., A pattern recognition technique for distinguishing surface and cloud types in polar regions, *J. Clim. Appl. Meterol.*, 26,1412-1427, 1987.

Garand, L, 1988: Automated recognition of oceanic cloud patterns. Part I: Methodology and application to cloud climatology. *J. Clim.*, 1, 20-39.

Giarratano, J., and G. Riley, *Expert Systems*, 632 pp., PWS-Kent, Boston, Mass., 1990.

Haralick, R., M., K. S. Shanmugam, and I. Dinstein, Textural features for image classification, *IEEE trans. Syst., Man Cybern., SMC-3(6)*, 610-621, 1973.

Tovinkere, V. R., M. Penaloza, A. Logar, J. Lee, R. C. Weger, T. A. Berendes, and R. M. Welch, An intercomparison of artificial intelligence approaches for polar scene identification, *J. Geophys. Res.*, 98, 5001-5016, 1993.

Welch, R. M., S. K. Sengupta, A. K. Goroch, P. Rabindra, N. Rangaraj, and M. S. Navar, Polar cloud and surface classification using AVHRR imagery: An intercomparison of methods, *J. Appl. Meterol., 31*, 405-420, 1992.

Weszka, J. S., C. R. Dyer, and A. Rosenfeld, A comparative study of texture measures for terrain classification, *IEEE Trans. Syst. Man. Cybern., SMC-6(4)*, 2269-2285, 1976.

(Poster)

A Nephanalysis Over the Western United States for the Validation of Cloud Radiative Properties in Numerical Models

Donald Wylie
University of Wisconsin-Madison
Madison, Wisconsin 53717

Most validations of the models are done by eyeball comparisons of satellite images or some cloud analysis made from satellite images to model fields of cloud or radiative parameters. These comparisons usually give the appearance that the model is producing something resembling clouds near the locations of the clouds seen on the satellite images. Model success is usually proclaimed without giving quantitative details. But clouds have large spatial variances in radiative properties. Some parts of the cloud field are completely opaque to terrestrial radiation and highly reflective to solar radiation while others are semi-transparent to both. Most models are capable of producing large cyclonic systems and the very dense opaque clouds associated with them. But the thinner semi-transparent clouds on the margins of the dense systems are very difficult to produce. The semi-transparent clouds occur where dynamic motions and moisture levels are small. Yet these semi-transparent clouds can have a very large impact on the heat balance of the atmosphere because they can either heat or cool the atmosphere depending their visible and infrared characteristics.

A detailed data set will be produced for one case in FIRE-II where modeling experiments are being made, 26 November 1991. This data set will concentrate on identifying the semi-transparent cloud forms and their radiative properties. All parts of the cloud field will be described to the best of our ability given the data from this day. The primary data source will be satellite multi-spectral data, infrared as well as visible data. This will give the height of the cloud top and some information on infrared transmissivity and visible reflectance. Other cloud information will be included from the SVCA weather reports and the moisture structure on raob soundings for estimating cloud base altitudes and the presence of layers. FIRE-II lidar and aircraft data will be included where they are available.

An additional study also can be made from this cloud analysis. A high temporal rawinsonde data set also was obtained on this day. Separate analyses of atmospheric motions and moisture structure from the model fields also will be made to study how different cloud forms are produced and maintained. This study will probably begin at the FIRE-II conference when the data sets from other investigators are examined.

522-47
197522
p. 6

N94-22314

Meteorological Analysis of the December 4–6 FIRE Cirrus-II Case

David O'C. Starr
NASA Goddard Space Flight Center
Greenbelt, MD 20771

Andrew R. Lare
Applied Research Corporation
Landover, MD 20785

1 Introduction

During the period 4–6 December 1991, three distinct and separate cirrus cloud systems were observed to move over the FIRE Cirrus-II field site at Coffeyville (COF) in southeastern Kansas (Figure 1). Meteorological analyses of the first and third events are presented here. These cases were well-sampled by the regional rawinsonde network, highly instrumented aircraft, and extensive ground-based remote sensors at COF. Our analyses are primarily based on the rawinsonde observations. Unfortunately, the intervening event was not well-observed by the regional rawinsonde network.

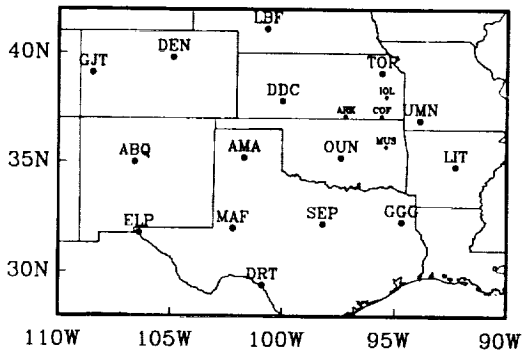

Figure 1: Map of rawinsonde stations located within the analysis region. Larger font indicates NWS stations, others are special FIRE CLASS stations.

Two large-scale synoptic features played a significant role in these cases. First, a closed-low circulation developed off the Baja coast on 4 December. This system drifted into the northern Gulf of California by the end of the period. This circulation pumped moisture to upper levels and resulted in extensive cirrus cloud formation over the southwestern U.S. in association with the leading ridge. Surges of upper level moisture and cirrus were also observed propagating northeastward across northern Mexico and southwestern Texas during this time period. Second, a persistent large-scale band of very dry air at middle and upper tropospheric levels, as evident on 6.7 μm GOES imagery, extended from the Great Basin eastward through central Kansas and into the southeastern U.S. As noted by Mace and Ackerman (1993), this feature was likely associated with a series of tropopause-fold events. Sassen (1992) speculated that aerosol-laden stratospheric air was brought down into the troposphere and undercut the moisture aloft.

2 Night of December 4–5 (0000–0900 UTC)

The first event occurred during the nighttime hours of 4–5 December 1991 and initially developed as a long thin cirrus band stretching in an anticyclonic arc from northeast New Mexico to COF. This cloud band appeared to propagate from an initial orographic forcing. Cirrus were first observed at COF by lidar after 0200 UTC. Significant cirrus development was later observed over Oklahoma on the south side of the cloud band. The event ended by about 1000 UTC as skies cleared. The 0600 UTC sounding from COF (Figure 2) showed relatively moist conditions at high levels with indications of two separate moist layers centered at about 10 and 11.5 km, respectively. Nominal sounding times are used here. Sampling at cirrus levels occurred $\sim$ 1/2 hour prior to the nominal times in most cases. These moist layers were not evident at 0000 UTC though some indication of moistening was seen in the 0200 UTC sounding. By 1000 UTC, only a moist layer at about 9 km remained.

Analysis of the temporal evolution of the heights of isentropic surfaces at COF (Figure 2) indicates that the static stability was minimal in the upper moist layer when cloud development was strongest (0600 UTC). However, there was little evidence for convective instability in the lower moist layer in contrast

to the lidar observations of very active convective development in this layer just after 0600 UTC. A very stable layer was observed below the region of cirrus cloud formation and lowered with time suggestive of an elevated warm frontal surface ($\sim$ 8 km at 0600 UTC).

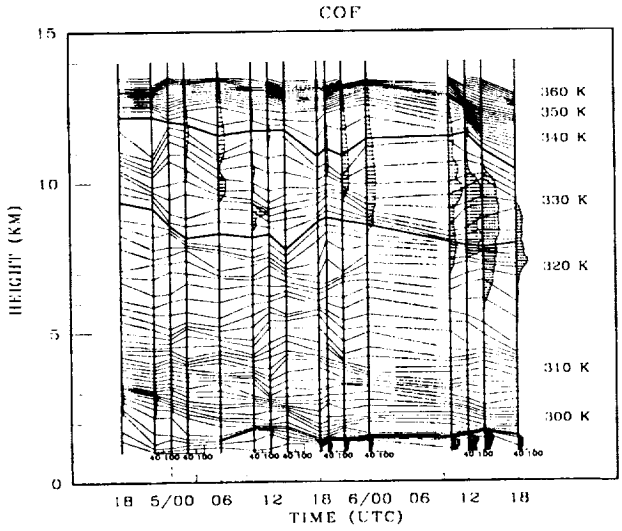

Figure 2: Time series of isentropic surfaces at 1 K intervals and percent relative humidity (shaded) as a function of height (km) from 1800 UTC on 4 December 1991 to 1800 UTC on 6 December 1991. The 325 K and 335 K isentropic surfaces are emphasized for comparison.

The 335 K isentropic surface cuts through the upper moist layer at COF, where high level cirrus occurred during this time period (Figure 2). Regional analysis of the geopotential height, horizontal wind, relative humidity, and vertical motion fields on this isentropic surface are shown in Figures 3 - 5 along with infrared satellite images for the same times. The vertical motions were derived from an objective analysis of the height and wind fields using the method of Starr and Wylie (1990). Estimated accuracy of this technique is generally about ± 2 cm sec^{-1}. Only data from NWS stations were used for these analyses.

At 0000 UTC, a large cloud shield extended into eastern Arizona from the upper level low, positioned west of Baja. A substantial area of cirrus was also observed over eastern New Mexico and western Texas (Figure 3). The analyzed relative humidity field (values exceeding 80%) corresponds well with the observed cloud pattern. The moisture pattern at higher levels was very similar. It must be noted that the humidity sensor in the SDD rawinsondes used at many of south-central and southwestern NWS stations are

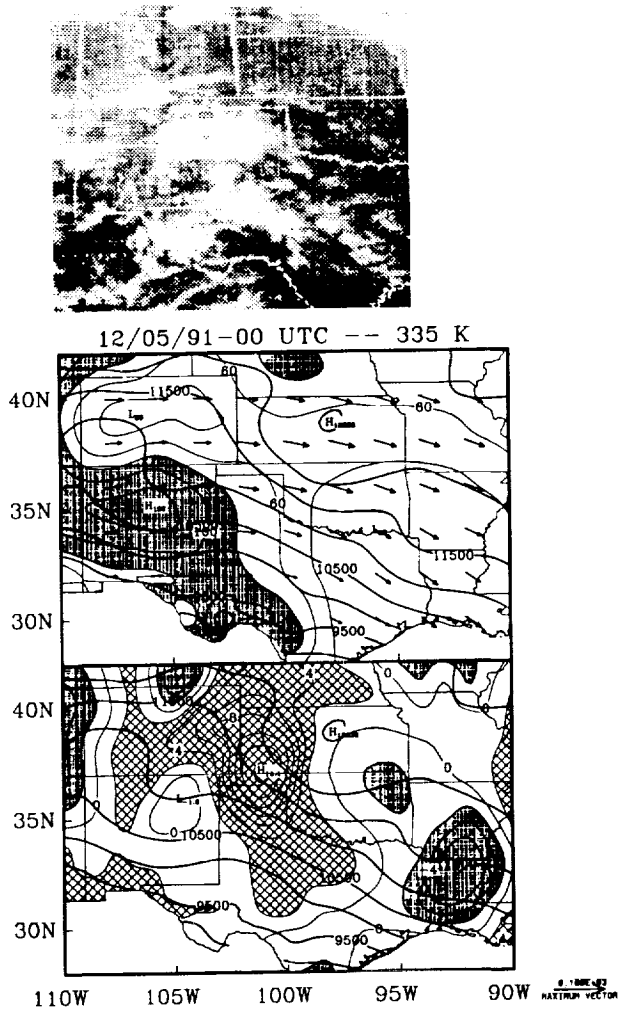

Figure 3: Infrared satellite imagery for 0000 UTC on 5 December 1991. Middle diagram shows lines of constant geopotential (thick solid) at 500 m intervals, percent relative humidity with respect to ice contoured at 20% intervals (thin solid), and wind vectors for the 335 K isentropic surface. Shaded regions indicate humidity levels exceeding 80%. The bottom diagram also shows lines of constant geopotential (thick solid), as well as vertical velocity (thin solid) contoured at 2 cm sec^{-1} intervals. Hatched regions indicate upward vertical velocities greater than 2 cm sec^{-1}, while shaded regions depict downward vertical velocities exceeding 2 cm sec^{-1}.

prone to becoming "stuck" once near-ice saturation is encountered in the upper troposphere. This was an unexpected finding. Occasional observations of very high values (supersaturation) can usually be attributed to this sensor problem; nonetheless, the analyzed humidity patterns appear qualitatively correct.

To the north over Colorado, significantly drier conditions were observed with relative humidity less than 40%. This dry region compares well with satellite imagery, where a noticeable swath of relatively cloud-free conditions was found. The northern 60% contour corresponds well with the northern boundary of the "dry" band observed in GOES water vapor channel (6.7 μm) imagery.

The vertical motion field shows a maximum of rising motion (14 cm sec^{-1}) located over the panhandle of Oklahoma along a north-south axis of rising motion. The axis of rising motion corresponds to the ridge axis evident in the cirrus cloud pattern, where upper level clouds appear densest. We often find that upper level moisture is maximized ahead of the axis of strongest upward vertical motion. Higher humidity is often observed ahead of strong upward motion because the air generally moves more rapidly than dynamical features. That the higher relative humidity observed over New Mexico lags the region of upward motion in this case likely indicates that the dynamical forcing responsible for that moistening actually occurred further to the west in association with the closed-low system. This case also illustrates that relatively strong upward motion, as found over eastern Colorado and western Kansas, is not necessarily associated with cloud formation. When the air is dry, an extended time may be required before the upward motion results in sufficient humidification. Subsidence was found over the eastern potions of Kansas, Oklahoma and Texas, where dry conditions (< 40%) and cirrus cloud dissipation were observed.

By 0600 on December 5, the cirrus cloud system had moved eastward extending from western Oklahoma into southern Missouri and Arkansas (Figure 4). Since only the 17 inner network NWS stations conducted launches at this time, the analysis area is considerably smaller. Relative humidity exceeded 80% over central Oklahoma in fair agreement with the satellite imagery although, as before, the apparently dissipating portion of the cloud field extended well into the drier air ahead. The center of maximum upward vertical velocity remained nearly constant in magnitude from the 0000 UTC analysis and moved southeastward to central Oklahoma, where it was located just on the southwestern side of the brightest cirrus clouds and just west of the ridge axis. It may also be seen that the band of high humidity extending southward into Texas now led the axis of strongest upward motion. Although relative humidity was high in the northwest portion of the analysis region, subsidence was diagnosed there consistent with the clearing seen in the satellite imagery. To the southeast, strong subsidence and drying were associated with cloud dissipation.

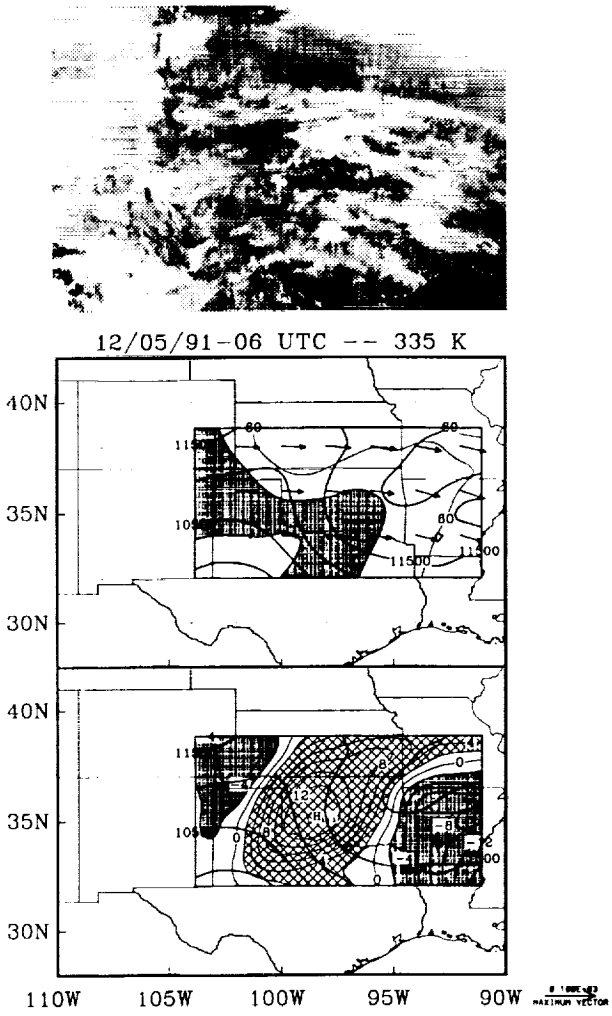

Figure 4: Same as in Figure 3 except at 0600 UTC.

The cirrus cloud system continued its rapid progression eastward and was situated over Arkansas by 1200 UTC on December 5 (Figure 5). Relative humidity exceeded 80% over western Texas, New Mexico, and southern Colorado in advance of an approaching band of strong upward motion. Subsidence was found in the lee side of the Rockies, where strong clearing and declining humidity were observed. The phasing of the upper level humidity and vertical motion fields were now more typical. Analyzed upward motions associated with the observed cirrus cloud system had moved eastward and diminished considerably (to $\sim$ 5 cm sec^{-1}) from the previous two analysis times.

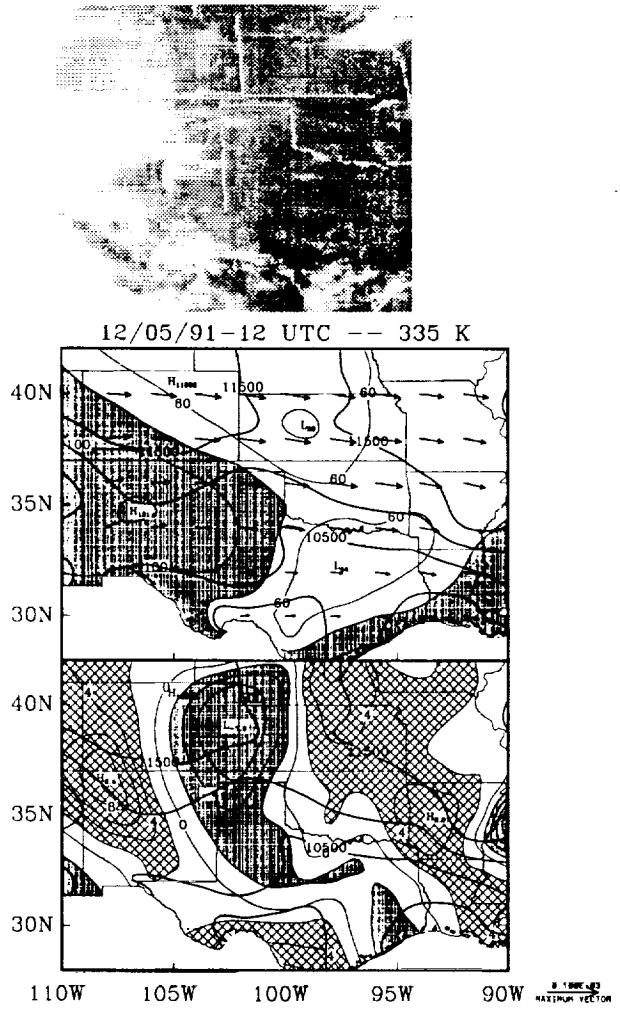

Figure 5: Same as in Figure 3 except at 1200 UTC.

Throughout this time period, two distinct layers (usually occurring together) of cirrus clouds were noted by lidar. The lower layer was initially observed around 9.5–10 km but progressively lowered and deepened to a height of 8.5–9.5 km. The upper layer extended from 10.5 km to 12.5 km or more with precipitation streamers occasionally reaching the lower cirrus layer. A time series plot of vertical motion analyzed for the Arkansas–Coffeyville–Muskogee (ARK–COF–MUS) triangle of special FIRE rawinsonde stations (Figure 1) is shown in Figure 6. Two distinct layers of weak upward vertical motion are evident at 0600 UTC and correspond very well with the observed cloud heights. Very weak upward motion was found from 8.5–9.5 km with somewhat stronger ascent from 11.0–13.0 km at 0600 UTC. Later at 1200 UTC, significant upward motions continue to be found in agreement with the analysis of NWS soundings shown in Figure 5. Thus, it appears that dry air rather than lack of upward motion caused the cessation of cirrus cloud formation over COF.

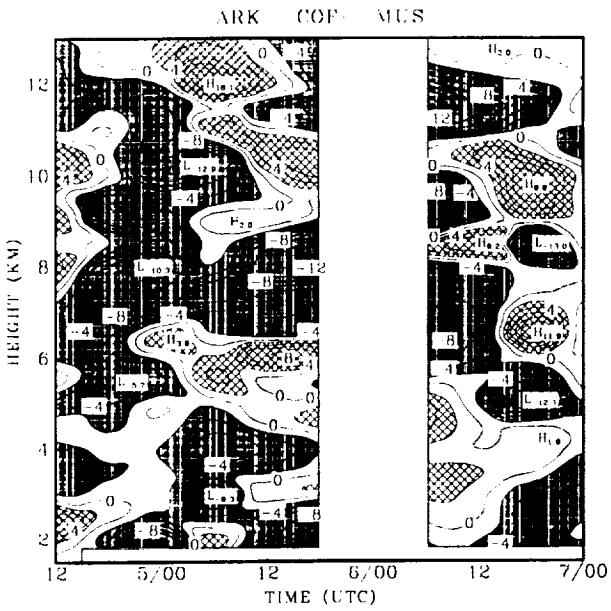

Figure 6: Contours of vertical motion for the triangle Arkansas – Coffeyville – Muskogee (ARK-COF-MUS) as a function of height (km) from 1200 UTC on 4 December 1991 to 0000 UTC on 7 December 1991. Contouring interval is 2 cm sec^{-1}. Hatched regions indicate upward vertical velocities exceeding 2 cm sec^{-1}, while shaded regions indicate downward vertical velocities greater than 2 cm sec^{-1}.

3 Morning of December 6 (1200–1800 UTC)

The third cirrus event occurred during the morning hours of 6 December 1991. Satellite imagery at 1230 UTC (Figure 7) shows cirrus associated with the subtropical jet stream covering southeastern Texas. Cirrus clouds are also found in central Oklahoma, eastern Kansas and central Missouri in association with a weak ridge-crest extending from western Oklahoma to southwestern Iowa.

Rawinsonde soundings from COF (Figure 2) show humid conditions over a fairly deep region of the upper troposphere (7–10 km) between 1000 and 1500 UTC on 6 December. By 1800 UTC, humidities had declined although somewhat moist conditions were still observed in the 7–9 km layer. Two other features are particularly noteable in the COF soundings. There is a rapid decline in tropopause height after 1200 UTC and a very stable layer was observed

in the lower portion of the humid layer. This latter feature was continuously defined from the prior day and progressively lowered with time. As in the first case discussed here, this is highly suggestive of an elevated warm frontal surface.

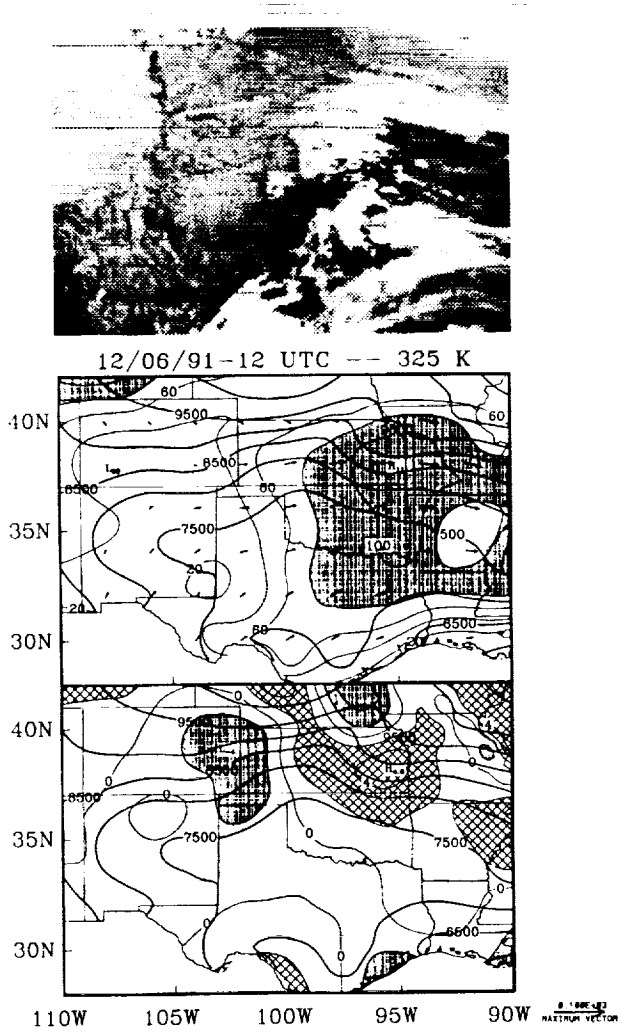

Figure 7: Infrared satellite imagery for 1230 UTC on 6 December 1991 (analysis is for 1200 UTC). Middle diagram shows lines of constant geopotential (thick solid) at 500 m intervals, percent relative humidity with respect to ice contoured at 20% intervals (thin solid), and wind vectors for the 325 K isentropic surface. Shaded regions indicate humidity levels exceeding 80%. The bottom diagram also shows lines of constant geopotential (thick solid), as well as vertical velocity (thin solid) contoured at 2 cm sec^{-1} intervals. Hatched regions indicate upward vertical velocities greater than 2 cm sec^{-1}, while shaded regions depict downward vertical velocities exceeding 2 cm sec^{-1}.

Aircraft and lidar observation indicated cirrus initially extended from between 9.5 and 10 km down to below 6 km. The cloudy region below 7.0 km was probably the result of ice crystal fallout from above. Generating cells were observed at upper levels. The lidar observations showed multi-layered structure although aircraft observers reported cloud at all internal flight levels. Some lowering of cloud top was noted during the mission although cloud top was apparently ill-defined. Cirrus rapidly dissipated after 1700 UTC.

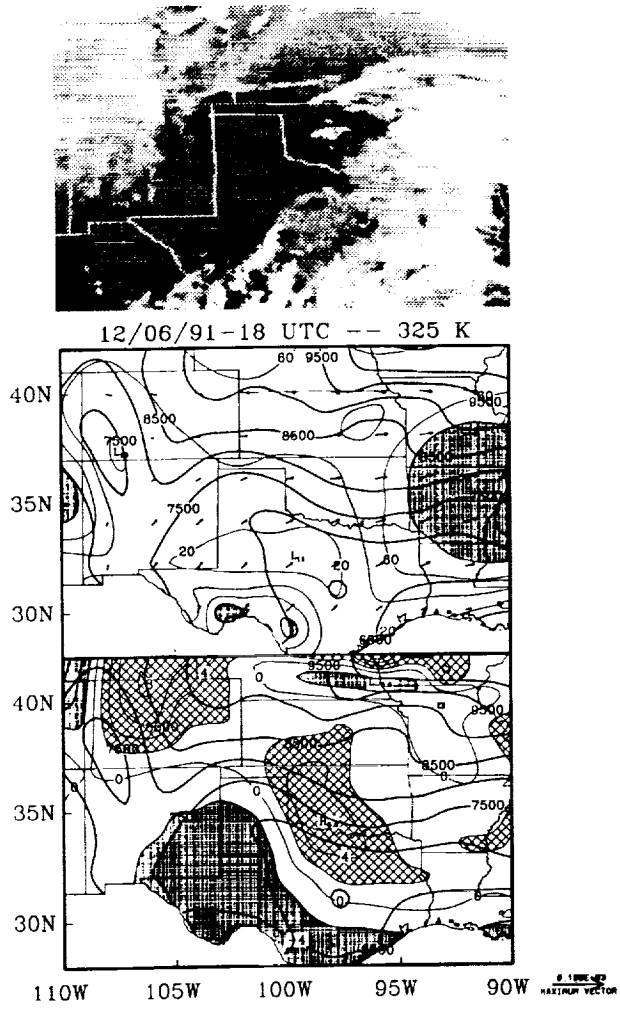

Figure 8: Same as in Figure 7 except satellite imagery and analysis are valid for 1700 UTC and 1800 UTC, respectively.

Analysis of the 325 K isentropic surface are presented for this case which corresponds to a height of about 8 km at COF (Figure 2). At 1200 UTC, relative humidity exceeded 80% over a fairly broad region to the east of the ridge axis lying through central

Kansas and western Oklahoma (Figure 7). The region of high humidity is also a region of weak upward motion. Strongest ascent ($\sim$ 4 cm sec^{-1}) in southeastern Kansas is well-correlated with the brightest and thickest part of the cirrus cloud system. To the north and west, subsidence was diagnosed, where clear regions were observed in the satellite imagery.

By midday, the cirrus cloud system and its associated region of high humidity had moved eastward (Figure 8) with the ridge axis. Vertical motion ahead of the ridge axis had declined to about zero. This is consistent with the observed dissipation of cirrus after about 1700 UTC. However, moderate upward vertical motion was now diagnosed in western Oklahoma in conjunction with the next approaching ridge crest. Lack of upper level moisture precluded formation of cirrus there.

4 Conclusions

Analysis of synoptic scale rawinsonde data for two of three cirrus events on 4–6 December 1991 revealed excellent correspondence between the satellite observed cloud patterns and the observed humidity and diagnosed vertical motion patterns. Upward motion from 4 to 14 cm sec^{-1} was found in association with upper level humidification and cirrus cloud formation. Highest humidity was generally observed ahead of the axis of strongest upward motion although this alignment took some time to develop in the first event. In each event, the cirrus clouds were associated with a weak shortwave ridge embedded in a generally westerly flow, i.e., ridge-crest cirrus (Starr and Wylie 1990). Analysis of data from the FIRE ARK-COFMUS mesoscale station array was generally consistent with the larger scale results and with the vertical location of the cloud layers observed around COF. Overall, a tendency for low static stability was observed at COF in association with cirrus cloud development. An underlying stable feature resembling an elevated warm front was also observed in both cases as was a lowering of the tropopause height during each case, dramatically in the third event. A regional analysis was not possible for the intervening second event due to the lack of observations.

One conclusion that may be drawn from our analysis is that the sharp northern boundary of the ridge-crest cirrus was not found to be associated with a distinct dynamical boundary in these results. Rather, this feature appears to correspond to a transition from "humid-enough" to "not humid-enough" in the moisture field since upward motion features tend to straddle the cloud boundary in these cases, i.e., moderate upward motion was diagnosed in dry air where cloud formation was precluded. Here, the dry air was likely the result of prior tropopause-fold events (Mace and Ackerman 1993). Other areas of upward motion in dry air without cloud formation were also observed. However, we cannot eliminate the possibility of the existence of some narrow mesoscale dynamical feature that may not have been captured by the observations used here.

Lastly, the humidity sensor on the SDD sonde used by NWS stations in the south-central and southwestern U.S. has been frequently observed to "stick" once near-ice-saturation is encountered in the upper tropopause. This sometimes results in apparent observations of highly ice-supersaturated conditions at higher levels, even extending into the lower stratosphere in some cases.

5 Acknowledgments

The authors wish to thank Gerald Mace (Penn State University) and Ken Sassen (University of Utah) for valuable discussions regarding this case study and for providing access to satellite imagery (GM) and lidar observations (KS).

6 References

Mace, G.G., and T.P. Ackerman, 1993: Examination of the observed synoptic scale cirrus cloud environment: The December 4–6 FIRE Cirrus case study. (this document)

Sassen, K., 1992: Evidence for liquid-phase cirrus cloud formation from volcanic aerosols: Climatic implications. *Science*, **257**, 516–519.

Starr, D.O'C., and D.P. Wylie, 1990: The 27–28 October 1986 FIRE Cirrus case study: Meteorology and clouds. *Mon. Wea. Rev.*, **118**, 2259–2287.

S23-47
197523
p 5

N94-22315

CIRRUS CLOUD RETRIEVALS FROM HIS OBSERVATIONS DURING FIRE II

S. A. Ackerman, W. L. Smith, X. L. Ma, R. O. Knuteson and H. E. Revercomb

ABSTRACT

This paper presents 1) retrieval methods applied to HIS observations during FIRE II and 2) doubling/adding model developed to simulate high-spectral resolution infrared radiances in a cloudy atmosphere. The capabilities of the retrieval methods and sensitivity studies of high-altitude aircraft based observations to cloud microphysical structure are conducted with the model.

OBSERVATIONS

Methods of detecting cirrus clouds and inferring their radiative properties have been developed at the University of Wisconsin-Madison under the High-resolution Interferometner Sounder (HIS) program (e.g., Smith and Frey, 1990; Ackerman et al, 1990; and Smith et al, 1993). The HIS instrument is a calibrated nadir viewing Michelson interferometer which flies on board the NASA high altitude ER-2 aircraft. Figure 1 is an example of the retrieved cloud pressure altitude using the CO_2 slicing method developed for high-spectral resolution observations (Smith and Frey 1990) for the period 17:50 to 18:04 UTC on December 5. The white line is the retrieved cloud altitude and the dark line the IR window equivalent blackbody temperature. Dotted lines indicate the HIS in its calibration mode or no cloud height retrieval. The HIS time series is overlain the CALS lidar image, provide by Dr. J. Spinhirne. While the CO_2 slicing method is detecting the presence of the cloud, its effective altitude varies more than the lidar observed cloud. The cloud is very inhomogeneous, making it a difficult situation for any cloud retrieval technique. We are employing model simulations to test the sensitivity of the CO_2 slicing method, and other cloud retrieval techniques, to cloud microphysical properties (this will be presented at the conference). Figure 2 depicts the tri-spectral approach to detecting cirrus cloud (Ackerman et al 1990) for the same period as Figure 1. Positive 8.3-11 μm brightness temperature differences are indicative of cloud. We are combing the tri-spectral technique with the CO_2 slicing technique and the cloud emissivity techniques of Ackerman et al (1990) and Smith at al (1993) to improve the detection of cirrus cloud and the retrieval of its radiative properties.

MODEL SIMULATIONS

Infrared observations at a spectral resolution of 1 cm^{-1}, or finer, have proven to be extremely valuable in assessing line-by-line radiative transfer models and in retrieving atmospheric temperature and moisture profiles (Smith et al 1989). Techniques have also been developed to infer, in cloudy sky atmospheric conditions, cloud radiative properties in addition to temperature and moisture profiles from the high spectral resolution observations. To develop, verify and test these cloud retrieval techniques requires accurate simulations of observed radiances. These model based simulations have to accurately account for multiple scattering by the cloud layer, as well as emission and absorption of the gases in the atmosphere.

Assuming a plane-parallel horizontally homogeneous cloud, the IR radiative transfer equation is

$$\mu \frac{dI(\delta,\mu)}{d\delta} = I(\delta,\mu) - (1-\omega_\circ)B(T) - \frac{\omega_\circ}{2}\int_{-1}^{1} P(\delta,\mu,\mu')I(\delta,\mu')\,d\mu'$$

where $I(\delta,\mu)$ is the azimuthally average monochronmatic intensity, δ is the optical thickness, $\omega_\circ$ is the single scattering albedo, $P(\delta,\mu,\mu')$ is the azimuthally averaged phase function, $B(T)$ represents the Planck function at temperature T, and $\mu = \cos\theta$ where θ is measured from the downward normal direction. An accurate numerical technique to solve equation (1) is the doubling/adding method which has been discussed in detail in previous atmosphere studies (Grant and Hunt, 1969; Wiscombe 1976; Wiscombe and Grams 1976; Wiscombe and Evans 1977, Stephens 1980).

For the purposes of this paper, we have assumed the cloud is composed of spherical ice particles distributed according to a modified gamma distribution. Scattering is neglected in the clear sky atmosphere so that, for a single cloud layer, the atmosphere is divided into three layers: above, within and below the cloud layer. Radiances and transmittances in the clear sky conditions are determined from FASCOD3 calculations. The incident radiances at the cloud boundaries must be specified. Rather than

run separate FASCOD3 calculations for each angle incident on the cloud, for the purposes of this paper, FASCOD3 is used to the nadir and zenith angle radiance, the angular distribution is derived by weighting the FASCOD3 radiance by the cosine of the incident angle. FASCOD3 is used to assign gaseous transmittance within the cloud.

Examples of model simulations which correspond to conditions observed during the coincident FIRE II Cirrus and SPECTRE field experiments, will be presented at the conference. Vertical profiles of temperature, moisture and ozone were measured during 5 December 1991. Both ground based and ER-2 based observations were also available during this time period. Lidar observations indicated a cirrus cloud between approximately 10 and 12.3 km. The model discussed above was used to simulate high-spectral resolution observations for a variety of assumed cloud microphysical properties. Here we want to briefly highlight the sensitivity of the observations to different microphysical properties.

An example of the sensitivity of the HIS observations to ice water path (IWP) is depicted in Figure 3. The reference spectra is computed for a cloud with IWP=6.9 g/m^2, an effective radius of 30 μm and a variance of 0.25. In each subsequent calculation, only the IWP was changed (values are: 0.23, 0.69, 1.61, 2.3, 16.1, 23., 69., and 161 g/m^2). Differences between the different IWP's are depicted in terms of the difference in equivalent brightness temperature from the reference spectra (ΔBT). Negative values indicate a larger IWP and positive values a smaller IWP. As expected the more opaque the band the less sensitivity to IWP and the cloud in general. Maximum sensitivity occurs in the regions between absorptance lines. For these high clouds, the aircraft based instrument has more sensitivity to the cloud IWP in the spectral regions 500-600 cm^{-1} and 1300-1500 cm^{-1}. Water vapor absorption is dominant in these spectral regions, the majority of which lies between the surface and the cloud base obscuring the view of the cloud from the ground-based instrument. In the region 1100-1300 cm^{-1}, the ER-2 view sees a constant ΔBT , at least in-between absorption lines. For the spectral region 850-1000 cm^{-1},the ΔBT is spectrally dependent. The spectral variation of ΔBT depends on the IWP though it is less than approximately 2°. This spectral variation in BT is driven by the spectral variation in the cloud optical properties and therefore rooted to the cloud particle size distribution.

Sensitivity of the simulated spectre to changes in cloud particle size distribution are depicted in figure 4. Again results are displayed in terms of the brightness temperature difference from a reference spectra. The reference spectra has a particle size distribution with a=30 μm and a variance of b=0.25; comparison are made for small effective radius (a=15μm) and larger effective radius (a=120μm). Comparisons were conducted for three equivalent IWP's, .23, 2.3 and 23 g/m^2. The positive ΔBT represent differences between the 30 μm effective radius distribution and the 15 μm distribution. As seen in Figure 4, the smaller the IWP the less difference between spectra with different effective radii. The scales were kept the same as the IWP comparison to demonstrate the dominating effect of the cloud ice water path. The spectral region that appears to be most sensitive to particle size is the 950-1050 cm^{-1} (>5 °). Variations in this spectral regime are larger than the IWP dependence. The magnitude depends on the IWP, while the particle size controls the shape of the ΔBT curve.

Further sensitivity studies and data analysis will be presented at the meeting.

REFERENCES

Ackerman, S. A., W. L. Smith, J. D. Spinhirne, and H. E. Revercomb, 1990: The 27-28 October 1986 FIRE cirrus case study: spectral properties of cirrus clouds in the 8-12 μm window. *Mon. Wea. Rev.*, **118**, 2377-2388.

Revercomb, H.E., H. Buijs, H.B. Howell, D.D. LaPorte, W.L. Smith, and L.A. Sromovsky, 1988: Radiometric Calibration of IR Fourier Transform Spectrometers: Solution to a Problem with the High Resolution Interferometer Sounder. *Applied Optics*, **27**, 3210-3218.

Smith W. L., H. E. Revercomb, D. D. LaPorte, H. M. Woolf, H. B. Howell, R. O. Knuteson, H. L. Huang, L. A. Sromovsky and S. Silverman, 1989: GHIS, the Geostationary High-resolution Interferometer Sounder. *CIMSS View*, **Vol. V**, No.1, available from the Space Science and Engineering Center, Universtiy of Wisconsin, Madison, Wisconsin, 53706.

Smith W.L., Xia Lin Ma, S.A. Ackerman, H.E. Revercomb, and R.O. Knuteson, 1993: Remote Sensing Cloud Properties from High Spectral Resolution Infrared Observations. *J. Appl. Met*, in press, 1993.

Smith, W. L. and R. Frey, 1990: On cloud altitude determinations from high resolution interferometer sounder (HIS) observations. *J. Appl. Meteor.*, **29**, 658-662.

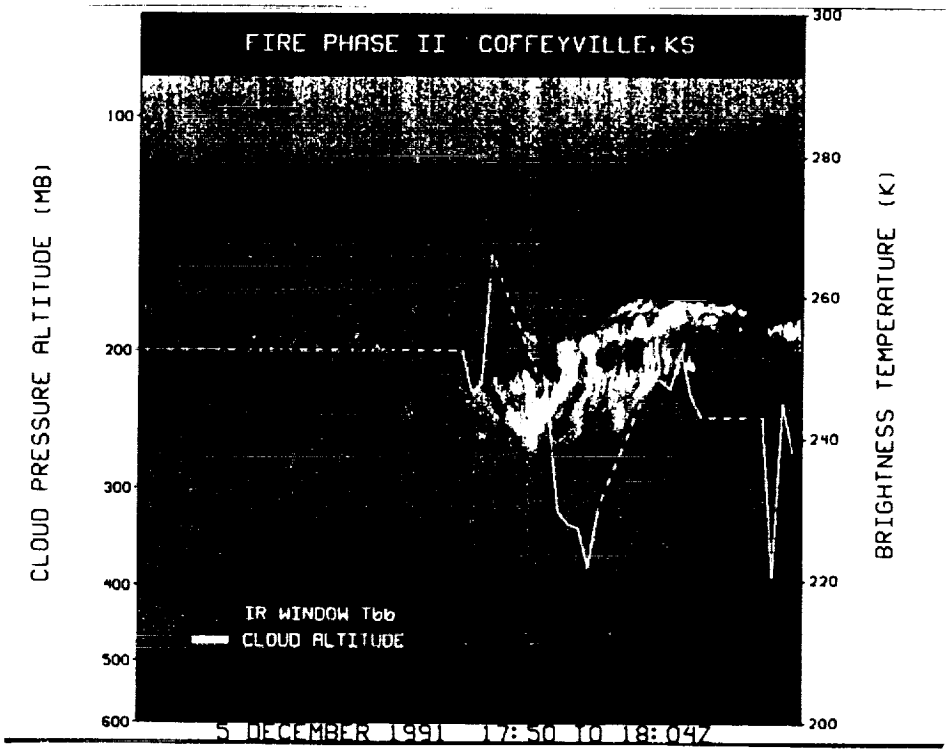

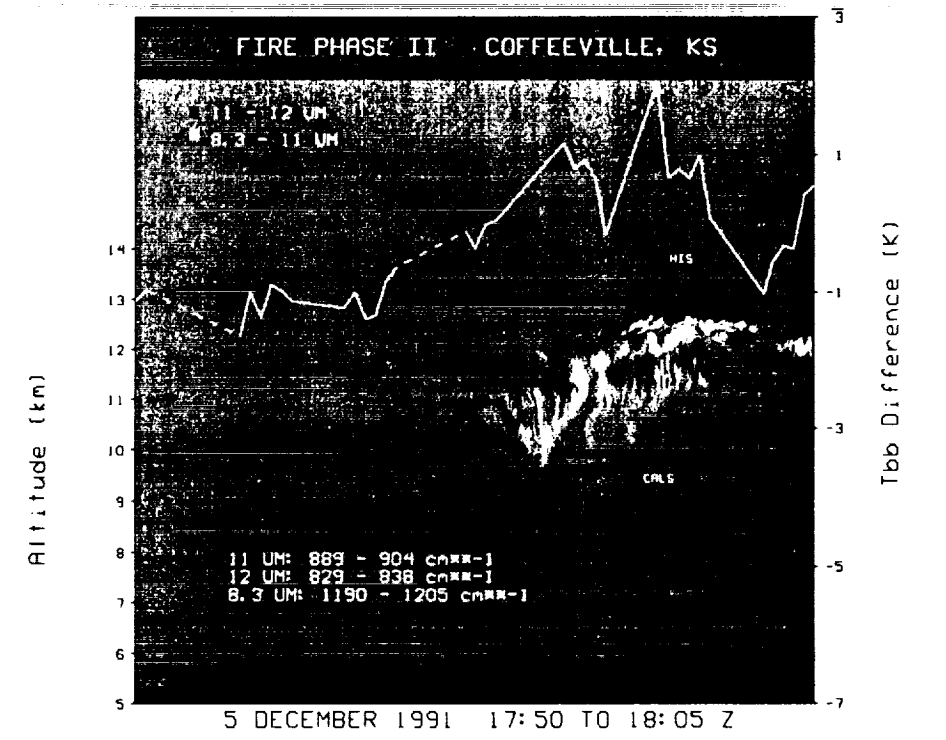

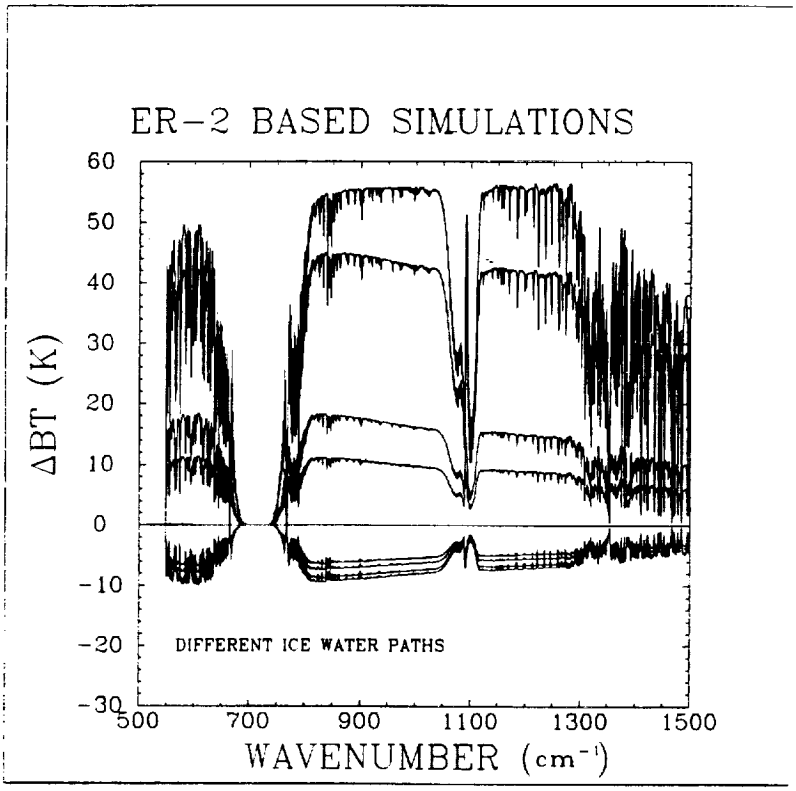
ER-2 BASED SIMULATIONS
ΔBT (K)
60
50
40
30
20
10
0
-10
-20
-30
DIFFERENT ICE WATER PATHS
500
700
900
1100
1300
1500
WAVENUMBER (cm⁻¹)

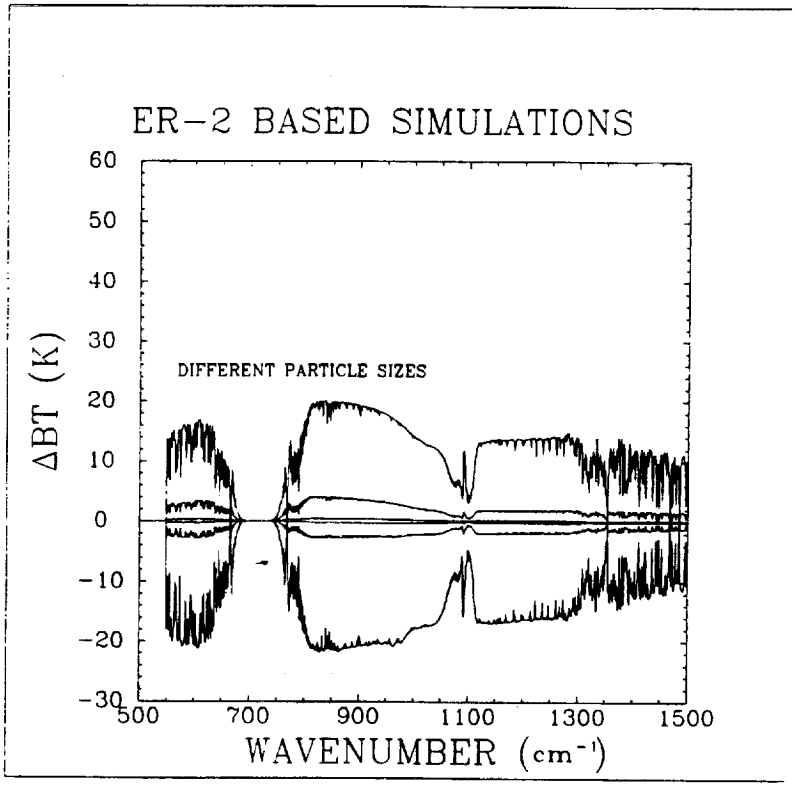
ER-2 BASED SIMULATIONS
ΔBT (K)
60
50
40
30
20
10
0
-10
-20
-30
DIFFERENT PARTICLE SIZES
500
700
900
1100
1300
1500
WAVENUMBER (cm⁻¹)

REFERENCES

Ackerman, S. A., W. L. Smith, J. D. Spinhirne, and H. E. Revercomb, 1990: The 27-28 October 1986 FIRE cirrus case study: spectral properties of cirrus clouds in the 8-12 μm window. *Mon. Wea. Rev.*, **118**, 2377-2388.

Revercomb, H.E., H. Buijs, H.B. Howell, D.D. LaPorte, W.L. Smith, and L.A. Sromovsky, 1988: Radiometric Calibration of IR Fourier Transform Spectrometers: Solution to a Problem with the High Resolution Interferometer Sounder. *Applied Optics*, **27**, 3210-3218.

Smith W. L., H. E. Revercomb, H. B. Howell, and M. -X. Lin; 1988: Multi-spectral window radiance observations of cirrus from satellite and aircraft - November 2, 1986 "Project FIRE", FIRE Science Results 1988, Proceeding of a conference held in Vail, CO July 11-15, pp 89-93.

Smith W. L., H. E. Revercomb, D. D. LaPorte, H. M. Woolf, H. B. Howell, R. O. Knuteson, H. L. Huang, L. A. Sromovsky and S. Silverman, 1989: GHIS, the Geostationary High-resolution Interferometer Sounder. *CIMSS View*, **Vol. V**, No.1, available from the Space Science and Engineering Center, Universtiy of Wisconsin, Madison, Wisconsin, 53706.

Smith W.L., Xia Lin Ma, S.A. Ackerman, H.E. Revercomb, and R.O. Knuteson, 1993: Remote Sensing Cloud Properties from High Spectral Resolution Infrared Observations. *J. Appl. Met*, in press, 1993.

Smith, W. L. and R. Frey, 1990: On cloud altitude determinations from high resolution interferometer sounder (HIS) observations. *J. Appl. Meteor.*, **29**, 658-662.

Smith, W. L., and R. Frey, 1991: Altitude specification of cloud motion winds. Workshop on Wind Extraction from Operational Meteorological Satellite Data, Washington, D.C. September 17-19.

Table 2. WISCONSIN AERI INSTRUMENT OPERATIONS

LOCATION: COFFEYVILLE, KANSAS
YEAR: 1991
REMARKS: (1) Observations are at 10 minute intervals betweenstated START and END times. (2) The letter H indicates that the ER-2 HIS was overhead. (3) OP # refers to an AERI operating period.

OP #	DATE	TIME PERIOD	CONDITIONS FROM VISUAL OBS
1	11 NOV	17:06 - 17:30	low overcast
2	12 NOV	23:26 - 02:29	cirrus
	13 NOV	02:53 - 04:28	cirrus/clear
3	13 NOV	18:18 - 01:26	cirrus
	14 NOV	02:13 - 03:41	thin cirrus
4	17 NOV	17:58 - 21:12	mixed cirrus to clear
	18 NOV	01:29 - 24:00	clear
	19 NOV	00:00 - 05:57	clear/cirrus/low thick cloud
5	20 NOV	17:20 - 23:33	clear
	21 NOV	00:12 - 24:00	clear
	22 NOV	00:00 - 19:07	cirrus/clear/rain
6	23 NOV	16:28 - 24:00	clear/mixed/overcast
	24 NOV	00:47 - 23:29	overcast/clear
	25 NOV	00:37 - 05:48	overcast
7	25 NOV	16:19 - 23:52	alto-cumulus/scatter cirrus
	26 NOV	00:29 - 24:00	clear/cirrus/mixed
8	27 NOV	14:01 - 17:21	low cloud
9	28 NOV	14:40 - 22:35	cirrus/overcast stratus
10	29 NOV	15:00 - 24:00	overcast/clear
	30 NOV	00:00 - 17:34	clear/overcast
11	03 DEC	00:25 - 23:08	overcast/ clear/ cold
	04 DEC	23:55 - 06:41	clear
12	04 DEC	17:16 - 24:36	clear/ aerosol
	05 DEC	01:23 - 24:00	clear/cirrus
	06 DEC	00:00 - 05:31	thin cirrus
13	06 DEC	14:52 - 20:33	mixed cirrus/alto cu
	07 DEC	00:54 - 05:52	clear/ aerosol/low cloud
14	07 DEC	14:49 - 21:23	low overcast/broken low

omit

AERI Observations and Analysis during FIRE/SPECTRE

W.L. Smith, R.O. Knuteson and H.E. Revercomb

(Short paper, not received in time for publication)

524-47
197524
p-3

N94-22316

ANALYSIS OF THE GOES 6.7 μm CHANNEL OBSERVATIONS DURING FIRE II

B. J. Soden[1] and S. A. Ackerman[1] D. O'C Starr[2]
Cooperative Institute of Meteorological Satellite Studies[1]
NASA Goddard Space Flight Center[2]

INTRODUCTION

Clouds form in moist environments. FIRE Phase II Cirrus Implementation Plan (August, 1990) noted the need for mesoscale measurements of upper tropospheric water vapor content. These measurements are needed for initializing and verifying numerical weather prediction models and for describing the environment in which cirrus clouds develop and dissipate. Various instruments where deployed to measure the water vapor amounts of the upper troposphere during FIRE II (e.g. Raman lidar, CLASS sonds and new cryogenic frost hygrometer on-board aircraft)

The formation, maintenance and dissipation of cirrus clouds involve the time variation of the water budget of the upper troposphere. The GOES 6.7 μm radiance observations are sensitive to the upper tropospheric relative humidity, and therefore proved extremely valuable in planning aircraft missions during the field phase of FIRE II. Warm 6.7 μm equivalent blackbody temperatures indicate a relatively dry upper troposphere and were associated with regions generally free of cirrus clouds. Regions that were colder, implying more moisture was available may or may not have had cirrus clouds present. Animation of a time sequence of 6.7 μm images was particularly useful in planning various FIRE missions. The 6.7 μm observations can also be very valuable in the verification of model simulations and describing the upper tropospheric synoptic conditions. A quantitative analysis of the 6.7 μm measurement is required to successfully incorporate these satellite observations into describing the upper tropospheric water vapor budget. Recently, Soden and Bretherton (1993) have proposed a method of deriving an upper tropospheric humidity based on observations from the GOES 6.7 μm observations. The method is summarized in the next section. In their paper they compare their retrieval method to radiance simulations. Observations were also compared to ECMWF model output to assess the model performance.

The FIRE experiment provides a unique opportunity to further verify the GOES upper tropospheric relative humidity retrieval scheme by providing

1. aircraft observations to cross-validate the calibration of the GOES 6.7 μm channel and
2. accurate upper tropospheric water vapor concentrations for verification.
3. veritical variablitity of upper tropospheric water vapor

DATA ANALYSIS

Several studies have used employed satellite observations in the 6.7 μm regime to estimate the relative humidity of the upper troposphere (Hayden *et al* 1981; Schmetz and Turpeinen, 1988; Van de Berg *et al* 1991; Soden and Bretherton 1993). This paper makes use of 6.7 μm spectral measurements made by the Visible Infrared Spin Scan Radiometer (VISSR) Atmospheric Sounder (VAS) onboard the GOES-7 satellite. The nadir resolution is approximately 16 km. Calibration of the VAS is described by Menzel *et al* (1982) and is based on comparison between satellite pre-launch tests and simulated radiance based on co-located radiosondes. These studies suggest possible biases of 1.9 °K and random noise of an individual observations of ±0.75°K.

Using the Goody random band model, assuming strongly absorbing pressure broadened lines, Soden and Bretherton (1993) demonstrated that for an atmospheric profile corresponding to a constant relative humidity and lapse rate, the 6.7 μm brightness temperature ($T_{6.7}$) varied logarithmically with the ratio of relative humidity and cosine of the viewing zenith angle. Detailed calculations of the 6. 7 m radiance using the CIMSS transmittance model suppor the presence of this relationship between T and r. Comparisons of the forward calculated $T_{6.7}$, versus

thecorresponding value of log of the normalized upper tropospheric relative indicated an rms error in using a simple retrieval of roughly 1°K or roughly 8% in terms of relative humidity.

$$\log(\bar{r} / \cos\theta) = a + bT_{6.7}$$

where, θ is the viewing zenith angle, and $\bar{r}$ is the mean upper tropospheric relative humidity. Recently we have derived a similar relationship for the HIRS/2 6.7 μm channel flown on the NOAA polar orbiting satellites (a=34.30, b=-0.125K^{-1}). The similarity in the between the HIRS/2 and GOES formulations gives us additional confidence in the theoretical foundations for this simple retrieval algorithm.

Using the above expression, the upper tropospheric relative humidity was derived over the FIRE central site for the entire field phase at 1/2 hourly time intervals. To faciliate comparison of pixel measuremnte over the FIRE site, cloud screening was performed by simply removing all estimates of $\bar{r}$ >100%.. Figure 1 is a time series plot of the $\bar{r}$. A histogram of the occurances of a given value for the entire period is shown in figure 2. Comparisons of these parameters, with observations made with the CLASS sondes and RAMAN lidar will be presented at the meeting.

REFERENCES

Hayden, C. M. and T. J. Schmit,1992: Quantitative applications of the 6 μm water vapor band measurements from satellites. Sixth Conference on Satellite Meteorology and Oceanography, Atlanta, GA, Amer. Meteor. Soc., 188-192.

Schmetz J. and O. M. Turpeinen, 1988: Estimation of upper tropospheric relative humidty field from METEOSAT water vapor image data, *J. Appl. Meteor.*, **27**, 889-899.

Soden, B. J. and F. P. Bretherton, 1993: Upper tropospheric relative humidity from GOES 6.7 μm channel method and climatology for July 1987. Accepted for publication in the *J. Geo. Res.*

Van de Berg, A. Pyomjamsri and J. Schmetz, 1991: Monthly mean upper tropospheric humidities in cloud-free areas from METEOSAT observations, *Int. J. Clim.*, **11**, 819-826.

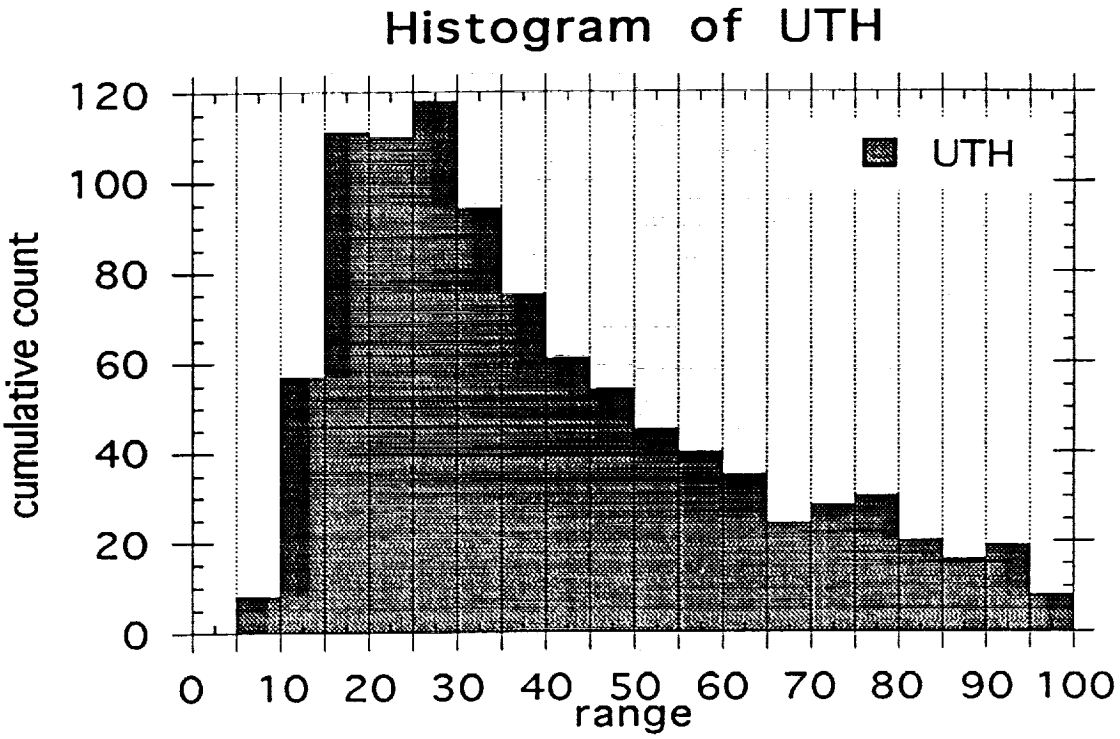
Histogram of UTH
UTH
cumulative count
range
0
20
40
60
80
100
120
0
10
20
30
40
50
60
70
80
90
100

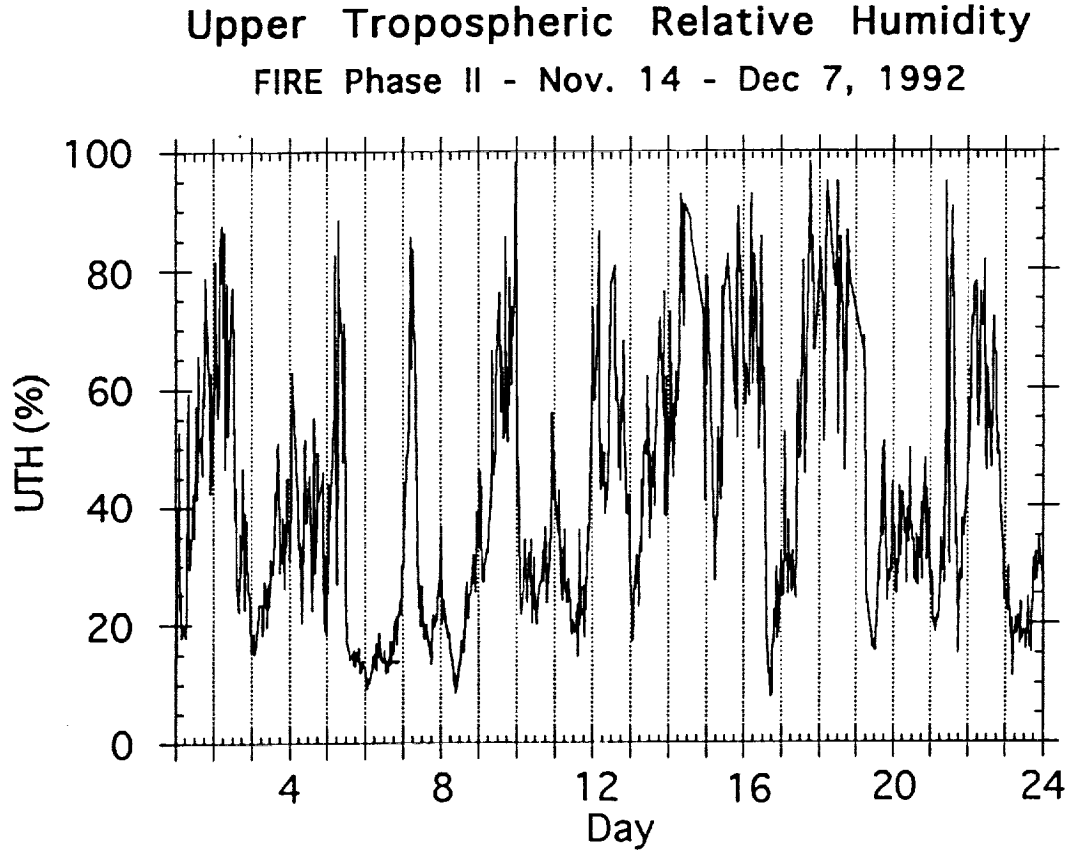
Upper Tropospheric Relative Humidity
FIRE Phase II - Nov. 14 - Dec 7, 1992
UTH (%)
Day
0
20
40
60
80
100
4
8
12
16
20
24

N94-22317
197525

As previously published in the

Combined Optical-Microwave Earth and Atmosphere Sensing Symposium 22-25 March 1993 Albuquerque, New Mexico

COMPARISON OF CLOUD BOUNDARIES MEASURED WITH 8.6 mm RADAR AND 10.6 μm LIDAR

Taneil Uttal
NOAA Wave Propagation Laboratory
325 Broadway, Boulder CO 80302

Janet M. Intrieri
Cooperative Institute for Research in the Environmental Sciences
University of Colorado, Boulder CO 80309

INTRODUCTION

One of the most basic cloud properties is location; the height of cloud base and the height of cloud top. The glossary of meteorology defines cloud base (top) as follows: "For a given cloud or cloud layer, that lowest (highest) level in the atmosphere at which the air contains a perceptible quantity of cloud particles" (1). Our studies show that for a 8.66 mm radar, and a 10.6 μm lidar, the level at which cloud hydrometers become "perceptible" can vary significantly as a function of the different wavelengths, powers, beamwidths and sampling rates of the two remote sensors.

THE EXPERIMENT

In November and December of 1991, the First ISCCP Regional Experiment II (FIRE II) was conducted in Coffeyville, Kansas for the purpose of studying cirrus clouds and their effects on planetary radiation budgets. This experiment was a large multi-organizational effort coordinated by NASA. It brought together a large number of surface, airborne, and satellite-based active and passive remote sensors.

The NOAA Wave Propagation Laboratory (WPL) brought a Doppler, 8.66 mm radar (2) and a Doppler, 10.6 μm lidar (3) and operated them side-by-side. Although both instruments have scanning capabilities, they operated primarily in a vertically pointing mode to obtain time-height cross sections of the cloud as it passed over the observation site. The radar pointed in a fixed vertical mode for 25 min of every 30 min observing period. The lidar pointed vertically and also rocked back and forth to determine periods when specular reflection might be occurring. Therefore, the lidar data was filtered in the post processing so that only the vertical beams of data were included in our analysis.

ANALYSIS

To determine echo boundaries from active, range-gated remote sensors, the NOAA/WPL radar group has developed the program CLDSTATS. This program is designed for maximum flexibility so that the user can choose different threshold criteria for determining echo boundaries. This allows CLDSTATS to operate on data sets collected by different remote sensors, as long as the data is in Common Doppler Exchange Format (4). While we have run CLDSTATS primarily on vertically pointing data, the algorithm is sensitive to elevation angle, and in theory can be run on different kinds of scans, for instance RHI scans.

The user specifies a threshold field (e.g. reflectivity), a threshold value, and a minimum number of consecutive range gates in which the threshold value must exist for the in-cloud condition to be met. To choose successful threshold values, the user must have familiarity with the instrument and it's response to backscattering targets in the atmosphere. It should be noted that CLDSTATS examines each beam of data separately, starting at a lower limit and ending at an upper limit which is also user specified. Therefore, this algorithm is a 1-D filter as opposed to similar cloud boundary detection program developed by Penn State University which imposes a 2-D filter (5).

CLDSTATS has been tested extensively on radar data, and we have settled on a thresholding criteria using the normalized coherent power field that appears to work well for all but the must tenuous cirrus clouds. Normalized coherent power is a measure of signal coherence from pulse to pulse. The lidar characterization was somewhat more difficult, since background values of lidar backscatter from aerosols were sometimes as high as in-cloud values. It was therefore necessary

to redefine the thresholding levels over even the short time intervals shown in this report.

RESULTS

For this preliminary study, we choose two days during the 1991 FIRE II project to compare cloud boundaries. On November 25, we examined a 1 h 52 min period when a thick stratus deck existed between 3 km and 9 km AGL. Figure 1 shows echo boundaries detected by the radar, and Figure 2 shows echo boundaries detected by the lidar. The radar shows a well defined boundary at both cloud base and cloud top with continuity between consecutive points. The lidar detects cloud base at the same altitude but sees a noisier boundary, with consecutive beams detecting an "in-cloud" condition separated by as much as 350 meters. The lidar echo is clearly attenuated around 6 km, well below the 8-9 km echo top detected by the radar.

These results are summarized in Figures 3 and 4 which show scattergrams of lidar versus radar bases and lidar versus radar tops, respectively. In Figure 3, it can be seen that a certain number of points lie along the 1 to 1 regression line, but the majority of points lie above it. This indicates that the lidar often detects a cloud base higher than that of the radar, sometimes by as much as 750 m. In figure 4, all of the points lie well below the 1 to 1 regression line, some by as much as 4.5 km, indicating that in optically thick clouds, the lidar can greatly underestimate the height of cloud top.

Figures 5 and 6 show radar and lidar echo boundaries for a 5.5 h period on November 26th. On this day, a high, optically thin cirrus formed at around 9 km, and slowly became thicker, with lowering bases throughout the period. The radar and lidar had good agreement on cloud bases throughout a wide range of altitudes (Figure 7). Again, there was a subset of points that lay upon the 1 to 1 regression line, as well as a significant fraction of points above this line, indicating the lidar often detected higher cloud bases, by as much a 1000 m. Figure 8, the scattergram of lidar and radar echo top heights shows a somewhat more surprising result. In this scattergram, a significant number of points lie above the 1 to 1 regression line. This indicates the lidar was seeing a *higher* echo top than the radar. This result has been demonstrated qualitatively using these same data sets by Intrieri et al., (6). They illustrate cases where 1) the lidar signal was attenuated before radar echo top, 2) the lidar detected clouds that were invisible to the radar, and 3) lidar echo tops that were higher than the radar echo tops.

DISCUSSION

There are several measurement factors that contribute to the differences in cloud boundaries detected by the two sensors. These include transmitted wavelength, transmitted power, beamwidth, sampling rate, and range gate spacing.

The effects of beamwidth, sampling rate, and range gate spacing are illustrated in figure 9 which shows a detailed look at a 30 min period. The radar has 0.5° beamwidth, and a pulse length of 37 m, so that by 10 km AGL the sample pulse volume is $\sim 2 \times 10^5$ m^3. The lidar has a narrower beam, and 75 m pulse length, and therefore the sample pulse volume is only about 60 m^3. The radar pulse repetition frequency (PRF) is 2000 Hz, and in the post processing we further average to 3 sec beams with 6000 samples. The lidar PRF is 4 Hz, and in this study there is no additional averaging in the post processing. Therefore, since the lidar does far less spatial and temporal averaging, it detects rapid, small scale variations in the cloud boundaries that are smoothed by the radar.

The situations where the radar and lidar detect extremely different boundaries, usually involving cloud top is a function of wavelength. Two general scenarios occur; either the lidar signal is attenuated before cloud top by optically thick clouds, or the lidar detects a significantly higher top where it measures backscatter from particles that are too small for the radar to detect. In the extreme case, the lidar detects an entire cloud layer that is invisible to the radar.

CONCLUSION

Clouds have many microphysical and macrophysical properties that affect weather and climate. It would seem cloud boundaries would be one

of these properties that would be the most easily observed. However, this paper has shown that the detection of cloud boundaries is not simple, and that different remote sensors can detect significantly different cloud boundaries.

This suggests that the definition of "cloud boundary" needs to be more precise, and may change depending on the application of the information used. For instance, while mm wavelength radars may be sufficient to define cloud boundaries for infrared radiation studies, it is clear that lidars are also necessary to detect very thin cirrus clouds which are important for shortwave radiation studies.

Researchers, particularly in the satellite community must use caution when using a ground-based remote sensor to establish "ground truth" for cloud boundary studies. Optimally, both sensors would be used to determine cloud boundaries for the wide variety of cases that can occur.

ACKNOWLEDGEMENTS

We would like to thank Ed Ash for making software modifications that made this analysis possible. As always, this study would not have been possible without the long hours put in by the FIRE II field crews.

REFERENCES

(1) R.E. Huschke, Editor: Glossary of Meteorology, American Meteorological Society, 1959.

(2) R.A. Kropfli, B.W. Bartram, and S.Y. Matrosov, "The Up-graded WPL dual-polarization 8 mm wavelength Doppler Radar for Microphysical and Climate Research", Proc. Amer. Meteor. Soc. Conf. on Cloud Physics, pp. 341-345, 1990.

(3) M.J. Post, and R.E. Cupp, "Optimizing a Pulsed Doppler Lidar," Appl. Opt., Vol 29, pp. 4145-4158, 1990.

(4) S.L. Barnes, "Report on a Meeting to establish a Common Doppler Radar Data Exchange Format," Bull. Amer. Met. Soc, Vol 61, pp. 1401-1404, 1980.

(5) T. Ackerman, personal communication. 1992.

(6) J.M. Intrieri, W.L. Eberhard, J.B. Snider, and T. Uttal, " Multi-wavelength Observations of a cirrus cloud event from FIRE II: Preliminary Lidar, Radar, and Radiometer Measurements", Proc. Amer. Meteor. Soc. 11th Conf. on Clouds and Precip., Vol 1, pp. 537-540, 1992.

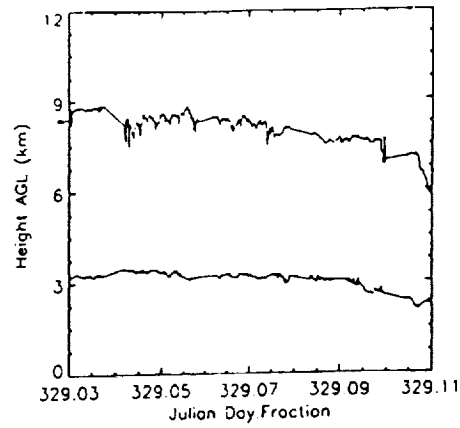

Fig.1 Radar Echo Boundaries November 25, 1991

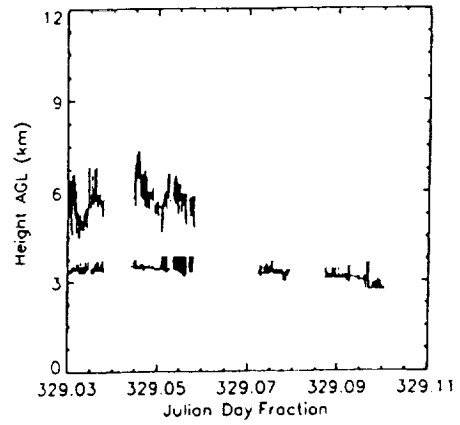

Fig.2 Lidar Echo Boundaries November 25, 1991

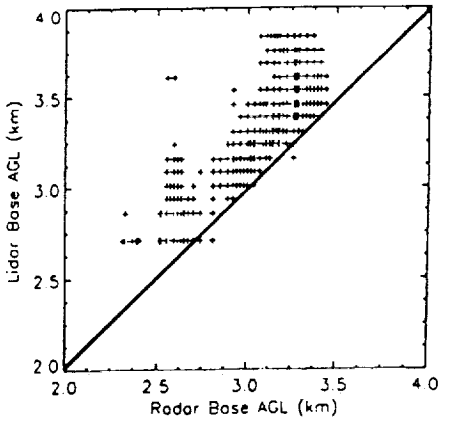

Fig.3 Lidar Base versus Radar Base November 25, 1991

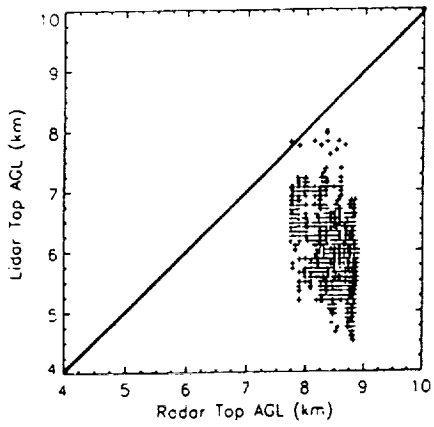

Fig.4 Lidar Top versus Radar Top
November 25, 1991

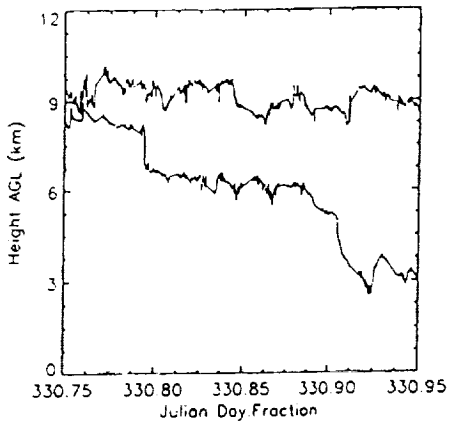

Fig.5 Radar Echo Boundaries
November 26, 1991

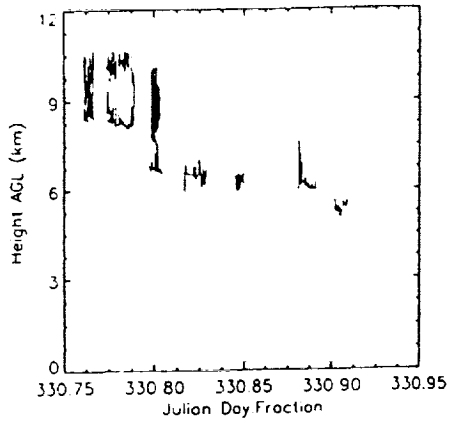

Fig.6 Lidar Echo Boundaries
November 26, 1991

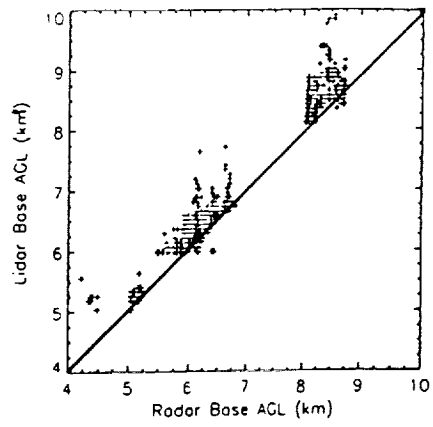

Fig.7 Lidar Base versus Radar Base
November 26, 1991

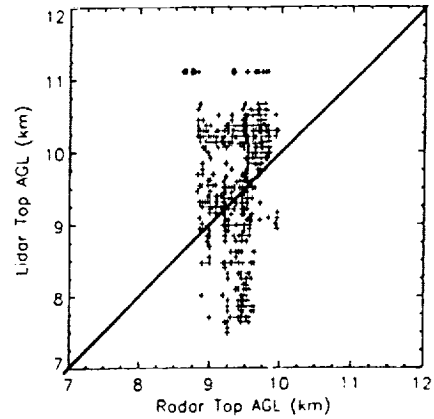

Fig.8 Lidar Top versus Radar Top
November 26, 1991

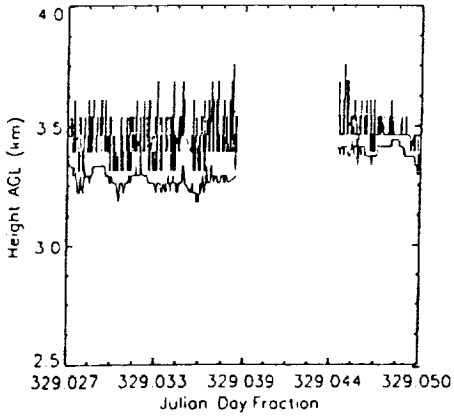

Fig.9 Detail of Radar and Lidar Base
Echoes - Radar Base offset
down 100 m for illustration

N94-22318

As previouly published in the

26th International Conference on Radar Meteorology, 24-25 May 1993, Norman, Oklahoma

526-47
197526
p. 3

CLOUD BOUNDARIES DURING FIRE II

Taneil Uttal and Scott M. Shaver
NOAA/Wave Propagation Laboratory
325 Broadway
Boulder, Colorado 80303

Eugene E. Clothiaux and Thomas P. Ackerman
Department of Meteorology
Pennsylvania State University
University Park, Pennsylvania 16802

1. BACKGROUND

Cirrus and stratus clouds are currently the subject of active research because of their importance in correctly modeling global climatic trends. Many cloud properties are of interest, including particle concentrations, size distributions, integrated ice mass path, ice mass fluxes, supercooled liquid water distributions and cloud location. Of these, cloud location would seem to be one of the simpler parameters to measure. However, Uttal and Intrieri (1993) have recently demonstrated that different range-gated remote sensors operating at different wavelengths often detect significantly different cloud boundaries. They concluded that care must be taken in choosing an appropriate combination of sensors to accurately record cloud boundary heights for a wide range of meteorological situations.

To our knowledge, previous observations of cloud boundaries have been limited to studies of cloud bases with ceilometers, cloud tops with satellites, and intermittent reports by aircraft pilots. Comprehensive studies that simultaneously record information of cloud top and cloud base, especially in multiple layer cases, have been difficult, and require the use of active remote sensors with range-gated information.

In this study, we examined a 4-week period during which the NOAA Wave Propagation Laboratory (WPL) 8-mm radar (Kropfli et al., 1990) and the Pennsylvania State University (PSU) 3-mm radar (Albrecht et al., 1992) operated quasi-continuously, side by side. By quasi-continuously, we mean that both radars operated during all periods when cloud was present, during both daytime and nighttime hours. Using this data, we develop a summary of cloud boundaries for the month of November for a single location in the mid-continental United States.

2. EXPERIMENT

The First International Satellite Cloud Climatology Project (ISCCP) Regional Experiment (FIRE) II Experiment conducted in Coffeyville, Kansas during the winter of 1991, was a large, multi-agency experiment designed to study the effects of cirrus clouds on the planetary radiation budget. During the experiment the NOAA/WPL 8-mm scanning Doppler radar and the PSU 3-mm radar pointed vertically, and collected high-resolution, range-gated data on clouds as they passed over the observation site. The WPL radar collected a beam (profile) of data every 0.25 sec, which were subsequently averaged to 3-s samples, with range-gate spacing of 37.5 m. The PSU radar collected a beam of data every 4-6 sec, which were averaged to 60-s samples, with range-gate spacing of 30 m.

To determine cloud boundaries, WPL uses a program which searches for user-defined threshold values in individual beams of data to determine in-cloud versus out-of-cloud conditions. PSU has developed an alternative cloud boundary detection algorithm that applies a box filter scheme. For each box, several pixels wide by several pixels high, the pixel in the center of the box is set to "on" for cloud or "off" for no-cloud depending on whether the total number of pixels in the box exceeds, or does not exceed a user-specified threshold. The different schemes for cloud boundary detection do not appear to produce significantly different results.

Both WPL and PSU divided information on cloud boundaries into 6-h periods for the entire experimental month. The data sets were time matched for this study to include only the 6-h periods when both sensors were operating. In this preliminary study, we have not yet corrected for short periods within a given 6-h period when the two sensors might not have been running at exactly coincident times. Also, the WPL radar always collected data from the surface up to 12 km, while the PSU radar was adjusted to bracket the clouds of interest. Occasionally, when the lowest range gate was too high, PSU lost some information on lower cloud boundaries. These factors contribute to some of the differences between radars in the following results.

3. RESULTS

Figures 1 and 2 show histograms of the frequency of occurrence of cloud base height for the WPL and PSU radars, respectively. The figures show a distinct bimodal distribution, suggesting that cloud bases tend to occur predominantly near 2.5 km and 7.5 km. Both distributions indicate that cloud base frequency is relatively low near 5 km. Clouds occurred with approximately equal frequency at stratus and cirrus levels, which is interesting because the generating mechanisms for the clouds at these two altitudes are quite different.

The WPL radar shows a third peak near the surface that is not seen is the PSU data. This peak is a result of the WPL radar operating in some heavy precipitation periods when the PSU radar shut down.

Figures 3 and 4 show histograms of the frequency occurrence of cloud top. Cloud top distributions are less centralized for lower level clouds which are more convective, but still show a well defined peak at near 8.5 km for the cirrus clouds which are less convective and often capped by the tropopause. The cloud top peak is slightly higher for the WPL radar (9 km) when compared to the PSU radar (8.3 km), and skewed towards higher altitudes, This is indicative of the fact that the 3-mm radar occasionally is attenuated before reaching cloud top. Figures 5 and 6 show histograms of cloud thickness from the WPL and PSU radars, respectively. Cloud thickness appears to be about 1.0 to 1.3 km on average.

Makhover and Nudelman (1989) report average cirrus bases and tops over the European Soviet Union at 7 and 9 km, respectively, with very little annual variation. These are in good agreement with our results.

4. DISCUSSION

This study is unique in that it was not limited by cloud thickness and/or multiple layer cases, and achieved information on both cloud bases and cloud tops simultaneously. Future work with this data set will include examining diurnal effects, differences between precipitating and non-precipitating cases, and the generation of separate statistics for the stratus and cirrus clouds.

5. ACKNOWLEDGEMENTS

The authors extend their thanks to the FIRE II field crews who collected this data. The WPL research was funded by the NOAA Office of Climate and Global Change, and the PSU research was funded by NASA Grant NAG-1-1095 and DOE ARM Grant DE-FG0290ER61071. E.E. Clothiaux is supported by an appointment to the Global Change Distinguished Postdoctoral Fellowships sponsored by the U.S. Department of Energy, Office of Health and Environmental Research, and administered by Oak Ridge Associated Universities.

6. REFERENCES

Albrecht, B.A., T.P. Ackerman, D.W. Thomson, M.A. Miller, and R.M. Peters, 1992: A surface based cloud observing system. Proceedings of the 11th International Conference on Clouds and Precipitation, 17-21 August, Montreal, Canada, ICCP/IAMAP, pp 935-937.

Kropfli, R.A., B.W. Bartram, and S.Y. Matrosov, 1990: The upgraded WPL dual-polarization 8.6 mm doppler radar for microphysical and climate research. Proceedings of the Conference on Cloud Physics, 23-27 July, San Francisco, CA, AMS, Boston, MA, pp 341-345.

Makhover Z.M. and L.A. Nudelman, 1989. Upper Level Clouds in Radiative Properties of Cirrus Clouds, NAUKA, Moscow (in Russian).

Uttal T. and J.M.Intrieri, 1993: Comparison of cloud boundaries measured with 8.6 mm radar and 10.6 μm lidar, Proceedings of the Combined Optical-Microwave Earth and Atmosphere Sensing Symposium, 22-25 March, Albuquerque, NM, IEEE, Piscataway, NJ.

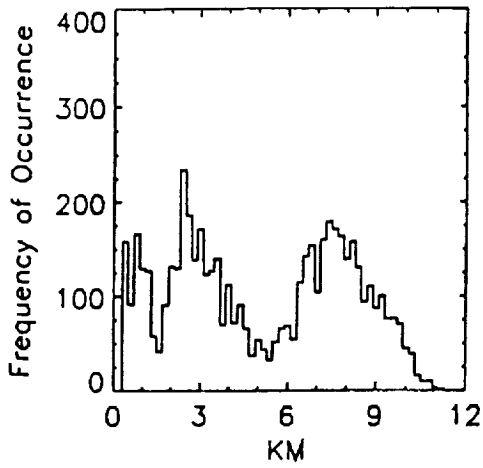

Figure 1. WPL cloud base frequency distribution

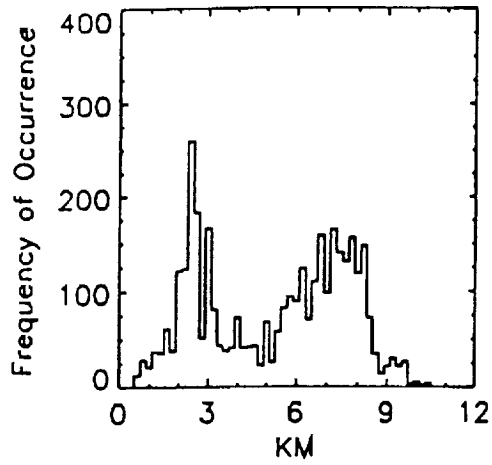

Figure 2. PSU cloud base frequency distribution

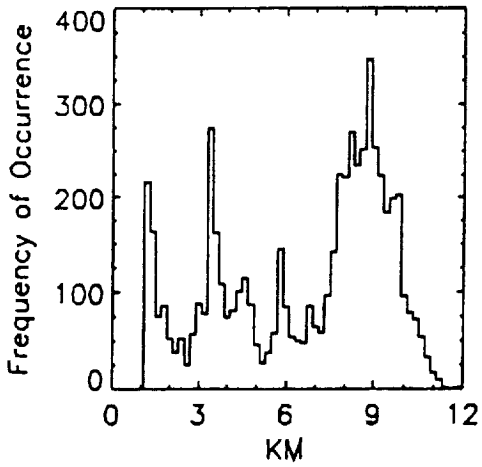

Figure 3. WPL cloud top frequency distribution

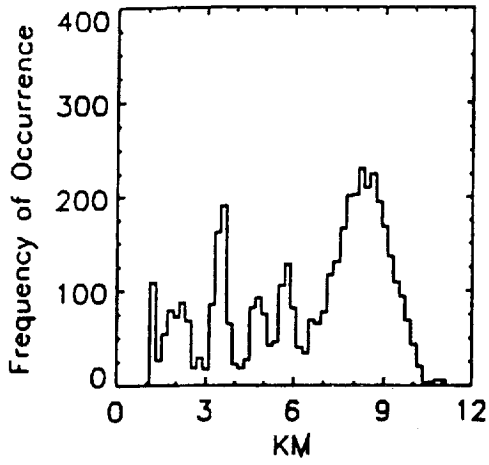

Figure 4. PSU cloud top frequency distribution

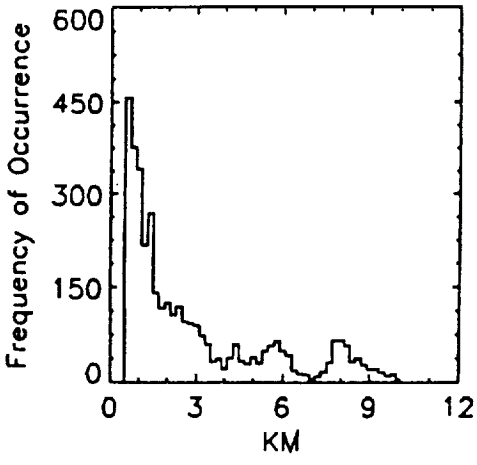

Figure 5. WPL cloud thickness frequency distribution

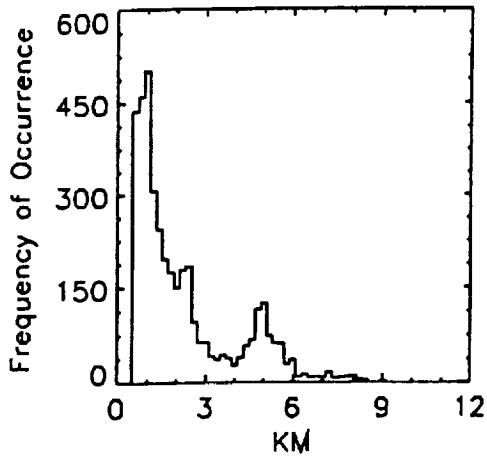

Figure 6. PSU cloud thickness frequency distribution

omit

(Talk)

Visible/Infrared Radiative Relationships in Cirrus as seen by Satellite and Scanning Lidar

Donald Wylie
Walt Wolf
Edwin Eloranta
University of Wisconsin-Madison
Madison, Wisconsin 5371

The ratio of the visible scattering of solar radiation to the attenuation of terrestrial radiation in clouds of various types is crucial to the understanding of the role of the clouds in the heating or cooling of the atmosphere. Cirrus clouds can either heat or cool the atmosphere depending on whether the visible scattering is stronger or weaker than the attenuation of infrared radiation. The visible/infrared relationships of cirrus clouds are not constant but can vary in different forms of cirrus. The combination of the Volume Imaging Lidar (VIL) and High Spectral Resolution Lidar (HSRL) with satellite infrared sensors, allowed an opportunity to quantify the visible-infrared relationships on small spatial scales that are caused by variations of the form of the cirrus cloud fields.

The VIL can provide a very detailed visible image. The combination of the VIL with the High Spectral Resolution Lidar (HSRL) allows quantitative interpretation of the VIL image as an image of the visible optical depths of the clouds. The HSRL is well known for its ability to measure visible optical depths of semi-transparent clouds. However, large spatial variances in clouds have made comparisons between lidar and satellite data very difficult. The use of the VIL removes the need for assuming that clouds are non-variant in the cross-wind direction which has been necessary in past lidar-satellite comparisons. The VIL clearly shows that cirrus clouds are highly variant in the cross wind direction. With the VIL the cloud visible radiative properties were calculated over the large field of view of satellite Infrared sensors to form an accurate comparison of visible-infrared relationships.

The visible-infrared comparisons are being made for two data sets where VIL and HSRL data were simultaneously obtained. The first data set came from pre-FIRE-II in a test of the two lidars. The second is from December 4 of FIRE-II. These data sets are being used to establish the variance of the visible-Infrared relationships on the scale of the clouds. Our first result has shown large variances in the visible-infrared relationship correlated with different forms of cirrus, cells, bands and multiple layered areas.

527-43
197527
N94-22379

Ground–Based Passive Remote Sensing During Fire IFO II

Peter Pilewskie and Francisco PJ Valero

NASA Ames Research Center, Moffett Field, CA

During the FIRE Cirrus IFO II, a set of passive radiometers were deployed at the Coffeyville, Kansas, Hub, site B, to compliment the Radiation Measurement System (RAMS) on board the NASA ER–2 and NCAR Sabreliner. The following three instruments were used at the surface:

1. Narrow–field–of View IR Radiometer (NFOV): The NFOV is a 10.5 μm (1 μm bandwidth) radiance measuring device, using a liquid nitrogen cooled blackbody reference. Brightness temperature is obtained from the radiance. The NFOV had an 8° field of view and was zenith–pointed.

2) Total–Direct–Diffuse Radiometer (TDDR): The TDDR is a seven channel visible and near–infrared radiometer with rotating shadow bands to separate the direct and diffuse components of the solar flux. The narrow (10 nm) bands are located outside atmospheric absorption bands, isolating the optical effects due to aerosols or clouds. The TDDR was pointed in the zenith direction at site B in Coffeyville, its primary purpose to obtain cirrus spectral optical thickness.

3) Near–Infrared Spectroradiometer (NIRS): The NIRS measures continuous transmission between 0.8 μm and 1.8 μm with a 10 nm resolution. Near–infrared measurements are very sensitive to microphysics and so are used to infer cloud phase and particle size, along with optical thickness. The NIRS was pointed towards the zenith, and had a 1 mrad field of view.

A time series of reduced surface radiation data is shown in Figure 1 for the November 26, 1991, case study. The upper panel shows the 10.5 μm brightness temperature derived from the NFOV. The middle panel shows 0.5 μm and 1.64 μm optical thickness from TDDR measurements. The lower panel shows the ratio, R, of transmission at 1.64 μm to that at 1.25 μm (detector response has not been removed) using the NIRS. Methods for deriving cloud properties, such as phase and particle dimension, from these data will be discussed.

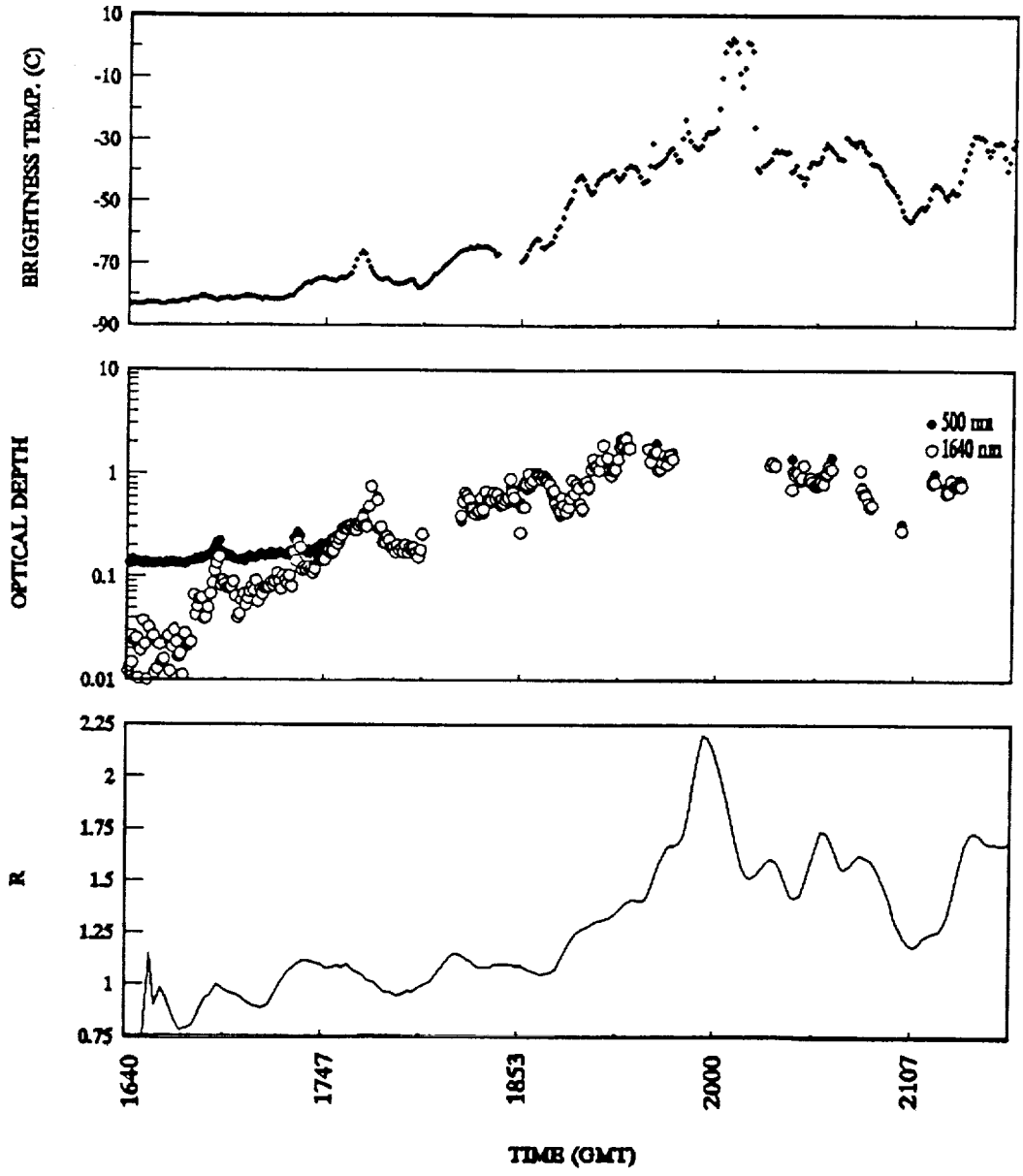

Figure 1. Time series of surface radiation measurements from the Coffeyville Airport Hub, site B, on November 26, 1991. The lower panel shows the ratio of 1.64 μm transmission to 1.25 μm transmission. This quantity is sensitive to both water phase and particle size.

S28-47
N94-22320

COMPARISONS OF DOWNWELLING RADIATION TO MODEL PREDICTIONS BASED ON GROUNDBASED MEASUREMENTS DURING FIRE'91

S.Kinne and R.Bergstrom NASA-Ames, Moffett Field, CA 94035

T.Ackerman Pennsylvania State, University Park, PA 16802

J.DeLuisi NOAA, Boulder, CO 80303

ABSTRACT. Surface radiation measurements and simultaneous ground-based measurements of the atmosphere during the FIRE'91 cirrus field experiment provided an opportunity to identify crucial measurements and parameterization deficiencies in current cloud-radiation models.

Comparisons between measured and calculated broadband surface fluxes with only a small data subset already reveal these needs:
(1) accurate humidity and aerosol vertical profiles for clear cases,
(2) accurate vertical extinction profiles and dimensions for clouds,
(3) understanding of the (solar) scattering properties of cirrus.

1. INTRODUCTION

The recent FIRE'91 cirrus field experiment provided an unique opportunity to validate atmospheric models. Concentrating on the radiative transfer modeling aspect - by comparing measured downward fluxes at the surface to modeled fluxes - we like to address the questions: 'How well can simple models simulate radiative properties of the atmosphere?' and 'How well can models translate directly and indirectly measured atmospheric properties into radiative fluxes?'.

The radiative transfer model is described first. The employed data are introduced next. Finally, comparisons for cloud-free and cloudy cases, in particular cirrus clouds cases, are discussed.

2. MODEL

Radiative transfer calculations of hemispheric downward broadband fluxes are based on a four-stream code at eight solar wavelengths and on a two-stream code at twelve infrared wavelengths, as the entire spectrum has been subdivided into twenty bands. Absorption by atmospheric gases in these bands is expressed via exponential sum-fitting and based on the HITRAN-database. Although the selection of radiative method, spectral resolution and absorption approximation can notably affect calculated fluxes, the chosen model is found to be sufficiently accurate. Deviations of surface broadband fluxes to values based on more accurate models and/or spectral resolution (less than 4%) are found to be small compared to the measurement errors. In all these models horizontal homogeneity has been assumed. This assumption, which is particularly poor for many cloud conditions, can create significant deviations between measured and calculated fluxes. To reduce errors due to the observed inhomogeneity only average flux values for time-periods of at least five minutes are used.

3. DATA

In-situ measurements and simultaneous remote sensing methods during the FIRE'91 field experiment characterized the atmosphere. Only those measurements are listed that are used in our study:

(1) Vertical profiles of atmospheric variables (e.g. temperature, humidity) are defined by up to 3 hour frequent NOAA radiosonde launches. For times between launches interpolations are used.

(2) Cloud properties are based on remote sensing data from the ground, including the Penn State University 94 Ghz radar for cloud dimensions and 10-channel sunphotometer for cirrus cloud optical depths. Ice cloud particles from the FIRE'86 cirrus experiment are adopted, as FIRE'91 data were not available yet.

(3) Downward hemispheric broadband solar and infrared fluxes are provided by Eppley radiometers of the Penn State University, and also by NOAA radiometers, employed as part of SPRECTRE.

Measurements (1) and (2) provide the input to the model. Calculated downward broadband surface fluxes, are compared to measurement (4).

4. COMPARISONS

Comparisons between measured and calculated fluxes carry a combination of model related errors, which are generally small, and an uncertain contribution of data related errors. Flux comparisons for four clear and four cloudy days are given in Figures 1 and 2.

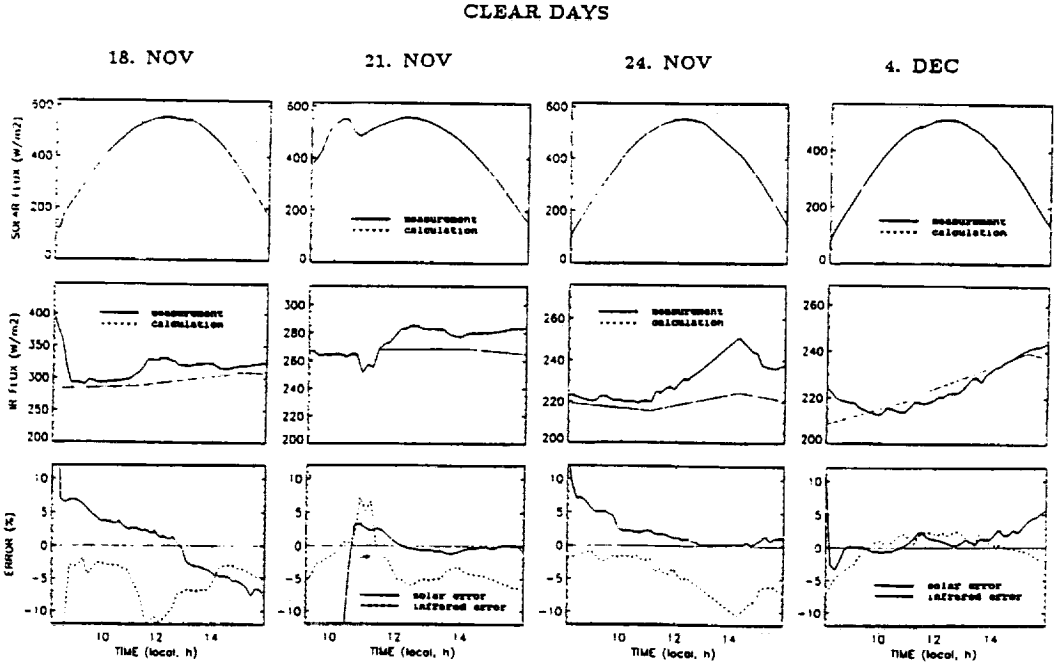

Figure 1. Comparison of measured and modeled hemispheric broadband downward solar and infrared fluxes on four cloud-free days. Errors (in %) for solar and infrared fluxes are given in the lower panels.

Clear sky flux comparisons are based on ten minute averages. For the solar spectral region, deviations of less than 5% are even smaller than expected from instrumental error analysis. For the infrared spectral region clear-sky deviations are larger, in part due to inaccurate humidity data, as radiosonde launches are sparse.

Cloudy sky flux comparisons are based on five minute averages. Average values reduce effects from often observed cloud horizontal inhomogeneities and from the lack of instrumental co-location. For the solar spectral region large deviations are found for situations involving optically thick clouds, as optical depths are uncertain. Under cirrus conditions (e.g. Dec.5), systematically higher modelled transmissions indicate solar asymmetry-factors smaller than 0.75. For the infrared region the good agreement of less than 10 W/m2 mainly reflects an accurate height positioning for the clouds base.

5. CONCLUSION

Simple radiation models can reasonably well reproduce surface fluxes under clear-sky conditions. However, the schemes frequently fail to reproduce surface fluxes for cloudy conditions, mostly due to insufficient information about cloud microphysics and structure.

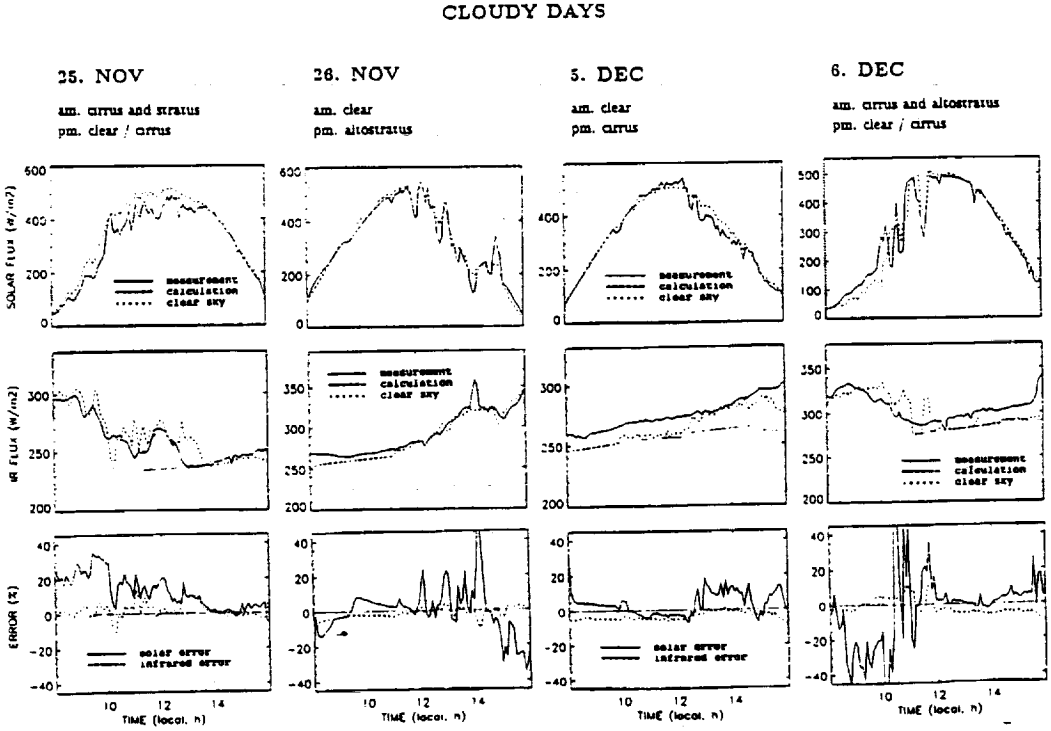

Figure 2. Comparison of measured and modeled hemispheric broadband downward solar and infrared fluxes on four (partly-) cloudy days. Corresponding flux errors and general cloud conditions are shown.

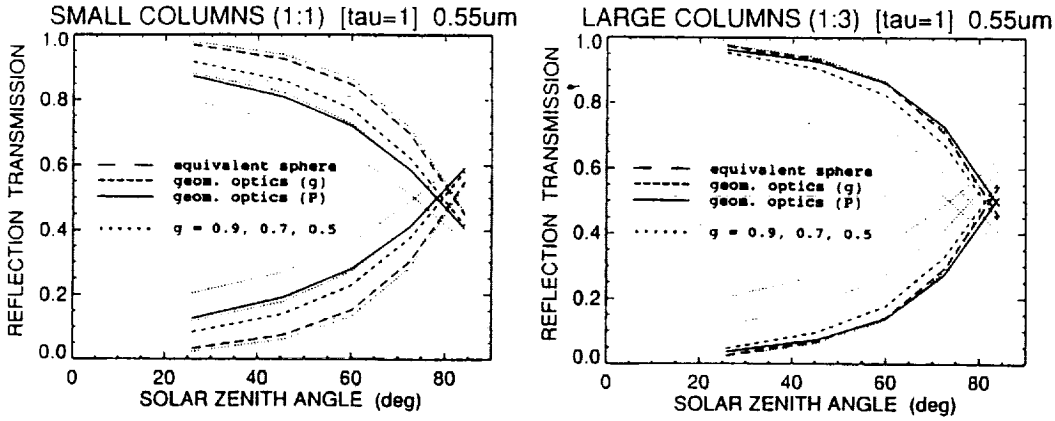

Figure 3. Comparison of reflection and transmission from different assumptions to single scattering properties of ice-crystal columns.

Particular disturbing is the current inability to model solar scattering of ice crystals. The results suggest asymmetry-factors of 0.70-0.75, which is lower than theoretical calculations on columns suggest (Takano et al., 1989). However, ice crystals are typically more complex, and often contain cavities (e.g., Milosevitch et al., 1992). New theoretical studies (e.g., Macke 1992) are encouraging. The use of asymmetry-factor in place of accurate phasefunctions in the model seems to lead to too much solar transmission, especially for smaller particles (Figure 3, also Fu et al., 1993) and may have contributed to the discrepancy in the flux comparison. Consequently, nonspherical single scattering corrections should be reevaluated.

This study reflects only an initial comparison with limited data-sets. The incorporation of more data, which were unavailable at this time for model calculations is in progress. This includes the use of in-situ cloud microphysical measurements (e.g. NCAR aircraft and balloon sondes) and additional ground based remote sensing data (e.g., NASA-Ames solar direct/diffuse and infrared radiometers, AFGL full sky camera, NOAA microwave radiometer and radar data).

REFERENCES

Fu Q. and Y. Takano
On the limitation of using the asymmetry factor for radiative transfer involving cirrus clouds. Atmos. Res., in press, 1993.

Macke, A.
Scattering of light by arbitrary shaped ice particles. Appl. Opt. in print 1992.

Miloshevich, L.M., A.J. Heymsfield, P.M. Norris
Microphysical measurements in cirrus clouds from ice crystal replicator sondes launches during Fire II. 11th Intern. Conf. on Clouds and Precip. Proceed. 1 525-528, 1992.

Takano, Y. and K.-N. Liou
Solar radiative transfer of cirrus clouds. Part 1: Single scattering and optical properties of hexagonal ice crystals. J. Atmos. Sci. 46, 3-19, 1989.

S29-47
N94-22321

Spectral Variation of Scattering and Absorption by Cirrus

by Paul F. Hein, John M. Davis, and Stephen K. Cox

Department of Atmospheric Science
Colorado State University
Fort Collins, CO 80523

1. Introduction

The impact of cirrus clouds on the radiative budget of the earth depends on the microphysics and scattering properties of the clouds. Cirrus clouds have been especially difficult to observe because of their high altitude and complex tenuous structure. Observations by Abakumova *et. al.* (1991) show that the near infrared wavelengths are more sensitive to the cirrus cloud properties than the shorter ultraviolet wavelengths. Anikin (1991) was able to show that collimated spectral measurements can be used to determine an effective particle size of the cirrus clouds. Anikin (1991) also showed that the effect of scattering through cloud causes the apparent optical depth of a 10° field of view pyrheliometer to be roughly half the actual optical depth. Stackhouse and Stephens (1991) have shown that the existence of small ice crystals do dramatically affect the radiative properties of the cirrus, though observations taken during the 1986 FIRE were not totally explained by their presence.

2. The Modelling Study

A forward Monte Carlo model, described by Davis *et. al.* (1979), was used to model the spectral variation of scattering and absorption by a cirrus cloud layer. Runs of the model were performed at four wavelengths (0.45, 0.70, 0.94, 1.38 m), for three optical depths of τ(0.70 m) = 1, 2, 3 using the equivalent sphere ice particle distributions of C5 (Deirmendjian, 1975), C6 (Deirmendjian, 1975), and CI175 (Griffith *et. al.*, 1980). The distributions are shown in Figure 1. Model irradiances were calculated for a 10° field of view, a zenith of 60° and a cloud positioned between 8 to 10km to allow comparison with pyrheliometric observations.

Figures 2, 3 and 4 show modeled ratios of cloudy to clear sky irradiances (for a 10° field of view) at 0.45, 0.70, 0.94, and 1.38 m. This ratio normalizes the data to the clear sky case. A distinct difference in spectral variation of irradiance ratios between the large particles of the CI175 size and the small particles of the C5 and C6 distributions is seen. In the CI175 distribution the magnitude of the slope of the irradiance ratio versus optical depth decreased with increasing wavelength (with the exception of the 0.70 m data), while for the small particle distributions the opposite was the case. The steepest slope of the ratio lines was seen in the C5 distribution, which contained the smallest particles. The results are summarized in Table 1. The nearly identical slopes of the 0.45 m irradiance ratios result from the method chosen to present the data. Since the ratios are approximately equal to transmittance values, the slopes of the 0.45 m irradiance ratio lines on the log plot are approximately equal to $-\sec(60°)\log_{10}(e)$.

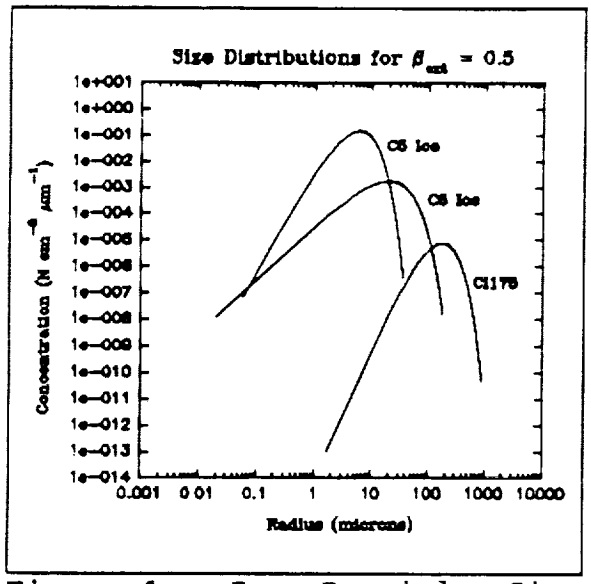

Figure 1 Ice Particle Size Distributions.

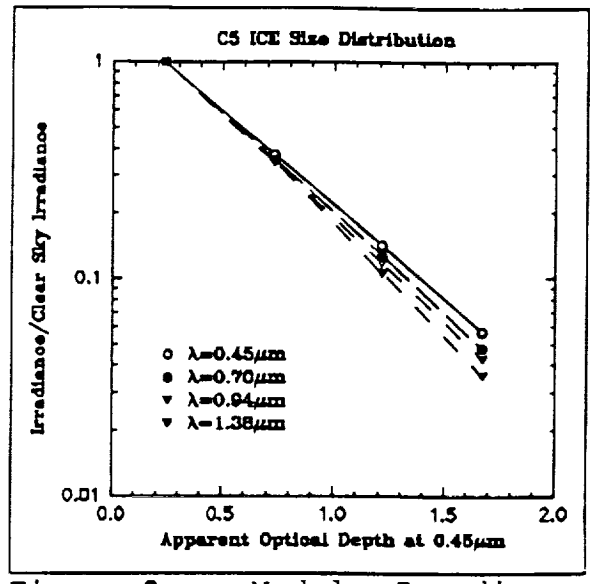

Figure 2 Model Irradiance Ratios from C5 Distribution.

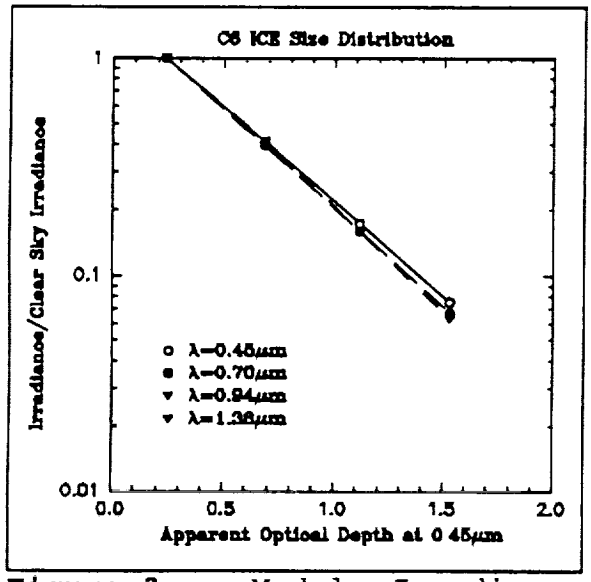

Figure 3 Model Irradiance Ratios from C6 Distribution.

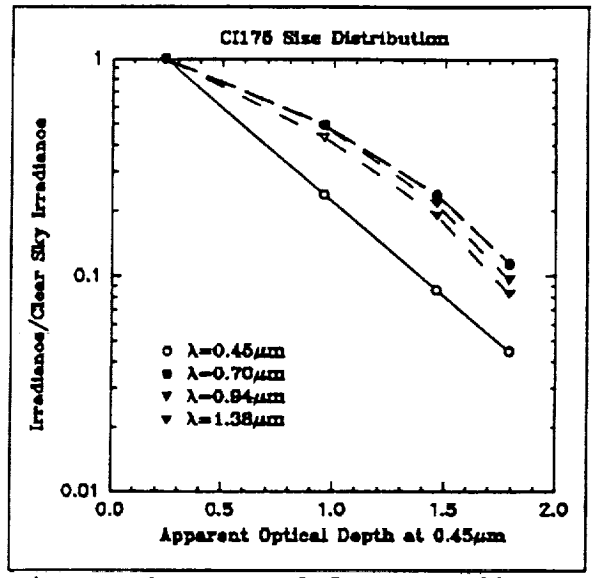

Figure 4 Model Irradiance Ratios from CI175 Distribution.

3. Pyrheliometer Observations

Simultaneous filtered and unfiltered pyrheliometric measurements were taken at Parsons, KS during the FIRE II Cirrus IFO. Longpass 0.53-2.8 m, 0.695-2.8 m and 1.0-2.8 m filters were used. On 26 November 1991, from about 1700 UTC through sunset (about 2300 UTC), the cirrus layer slowly thickened and lowered. The cirrus was too inhomogeneous to allow for a direct comparison between the filtered measurements which were about 23 seconds apart, so the apparent optical depth deduced from measurements by the unfiltered pyrheliometer was used to stratify the filtered data as a function of optical depth so that a comparison would be

possible. From the medians of each interval of the filtered irradiances (corrected to a 60° zenith), irradiance values, normalized to clear sky, were calculated for the 0.28-0.53 m, the 0.53-0.695 m, the 0.695-1.0 m, and the 1.0-2.8 m spectral region.

Figure 5 displays these observations in a format similar to the model results shown in Figures 2, 3 and 4. The slopes of the lines are generally consistent with those from the small particle calculations, suggesting that the cirrus clouds observed on 26 November 1991 did contain small ice crystals. Adding a volcanic aerosol layer to the model, did not significantly affect the model results.

Table 1. Size Distribution Parameters and Irradiance Ratio Regression Line Slopes.

		$\beta_{ext}(0.70\ m) = 0.5$		Irradiance Ratio Regression Line Slopes			
Size Distribution	Modal Radius (m)	Concentration (cm^{-3})	Ice Water Content ($g\ m^{-3}$)	0.45 m	0.70 m	0.94 m	1.38 m
C5	5	1.1196	0.0030	-0.8686	-0.9203	-0.9577	-1.0108
C6	20	0.0651	0.0150	-0.8686	-0.9073	-0.9280	-0.9280
CI175	175	0.0015	0.0851	-0.8686	-0.5921	-0.6794	-0.6378
Observations from 26 November 1991				0.28-0.53 m	0.53-0.695 m	0.695-1.0 m	1.0-2.8 m
				-0.8686	-1.6363	-1.4534	-1.0598

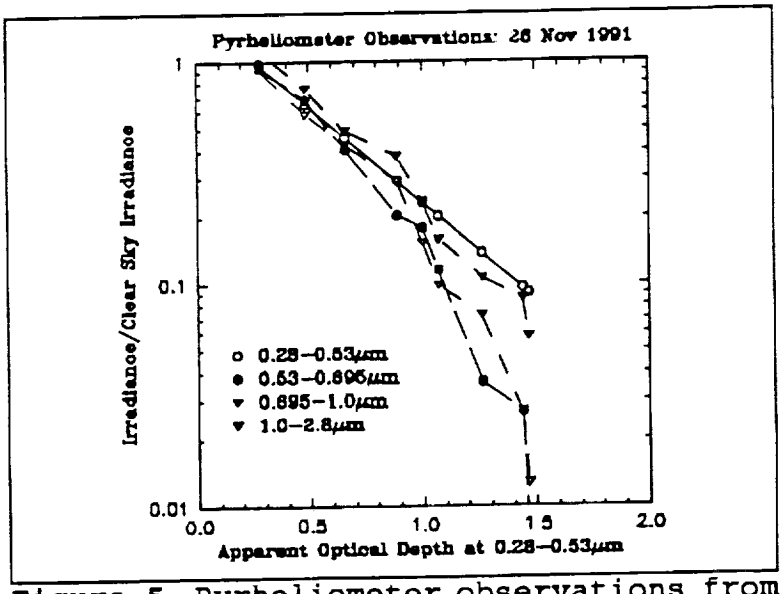

Figure 5 Pyrheliometer observations from 26 November 1991.

Acknowledgments. This research has been supported by The Office of Naval Research under Contract No. NOOO14-91-J-1422, P00002, and the National Aeronautics and Space Administration under Grant NAG 1-1146.

References

Abakumova, G.M., T.V. Yevnevich, Ye.I. Nezval', O.A. Shilovtseva and Ye.V. Yarkho, 1991: Effect of high clouds on the scattered and total radiation in different sections of the spectrum. *Izvestiya*, **27**, 654-662.

Anikin, P.P., 1991: Determination of the spectral optical thickness and effective particle size of cirrus clouds. *Izvestiya*, **27**, 673-680.

Davis, J.M., S.K. Cox and T.B. McKee, 1979: Total shortwave radiative characteristics of absorbing finite clouds. *J. Atmos. Sci.*, **36**, 508-518.

Deirmendjian, D., 1975: Far-infrared and sub-millimeter wave attenuation by clouds and rain. *J. Appl. Meteor.*, **14**, 1584-1593.

Griffith, K.T., S.K. Cox and R.G. Knollenberg, 1980: Infrared radiative properties of tropical cirrus clouds inferred from aircraft measurements. *J. Atmos. Sci.*, **37**, 1077-1087.

Stackhouse, P.W., Jr. and G.L. Stephens, 1991: A theoretical and observational study of the radiative properties of cirrus: results from FIRE 1986. *J. Atmos. Sci.*, **48**, 2044-2059.

530-47
197530
N94-22322

SPECTRAL EMISSIVITY OF CIRRUS CLOUDS

Beck, Gordon H., Davis, John M. and Cox, Stephen K.

1. Introduction

The inference of cirrus cloud properties has many important applications including global climate studies, radiation budget determination, remote sensing techniques and oceanic studies from satellites.

Data taken at the Parsons, Kansas site during the FIRE II project are used for this study. On November 26 there were initially clear sky conditions gradually giving way to a progressively thickening cirrus shield over a period of a few hours. Interferometer, radiosonde and lidar data were taken throughout this event.

Two techniques are used to infer the downward spectral emittance of the observed cirrus layer. One uses only measurements and the other involves measurements and FASCODE III calculations. FASCODE III is a line-by-line radiance/transmittance model developed at the Air Force Geophysics Laboratory.

2. Instrumentation

The infrared interferometer employed in this study is a dual port emission Michelson interferometer manufactured by Bomem, Inc. It has an adjustable resolution ranging from 1 cm-1 to 128 cm-1; the FIRE II data were taken with the interferometer at the 1 cm-1 setting. The detector is liquid nitrogen cooled and has a useful range from 500 cm-1 to 2000 cm-1.

The spectral range used for this investigation extends from 740 cm-1 to 1260 cm-1. This range includes all of the atmospheric window and reaches beyond it's edges (see fig.1). The edge of the CO_2 absorption band is apparent on the low wavenumber end and the edge of the H_2O absorption region is apparent on the other.

3. Methodology

Two techniques are developed for inferring the infrared emittance of cirrus layers from surface-based interferometer measurements. The first technique is the observational method. This method requires interferometric clear sky and cirrus sky spectra, lidar returns and radiosonde data. The second technique is the semi-empirical method. The semi-empirical method uses FASCODE III calculations, clear sky interferometer spectra, lidar returns and radiosonde data.

The effects of scattering were ignored for the FASCODE calculations. The scattering of IR radiation by air molecules is negligible although the scattering caused by aerosols falls into the Rayleigh regime and for cloud droplets or ice crystals it enters the Mie regime, however, the absorption and emission by these larger particles is far more significant than any effect of scattering.

The effects of reflection are ignored for the calculations of the emittance and transmittance of the cirrus.

3.1 Observational technique

In the observational technique interferometric data obtained just before the onset of the cirrus are used with the data obtained following the advancement of the cirrus shield overhead. The data used for this analysis were taken at 1610Z and 2005Z respectively Nov. 26 (see fig.1). The effective radiance from the cirrus cloud is found by spectral differencing, i.e. the cirrus sky radiance minus the clear sky radiance. Using a simple 3 layer model (see fig.2), the equations for the cirrus sky radiance and the clear sky radiance are as follows:

$$(1)\quad N_{mcld} = N_l + N_{cld}\,T_l + N_u\,T_{cld}\,T_l$$
$$(2)\quad N_{mclr} = N_l + N_{clr}\,T_l + N_u\,T_{clr}\,T_l$$

where N_{mcld}: measured radiance at the surface with cirrus present
N_{mclr}: measured radiance at the surface with clear sky
N_l : radiance from the atmosphere below the cirrus layer
N_{cld} : radiance from the cirrus layer with the cloud present
N_{clr} : radiance from the cirrus layer if it were clear
T_l : transmittance of the atmosphere below the cirrus layer
N_u : radiance from the atmosphere above the cirrus layer
T_{cld} : transmittance of the cirrus layer with the cloud present
T_{clr} : transmittance of the cirrus layer if it were clear

The layer radiances are as would be seen at the respective lower boundary of the layer looking upward with no effects from outside that layer.

For spectral differencing, equation (2) is subtracted from equation (1) to obtain the effective downward radiance from the cirrus cloud:

$$(3)\quad N_{eff} = N_{mcld} - N_{mclr} = [(N_{cld} - N_{clr}) - N_u\,(T_{clr} - T_{cld})]\,T_l$$

In equation (3), the effective downward radiance N_{eff} (see fig.3) is the composite of two terms multiplied by the transmittance (T_l) of the sub-cloud layer. $N_{cld} - N_{clr}$ represents the increase in radiance from the cirrus layer with the cloud present. The $N_u\,(T_{clr} - T_{cld})$ term represents the decrease in the radiance (N_u) from above the cirrus layer due to the decrease in transmittance of the cirrus layer when the cloud is present, as seen from the base of the cloud layer. An effective emittance (see fig.4) may be found via equation (4), again ignoring reflection:

$$(4)\quad E_{eff} = N_{eff} / B_{cld}$$

B_{cld} is the Planck function of the cirrus layer temperature. The cloud base temperature determined from lidar and sounding data was used for this study.

3.2 Semi-empirical technique

Interferometric cirrus sky spectra taken at 2005Z were used in this application. The sounding data used to initialize FASCODE was from a sonde launched at 1936Z. The sonde travelled through the cirrus layer from 2000Z to 2015Z according to lidar data which showed the cirrus layer extending from 6.5 km to 10 km. Restating equation (1) from the previous page:

$$(5)\quad N_{meld} = N_l + N_{cld}\, T_l + N_u\, T_{cld}\, T_l$$

In equation (5), N_l, T_l and N_u can be calculated using FASCODE with the available sounding data. This leaves two unknowns, N_{cld} and T_{cld}. Since we are ignoring the effects of reflection:

$$(6)\quad E_{cld} = 1 - T_{cld}$$

E_{cld} is the emissivity of the cirrus layer. Since the radiance from the cloud layer is given by (E_{cld} * B_{cld}), using equation (6):

$$(7)\quad N_{cld} = B_{cld}\,(1 - T_{cld})$$

Substituting equation (7) into equation (5):

$$(8)\quad N_{meld} = N_l + B_{cld}\,(1 - T_{cld})\, T_l + N_u\, T_{cld}\, T_l,$$

And solving for the cirrus layer transmittance T_{cld}:

$$(9)\quad T_{cld} = (N_{meld} - N_l - B_{cld}\, T_l) / [(N_u - B_{cld})\, T_l]$$

After solving for the transmittance, the radiance of the cirrus layer may then be found using equation (7). This is the downward radiance from the cirrus as would be observed at the lower boundary of the layer (see fig.5) excluding any effects from above the layer. The emittance (see fig.6) of the cirrus layer may then be found using equation (6).

3.3 Comparison of the two techniques

A direct comparison of these two methods can be made by normalizing the cirrus layer properties found with the semi-empirical method. Since the information found in the semi-empirical method is for the cirrus layer exclusively, equation (3) may be applied to deduce a simulated finite difference radiance, i.e., to simulate the radiance as seen by the surfaced-based inteferometer. N_u and T_l were previously found with FASCODE in the semi-empirical method, then N_{cld} and T_{cld} were found. By using FASCODE to calculate the radiance (N_{clr}) and transmittance (T_{clr}) of the cirrus layer if it were clear, all the information needed to solve for the effective radiance is available. Finally, a direct comparison may be made by solving for the resulting effective emittance (see figs.7 and 8) via equation (4).

4. Conclusions

The radiance curves deduced from the two methods are very similiar. The observational method (see fig.3) yielded an integrated radiance of 6.31 W m-2 sr-1 and the semi-empirical method (see fig.7) 6.50 W m-2 sr-1. A comparison of the emittances also shows very similiar structure. The spectrally averaged emittance from 740 cm-1 to 1260 cm-1 for the observational method (see fig.4) is 0.3537 while the average emittance for the semi-empirical method (see fig.8) is 0.3542 although the semi-empirical method yielded higher values throughout most of the window. These higher values were offset by the near zero values caused by noise in the nearly opaque water vapor absorption lines in the high wavenumber end of the spectrum and resulted in the average emissivity values being nearly identical.

A main source for discrepancy between the two datum is that the interferometric data and the FASCODE output are not processed in precisely the same manner. The numerical equivalent of the apodization used for the FASCODE analysis is currently under study. Another source of uncertainty is that the interferometer atmospheric data are taken within a period of about 2 minutes, while the sounding data used for FASCODE simulations isn't exact since it takes over an hour to acquire data and also drifts away from the launch site as a function of time.

5. Acknowledgments

This research has been supported by the National Aeronautics and Space Administration under Grant NAG 1-1146 and the Department of Energy, Contract No. DE-FG02-90ER60970.

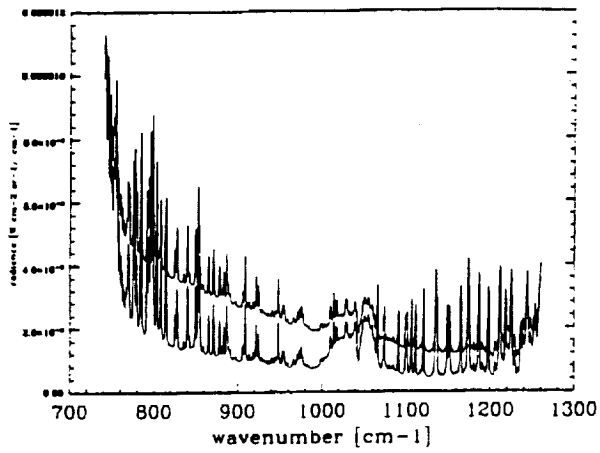

Fig.1. Comparison of the spectral radiance seen by the surfaced-based interferometer for clear sky (lower curve) and cirrus sky (upper curve) taken on Nov. 26 at Parsons.

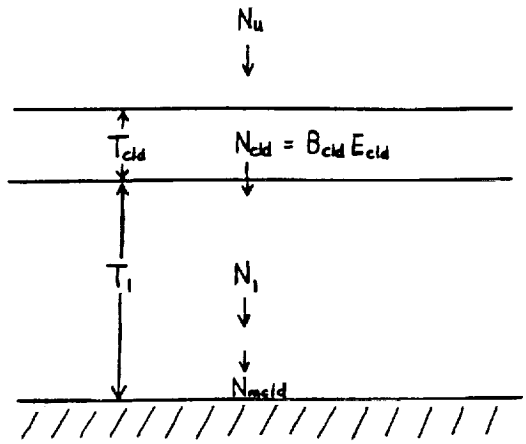

Fig.2. The three layer model used for this study.

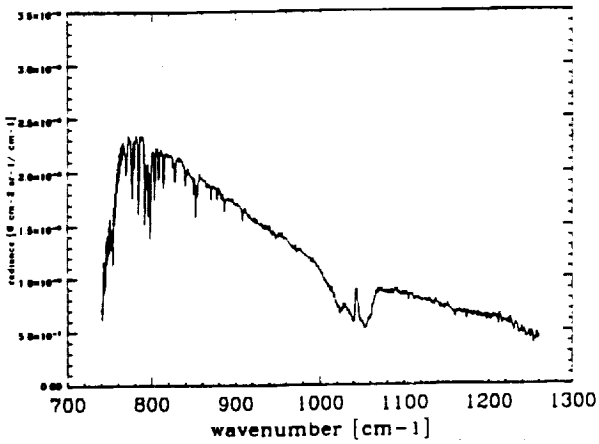

Fig.3. Effective spectral radiance found by spectral differencing the two curves in Fig.1.

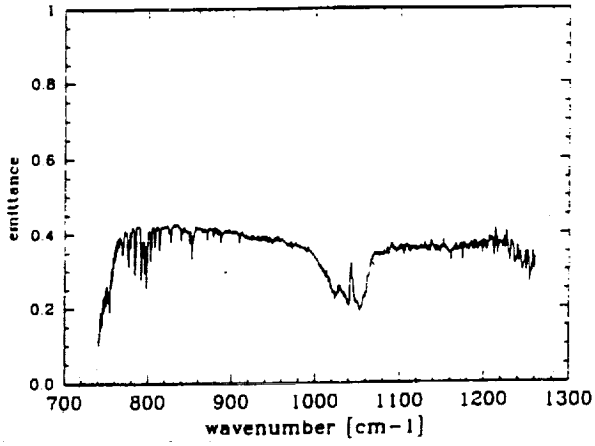

Fig.4. An effective spectral emmitance derived from the effective radiance shown in Fig.3.

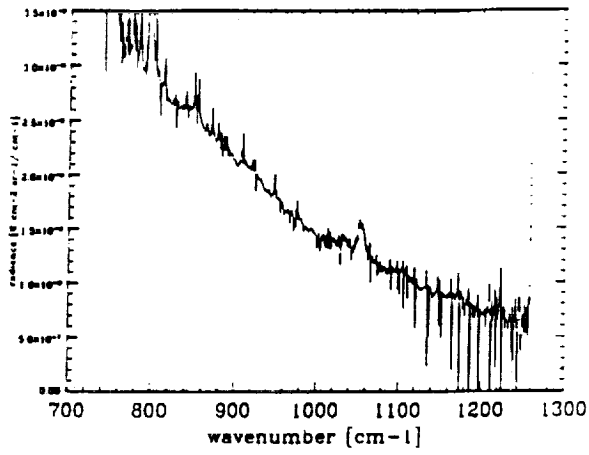

Fig.5. The downward spectral radiance of the cirrus layer as seen from the lower boundary of the cirrus layer.

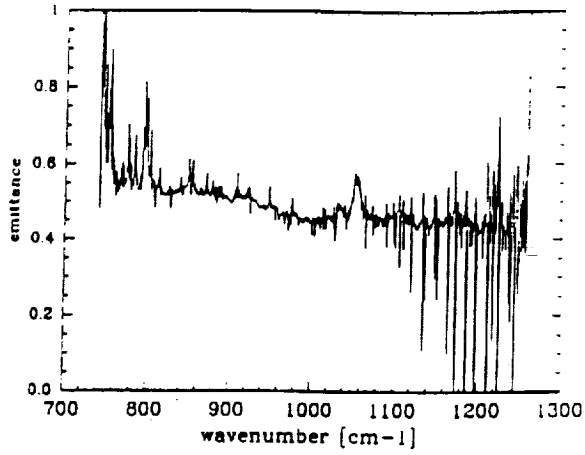

Fig.6. The spectral emittance of the cirrus layer.

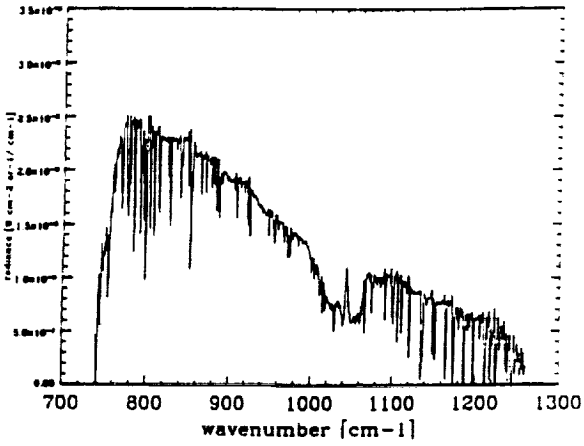

Fig.7. The simulated effective spectral radiance inferred from the interferometric cirrus radiance and FASCODE calculations.

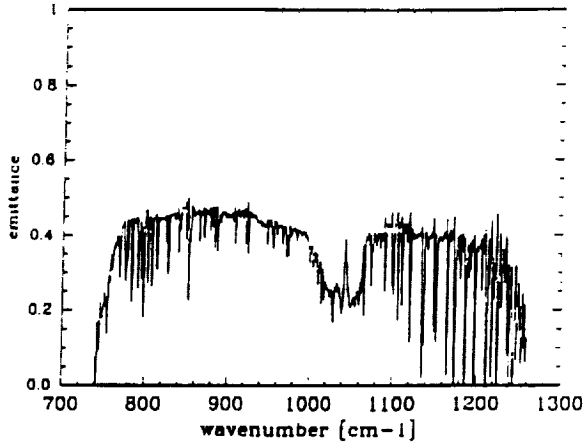

Fig.8. The simulated effective spectral emittance found using the information in Fig.7.

CIRRUS SCIENCE CONFERENCE
Beaver Run Resort and Conference Center
Breckenridge, Colorado
June 14-17, 1993

omit

NAME: John M. Davis and Stephen K. Cox PHONE NO: (303) 491-8594

ORGANIZATION: Department of Atmospheric Science
Colorado State University
Fort Collins, CO 80523

TITLE: "Cirrus Emittance from Ozone Emission"

SUGGESTED SESSION: ORAL: POSTER:

SHORT ABSTRACT

The emittance of cirrus clouds is derived using the downwelling radiance in the 9.6 μm ozone emission region. The study investigates the advantages and disadvantages of using a semitransparent region of the atmospheric window to infer cloud emittance. Assuming constant ozone concentration in the short term, the method examines the benefit in utilizing the ozone emission from above the cirrus layer as a radiance source, against drawbacks imposed by the absorption and emission by the gas below the cloud. The study utilizes interferometer measurements collected during the FIRE II Cirrus IFO at Parsons, Kansas. The resulting values of cirrus cloud emissivity will be compared to results derived by more conventional methods.

531-47
19753
P. 4

N94-22323

CO_2 Lidar Observations of Mount Pinatubo Debris: FIRE II and Longer-Term Measurements

David H. Levinson
Cooperative Institute for Research in Environmental Sciences
University of Colorado/NOAA
Campus Box 449
Boulder, Colorado 80309-0449

Madison J. Post and Christian J. Grund
NOAA Wave Propagation Laboratory
325 Broadway
Boulder, Colorado 80303

Introduction

The volcanic debris in the stratosphere from the June 1991 eruption of Mt. Pinatubo first appeared over the NOAA Wave Propagation Laboratory (WPL) field site near Boulder, Colorado (40.15° N, 105.23° W), in July of 1991. The presence of the Pinatubo cloud has allowed us to characterize both the tropospheric and stratospheric aerosol backscatter using the NOAA/WPL CO_2 Doppler lidar. The lidar has measured vertical backscatter profiles at $\lambda = 10.59\ \mu m$ for over a decade (Eberhard and McNice, 1986). Analysis of this dense set of profiles reveals the effects of atmospheric and microphysical processes during the buildup and decay of Mt. Pinatubo's clouds. Further information on the NOAA lidar, specifically calibrations using a hard target, can be found in Post and Cupp (1990).

We present results of those measurements for June 15, 1991, through December 31, 1992. During that period of longer-term measurements, WPL took part in FIRE II (First ISCCP[=International Satellite Cloud Climatology Project] Regional Experiment II), from November 12 through December 8, 1991, measuring vertical backscatter profiles almost daily.

One of the mechanisms for purging stratospheric aerosols is tropopause folding (Post, 1986), which occurs in cold-core extratropical cyclones. Tropospheric mass loading occurs during folding events (Shapiro and Keyser, 1990), which can substantially increase the amount of ice nuclei in the upper troposphere (Sassen, 1992), and may affect the formation of cirrus in that region. Spring and fall are prominent times for tropopause folding events because of the migration of the subtropical and polar jet streams during the transition seasons. Sassen (1992) has suggested that the volcanic aerosols from Pinatubo played a role in the formation of cirrus during FIRE II, particularly during a period of moist subtropical flow on December 5-6, 1991.

Longer-Term Measurements

Figure 1 shows the time series of backscatter profiles taken by the CO_2 system from June 1991 through December 1992 (profiles were obtained at the field site near Boulder, except for several periods when the lidar system was in White Sands Missile Range, New Mexico, and Coffeyville, Kansas). The increase in range into the stratosphere that occurred with the first appearance of the cloud in July 1991 is very clear from this time series. From July 1991 until January 1992 the stratospheric backscatter steadily

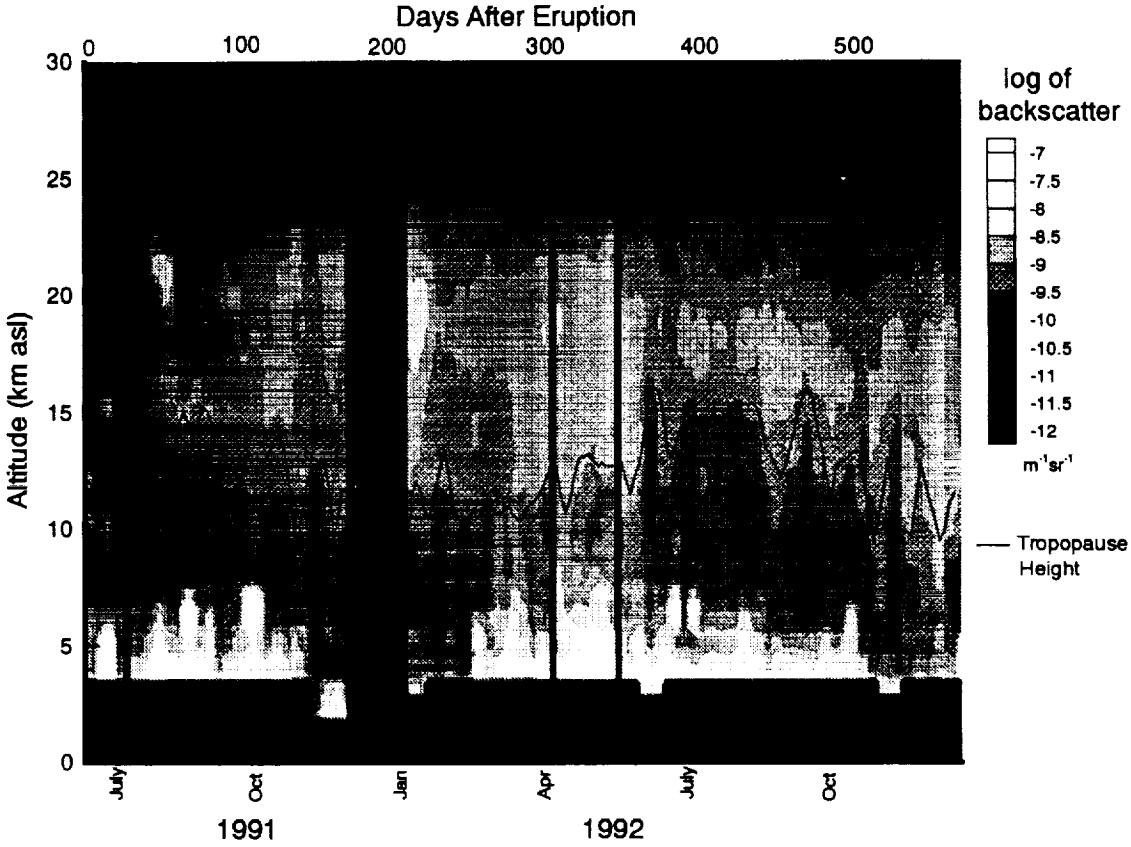

Figure 1. Time series of lidar backscatter β (m^{-1} sr^{-1}) profiles for June 15, 1991, until December 31, 1992. The height of the tropopause (solid line), determined from NWS soundings, is also included. Note the increase in stratospheric backscatter after July 1991.

increased; this is observed as a wedge-shaped broadening of the region of high backscatter centered on 17 km MSL. The high-backscatter portion of the cloud extended up to 23 km and downward to 11 km MSL by the end of 1991. Simultaneous with the appearance of stratospheric debris, tropospheric backscatter increased markedly, and it has remained well above nonvolcanic levels since.

FIRE II Observations

The measurements taken during FIRE II occurred in a period when the volcanic cloud was beginning to advect substantially toward higher latitudes. The time series of integrated backscatter observed by the NOAA lidar during FIRE II is shown in Fig. 2. The intervals of integration were from 6 km ASL to the tropopause level (upper troposphere), and from the tropopause to 22 km ASL (lower stratosphere). Tropopause levels were determined from the National Center for Atmospheric Research (NCAR) CLASS soundings at Coffeyville, Kansas. The integrated stratospheric backscatter fluctuates over the period; the trend is for slightly increasing backscatter. The tropospheric backscatter fluctuates much more, and there are short periods when enhancements are greater than 1 order of magnitude in that region. Several periods are of note: November 18-19, which has a drop and increase in backscatter in

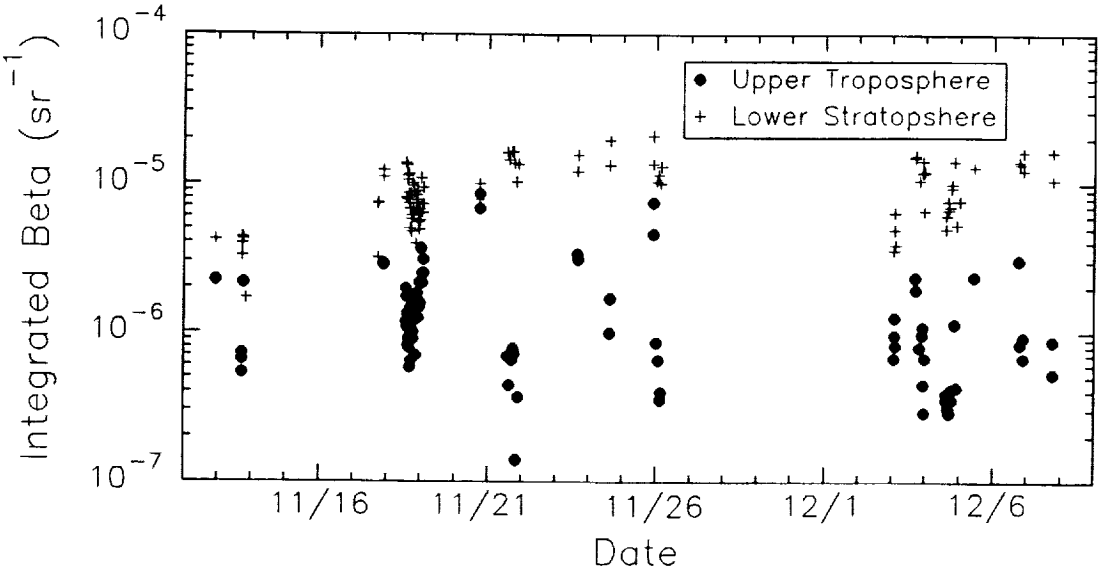

Figure 2. Integrated backscatter for the upper troposphere and lower stratosphere during the FIRE II field experiment (November 12 to December 8, 1991). The tropospheric integration was done from 6 km MSL to the tropopause, and the stratopsheric integration from the tropopause to 22 km MSL. The height of the tropopause was determined from NCAR CLASS soundings at Coffeyville, Kansas.

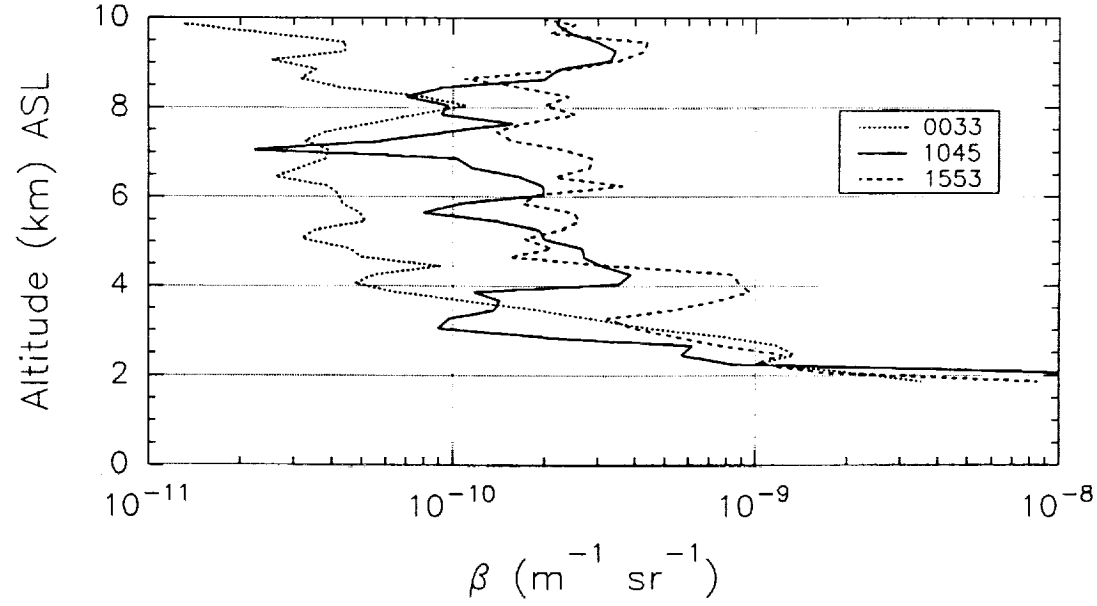

Figure 3. Lidar tropospheric backscatter profiles from Coffeyville, Kansas, on December 5, 1991, at 0033 UTC (short dash), 1045 UTC (solid), and 1553 UTC (long dash). Note the increase in backscatter above 4 km MSL, especially between 0033 and 1045 UTC.

the upper troposphere over a short time period; November 24-26, which has several sharp fluctuations in the upper troposphere; and the December 5-6 case (mentioned earlier) which is a possible tropopause fold case.

The December 5-6 case is a candidate for a tropopause folding event for several reasons, the most convincing is the increase in upper tropospheric backscatter observed on December 5. The moist subtropical flow observed during this case was due to the northward migration of the subtropical jet and to the amplification of a long wave trough to the west which brought southwesterly flow aloft over the project area. Figure 3 shows tropospheric backscatter profiles taken at three different times on December 5. There is a substantial enhancement in backscatter in the region above 4 km ASL over the 15 hour period between the first and last profile. Caution must be used in interpreting these data as a tropopause fold without more supporting evidence. Specifically, an in-depth case study of the meteorological conditions that were present on December 5-6 would substantiate the synoptic conditions that were present. It is quite possible that the tropopause folding occurred upstream, and the airmass then advected over Coffeyville causing the increased backscatter observed in the profiles. In a more recent case, a tropopause folding event was observed by the WPL lidar at the Boulder site on September 25, 1992 (Post et al., 1993). The lidar-measured backscatter increased by up to 2 orders of magnitude from 5 to 10 km MSL at that time. The upper tropospheric enhancement for the December 5-6 case was an order of magnitude weaker than for the September 25, 1992, case.

Summary

CO_2 lidar observations from the FIRE II field program show fluctuations in the upper tropospheric backscatter that are likely enhanced by the volcanic debris from the June 1991 eruption of Mt. Pinatubo. The FIRE II measurements occurred during a period when the volcanic cloud was spreading northward into the midlatitudes and increasing in depth. Tropopause folding is the primary mechanism for tropospheric mass loading by stratospheric debris, and several periods of enhanced integrated backscatter in the upper troposphere served as possible cases to study this. In particular, backscatter profiles taken on December 5-6, 1991, showed a 1 order of magnitude enhancement from 4 to 10 km MSL over a 15 hour period. Further research on the meteorological conditions, particularly the synoptic-scale environment, is needed to more fully understand the impact of the volcanic clouds during FIRE II.

References

Eberhard, W.L. and G.T. McNice, 1986: Versatile lidar for atmospheric studies, including plume dispersion, clouds, and stratospheric aerosols. *J. Atmos. Oceanic Tech.*, **3**, 614-622.

Post, M.J., 1986: Atmospheric purging of El Chichòn debris. *J. Geophys. Res.*, **91**, 5222-5228.

Post, M.J., and R.E. Cupp, 1990: Optimizing a pulsed Doppler lidar. *Appl. Opt.*, **29**, 4145-4158.

Post, M.J., P.J. Neiman, F.M. Ralph, and L.D. Olivier, 1993: Doppler lidar observations of a frontal passage in the vicinity of steep topography. In *Optical Remote Sensing of the Atmosphere, Technical Digest 5*, Optical Society of America, Washington, D.C., 231-234.

Sassen, K., 1992: Evidence for liquid-phase cirrus cloud formation from volcanic aerosols: climatic implications. *Science*, **257**, 516-519.

Shapiro, M.A., and D. Keyser, 1990: Fronts, jet streams, and the tropopause. In *Extratropical Cyclones, the Erik Palmén Memorial Volume*, C.W. Newton and E. Holopainen, Eds., American Meteorological Society, Boston, Mass., 167-191.

D32-47
197532
P. 4

N94-22324

ANALYSIS OF THE TROPOSPHERIC WATER DISTRIBUTION DURING FIRE-II

Douglas L. Westphal

NASA Ames Research Center, Moffett Field, California

1. INTRODUCTION

We have been using the Penn State/NCAR mesoscale model, as adapted for use at ARC, as a testbed for the development and validation of cloud models for use in GCMs. This modeling approach also allows us to intercompare the predictions of the various cloud schemes within the same dynamical framework. The use of the PSU/NCAR mesoscale model also allows us to compare our results with FIRE-II observations, instead of climate statistics.

Though a promising approach, our work to date has revealed several difficulties. First, the model by design is limited in spatial coverage and is only run for 12 to 48 hours at a time. Hence the quality of the simulation will depend heavily on the initial conditions. The poor quality of upper-tropospheric measurements of water vapor is well known and the situation is particularly bad for mid-latitude winter since the coupling with the surface is less direct than in summer so that relying on the model to spin-up a reasonable moisture field is not always successful. Though one of the most common atmospheric constituents, water vapor is relatively difficult to measure accurately, especially operationally over large areas. The standard NWS sondes have little sensitivity at the low temperatures where cirrus form and the data from the GOES 6.7 μm channel is difficult to quantify. For this reason, the goals of FIRE Cirrus II included characterizing the three-dimensional distribution of water vapor and clouds.

In studying the data from FIRE Cirrus II we find that no single special observation technique provides accurate regional distributions of water vapor. The Raman lidar provides accurate measurements, but only at the Hub, for levels up to 10 km, and during nighttime hours. The CLASS sondes are more sensitive to moisture at low temperatures than are the NWS sondes, but the four stations only cover an area of two hundred kilometers on a side. The aircraft give the most accurate measurements of water vapor, but are limited in spatial and temporal coverage.

This problem is partly alleviated by the use of the MAPS analyses, a four-dimensional data assimilation system that combines the previous 3-hour forecast with the available observations, but its upper-level moisture analyses are sometimes deficient because of the vapor measurement problem.

In our work we are attempting to create a consistent four-dimensional description of the water vapor distribution during the second IFO by subjectively combining data from a variety of sources, including MAPS analyses, CLASS sondes, SPECTRE sondes, NWS sondes, GOES satellite analyses, radars, lidars, and microwave radiometers.

2. WATER VAPOR MEASUREMENTS

The primary technique for determining the regional vapor distribution is the rawinsonde. But the AIR (CSU) and VIZ (NWS, SPECTRE) sondes seldom report relative humidities below 25% and become temperature sensors in the upper troposphere. The Vaisala sonde (NCAR CLASS) appears to be more accurate. Three intercomparisons are shown in Figure 1. In the first, the CLASS sonde agrees with the GSFC Raman Lidar data while the SPECTRE sonde indicates values that are too high between 300 and 650 mb. In the second example, the SPECTRE sonde is again unable to detect the dryness of some layers in the troposphere and, more importantly, parallels the temperature curve above about 400 mb showing no sensitivity to moisture. In Figure 1c, we show another example of the good agreement between the CLASS and Raman data, although comparison above 400 mb is difficult because the Raman signal becomes weak. Apparently, the VIZ sondes (NWS, SPECTRE) will always indicate too much upper-tropospheric water vapor, except when high values actually occur. This has a significant impact when using them for validating satellite retrievals, interpreting ground-based radiative measurements, and initializing or validating a numer-

ical model.

3. MOISTURE ANALYSIS

After many frustrating days of clear skies, rain, or dissipating cirrus at the FIRE Cirrus II Hub, a cirrus cloud field developed as it moved eastward across Kansas on November 26, 1991. Analyses by Mace et al. associates the clouds with a jet streak that propagated across Kansas on that day. The model simulation for the period is in agreement with Mace et al. revealing the jet streak, the passage of a shortwave, a divergence/convergence couplet, and vertical velocities of 8 cm/s.

As an example of the difficulties encountered in water vapor analyses, we present in Figures 2a and 2b the N-S cross-sections of relative humidity with respect to ice for 2000 UTC on 26 November which is near the time of maximum cloudiness at the Hub site (37.1N, 95.6W). The radiosonde data are used in 2a and the MAPS analysis (only available at 2100 UTC) is shown in 2b. We see similarities in both analyses, but the MAPS analysis is missing the thin layer of high humidity at 370 mb that covers the Hub. The absence of this layer would no doubt impact the interpretation of FIRE observations at the Hub. Above 300 mb at OMA, TOP, and GGG we see the high humidities typical of the NWS sondes and cannot say whether the MAPS analyses are in error for not having high humidities above 300 mb. In Figure 2c we present the 2000 UTC cross-section predicted by the PSU/NCAR mesoscale model initialized with the 1200 UTC MAPS analyses. The model more accurately resolves the 370 mb layer of moisture over the Hub than does the MAPS analyses but misses the layer at 680 mb. Initializing the model from earlier MAPS analyses yields significantly different results (not shown). We are investigating these differences now and will determine whether the errors are due to initial conditions, model physics, or model dynamics.

4. CONCLUSIONS

We conclude that much subjective analysis will be required to understand the water vapor fields during the case study days and the rest of FIRE Cirrus II. Automated processing of all the FIRE dynamical data is unlikely to yield fields of practical use to the instrumentalists.

5. ACKNOWLEDGEMENTS

We thank H. Melfi, D. Starr, S. Benjamin, R. Ellingson for the use of their data from the FIRE Cirrus II program. This work is supported by NASA's FIRE program and DOE ARM Grant DE-AI05-90ER61074.

6. REFERENCES

Mace, G.M., T.P. Ackerman, B.A. Albrecht, and E.E. Clothiaux, 1993: A comparison of methods for computing the atmospheric kinematic properties using wind profiler data, Submitted to Mon. Wea. Rev.

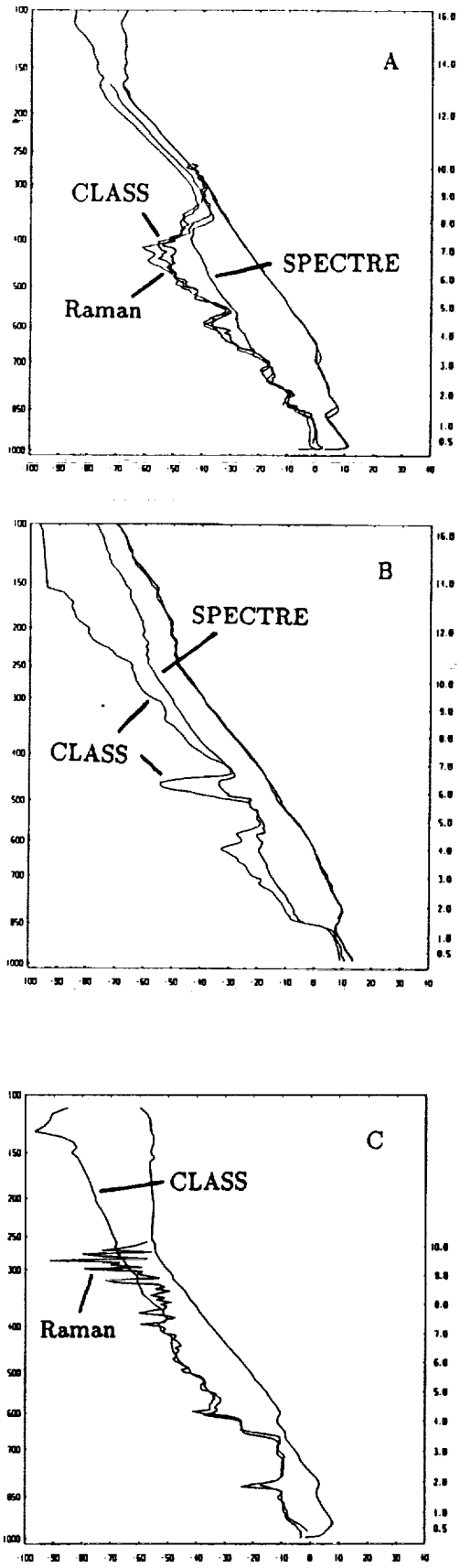

Figure 1. Vertical profiles of temperature and dewpoint temperature at the Hub (Coffeyville, KS). Data sources include NCAR CLASS sondes (Vaisala), SPECTRE sondes (VIZ), and GSFC Raman lidar. The temperature profile from the nearest (in time) CLASS sonde was used to complete the Raman lidar profiles.
a: Comparison of CLASS, SPECTRE, and Raman lidar for times within one half hour of 0100 UTC 6 December, 1991. The two Raman dewpoint profiles and the CLASS sonde are in good agreement, while the SPECTRE sonde is too moist between 300 and 650 mb. The atmosphere is probably saturated above 300 mb.
b: CLASS and SPECTRE sondes launched within 13 minutes of each other at 2300 UTC 6 December. The SPECTRE sonde indicates a moister atmosphere at almost all levels and becomes a temperature sensor above about 400 mb.
c: CLASS and Raman profiles for 0537 UTC 26 November, 1991. The Raman measurement is a ten minute average, while the CLASS sonde takes over an hour to complete. Nevertheless, note the good comparison at nearly all levels up to 400 mb, above which the Raman lidar signal becomes weak.

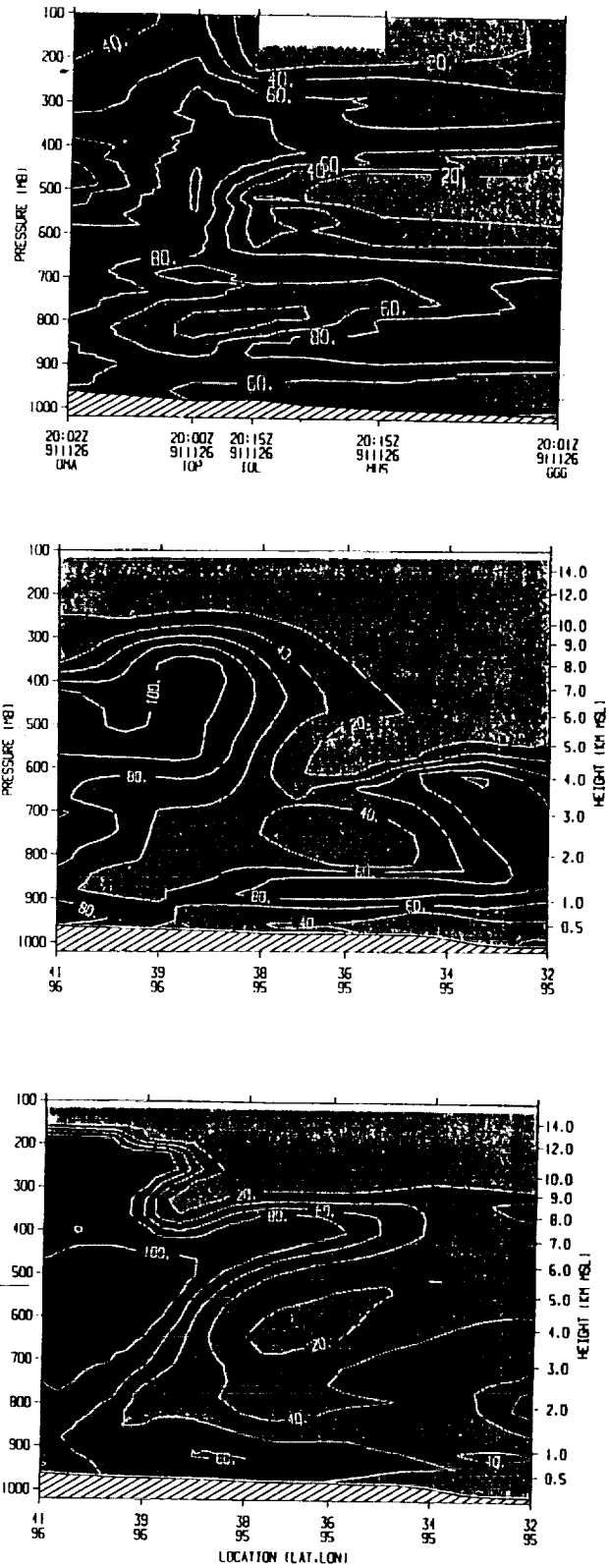

Figure 2. Meridional cross-section of relative humidity with respect to ice running from Omaha NB (OMA),through the Hub, to Midland TX (GGG).
a: Analyis of NWS and CLASS sondes for 2000 UTC, 26 November, 1991;
b: MAPS analyses for 2100 UTC, 26 November;
c: 20-hour model prediction, valid at 2000 UTC.

533-47
197533
p-4

N94-22325

Examination of the Observed Synoptic Scale Cirrus Cloud Environment: The December 3-6 FIRE Cirrus Case Study

Gerald G. Mace and Thomas P. Ackerman

Department of Meteorology
The Pennsylvania State University
503 Walker Building
University Park, PA 16802

1. Introduction

Recently, Sassen (1992) provided evidence for supercooled water droplets in cirrus uncinus cell heads at temperatures between -40° and -50°C. Chemistry related to volcanic aerosol of stratospheric origin was evoked as an explanation fo this phenomenon. Sassen speculated that injections of sulfuric acid droplets into the upper troposphere were accomplished by tropopause folds associated with subtropical jet streams. He also postulated global climatic perturbations due to the effect of these cirrus microphysical perturbations on radiative fluxes.

Using data processing and objective analysis techniques described by Mace and Ackerman (1993, this issue), we examine the synoptic scale environment for evidence of tropopause folds that may have served as a source mechanism of stratospheric aerosol in the upper troposphere.

2. The Synoptic Scale Environment

Even though the cirrus cloud systems reported by Sassen (1992) occurred on 5 and 6 December, we chose to begin our examination of the broad-scale environment on 3 December 1991 during a highly perturbed period in the upper level air-flow. At 12 UTC 3 December 1991 (3/12), a sharp trough in the upper troposphere extended from a low near Hudson Bay through the central United States and into the Gulf of California. A southwesterly jet with speed maximum of 75 m/s extended from central New Mexico into the Canadian Maritime Provinces and northwesterly jet with speed

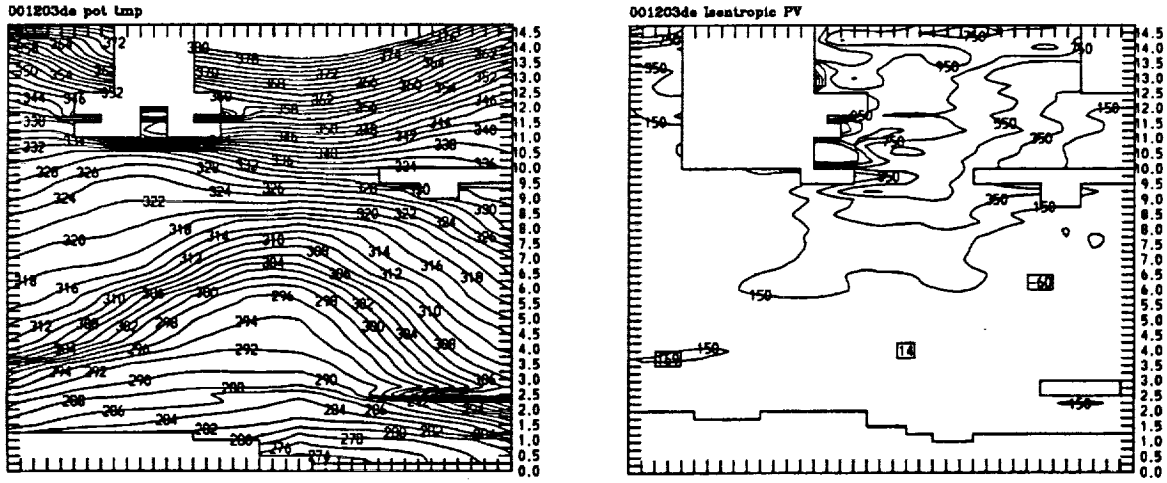

Fig. 1. Vertical cross sections of a) potential temperature and b) Isentropic Potential Vorticity normal to the airflow at 12 UTC 3 December 1991. The cross sections extend along a line from southwestern New Mexico to central Kansas and thence southeastward to central Louisiana. Blocked out portions of the figures denote regions of missing or erroneous data. Units of pontential are 10^{-7} K mb^{-1} s^{-1}.

maximum of 60 m/s extended from the Gulf of Alaska to the Desert Southwest of the United States.

Fig. 1 shows the vertical cross sections of potential temperature and potential vorticity along lines normal to the upper tropospheric flow. The vertical column where the cross section crosses the trough axis is evident by examining the potential temperature contours; the contours bend upward in the troposphere and downward in the stratosphere. To the left of the trough axis in the northwesterly flow, a well defined elevated frontal zone is evident. The frontal zone, roughly bracketed by the 304K and 310K isentropes extends from the tropopause near the trough axis downward to approximately 3 km in southwestern New Mexico. Associated directly with the upper front is a discontinuity in isentropic potential vorticity. This quantity can be considered a quasi-conservative tracer of air parcels in the upper troposphere. Fig. 1b shows that values of potential vorticity denoting air parcels of stratospheric origin (greater than 150 units) are diagnosed along the upper tropospheric frontal zone. This characteristic feature of upper tropospheric baroclinic zones has been shown to be indicative of extrusions of

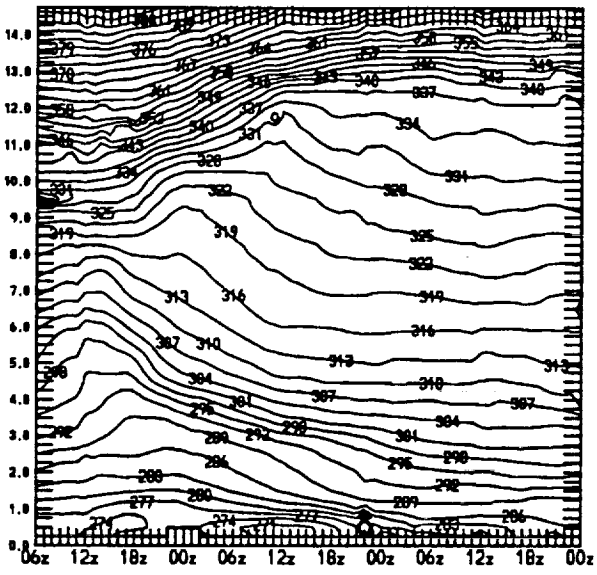

Fig. 2. Time-Height cross sections of potential temperature over Coffeyville, Kansas from 0000 UTC 3 Dec. 1991 to 1800 UTC 6 Dec. 1991.

stratospheric air into the middle and upper troposphere; these extrusions are known as tropopause folds (Danielson, 1968; Shapiro, 1976). While no cirrus were directly associated with this event, tropopause folds have been documented as an injection mechanism of stratospheric aerosol of volcanic origin into the middle and upper troposphere (Shapiro, 1984). If enhanced aerosol loading existed in the lower stratosphere over the western third of North America, stratospheric aerosol were likely deposited into the middle and upper troposphere over a large portion of the western and southwestern United States by this fold event.

The geographical extent of the elevated frontal surface becomes evident in light of Fig. 2. This time height cross section of potential temperature over Coffeyville show the elevated frontal surface in the northwesterly flow upstream of the trough axis after 3/12. This layer of enhanced static stability defined by the 292K and 304K isentropes was continuously observed at lower levels with the passage of time and could still be recognized as a distinct entity 36 hours later. Given a conservative mean advective speed of 20 m/s in the northwesterly flow, the longevity of this feature suggests an along-trajectory length scale of more than 2500 km.

A considerable deamplification of the upper level pattern took place on 4 Dec. The jet-trough system propagated northeastward in response to rising heights over much of western North America. This process is also evident in Fig. 2 as tropopause heights increased from 8 km late on 3 Dec. to near 12 km by 4/12.

By 5/00 the main belt of westerlies extended across southern Canada and the northern United States. A weak subtropical jet stream extended from the Four Corners region eastward along the Kansas-Oklahoma border. A band of cirrus existed at and below the level of maximum wind along the anticyclonic shear side of the jet streak. The position of the cirrus relative to the upper tropospheric flow is qualitatively in line with theoretical expectations of reduced static stability and upward motion below the level of maximum wind in the left rear quadrant of a jet streak (Maddox and Bleck, 1986). Vertical cross sectional analysis (not

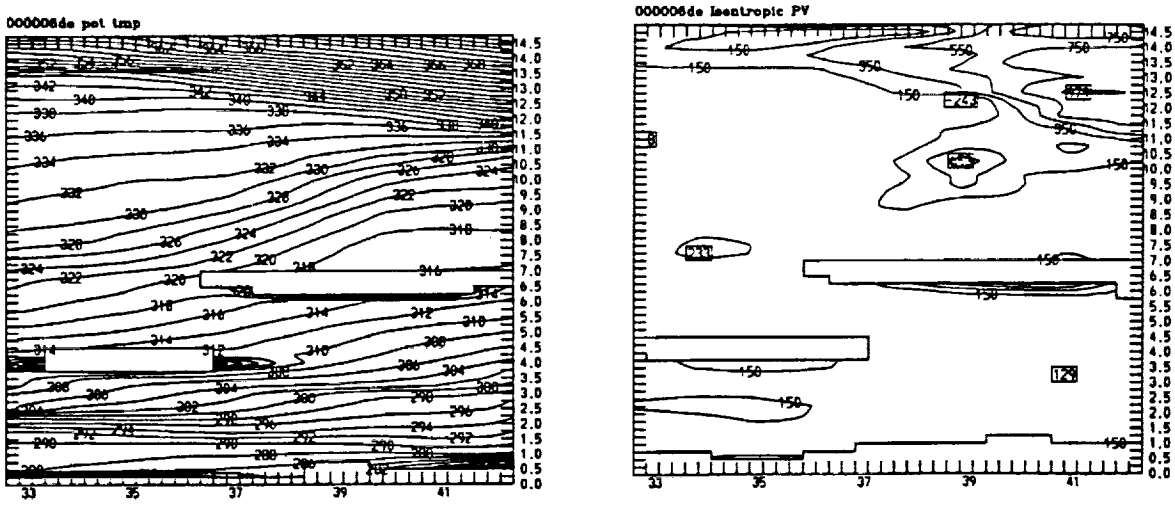

Fig. 3. Vertical cross sections of a) potential temperature and b) Isentropic Potential Vorticity normal to the airflow at 00 UTC 6 December 1991. The cross sections extend along a line from south-central Oklahoma to southern Nebraska..

shown) of this feature shows no near-tropopause baroclinic zones or obvious fold event associated with it.

The thermodynamic and wind structure of the next jet streak (centered at 5/20 and 11.5 km over Coffeyville) was better defined. The vertical cross sections normal to the upper tropospheric air flow at 6/00 (Fig. 3) reveal a weak elevated frontal zone bounded by the 320K and 330K isentropes that was well correlated with the region of largest cyclonic shear vorticity associated with the jet streak. Corresponding values of isentropic potential vorticity reveal a discontinuity from tropospheric to stratospheric values at the frontal interface strongly suggestive of a folded tropopause over central and northern Kansas. Satellite imagery shows that the cirrus observed during this period was part of an elongated shield of cirrus that extended eastward from central Colorado. The base of the cirrus clouds observed over Coffeyville (~ 37N) at this time were just above 9 km with tops near 11 km. The base height corresponds to the upper portion of the elevated frontal zone and the southern extent of the stratospheric potential vorticity in the cross section. Additionally, data from an ozone sonde launched at this time (Fig. 4) reveal a well defined spike in the ozone profile centered at 8.75 km. We conclude that the cirrus observed over Coffeyville at this time existed at and above the upper boundary of the elevated frontal surface and based on this analysis, the base of the cirrus clouds appear to have been in direct contact with air of very recent stratospheric origin.

The layer of enhanced static stability attributed to the upper front continues to be evident in the potential temperature cross sections at 6/12 and 6/18 (not shown) although the frontal zone appears to be disconnected from the tropopause and the IPV discontinuity is no longer evident. This six hour period roughly brackets the third cirrus event of this case study.

3. Summary, Conclusions and Future Work

We have provided evidence suggesting that the dynamic mechanisms necessary to explain a tropospheric source of volcanic aerosol did indeed exist during this case study period. An intense upper tropospheric polar jet-front system and associated tropopause fold affected much of western North America on 3 Dec. The following day (4 Dec) aerosol induced twilight affects were noted (Sassen, 1992) and the first cirrus cloud event of the case study (5/03-5/18) occurred. Although associated with a weak subtropical jet stream, this first cirrus event was not directly associated with any obvious

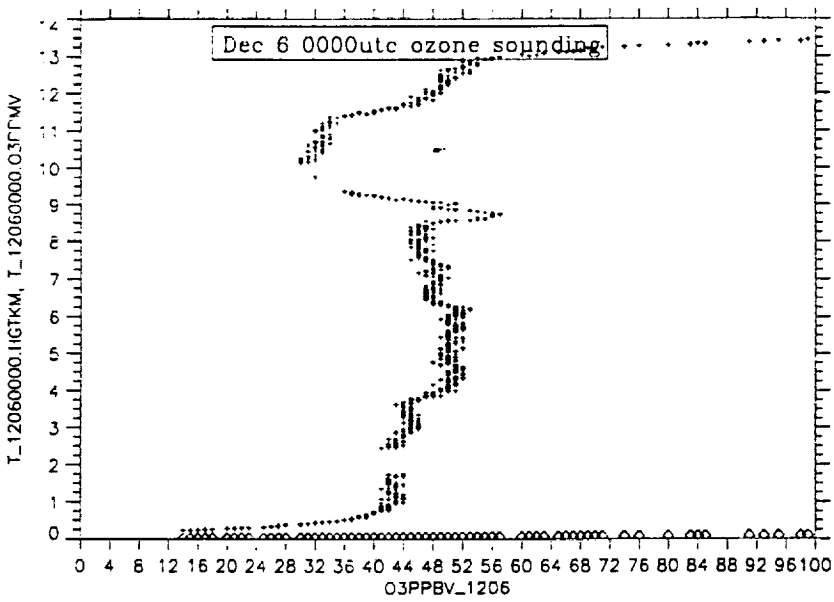

Fig. 4. Tropospheric ozone profile recorded by a sonde launched at the FIRE II hub site in Coffeyville, KS at 00 UTC 6 December 1991.

elevated frontal zone. The second cirrus cloud event took place from 5/18 to 6/06. The cirrus was also associated with a subtropical jet streak and the data revealed a weak elevated baroclinic zone in the upper troposphere with an associated region of high isentropic potential vorticity suggestive of a weak tropopause fold. Increased ozone in this layer provided supporting evidence.

Further analysis of these cirrus cloud events needs to concentrate on the moisture budget of the upper troposphere. While we have provided evidence to suggest that volcanic aerosol injection is a plausible in this situation, we have not addressed the troubling question of how the dehydrated stratospheric air parcels containing the sulfuric acid droplets gain enough moisture to form cirrus clouds.

Acknowledgments: This research was supported in part by NASA grants NAG-1-1095 and NAG-1-999 and by DOE grant DE-FG02-90ER61071. This work was done while one of us (GM) held a NASA Goddard Graduate Student Fellowship.

References

Danielson, E. F., 1968: Stratospheric-tropospheric exchange based upon radioactivity, ozone and potential vorticity. *J. Atmos. Sci.*, **25**, 502-518.

Sassen, K., 1992: Evidence for liquid-phase cirrus cloud formation from volcanic aerosols: climatic implications. *Science*, **257**, 516-519

Shapiro, M. A., 1976: The role of turbulent heat flux in the generation of potential vorticity in the vicinity of upper-level jet stream systems. *Mon. Wea. Rev.*, **104**, 892-906.

Shapiro, M. A., R. C. Schnell, F. P. Parungo, S. J. Oltmans and B. A. Bodhaine, 1984: El Chichon volcanic debris in an arctic tropopause fold. *Geophys. Res. Lett.*, **11**, 421-424.

Mattocks, C. and R. Bleck, 1986: Jet streak dynamics and geostrophic adjustment processes during the initial stages of lee cyclogenesis. *Mon. Wea. Rev.*, **114**, 2033-2056.

534-47
ABS. ONLY
197534
P-1

N94-22326

The 5-6 December 1991 FIRE IFO II Jet Stream Cirrus Case Study: The Influence of Volcanic Aerosols

Kenneth Sassen[1], Gerald G. Mace[2], David O'C. Starr[3], Michael R. Poellot[4], S.H. Melfi[3], Wynn L. Eberhard[5], James D. Spinhirne[3], E.W. Eloranta[6], Donald E. Hagen[7], and John Hallett[8]

ABSTRACT

In presenting an overview of the cirrus clouds comprehensively studied by ground-based and airborne sensors from Coffeyville, KS, during the 5-6 December 1992 Project FIRE IFO II case study period, evidence is provided that volcanic aerosols from the June 1991 Pinatubo eruptions significantly influenced the formation and maintenance of the cirrus. Following the local appearance of a spur of stratospheric volcanic debris from the subtropics, a series of jet streaks subsequently conditioned the troposphere through tropopause foldings with sulfur-based particles that became effective cirrus cloud-forming nuclei. Aerosol and ozone measurements suggest a complicated history of stratospheric-tropospheric exchanges embedded within the upper level flow, and cirrus cloud formation was noted to occur locally at the boundaries of stratospheric aerosol-enriched layers that became humidified through diffusion, precipitation or advective processes. Apparent cirrus cloud alterations include abnormally high ice crystal concentrations (up to ~600 l^{-1}), small but complex radial ice crystal types, and relatively large haze particles in cirrus uncinus cell heads at temperatures between -40° to -50°C. Implications for volcanic-cirrus cloud climate effects, and usual (non-volcanic aerosol) jet stream cirrus cloud formation are discussed.

---

1. Meteorology Dept., University of Utah, SLC, UT. 2. Meteorology Dept., Pennsylvania State University, University Park, PA. 3. NASA Goddard Space Flight Center, Greenbelt, MD. 4. Atmospheric Sciences Dept., University North Dakota, Grand Forks, ND. 5. NOAA Wave Propagation Laboratory, Boulder, CO. 6. Meteorology Dept., University of Wisconsin, Madison, WI. 7. Physics Dept., University of Missouri - Rolla, MO. 8. Desert Research Institute, Reno, NV.

N94-22327

Three Dimensional Modeling of Cirrus During the 1991 FIRE IFO II: Detailed Process Study

Eric J. Jensen, Owen B. Toon, Douglas L. Westphal

NASA Ames Research Center, Moffett Field CA 94035

We have used a three-dimensional model of cirrus cloud formation and evolution, including microphysical, dynamical, and radiative processes, to simulate cirrus observed in the FIRE Phase II Cirrus field program (November 13 - December 7, 1991). Sulfate aerosols, solution drops, ice crystals, and water vapor are all treated as interactive elements in the model. Ice crystal size distributions are fully resolved based on calculations of homogeneous freezing of solution drops, growth by water vapor deposition, evaporation, aggregation, and vertical transport. Visible and infrared radiative fluxes, and radiative heating rates are calculated using the two-stream algorithm described by Toon et al. [1989]. Wind velocities, diffusion coefficients, and temperatures were taken from the MAPS analyses and the MM4 mesoscale model simulations [Westphal and Toon, 1991]. Within the model, moisture is transported and converted to liquid or vapor by the microphysical processes.

The simulated cloud bulk and microphysical properties will be shown in detail for the Nov. 26 and Dec. 5 case studies. Comparisons with lidar, radar, and in situ data will be used to determine how well the simulations reproduced the observed cirrus. The roles played by various processes in the model will be described in detail. The potential modes of nucleation will be evaluated, and the importance of small-scale variations in temperature and humidity will be discussed. The importance of competing ice crystal growth mechanisms (water vapor deposition and aggregation) will be evaluated based on model simulations. Finally, the importance of ice crystal shape for crystal growth and vertical transport of ice will be discussed.

S36-47
197536
p-3

N91-22328

Meteorological Analysis of the November 25 FIRE Cirrus-II Case: A Well-Defined Ridge-Crest Cirrus System over Oklahoma

David O'C. Starr
NASA Goddard Space Flight Center
Greenbelt, MD 20771

Andrew R. Lare
Applied Research Corporation
Landover, MD 20785

1 Introduction

On the morning of November 25 1991, a cirrus cloud system formed in a region extending eastward from the continental divide into central Oklahoma and southwestern Kansas (Figure 1). The system moved slowly eastward during the day and maintained a relatively constant scale and shape. From the satellite perspective, this cloud system had a number of morphological similarities to the 27-28 October FIRE Cirrus-I case analyzed by Starr and Wylie (1990). By comparison, the present case had much better rawinsonde coverage. The rawinsonde network was much more extensive and the cloud system was relatively slow moving and well-located with respect to the enhanced sounding network (Figure 2) and the NWS Wind Profiler Network.

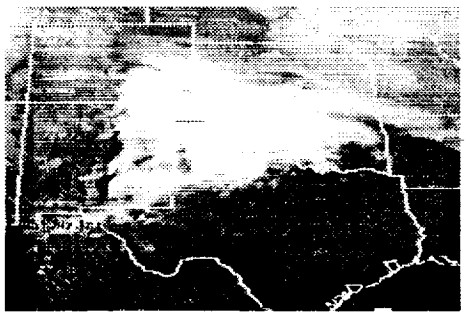

Figure 1: Infrared satellite imagery for 1200 UTC on 25 November 1991.

In addition to the rawinsonde soundings (1200 and 1800 UTC on 25 November and 0000 and 0600 UTC on 26 November) and satellite observations, four aircraft sorties were flown in the northern portion of this cirrus cloud system from mid-morning to mid-afternoon. These included microphysical-radiation profiling missions by the NCAR Sabreliner near Tulsa (about midway between COF and OUN in Figure 2) and the NCAR King Air near Ponca City (about 80 km upwind of Tulsa), a microphysical profiling mission by the UND Citation near Tulsa, and a NASA ER-2 overflight. Thus, very good data are available for this case although, unfortunately, the cloud system remained south of the FIRE Hub site at Coffeyville (COF) where extensive ground-based remote sensor were located. The northern edge of the cloud system was visible from COF during most of the day.

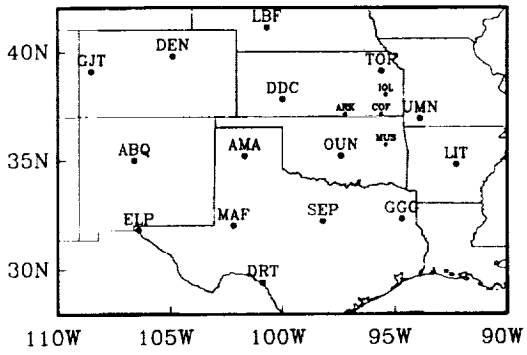

Figure 2: Map of rawinsonde stations located within the analysis region. Larger font indicates NWS stations, others are special FIRE CLASS stations.

Given the wealth of available in situ and remote sensing observations, the similarity to the FIRE Cirrus-I focal case study, and the particularly good match in scale and location of the cloud system with the rawinsonde and profiler networks, analysis of this case may yield very useful results on the life-cycle of this cirrus cloud system. We here assess the quality of the meteorological description for this case based on our preliminary analysis of the rawinsonde observations.

2 Observations

Shown in Figure 3 is the sequence of GOES infrared imagery for this case. Development and eastward propagation are evident. By mid-morning (1500 UTC), satellite imagery gives the distinct impression that there were two centers of development: one over the Texas-Oklahoma Panhandle and a second over southern Oklahoma. The latter strongly resembles a ridge-crest cirrus formation (Starr and Wylie 1990) and was distinguishable throughout the day. The fairly sharp upwind boundary of the cloud system could no longer be attributed to the effects of orographic lifting as might have been presumed based on the 1200 UTC imagery (Figure 1). Rather, this feature strongly resembled the clearing-line event described in Starr and Wylie (1990) that marked the end of the ridge-crest cirrus and preceded cirrus development associated with a trailing cold front. The satellite imagery indicates that northeastern Oklahoma, where the aircraft observations were obtained, was a region of cirrus cloud dissipation or minimal cirrus formation. Nonetheless, aircraft observations between 1700 and 1800 UTC near Tulsa indicated cloud top at about 10 km and cloud base near 6 km. Aircraft observers (M. Poellot, personal communication) described the clouds as "not dense but very diffuse" with only small crystals observed near cloud top but larger crystals (200-400 μm) at lower levels. A halo was observed. Upwind of that location, large ice crystals were also observed at about 9 km.

Figure 3: Infrared satellite imagery for 1500, 1800, 2100, and 2400 UTC on 25 November 1991.

Rawinsonde observations from Norman (OUN) indicated a deep humid layer extending from 5 km to above 10 km at 1200 UTC with a similar situation observed at 1800 UTC (Figure 4). Tropopause height declined during the day and a noticeable lowering of the top of the humid layer was observed between 1800 on November 25 and 0000 UTC on November 26

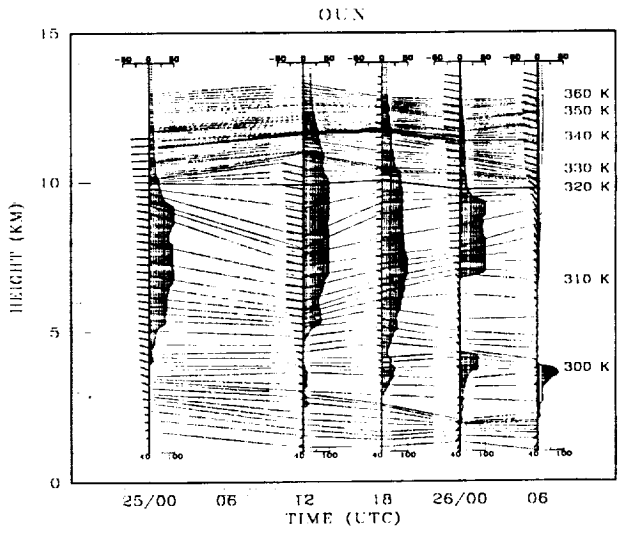

Figure 4: Time series of isentropic surfaces at 1 K intervals, percent relative humidity (shaded), and wind vectors as a function of height (km) from 0000 UTC on 25 November 1991 to 0600 UTC on 26 November 1991. The 320 K isentropic surface, which is used for analysis, is emphasized.

(from 10.5 to 9.5 km). The upper portion of this humid region of cirrus cloud formation exhibited a fairly unstable thermal stratification (*e.g.*, 8–10 km at 1200 UTC as evident by the separation of the isentropes).

An underlying stable zone, located through the lower portion of the moist layer, lifted with time. Overall, the situation resembled overrunning of an elevated warm frontal surface. Ridge passage during the midday hours was indicated by the wind field although wind directions never turned to southerly but rather swung back to northwesterly by 0600 UTC in conjunction with marked drying and clearing of the upper level clouds. We note that observations from Amarillo (AMA) indicate that northwesterly flow and dry conditions also likely existed over OUN between 0000 and 1200 UTC on 25 November (Figure 4). Observations at AMA, OUN, and Little Rock (LIT) yielded a consistent picture.

3 Meteorological Analysis

Regional analyses of the geopotential height, horizontal wind field, relative humidity (upper panel) and vertical motion (lower panel) on the 320 K isentropic surface are shown for 1200, 1800 and 0000 UTC in Figures 5–7. Relative humidity is with respect to ice for temperatures colder than -20C on all figures in this paper. It must be noted that the humidity sensor in the SDD rawinsonde used at many of south-central and southwestern NWS stations is prone to becoming "stuck" once near-ice saturation is encountered in the upper troposphere. This was an unexpected finding. Occasional observations of very high values (supersaturation) can usually be attributed to this sensor problem; nonetheless, the analyzed humidity patterns appear qualitatively correct. The vertical motions fields were derived by applying the adiabatic triangle method of Starr and Wylie (1990) to data from various combinations of NWS rawinsonde stations. Sonde drift was taken into account. The results were then objectively analized to the grid shown here. Estimated accuracy of this technique is generally about $\pm$ 2 cm sec^{-1}.

Excellent correspondence was found between features in the analyzed humidity (shaded for 80% and greater) and vertical motion fields (cross-hatched or shaded for greater than $\pm$ 2 cm sec^{-1}) and the satellite cloud observations. The shape and movement of the system was well-captured. The analyses show strong upward motion ($\sim$ 10 cm sec^{-1}) located at the upwind edge of the cirrus cloud system at 1200 UTC (Figures 1 and 5) with the region of high humidity and cloudiness exetnding eastward to the edge of the leading subsidence zone. At 1800 UTC, the region of high humidity (shaded in Figure 6) still mapped the area of cirrus cloudiness quite well (Figure 3). The analyzed vertical motion field at this time also corresponded quite well with the satellite imagery supporting our interpretation that two centers of cloud formation had developed where the strongest ($\sim$6 cm sec^{-1}) was located in southern Oklahoma and northern Texas. The analyses at 0000 UTC (Figure 7) continued to exhibit good correspondence with the satellite-observed cirrus cloud field. The system had contracted as the vertical motion weakened considerably. A small region of upward motion ($\sim$ 3 cm sec^{-1}) was analyzed at this time corresponding to the band of brightest cirrus cloudiness near Texarkansas. The band of weak upward motion extending through

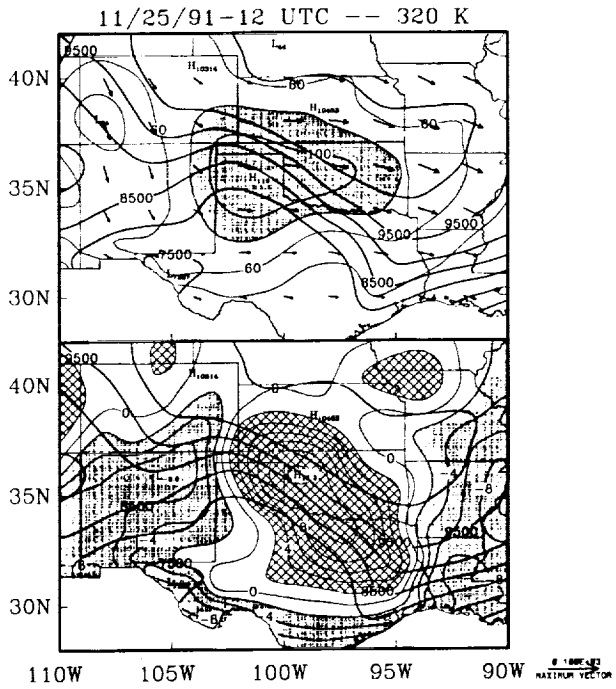

Figure 5: Analysis valid for 1200 UTC on 25 November 1991. Top diagram shows lines of constant geopotential (thick solid) at 500 m intervals, percent relative humidity with respect to ice contoured at 20% intervals (thin solid), and wind vectors for the 320 K isentropic surface. Shaded regions indicate humidity levels exceeding 80%. The bottom diagram also shows lines of constant geopotential (thick solid), as well as vertical velocity (thin solid) contoured at 2 cm sec^{-1} intervals. Hatched regions indicate upward vertical velocities greater than 2 cm sec^{-1}, while shaded regions depict downward vertical velocities exceeding 2 cm sec^{-1}.

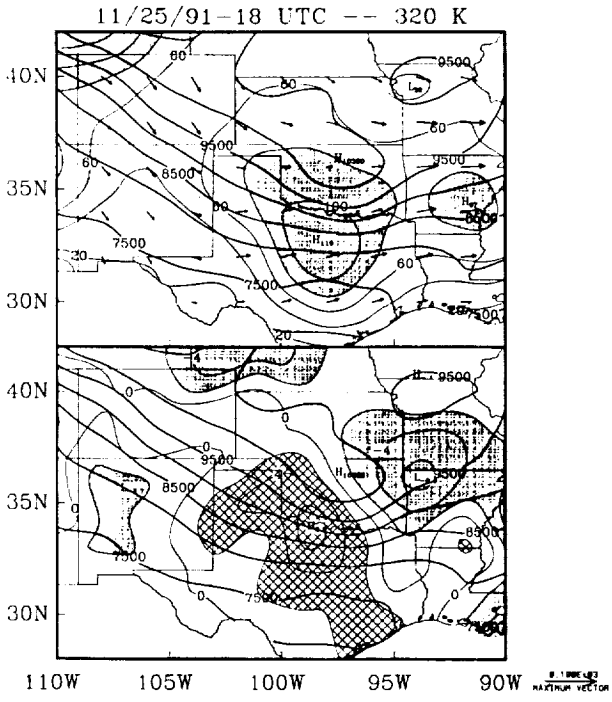

Figure 6: Same as in Figure 5 except at 1800 UTC.

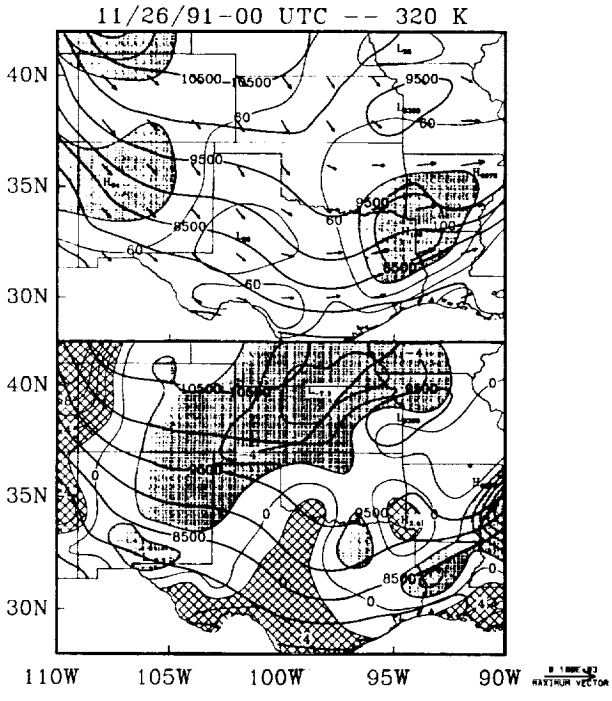

Figure 7: Same as in Figure 5 except at 2400 UTC.

central Texas may correspond to the trailing-cold-frontal zone of cirrus cloud formation seen in Starr and Wylie (1990). However, the air was too dry in the present case to allow cloud formation at this time. Such development did occur on the following day (Mace and Ackerman 1993).

4 Conclusions

Preliminary meteorological analysis of synoptic scale rawinsonde data for the 25 November 1991 FIRE Cirrus-II cirrus system over Oklahoma revealed excellent correspondence between the satellite observed cloud patterns and the observed humidity and diagnosed vertical motion patterns for this ridge-crest cirrus cloud system. The spatial and temporal evolution of this moderately-sized system appears to have been well-captured. The analyses reveal that the extensive in situ observations of cirrus cloud microphysical and radiative structure over northern Oklahoma were likley made in a region of cirrus cloud dissipation or very minimal cloud generation. Nonetheless, the similarity to the FIRE Cirrus-I focal case study and the particularly good match in scale and location of the cloud system with the rawinsonde and profiler networks indicates that further analysis of this case may yield very useful insights on the life-cycle of this cirrus cloud system. In the future, we intend to integrate our analyses with quantitative analyses of the satellite and aircraft observations and compare these results to the output of suitably initialized/forced numerical simulations of cirrus cloud life-cycle for this case.

5 Acknowledgments

The authors wish to thank Gerald Mace (Penn State University) for providing access to the satellite imagery.

6 Reference

Mace, G.G., and T.P. Ackerman, 1993: Cirrus cloud development in a mobile upper tropospheric trough: The November 26 FIRE Cirrus case study. (this document)

Starr, D.O'C., and D.P. Wylie, 1990: The 27-28 October 1986 FIRE Cirrus case study: Meteorology and clouds. *Mon. Wea. Rev.*, **118**, 2259-2287.

S37-47
197537
p 5

N94-22329

Cirrus Cloud Development in a Mobile Upper Tropospheric Trough: The November 26th FIRE Cirrus Case Study

Gerald G. Mace and Thomas P. Ackerman

Department of Meteorology
The Pennsylvania State University
University Park, PA 16802

1. Introduction

The period from 18 UTC 26 November 1991 to roughly 23 UTC 26 November 1991 is one of the study periods of the FIRE II field campaign. The middle and upper tropospheric cloud data that was collected during this time has allowed FIRE scientists to learn a great deal about the detailed structure, microphysics and radiative characteristics of the mid latitude cirrus that occurred during that time. Modeling studies that range from the microphysical (Mitchell et al., this issue) to the mesoscale (Jensen et al. , this issue) are now underway attempting to piece the detailed knowledge of this cloud system into a coherent picture of the atmospheric processes important to cirrus cloud development and maintenance. An important component of the modeling work, ether as an input parameter in the case of cloud-scale models, or as ouput in the case of meso and larger scale models, is the large scale forcing of the cloud system. By forcing we mean the synoptic scale vertical motions and moisture budget that initially send air parcels ascending and supply the water vapor to allow condensation during ascent. Defining this forcing from the synoptic scale to the cloud scale is one of the stated scientific objectives of the FIRE program.

from the standpoint of model validation, it is also necessary that the vertical motions and large scale moisture budget of the case studies be derived from observations. We consider it important that the models used to simulate the observed cloud fields begin with the correct dynamics and that the dynamics be in the right place for the right reasons.

2. Data, Data Processing and Objective Analysis

The FIRE Cirrus hub in Coffeyville, Kansas was uniquely positioned near the center of a large observational array of wind profilers and radiosonde sites. Spacing between wind profilers in this region was on the order of 175 km. This spacing increased to approximately 400 km away from the hexagonal array of wind profilers in central Oklahoma and southern Kansas. The wind profilers provided six minute radial velocities for each of their three beams (two oblique and one vertical) from 500m above ground level to 16.25 km above ground level with vertical resolution of 250m up to approximately 7 km and 1 km resolution to 16.25 km. The six-minute radial velocity data were processed using a mode filter and consensus averaging. The data were averaged to the top of each hour. The consensus average required that at least four of the ten six minute observations in a sixty minute period be within a predefined range. Otherwise the data were flagged as missing.

The radiosonde data consisted of five Chain Link Atmospheric Sounding System (CLASS) sites as well as supplemental radiosonde data provided by the conventional National Weather Service radiosonde network. During this particular cloud event the 15 NWS radiosonde sites nearest Coffeyville and the CLASS sites were launching radiosondes at three hour intervals, while the remainder of the radiosonde network in the western 2/3 of nation was launching balloons at six hour intervals. The raw NWS radiosonde data were processed at full vertical resolution using techniques designed by Starr and Lare (personal communication) and the raw CLASS data were filtered for erroneous data by the National Center for Atmospheric Research.

Combining the wind profiler and radiosonde datasets into a single product is necessary for further analysis. Both networks have a horizontal resolution that is very coarse relative to most mesoscale models. However, the vertical resolution of both the rawinsonde and the wind profiler data and the temporal resolution of the wind profiler data is a significant advantage of the large-scale datasets collected during FIRE II.

In order to successfully combine the wind profilers and radiosonde datasets into a single

product, we must account for the differences in the two observational platforms. The wind profilers provide a close approximation to true vertical and temporal averages over single vertical columns. The radiosonde data, on the other hand, represents point measurements spread over some finite flight period along a vertical column tilted upshear. In a spatially and temporally enhanced rawinsonde network both the flight time and the instrument drift become significant factors in accurate data analysis.

Since the wind profiler data exist at hourly intervals and 250 m vertical resolution, our goal is to generate regional analyses valid at the nominal radiosonde launch times with 250 m vertical resolution. We chose to retain physical height coordinates in this analysis since no information exists in the wind profiler data to map it unambiguously onto an alternate vertical coordinate. On the other hand, the radisonde data contain sufficient information to place it on any vertical coordinate we choose.

Since the wind profiler data reprsent true layer-mean quantities, the first step in the objective analysis process requires vertical averaging of the radiosonde data. For the radiosonde data, we average individual observations 125m above and below the nominal height level. This averaging is performed with all the radiosonde data components including the latitude, longitude and time of each measurement. A time series of vertically averaged data are created by combining several soundings from a given location into a time-height array. This time series is then used to linearly interpolate the data at each level to the nominal sounding time. The actual launches occur generally 30-60 minutes before the nominal time and, depending on the ascent rate, may last 1-2 hours. It is important to note here that each data level of the time-interpolated, vertically averaged sounding retains a similarly interpolated latitude and longitude. This method, which is similar to one described by Frankhauser (1969), effectively accounts for both the drift in the radiosonde during flight and also the time interval of the ascent. Thus, displacement of the observations in both space and time will not add error to the horizontal or temporal derivitives necessary for further analysis.

We combine the wind profiler and radiosonde winds at this stage into a single dataset that is mapped to a one degree latitude and longitude grid using a bilinear interpolation scheme described by Hiroshi (1978). This procedure is performed at each data level from sea level to 16 km.

Since no account has been taken of observational error or of observed meteorological signal below the temporal or spatial scale of the observing netwrok it is important that a filtering technique be applied. As shown recently by Davies-Jones (1993) and by Thiebaux and Pedder (1987), over-determined polynomial fitting techniques are able to smooth observational fields, effectively decreasing random uncertainty and maximizing the desired atmospheric signal. Therefore, after mapping the observations to the grid, each interior gridpoint is smoothed by fitting an over determined plane to the gridpoint in question and to 12 unsmoothed surrounding gridpoints using ordinary least squares regression techniques. The over-determined plane minimizes the sum of squared residuals between the analysis and observational values. The slope of this plane in horizontal space also defines the spatial derivatives of the quantity at the central gridpoint. This technique removes much of the random observational error and small scale atmospheric signal. What remains is a synoptic scale analysis with horizontal resolution of about 2.5 x 2.5 degrees.

In order to gauge the effectiveness of the objective analysis technique, we performed the

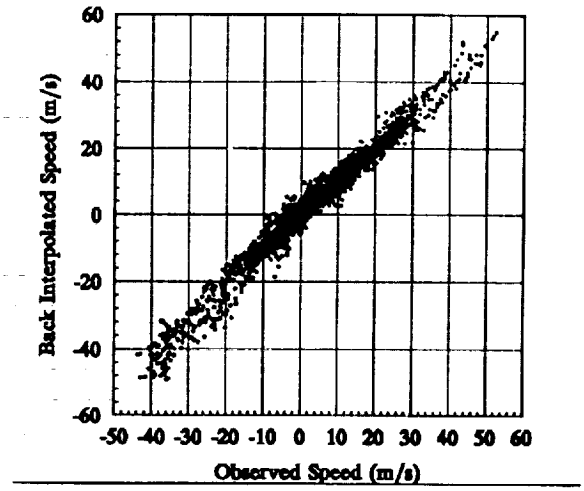

Figure 1. Scatter plot comparing the profiler observed horizontal wind components with the wind components interpolated to the profiler locations using the objective analysis techniques described in the text and data valid at 18 and 21 UTC 26 November 1991.

C-3

analysis as described above and then back interpolated the horizontal wind data at each analysis level to the wind profiler locations. The interpolated horizontal wind components were then compared with the observed horizontal wind components. The result is shown in Fig. 1. We find that the analysis technique closely fits the observations. The linear correspondence is strong in this plot with a correlation coefficient of 0.97. The root mean square difference between the observations and the objectively analyzed values is 2.5 m/s. Strauch et al. (1989) compared horizontal winds measured by two sets of orthogonal beams in a five beam profiler and found the RMS of the observations to be on the order of 2 m/s. Also, Benjamin (1991) reports that a similar comparison of the MAPS analyses and NGM analyses to radiosonde wind observations have an RMS difference of 4.0 and 5.1 m/s respectively. The objective analysis technique we describe fits the data more closely than MAPS or the NGM but still accounts for the RMS uncertainty in the observations.

3. The November 26th Case Study

The middle and upper tropospheric cloud band that was sampled during the local afternoon of 26 November 1991 was closely coupled to the synoptic scale dynamics embedded in the exit region of the strong northwesterly jet stream evident in Fig. 2. The jet extended from a ridge in the northwestern United States southeastward into the Texas Panhandle and a jet streak of 63 m/s was propagating southeastward near the flow inflection point in eastern Colorado. Immediately downstream of the jet core a difluent trough axis extended from eastern Texas northward into the Dakotas. Analysis of the Geopotential height field (not shown) shows that the trough axis had a well defined southeast-northwest tilt. This situation bears strong resemblance to a classic description of an upper jet-front system propagating through a synoptic scale baroclinic wave presented by Shapiro (1983) and Keyser and Shapiro (1987). This stage of development is marked by barotropic amplification through the tilt in the height field and by baroclinic amplificaition indicated by the weak cold advection in the northwesterly flow (Keyser and Shapiro, 1987). The amplification process is displayed quite markedly by examining the evolution of the dynamics between 18 UTC and 21 UTC. Fig. 3 shows a vertical east-west cross section of relative vorticity at 18 and 21 UTC. The cross section extends from the jet core in southeastern Colorado across the trough axis north of the Kansas-Oklahoma border and into the difluent zone in western Missouri. The vorticity pattern shows a region of cyclonic vorticity extending through the depth of the troposphere and situated from the jet core eastward into the difluent trough with maximum amplitude near 10 km. The vertical structure of the relative vorticity is nearly identical to that reported by Sanders (1988) in an observational study of mobile troughs in the upper westerlies. He found that upper tropospheric

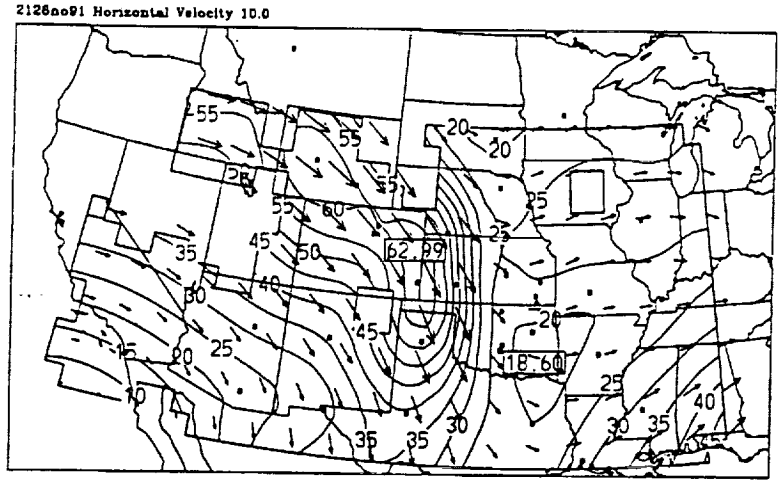

Fig. 2. 10 km horizontal winds at 21 UTC 26 November 1991. The contours are of wind speed in m/s and the vectors are compass direction with the length of the vector corresponding to the speed of the horizontal wind. The small squares within the analysis region represent the positions of radiosonde and wind profiler wind observations used in the objective analysis scheme .

mobile troughs tended to amplify preferentially leeward of the major topographic regimes in the northern Hemisphere and had length scales on the order of 2500 Km. Similarly, Whitaker and Barcilon (1992) argued from a theoretical basis that these mobile troughs with maximum amplitude in the upper troposphere tended to amplify under conditions of weak low-level baroclinicity, large low level static stability and large surface roughness.

The evolution of the vorticity pattern associated with the jet-trough system is clearly evident. The entire pattern appears to progress eastward during the three hour period while the amplitude of the disturbances changes very little in the middle and lower troposphere. However, a significant amplification of the disturbance occurs between 8.5 and 12 km.; the maximum vorticity increases from 15 to 19 /s in three hours. The negative vorticiity values in the flanking migratory ridges show little change aside from a eastward progression during the period.

The vertical velocity was calculated as a residual from the first law of thermodynamics assuming adiabatic flow. Results at 7.5 km are shown in Fig. 4. At 18 UTC weak rising motion is diagnosed in eastern Oklahoma and Kansas while relatively strong subsidence occurred in eastern New Mexico and west Texas. Amplification of the vertical motion pattern occurred by 21 UTC. The subsidence center had more than doubled in intensity and was oriented near the left front exit region of the advancing northwesterly jet streak. The region of rising motion in the difluent trough had also intensified, more than doubling in magnitude in eastern Kansas and northeastern Oklahoma. Cross sections of the adiabatic vertical velocity show a similar amplification of the vertical motion pattern through much of the troposphere between 18 and 21 UTC.

The cloud system extended from Nebraska to eastern Texas along and ahead of the strong horizontal shear associated with the advancing jet. Cirrus was first observed between 8 and 9 km over Coffeyville by cloud radar at approximately 18 UTC. The advancing cirrus quickly thickened to include the layer between 6 and 9 km. Bases descended to 2-3 km after 21 UTC while the cloud tops remained near 9 km. Reflectivities through the depth of the cloud system also increased after 21 UTC. As the strong subsidence zone moved over southeastern Kansas, skies cleared over Coffeyville after 23 UTC .

3. Conclusions and Future Work

The evolution of the cloud system extensively observed on 26 November can be seen as a response to vertical circulations associated with synoptic scale forcing. As the rapidly advancing jet streak passed the flow inflection point after 18 UTC, the system became predisposed to large scale amplification through the orientation of the trough axis and cold air advection. The strong gradient in velocity insured that parcels exiting the jet were strongly

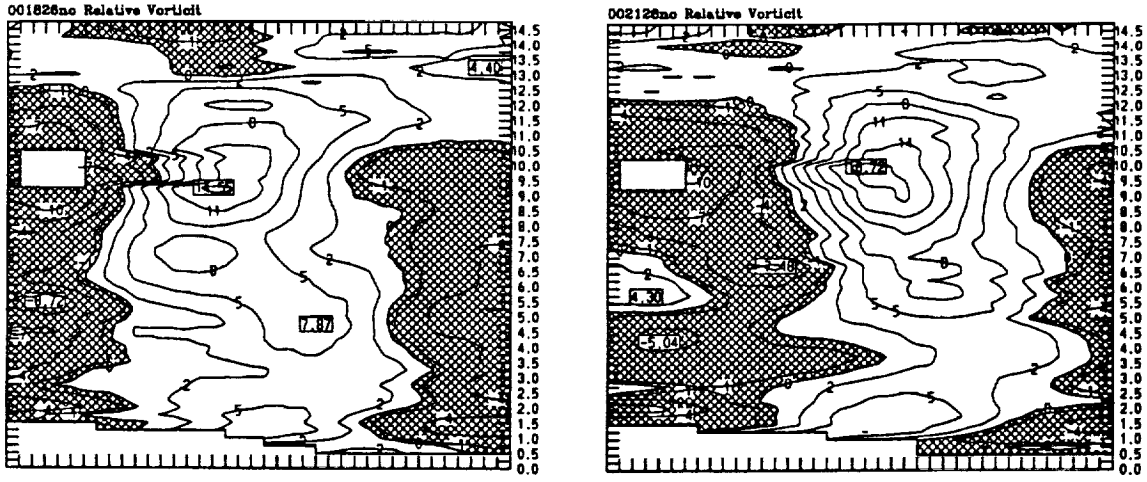

Fig. 3. Cross sections of the vertical component of the relative vorticity for a) 18 UTC 26 Nov 91 and b) 21 UTC 26 Nov 91. The cross sections extend in an east west line from south-central Colorado to southwestern Missouri. The location of Coffeyville, Kansas is marked with an arrow on each plot. Units are in 10^{-5} s^{-1} and negative values are shaded.

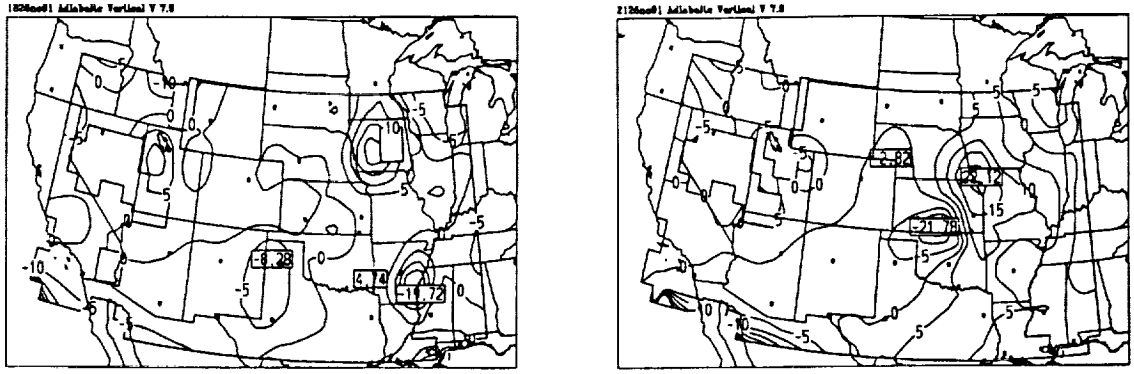

Fig. 4. Adiabatic vertical velocity for a) 18 UTC 26 Nov 91 and b) 21 UTC 26 Nov 91. Units are cm s^{-1}

ageostrophic as they passed through the difluent trough. The geostrophic adjustment process then contributed to upper level divergence and vertical motion.

Our future plans with this particular case study include investigating the source of the synoptic scale forcing in more detail. This includes examining the contributions of thermal advection and flow curvature on the vertical circulations that are evident from the present analysis. It is also necessary to show how the large scale water vapor budget contributed to the formation of the cloud system. Finally it is necessary to quantify the response of the macroscale cloud system to the dynamical forcing. This will be pursued using geostationary satellite imagery and cloud radar data.

Acknowledgments: This research was supported in part by NASA grants NAG-1-1095 and NAG-1-999 and by DOE grant DE-FG02-90ER61071. This work was done while one of us (GM) held a NASA Goddard Graduate Student Fellowship.

References

Davies-Jones, R. 1993: Useful formulas for computing divergence, vorticity, and their errors from three or more stations. *Mon. Wea. Rev.*, **121**, 713-725.

Hiroshi, A. 1978: A method of bivariate interpolation and smooth surface fitting for values given at irregularly distributed points. ACM-TOMS, Vol. 4, No. 2, June 1978.

Jensen, E. J., O. B. Toon, D. L. Westphal, 1993: Three dimensional modeling of cirrus during the 1991 FIRE IFO II: detailed process study. this issue

Keyser, D. and M. A. Shapiro, 1987: A review of the structure and dynamics of upper-level frontal zones. *Mon. Wea. Rev.*, **114**, 452-499.

Mitchell, D. L., S. K. Chai, Y. Dong, W. P. Arnott, J. Hallett, and A. J. Heymsfield, 1993: Importance of aggregation and small ice crystals in cirrus clouds, based on observations and an ice particle growth model. this issue

Sanders, F. 1988: Life history of mobile troughs in the upper westerlies. *Mon. Wea. Rev.*, **116**, 2629-2648

Shapiro, M. A., 1983: Mesoscale weather systems of the central United States. *The National STORM Program: Scientific and Technological Bases and Major Objectives*, R. A. Anthes, Ed., University Corporation for Atmospheric Research, P. O. Box 3000, Boulder, CO 80307, 3.1-3.77.

Thiebaux, H. J., and M. A. Pedder, 1987: *Spatial Objective Analysis*. Academic Press, 299 pp.

Whitaker, J. S., and A. Barcilon, 1992: Genesis of mobile troughs in the upper westerlies. *J. Atmos. Sci.*, **49**, 2097-2107.

538-47
197538
N94-22330

VERTICAL VELOCITY IN CIRRUS CASE OBTAINED FROM WIND PROFILER

Ran Song and Stephen K. Cox
Department of Atmospheric Science
Colorado State University
Fort Collins, CO 80523

1. INTRODUCTION

Cirrus clouds play an important role in the climate and general circulation because they significantly modulate the radiation properties of the atmosphere. However understanding the processes that govern their presence is made difficult by their high altitude, variable thickness, complex microphysical structure, and relatively little knowledge of the vertical motion field.

In the FIRE II experiment, a 404MHz wind profiler was set up to provide continuous measurements of clear air wind field at Parsons, Kansas. Simultaneously, the NOAA wind profiler network supplied a wider spacial scale observation. On Nov. 26, 1991, we had the most significant cirrus cloud phenomena during the experiment with a jet streak at 250 Mb. Analyses of the vertical wind velocity are made by utilizing different methods based on wind profiler data, among them the direct measurements from CSU wind profiler and NOAA network wind profilers, VAD(Velocity Azimuth Display) technique and the kinematic method.

On Nov. 26, the Parsons' site was just at the cold exit region of the jet streak which is shown in Fig.1. According to the conceptual model of a jet streak by Mattocks and Bleck (1986) (MB) shown in Fig.2, the vertical velocity should have from ascent below to descent above the height of the maximum horizontal wind. An agreement between the observations in the cold exit area and the conceptual model is shown first time using high resolution wind profiler data.

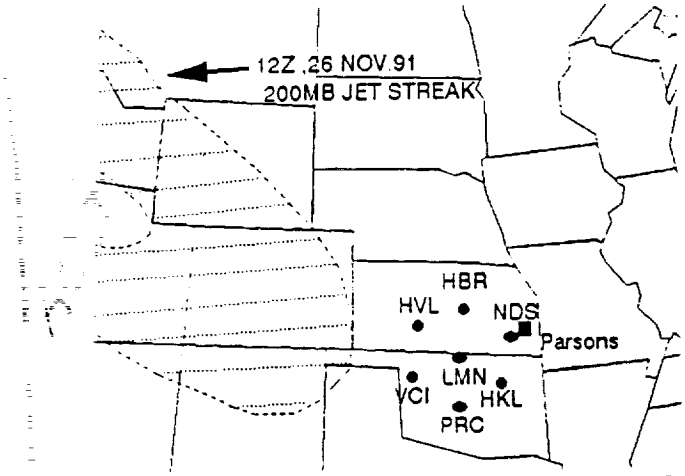

Figure 1. Location of CSU wind profiler(square) and some of the network stations(circle). The 1200Z jet streak is denoted by shaded area.

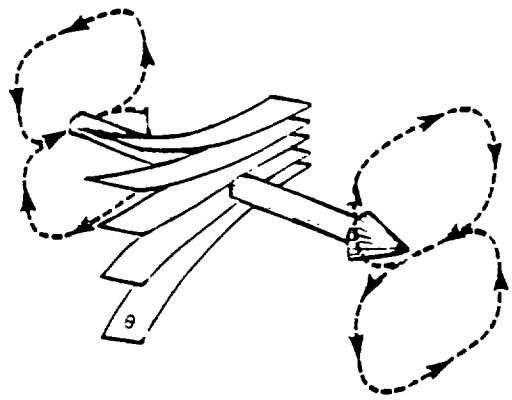

Figure 2. Three-dimensional schematic of the circulation induced by a jet streak. (from Mattocks and Bleck, 1986)

2. METHODS

2.1 Direct Doppler Method:

The CSU wind profiler was operated in a 10-minute cycle which consists of measurements along five directions: one pointing vertically with the other four beams tilted 15° from zenith toward east, north, west and south. The NOAA network radars had three directions of operation (one vertical, two tilted away from zenith toward east and north respectively) with a 6-minute cycle. The direct Doppler method deduces vertical velocities from the radial velocities of the

vertical beam. In the past, several works (Larsen et al.,1991a,b; Yoe et al.,1992) have shown the uncertainties in direct measurements of vertical velocity and have also given some comparisons between these radar direct measurements and other data sources or other techniques based on radar data.

2.2 VAD Method:

The VAD method was originally derived to retrieve horizontal wind components from the radial velocities of a radar azimuth scan (Browning and Wexler 1972; Wilson and Miller 1972). By applying the mass continuity equation under assumption that air density is locally stationary and horizontally strtified, one can derive the vertical components of wind fields (Larsen et al. 1991; Doviak and Zrnic 1984). In our experiments, the CSU wind profiler's five-beam data was employed in a quasi-VAD technique.

The VAD sampling scheme is shown in Fig.3, U is the horizontal wind vector, and w is the vertical velocity. In ideal cases, which have a nearly linear horizontal wind field within the measurement circle so that the components u, v and w are well approximated by the zeroth- and first-order terms of a Taylor series, the measured radial velocity at sampling points will fit a sine curve as shown in the lower panel. Here, the offset C_0 at each height is equal to the average of radial velocities at all sampling points in one circle at that height and can also be expressed as equation(1) through a Taylor expansion (Larsen et al., 1991).

$$C_0 = [\, w + \frac{z}{2} \tan^2\theta (\nabla_h \cdot U)] \cos\theta \qquad (1)$$

By assuming the density is stationary in time locally and that the medium is horizontally stratified, we write the mass continuity equation:

$$\nabla_h \cdot \rho U = \rho \nabla_h \cdot U = -\frac{\partial}{\partial z}(\rho w) \qquad (2)$$

Combining the above equations and integrating the differential equation from an upper height boundary z_T by assuming zero w at z_T, we have equation (3):

$$-(\rho w)_z + \frac{2\cos\theta}{\sin^2\theta}\int_z^{z_T} \frac{\rho C_0}{z} dz - 2c\tan^2\theta \int_z^{z_T} \frac{\rho w}{z} dz = 0 \qquad (3)$$

Eq.(3) can be solved numerically for w, the vertical velocity.

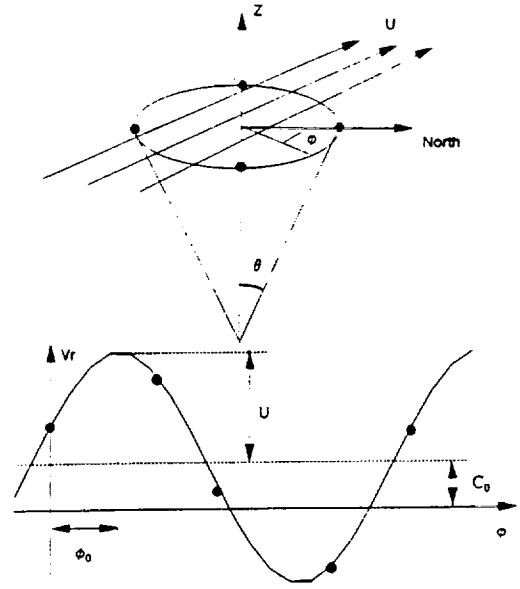

Figure 3.Schematic of the VAD sampling and sine curve fitted by the sample data.

2.3 Kinematic Method:

The kinematic method was carried out by Bellamy(1949) as an objective calculation of divergence and vertical velocity. In this method, we have an assumption that the wind field is a linear function of space between the observation points which are non-collinear located. Then the horizontal divergence can be calculated from the rate of change of the outflow through the unit vertical sides of the volume. The vertical velocity in height coordinates can be computed based on the known horizontal divergence and mass continuity equation by assuming incompressible air medium (cf. Bellamy,1949). In this study, we use NOAA network stationd NDS, HBR and LMN to form a triangular area(Fig.1).

3. RESULTS AND DISCUSSIONS

As described in the above section, three methods are used to derive vertical velocity. They are the direct doppler measurement, VAD and kinematic method. Figs.4, 5 and 6 are the 3-period averaged vertical velocities from the direct doppler measurements of the CSU and network wind profiler at NDS, and also the VAD calculation. The appearance of thin cirrus clouds was confirmed by lidar from about 1600Z, and after 1820Z, clouds became much thicker with

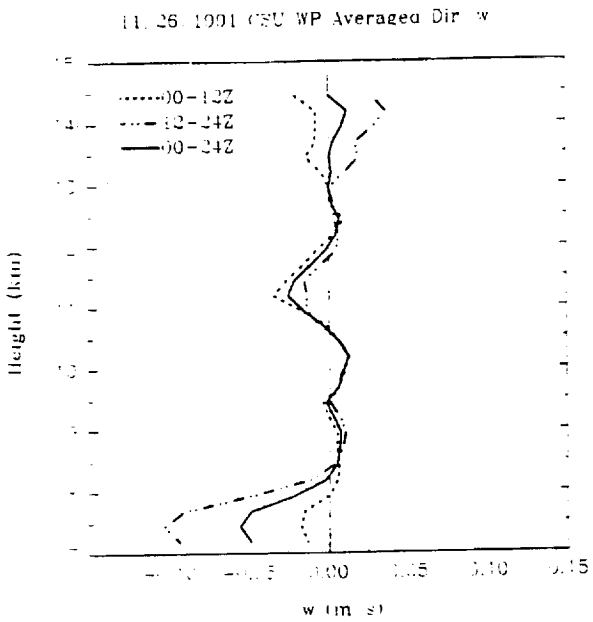

Figure 4. Profiles of averaged vertical velocity measured in the vertical beam of CSU wind profiler at Parsons on Nov. 26, 1991

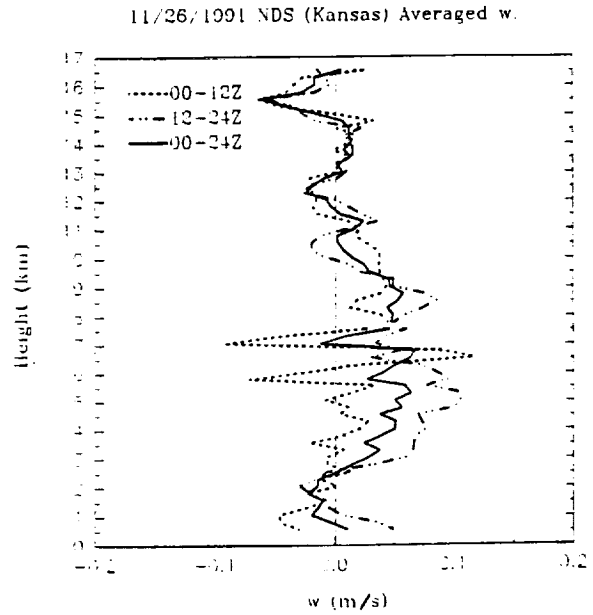

Figure 5. As same as Fig.4, but from network profiler at NDS.

cloud tops consistently at about 10km and bases down to 8km and even lower. All plots in Figs.4, 5 and 6 present the evidence of a continuously upward motion in this layer. Since both CSU and network wind profilers are operating at 404MHz, which corresponds to a wavelength of 75cm, ice particles are expected to be relatively transparent to the profiler radars.

Above the cloud, the 12-24Z averaged plots exhibit a change from upward motion to downward motion at slightly different locations: 10.7km for CSU direct measurement, and about 9.95km for both NDS direct measurement and CSU VAD calculation. In MB model, this reversal is expected to be close to the maximum horizontal wind level(Fig.2). A vertical cross section(from (30°N,110°W) to (45°N,90°W)) perpendicular to the jet streak indicates the maximum wind layer is located at 10.5km (Fig.7). The observations agree extremely well with the model study.

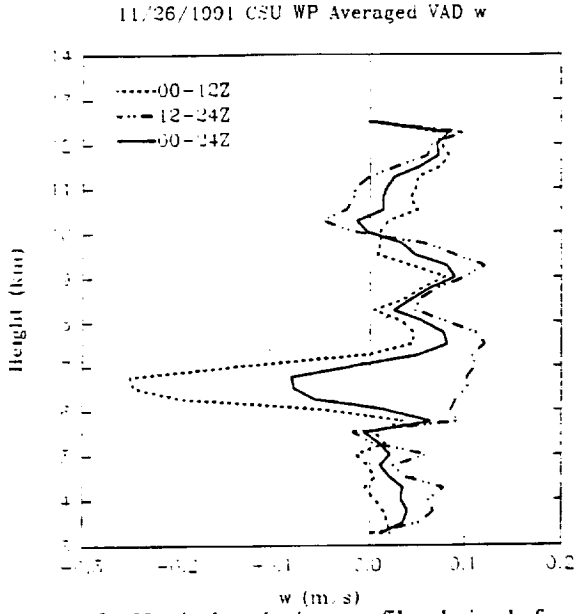

Figure 6. Vertical velocity profile derived from VAD. Parsons, Nov. 26, 1991.

Fig.8 presents the time-height contouring of the vertical velocity derived from the kinematic method. A very thick line which clearly separates the downward motion and upward motion is evident. The figure shows this change at cloud level starting from about 1400Z which was shortly before clouds were detected by the lidar. This reversal level settled at about 10km from 1700Z to 2000Z, which is what is expected according to the MB model. From 2000Z, this level dramatically dropped down to lower levels after the jet streak already passed over the area.

ORIGINAL PAGE IS
OF POOR QUALITY

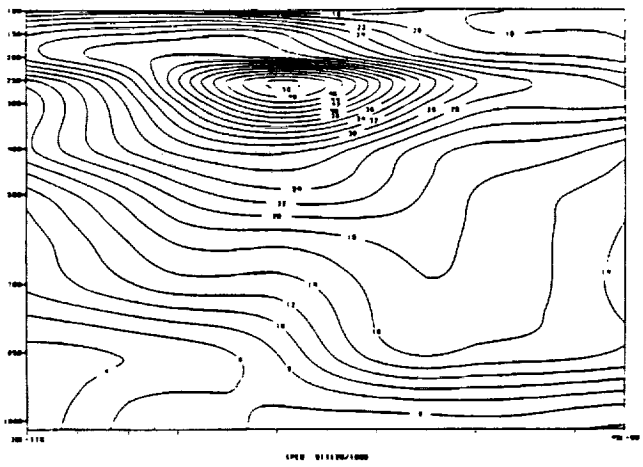

Figure 7. vertical velocity w(m/s) derived from the kinematic method on Nov.26,1991.Dash line is negative w; thin solid line is positive w; thick solid line is zero w.

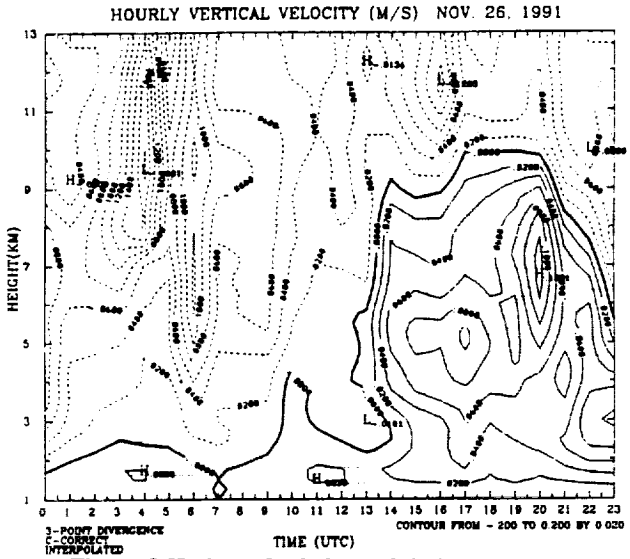

Figure 8. Horizontal wind speed (m/s)contours in a vertical cross section perpendicular to the jet streak at 1800Z, Nov. 26, 1991.

4.CONCLUSIONS:

The study in this paper shows good consistencies among vertical velocity measurements-from the direct doppler method, VAD method and kinematic method. And the observation results agree very well with the theoretical model. Upward air motions exist at and below the cirrus cloud layer with weaker downward motions above. More confidence is gain for utilizing wind profiler data in our future researches.

5. ACKNOWLEDGEMENTS

This research has been supported by National Aeronautics and Space Administration under Grant NAG 1-1146, The Department of Energy under Contract No.DE-FG02-90ER60970.

6. REFERENCES

Bellamy, J.C., 1949: Objective calculations of divergence, vertical velocity and vorticity. *Bul. Am. Mrt. Soc.*, **30**, 45-49

Browning, K.A., and R.Wexler, 1972: A determination of kinematic properties of a wind field using Doppler radar. *J. Appl. Meteor.*, 7, 105-113.

Doviak, R.J., and D.S. Zrnic, 1984: *Doppler Radar and Weather Observations*. Academic Press, 458 pp.

Larsen, M.F., S. Fukao, O. Aruga, M.D. Yamanaka, T. Tsuda and S. Kato, 1991a: A comparison of VHF radar vertical-velocity measurements by a direct vertical-beam method and by a VAD technique. *J. Atmos. Oceanic. Technol.*, **8**, 766-776

Larsen,M.F.,and J.Rottger,1991b:VHF radar measurements of in-beam incidence angles and associated vertical-beam radial velocity corrections. *J. Atmos. Oceanic Technol.* **4**, 477-490

Mattocks, C. and R. Bleck, 1986: Jet streak dynamics and geostrophic adjustment processes during the initial stages of lee cyclogenesis. *Mon. Wea. Rev.*, **114**, 2033-2056

Wilson, D.A., and L.J. Miller, 1972: Atmospheric motion by Doppler radar. Chapter 13, *Remote Sensing of the Troposphere*, V. E. Derr, Ed., U.S. Department of Commerce, NOAA (13)1-(13)34.

Yoe,J.G., M.F.Larsen and E.J. Zipser,1992: VHF wind-profiler data quality and comparison of methods for deducing horizontal and vertical air motions in a mesoscale convective storm. *J. Atmos. Oceanic Technol.*, **9**, 713-727

Omit

Vertical Velocities in Cirrus Clouds

Taneil Uttal and Brad Orr

NOAA/ERL Wave Propagation Laboratory
R/E/WP6
325 Broadway
Boulder, Colorado 80302

Model simulations and aircraft observations indicate that there is a close relationship between the microphysical structure and the dynamic structure of cirrus clouds. Observing the small scale dynamic structure of cirrus clouds has been difficult, especially spatial and temporal scales necessary to resolve small scale oscillations. The NOAA Wave Propagation Laboratory operated a scanning, Doppler 8 mm radar during the FIRE II project. Theoretical calculations of velocity variance indicate that this radar should be able to resolve vertical velocities with an accuracy of ± 2 cm s^{-1}, and examination of the data indicate that estimates are no worse than ± 5 cm s^{-1}. The Doppler velocities are corrected for particle fall speed based on radar reflectivities to achieve an estimate of true air motions. Brunt Vaisala frequencies and Richardson numbers are calculated to compare to observed oscillations.

ORIGINAL PAGE IS
OF POOR QUALITY

539-47
197539
p. 4

N94-22831

Mesoscale Simulations of the November 25-26 and December 5-6 Cirrus Cases using the RAMS Model

J.L. Harrington, Michael P. Meyers, and William R. Cotton

Colorado State University, Dept. of Atmospheric Science, Fort Collins, CO 80523

May 7, 1993

1 Introduction

The Regional Atmospheric Modeling System (RAMS), developed at Colorado State University, was used during the First ISCCP Regional Experiment (FIRE) II (13 November through 6 December, 1991) to provide real time forecasts of cirrus clouds. Forecasts were run once a day, initializing with the 0000 UTC dataset provided by NOAA (Forecast Systems Laboratory (FSL) Mesoscale Analysis and Prediction System (MAPS)). In order to obtain better agreement with obsevations, a second set of simulations were done for the FIRE II cases that occured on 25-26 November and 5-6 December. In this set of simulations a more complex radiation scheme was used, the Chen/Cotton radiation scheme, along with the nucleation of ice occuring at ice supersaturations as opposed to nucleation occuring at water supersaturations that was done in the actual forecast version. The runs using these more complex schemes took longer wall clock time (7-9 hours for the actual forecasts as compared to 12-14 hrs for the runs using the more complex schemes) however, the final results of the simulations were definately improved upon. Comparisons between these two sets of simulations are given in a following section.

Now underway are simulations of these cases using a closed analytical solution for the auto-conversion of ice from a pristine ice class (sizes less than about 50 μm in effective diameter) to a snow class (effective diameters on the order of several hundered μm. This solution is employed along with a new scheme for the nucleation of ice crystals due to Meyers et al (1992) and Demott et al (1993). The scheme is derived assuming complete gamma distributions for both the pristine and snow classes. The time rate of change of the number concentration and mass mixing-ratio of each distribution is found by calculating either the flux of crystals that grow beyond a certain critical diameter by vapor deposition in an ice supersaturated regime or by calculating the flux of crystals that evaporate to sizes below that same critical effective diameter.

2 The Model Description

The purpose of this section is to give a brief description of the set-up of RAMS that was used for the FIRE II experiment. As was mentioned earlier RAMS was initialized with the 0000 UTC MAPS data set because of it's 60 km grid spacing. The set-up of the model included two interactive grids. The first being a course grid of 80 km grid spacing that covered approximately three quarters of the western U.S. The second, fine grid was placed so that it completely covered Kansas and portions of it's boardering states. The fine grid spacing was set to be 20 km. For the vertical resolution, 42 total levels were used with 300m constant spacing up to 9 km. Beyond 9 km the 300 m spacing was slowly stretched until at 16 km the vertical spacing reached 1000 m. For all of the runs, the non-hydrostatic version of RAMS was used with explicit bulk microphysics. Because of the complexity and time considerations, the simulations were done on the National Center for Atmospheric Research's (NCAR'S) CRAY YMP.

3 Comparison of RAMS Forecast Results and Chen/Cotton Radiation Results with Observations

On November 26, 1991 Lidar time height observations (see figure 1) began to pick up cirrus signatures at around 1615 UTC and at a height of about 10km. The cirrus gradually thickend with time; the cloud top remained fairly constant at 10km until around 2024 when it began to vary between values of about 9 and 11 km. The base of the cloud gradually lowered after onset until it reached it lowest point of about 4 km at around 2330 UTC.

Comparing the forecast simulations of the time height profile (Figure 2) with the lidar images shows that the forecast runs were fairly successful in depecting the onset of the cloud and it's basic thickness. The cloud height depicted in the simulation results was a little lower than the 10 km that was observed and the forecast model did not show the low base that the cloud finally achieved. Also, as was noted by Thompson (1993) the mixing ratio values were too small (about one order of magnitude). The simulations that included the more complex radiation scheme (Figure 3) did a noticably better job in the simulation of the time-height cloud profile. Cloud top was at an approximately constant value of 10 km and showed the cloud base lowering; the lowering of the cirrus base was, however, simulated to drop a little below the observed values (about 3.8 km). Another significant improvement was that of larger values of the pristine ice mixing-ratio. Maximum values in the forecast simulation were around 1.8×10^{-6} while the simulations with the Chen/Cotton radiation scheme gave maximums of 0.32×10^{-5}.

Comparison with the satillite image shown in Figure 4 shows that the simulations that included the Chen/Cotton radiation scheme (see Figure 5) predicted the overall placement of the cirrus deck over Kansas very well. The Chen/Cotton scheme has a much lower pristine ice mixing-ratio than the forecast version (not shown), however this is due to the height that the cross-section was taken, maxima in the mixing ratios were as given above.

4 The Auto-Conversion Scheme

As mentionted in the introduction, the auto-conversion scheme is derived assuming that both pristine ice (PI) and snow can be described by complete gamma distributions of the form

$$(1) \qquad n_{pi,s}(D) = \frac{N_t}{\Gamma(\nu)} \frac{D}{D_n} \frac{1}{D_n} exp(\frac{-D}{D_n})$$

where N_t is the total number, ν is the shape parameter, and D_n is the characteristic diameter of the crystal distribution. Using (1) the mass mixing-ratio and total number are defined as:

$$(2) \qquad \bar{r}_{pi,s} = \frac{1}{\rho_a} \int_0^\infty m(D) n_{pi,s}(D,t) dD$$

$$(3) \qquad N_{pi,s}(D,t) = \int_0^\infty n_{pi,s}(D,t) dD$$

where the subscripts pi and s describe the pristine ice and snow distribution respectively. Equations for the flux of vapor onto or away from the total distributions, flux of number and mass from one distribution to another (auto-conversion), and number concentration that evaporates from the PI distribution are derived. Only for vapor depositional growth is considered. The equations for the growth/evaporation of the mass of the complete distributions is calculated by time differentiating (2) above and substituting in the depositional growth equation. For the flux of mass and number, the equations were rewritten in flux form by using the relation

$$(4) \qquad \frac{\partial n(D,t)}{\partial t} = -\frac{\partial}{\partial t}\{I(D,t) n(D,t)\}$$

where I(D,t) is the time derivative of the effective diameter. This relation is then substituted into the time differentiated versions of (2) and (3) above and gives the number and mass of crystals that flux from the PI to the snow distribution during growth conditions or from the snow to the PI distribution during evaporation

conditions. Nucleation of ice crystals is implemented using the emperical relation by Meyers et al (1992) and is given as a simple exponential function of the supersaturation S_i,

$$(5) \qquad NUC = exp\{a + b\{100(S_i - 1)\}\}$$

where a and b are constants used in the emperical fit. The number of crystals that completely evaporates from the PI distribution is found by determining the diameter (D_e) of a particle that will completely evaporate in any given time step. The mass flux of water vapor away from the PI distribution is then broken up into two parts. The first being the mass of PI that completely evaporates and the second term is the amount of mass that is removed from the larger crystals that still remain. Using this method, D_e can then be solved for and the integral of the number concentration up to this D_e can be solved, giving the number of crystals that completely evaporates. An example of the time evolution of the two distributions using this scheme in a simple one-dimensional Lagrangian model is given in Figure 6.

5 Conclusions

RAMS was used to predict the developement of cirrus clouds over Kansas during the FIRE II experiment. The forecast model did a good job of predicting the onset of the November 26 cloud system and also the cloud depth. However, the model had trouble with the cloud top height and the simulation of cloud base. The version of the model that utilized the Chen/Cotton radiation scheme did a better job with these cloud parameters.

Now implemented into a newer version of RAMS is an auto-conversion scheme that allows for the coexistence of small and larger ice crystals. It is expected that this scheme will provide better overall results.

Acknowledgements

Thanks are extended to Greg Thompson for his valuable help with the RAMS model and the FIRE II case study, especially for his help with the Chen/Cotton simulations. Cray Research provided funding (grant # 35081185) for the use of the CRAY YMP during the FIRE II project. This research was supported by the Air Force Office of Scientific Research's grant # AFOSR-91-0296.

References

DeMott, P.J., M.P. Meyers, and W.R. Cotton, 1993: Parameterization and impact of ice initiation processes relevant to numerical model simulations of cirrus clouds. Submitted to *J. Atmos. Sci.*

Meyers, M.P., P.J. DeMott, and W.R. Cotton, 1992: New primary ice nucleation parameterizations in an explicit cloud model. *J. Appl. Met.*, **31**, 708-721.

Thompson, Greogory, 1993: Prototype real-time mesoscale prediction during the 1991-92 winter season and the statistical verification of model data. Masters thesis, Atmos. Sci. Paper No. 521, Colorado State University, Fort Collins, CO, 105pp.

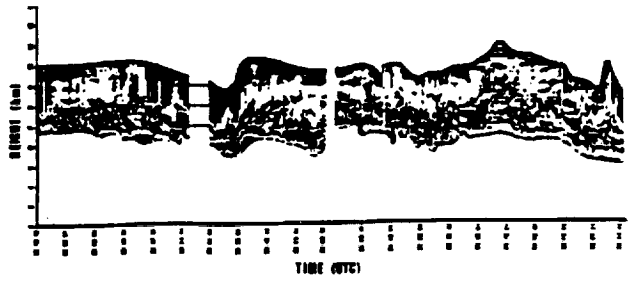

Figure 1: Lidar time-height observations from 1948 UTC to 2214 UTC on November 26, 1991.

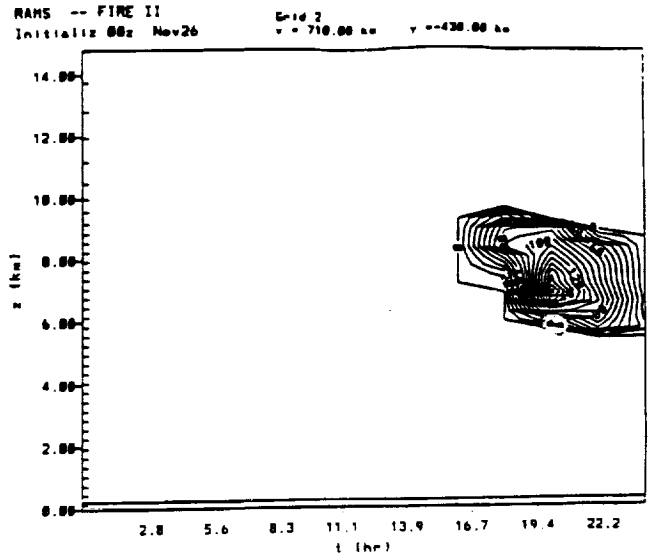

Figure 2: Time-height simulation of the PI mixing-ratio for the actual forecast.

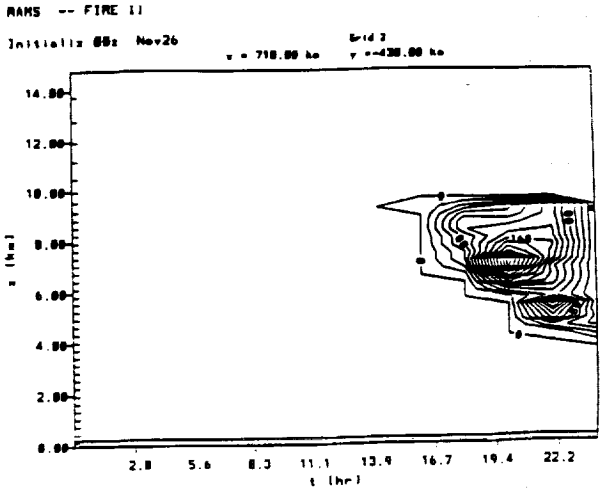

Figure 3: Time-height simulation of the PI mixing-ratio fields for the Chen/Cotton radiation simulations.

Figure 4: Satellite image taken at 1443 UTC on November 26, 1991

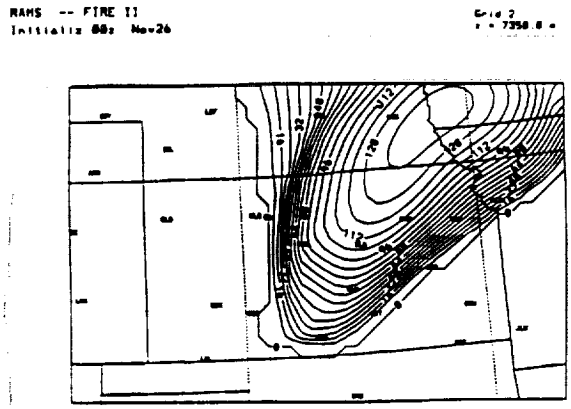

Figure 5: Horizontal cross-section at z = 7350.0 m of the simulated PI mixing-ratio field.
16HR FCST VALID 1600 UTC 11/26/91

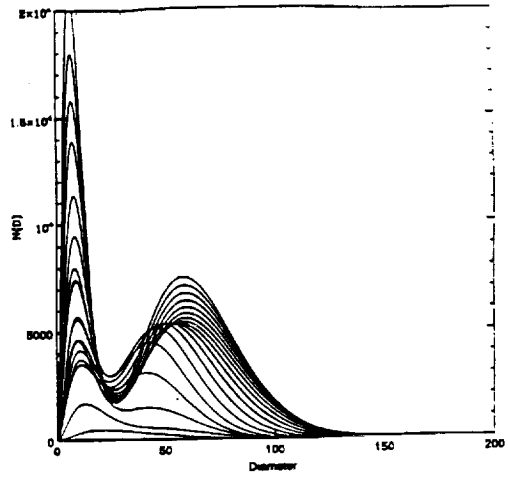

Figure 6: Evolution of the exponential gamma distributions for PI and snow

ORIGINAL PAGE IS
OF POOR QUALITY

540 47
197540
p. 4

N94-22332

DYNAMICAL CHARACTERISTICS OF CIRRUS CLOUDS FROM AIRCRAFT AND RADAR MEASUREMENTS

I. Gultepe and D. O'C. Starr
NASA, GSFC, Code 913 Greenbelt MD 20771
A. J. Heymsfield
NCAR, P.O. Box 3000, Boulder CO 80307
M. Poellot
UND Depart. of Atmos. Sci.
Grand Forks, ND 58202
T. Uttal
NOAA WPL, Marine street, RL6, Boulder CO 80307
T. Ackerman
Pennsylvania State Uni., University Park, PA 16802

1. INTRODUCTION

Cirrus clouds play an important role in climate and in the development of other types of clouds. Although there are many studies of clouds within the boundary layer, cirrus clouds have been neglected up until the last decade. New tools and in-situ measurements of various physical and dynamical parameters permit us to now study cirrus clouds in much greater detail. Physical and dynamical structures of cirrus clouds were studied in detail by Heymsfield (1975) using aircraft measurements. He emphasized the importance of interactions among physical and dynamical processes. Cirrus clouds often exhibit complex physical and dynamical structure. Upper tropospheric flows contain not only coherent structures, but also chaotic movements (Pinus, 1989). The coherent structures (organized movements) transfer significant amounts of heat and momentum while their form, size, and intensity depend strongly on environmental instability (Starr and Wylie, 1990).

In this study, various dynamical structures including cells, waves, and turbulence are studied in order to understand cirrus cloud formation and development.

2. DATA

Data for this study were collected by the NCAR King Air and UND Citation aircraft in conjunction with ground-based PSU 3 mm conventional and NOAA 8.66 mm Doppler radar observations, and radiosondes during FIRE Cirrus-II field project that took place over Kansas. The cases of November 26 and December 6 1991 were studied because of the strong dynamical activity occuring on those days.

Aircraft measurements from the NCAR king Air and UND Citation were sampled at 20 and 24Hz, respectively. The measurements of temperature, wind components, and particle size and concentrations from aircraft were used to analyze the size and intensity of dynamical structures. Aircraft measurements are interpolated to the individual points by a cubic spline technique with 0.05 second time interval.

Measurements of Doppler velocity and backscatter power from a vertical pointing NOAA Doppler radar were also used for the analysis of dynamical activity. The NOAA Doppler radar data were only available for the November 26 case. The PSU radar measurements used only to obtain reflectivity factor were available for both the November 26 and December 6 cases.

Analysis of the NOAA Doppler radar and PSU radar data are described by Uttal et al. (1993).

3. METHOD

a. Coherent structures and fluxes from aircraft measurements

Turbulent heat and momentum fluxes within coherent structures (e.g., cells and waves)

in the upper troposphere can play an important role for cirrus development. Cloud dynamical structure was analyzed for coherence and swirling. Swirling was analyzed at two different scales: 1) less than 1 km and 2) larger than 1 km. Separation of scales is made through the use of a running-average filter technique.

The parameter of vortex spirality (swirling) used to analyze coherent structures is calculated from fluctuations of vertical and horizontal winds collected at constant altitudes. The intensity of spirality (swirling), assuming that the spiral is swirled as a whole, is estimated from the following equation (Pinus, 1989):

$$S_{sw} = \frac{G/2}{1-(G/2)} \tag{1}$$

where $G = \sigma_w/\sigma_u$ and σ_u and σ_w represent the root mean squares (rms) values of horizontal and vertical wind fluctuations. The swirling intensity is divided into the three categories: 1) weak ($S_{sw} < 0.4$), 2) moderate ($0.4 < S_{sw} < 0.6$), and 3) strong ($S_{sw} > 0.6$). Moderate to strong swirling indicates the presence of coherent structures (organized eddies). In additon to the swirling parameter, another indication of the presence of coherent structures is obtained by using the calculation of coherence coefficients. The coherence of two time series is determined by Konyaev (1981) as

$$H(f) = \frac{\overline{c_i(f)c_j^*(f)}}{(\overline{c_i(f)c_i^*(f)c_j(f)c_j^*(f)})^{0.5}} \tag{2}$$

where the $c_i(f)$ and $c_j(f)$ are the amplitude spectra of time series observed at points i and j, respectively. The $c_{i,j}^*(f)$ is the complex conjugate of $c_{i,j}(f)$. We also use Eq. (2) to identify coherent structures. If the coherence coefficient $H(f)$ between two parameters is greater than 0.15, then vertical and horizontal fluctuations in the turbulent flow are correlated and a coherent structure is present at the corresponding wave number (Pinus, 1989).

Momentum and heat fluxes were calculated using a technique similar to eddy-accumulation technique. In this technique, fluxes of some parameter c are estimated separately for both upward and downward directions and summed as:

$$\overline{c'w'} = \overline{c'w'}^{(+)} + \overline{c'w'}^{(-)} \tag{3}$$

where the left hand side is equal to the net flux over a constant altitude flight leg. The first term on the right hand side of Eq. (3) is the averaged positive flux and the second term of the r.h.s. is the averaged negative flux.

b. Coherent structures from radar measurements

Calculation of the size of the dynamical structures from radar measurements (vertically pointing) is made using reflectivity factor (in dBZ) and Doppler wind measurements. Although vertical air velocity calculation from Doppler radar measurements should be made by subtracting particle terminal velocity from Doppler velocity, here we used Doppler velocity and reflectivity factor to identify the cells (coherent structures). This is sufficient for our purpose of locating cells. Size of the strong reflectivity areas L_r is calculated using the aircraft constant altitude wind measurement (U_h).

c. Vertical velocity estimation

Vertical velocity w obtained from aircraft measurements may include large errors. Therefore, mean values are substracted from measurements at each constant altitude flight leg. Size

of the cells is estimated from coherence analysis and visual analysis of w time series. The w's from the PSU and NOAA radars within the generating cells are estimated using shear region characteristics of falling ice crystals (Marhall and Gordon, 1957). In generating cells, when ice crystals grow large enough, gravity causes the ice crystals to fall and fall streaks occur in the shear region. In this case, terminal velocity V_t is estimated as

$$V_t = (U_h - U_c)\frac{\Delta z}{\Delta s}, \tag{4}$$

where U_c is the cell speed, U_c the wind speed in the shear zone, z the vertical distance, s the distance along streak. Falling conditions of ice crystals occur when V_t is slightly larger than w in the generating cell. As a first approximation, we assume $w \approx V_t$ where w is the vertical motion in the generating cell.

4. RESULTS AND CONCLUSIONS

Results show that the size of coherent structures estimated from aircraft measurements ranged from 0.2 km up to 10 km (Table 1). They were comparable to those found from radar measurements. The w from aircraft measurements at constant altitudes was found between a few cm s^{-1} and 1 m s^{-1} in both small and large mesoscales (see Fig. 1). Vertical velocity within generating cells (see Figure 2) was found to be about 1 m s^{-1}. The swirling coefficient S_{sw}, which also shows degree of coherency, ranged from 0.2 to 1.4 in the large scale and 0.4 to 1.0 in the small scale. The ratio between small scale eddy fluxes and larger mesoscale eddy fluxes was found to be between 0.20 and 0.40 (see Table 2). For upward heat fluxes, the ratio was much higher (0.43) than for the downward heat fluxes (0.27). Eddy size ranged between 2 and 10 km on leg 4 of November 26 (Fig. 3). Gust vectors in Fig. 3 are obtained from fluctuations of w and U_h. A suggested flow pattern is marked by dashed lines. Overall, estimated values of cirrus dynamical characteristics for the November 26 case were found to be more intense than those of the December 6 case.

Acknowledgement: Authors would like to thank Dr. Eugene Clothiaux of PSU in Pennsylvania for generating of radar images. This work was done while first author held a NRC Associateship at NASA/GSFC in Greenbelt Maryland and it is supported by the NASA Office of Space Science and Applications under the director of Dr. John T. Suttles.

REFERENCES

Gultepe, I., and D. O'C Starr, 1993: Dynamical structure and turbulence in cirrus clouds: Aircraft observations during FIRE. *J. Atmos. Sci.*, Accepted.

Heymsfield, A. J., 1975: Cirrus uncinus generating cells and evolution of cirrform clouds: Part II: Structure and circulations of the cirrus uncinus generating head. *J. Atmos. Sci.*, 32, 809-819.

Konyaev, K. V., 1981: *Spectral Analysis of Physical Oceanography Data.* Translated from Russian., Amerind Publishing Co.. New Delhi. 200 pp.

Marshall, J. S., and W. E. Gordon, 1957: Radiometeorology. *Meteorological Res. Rew.*, 3, 73-98.

Pinus, N. Z., and G. N. Shur. 1989: Experimental investigation of the coherent structure of turbulent currents in the lower troposphere. *Soviet Meteor. and Hydrol.*, 5, 19-24.

Starr, D. O'C., and D. P. Wylie, 1990: The 27-28 October 1986 FIRE cirrus case study: Meteorology and clouds. *Mon. Wea. Rev.*, 118, 2259-2287.

Uttal, T., R. A. Cropfli, E. Clothiaux, and T. P. Ackerman, 1993: Comparison of 3 mm and 8 mm radar radar reflectivities. Preprints. *26th Conference on Radar Meteorology.* Norman Oklahama.

$\frac{\lambda}{Log[Z(km)]}$	10 km	5 km	1 km	0.5 km	0.2 km
1 (6.0)	0.3	*	0.5	0.6	0.4
2 (6.3)	0.1	*	0.4	0.6	*
3 (6.6)	*	0.5	*	0.6	0.7
4 (6.9)	*	0.4	0.4	0.5	*
5 (7.2)	0.3	*	0.5	0.8	*
6 (7.5)	*	0.6	0.9	0.7	0.8
7 (8.8)	0.6	*	0.5	0.6	0.7

Table 1: Coherence values between T and w at constant altitude flight legs for December 6 case. λ is obtained from true air speed and frequency f. Coherence is less than 0.20 is indicated by *.

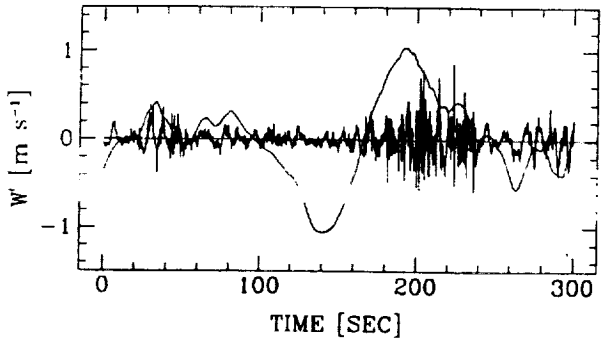

Figure 1: Vertical velocity w fluctuations at 7.3 km. Data are collected from NCAR King Air measurements on 26 November 1991. Aircraft true air speed was $\approx$100 m s^{-1}. Smooth line is for large mesoscale and other one is small mesoscale. Separation of scales is at 1 km.

Leg	R^+_{wT}	R^-_{wT}	R^+_{ww}	R^-_{ww}	R^+_{wu}	R^-_{wu}
1	0.27	0.20	0.24	0.18	0.19	0.10
2	0.33	0.40	0.45	0.41	0.32	0.31
3	0.20	0.05	0.08	0.10	0.07	0.08
4	0.15	0.14	0.18	0.11	0.13	0.14
5	0.06	0.15	0.08	0.24	1.22	1.21
6	1.70	0.83	0.72	0.37	0.59	0.82
7	0.30	0.10	0.25	0.04	0.16	0.14
Mean	0.43	0.27	0.29	0.21	0.38	0.40

Table 2: Ratio R between small and large scale fluxes for upward (+) and downward (-) for December 6 case.

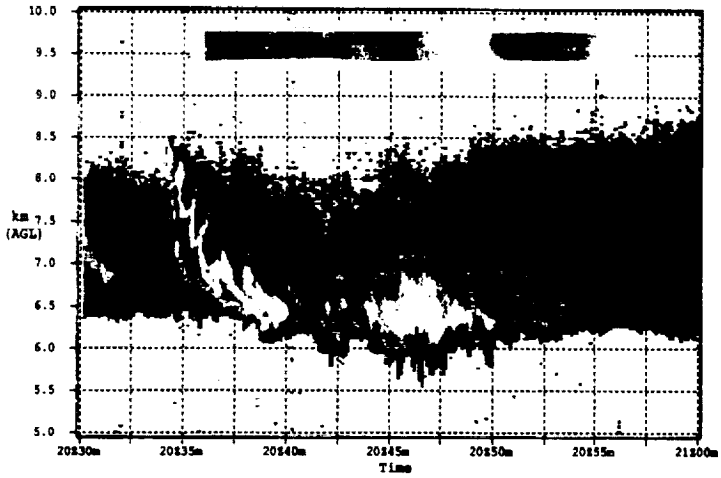

Figure 2: Relative radar reflectivity (dBZ) is obtained from the PSU radar on 26 November 1991.

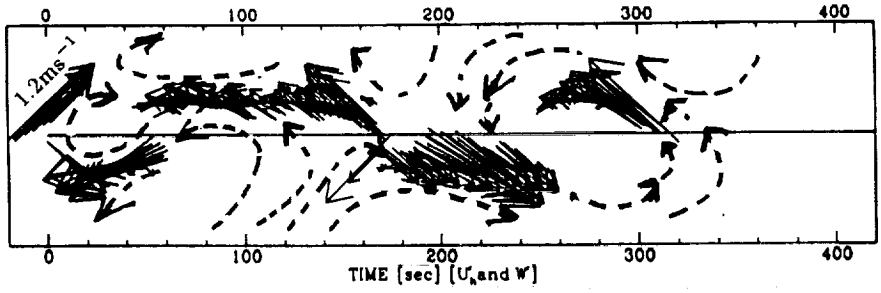

Figure 3: Shows gust vectors obtained from w and U_h wind fluctuations at constant altitude about 7.9 km on November 26, 1991. A suggested flow pattern is marked by dashed lines.

S41-47
19754
P-3

N94-22333

Estimation of Cirrus Cloud Particle Fallspeeds from Vertically Pointing Doppler Radar

Brad W. Orr and Robert A. Kropfli

325 Broadway
NOAA/ERL Wave Propagation Laboratory
Boulder, Colorado 80303

(reprinted from 26th International Conference on Radar Meteorology, 1993)

1. Introduction

The First ISCCP Regional Experiment II (FIRE II) was conducted in Coffeyville, Kansas in late 1991 to study the microphysical and radiative properties of cirrus clouds. A variety of active and passive remote sensors were employed, including an 8-mm-wavelength cloud-sensing Doppler radar developed at the Wave Propagation Laboratory (WPL). The radar, having excellent sensitivity to cloud particles (-30 dBZ at 10 km), good spatial resolution (37 m), and velocity precision (.05 ms^{-1}), is an excellent tool for observing cirrus clouds (Kropfli et al., 1990; Martner and Kropfli, 1993). Having this radar directed toward the zenith for long periods of time during FIRE II permitted the reflectivity-weighted particle fallspeed to be related to reflectivity which allowed a separation of ice particle fallspeeds from vertical air motions. Additionally, such relationships have proved useful in other multi-sensor techniques for determining vertical profiles of ice particle characteristic size and ice water content in cirrus clouds (Matrosov et al., 1993). This paper discusses the analysis method and the results of applying it to cirrus cloud reflectivity and velocity data collected during FIRE II.

2. Methodology

Radial velocity data obtained by a vertically pointing Doppler radar (V_r) is the sum of the reflectivity-weighted hydrometeor fallspeed (V_t) and the vertical air motion (V_a).

$$V_r = V_t + V_a . \tag{1}$$

To arrive at relationships between radar reflectivity and reflectivity-weighted particle fallspeed, a straightforward method was devised. The underlying assumption is that an appropriately long temporal average of radial velocity will result in the air motion term being small compared to the fallspeed term in cirrus clouds. Although the optimal amount of averaging is a subject currently under investigation with combined wind profiler/cloud radar measurements, it is believed that an averaging time of 1-3 hr is suitable for most cirrus clouds. Under this assumption, the resulting averaged radial velocities will be due solely to particle motions ($V_r \approx V_t$). If this averaging is performed for various radar reflectivity intervals, a formula of the form

$$V_t = \alpha Z_e^{\beta} \tag{2}$$

can be derived where Z_e is the effective radar reflectivity and α and β are empirically determined constants. In order to ensure the representativeness of the resulting formula and account for spatial variation in particle habits and densities in the vertical, the averaging is performed over several height intervals within the cloud. Least-squares methods are then used to determine α and β at all levels within the cloud.

A variation of the above is a multiple-linear regression analysis that incorporates height as a proxy for the temperature dependence. This analysis requires Z_e to be given in decibels to account for the nonlinearity expressed in (2). The final product is one equation of the form

$$V_t = a + b(10 \log Z_e) + c(h) , \tag{3}$$

where a, b, and c are constants derived from the linear regression of the averaged Doppler velocity against reflectivity (dBZ) and the height, h, (or temperature). An advantage of this method is that both the reflectivity and height dependencies of hydrometeor fallspeeds are incorporated into one equation. (2), on the other hand, requires one formula for each height or a secondary analysis to determine height dependencies of α and β.

3. Discussion

Figure 1 is a 3-hr time-height display of reflectivity (dBZ) from a cirrus cloud observed on 25 November, 1991 during FIRE II. Time increases from left to right, and height is given in km AGL on the right side. The results of (2) applied to this time period are shown in Fig. 2. The individual curves were derived from 3-hr averages corresponding to Fig. 1 over height intervals of approximately 560 m. The resolution in Z_e is equivalent to 1 dB. A minimum of 300 velocity estimates, each acquired over a 3-s dwell, was required at each point in Fig. 2 before the least-squares analysis was performed. This threshold was determined by noting the magnitude of the improvement in the curve-fitting result as higher threshold values were imposed. Noteworthy features in Fig. 2 are the

systematic vertical variation of the derived relationships and the small scatter about the best fit curves. The standard deviation about each curve in Fig. 2. was less than 4 cm s^{-1}. Note that although the entire record was 3 hr in length, the top level of the cloud was dissipating so that the effective averaging time for that level was on the order of only 1 h. The scatter of data about the best fit curve seems unaffected by the reduced averaging time, however.

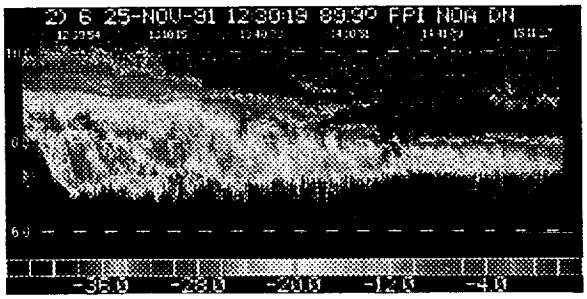

Figure 1. Time-height display of cirrus cloud reflectivity (dBZ) from vertically pointing radar data, 12:30 -15:30 UTC 25 November, 1991. Vertical scale is km AGL.

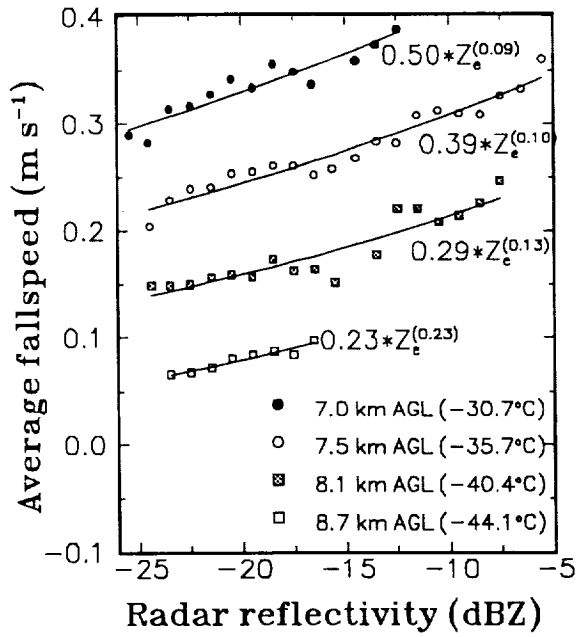

Figure 2. Power law fit of data in Fig. 1 using (2).

Several other data sets, spanning three days from the FIRE II data set, have been analyzed in a similar manner. The general trend of higher fallspeeds at cloud base is evident in all cases, although the vertical stratification is not always as well defined as in Fig. 2. This result is consistent with the notion that the larger and/or denser particles are found in the lower portions of cirrus clouds. Fallspeeds obtained from all three data sets ranged from 0.05 m s^{-1} up to 0.9 m s^{-1} over a height range of 6.0 to 10.0 km AGL which is within the expected range of values for cirrus cloud particles (Pruppacher and Klett, 1978).

Values for α and β covering three different days ranged from 0.21 to 0.87 and from 0.05 to 0.24, respectively. The results are summarized in Fig. 3. For a given analysis period, there was typically a large variation in α with height. However, although β remained relatively constant during a given analysis period, it was seen to vary considerably from case to case. A general trend can be seen in the results from 22 and 25 November (Fig. 3). The 26 November case, however, exhibits a different characteristic in the α and β values. Microphysical data also indicate significant differences. A bimodal distribution is evident on November 26, while the other two cases are more representative of single mode distributions (Miloshevich, L., (NCAR/MMM), personal communication, November, 1992).

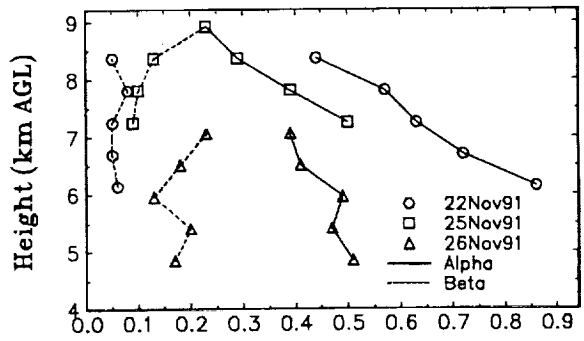

Figure 3. Vertical variations in α and β where β is dimensionless and α has dimensions of (m s^{-1})(mm^6 m^{-3})$^{\beta}$.

Heymsfield (1975) arrived at a relationship similar to the above using combined radar and aircraft observations of a cirrus uncinus generating cell. His values for α and β were 0.84 and 0.074, respectively. Heymsfield (1977) presents results for stratiform ice clouds with α values between 0.59 and 0.67, and β ranging from 0.06 to 0.095. The K_a-band results are in general agreement with these results, although the spread in our data is somewhat larger.

Figures 4 and 5, respectively, show a 24-min average of vertical velocity data before and after removing the particle fallspeed contribution. These data are from a cloud system that persisted for over 12 h. A multiple-linear regression analysis of the form shown in (3) was used for these data in order to more easily incorporate the height dependencies. Figure 4 was obtained by applying (4) to the data in Fig. 3:

$$V_t = 0.6644 + 0.0112(10\log Z_e) - 0.0349(h) . \quad (4)$$

The fallspeed correction was applied on a beam-by-beam basis and an average was then performed over the 24-min period. The vertical air motion in Fig. 4 shows upward motion throughout most of the cloud and with a peak value of 0.13 m s^{-1} near the cloud center.

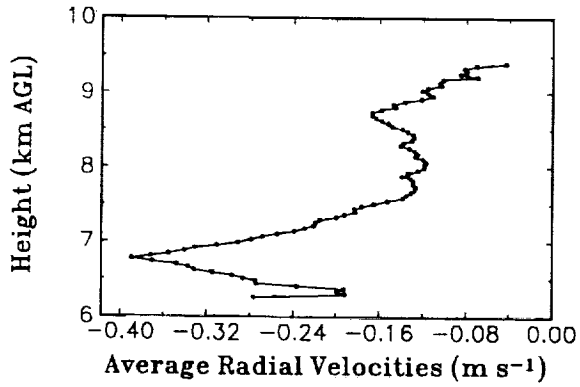

Figure 4. 24-min average of vertically pointing Doppler radial velocities (m s^{-1}) beginning 19:00 UTC on 26 November, 1991.

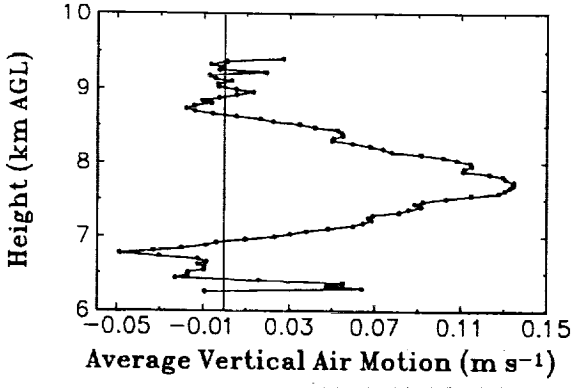

Figure 5. 24-min average air motion (m s^{-1}) beginning 19:00 UTC on 26 November, 1991. Derived from Fig. 4 after using (4).

4. Conclusions

A method has been demonstrated that allows the estimation of hydrometeor fallspeeds within cirrus clouds from a vertically pointing Doppler radar. These initial results are supported by other theoretical and observational studies, which lends promise to this technique. Continuing studies will include the application of improved data thresholding schemes over the larger data set acquired in FIRE II and other programs. Comparisons with in situ observations will also be performed.

5. Acknowledgments

We would like to acknowledge the excellent radar engineering support provided by Bruce Bartram and Kurt Clark. This research was funded in part by the NOAA Climate and Global Change Program.

6. References

Heymsfield, A. J., 1975: Cirrus uncinus generating cells and the evolution of cirriform clouds. Part II: The structure and circulations of the cirrus uncinus generating head. *J. Atmos. Sci.*, **32**, 809-819.

--------, 1977: Precipitation development in stratiform ice clouds: A microphysical and dynamical study. *J. Atmos. Sci.*, **34**, 367-381.

Kropfli, R. A., B. W. Bartram, and S. Y. Matrosov, 1990: The upgraded WPL dual-polarization 8-mm wavelength Doppler radar for microphysical and climate research, Proc., Conference on Cloud Physics, July 23-27, 1990, San Francisco, California, 341-345.

Martner, B. E. and R. A. Kropfli, 1993: Observations of multi-layered clouds using K-band radar, Proc., 31st Aerospace Sciences Meeting and Exhibit, Jan. 11-14, 1993, Reno, NV, AIAA, 8 pp.

Matrosov, S. Y., B.W. Orr, R.A. Kropfli, and J.B. Snider, 1993: Retrieval of vertical profiles of cirrus cloud microphysical parameters from Doppler radar and IR radiometer measurements, submitted to *J. Atmos. Sci.*

Pruppacher, H.R., and J.D. Klett, 1978: Microphysics of Clouds and Precipitation. Reidel Publishing Co., Dordrecht, Holland, 714 pp.

542-47
197542
P. 4

Normalized vertical ice mass flux profiles from vertically pointing 8-mm-wavelength Doppler radar

N94-22334

Brad W. Orr and Robert A. Kropfli
NOAA Wave Propagation Laboratory

I. Introduction

During the FIRE II project, NOAA's Wave Propagation Laboratory (WPL) operated its 8-mm-wavelength Doppler radar extensively in the vertically pointing mode. This allowed for the calculation of a number of important cirrus cloud parameters, including cloud boundary statistics (Uttal and Intrieri, 1993), cloud particle characteristic sizes and concentrations, and ice mass content (*imc*) (Matrosov et. al. 1992; 1993). The flux of *imc*, or, alternatively, ice mass flux (*imf*), is also an important parameter of a cirrus cloud system. Ice mass flux is important in the vertical redistribution of water substance and thus, in part, determines the cloud evolution.

It is important for the development of cloud parameterizations to be able to define the essential physical characteristics of large populations of clouds in the simplest possible way. One method would be to normalize profiles of observed cloud properties, such as those mentioned above, in ways similar to those used in the convective boundary layer. The height then scales from 0.0 at cloud base to 1.0 at cloud top, and the measured cloud parameter scales by its maximum value so that all normalized profiles have 1.0 as their maximum value. The goal is that there will be a "universal" shape to profiles of the normalized data.

We have applied this idea to estimates of *imf* calculated from data obtained by the WPL cloud radar during FIRE II. Other quantities such as median particle diameter, concentration, and ice mass content can also be estimated with this radar, and we expect to also examine normalized profiles of these quantities in time for the 1993 FIRE II meeting.

II. Methodology

Using the empirical relationship of Sassen (1987), it is possible to estimate *imc* from 8-mm radar reflectivity. Multiplying this *imc* by the Doppler velocity produces an estimate of *imf*. This calculation was performed on a beam-by-beam basis and then averaged for 25 min (during every half hour the radar was operated 25 min in the vertically pointing mode). Calculations of *imf* have been performed for a number of intervals from 22, 25, 26, and 28 November 1991 during FIRE II.

Since cloud top and base will fluctuate, sometimes considerably over a given averaging period, it was necessary to impose certain thresholding criteria. First, at least 300 beams out of a possible 480 during a 25 min averaging period were required to have "good data". This "good data" classification was considered conservative and applied separately to the velocity and reflectivity data fields before the calculation of *imf* was performed and included considerations of signal strength, and pulse to pulse correlations of returned power.

Secondly, since the relationship of Sassen (1987) is an empirical relationship for ice clouds, it was necessary to eliminate cases which might have significant liquid water content. A value of -20°C was chosen as a threshold value; any cloud that had an average base temperature warmer than -20°C was eliminated from the analysis. This ensured to a reasonable degree that the radar was observing ice clouds. After the above thresholding had been applied, the data were normalized as described and plotted separately for each day.

III. Results and Discussion

The plots in Figs. 1-3 summarize the results from 25, 26, and 28 November. A total of 18 hrs of data were examined from these three days with 9 hrs passing the thresholding criteria. The times noted in the legend are in GMT and are the start of each 25 min averaging period. The vertical scale is normalized cloud depth as defined by the radar after all thresholding tests were applied. The darker line is an eighth degree polynomial fit that is presented to outline the general shape of the normalized data. No attempt is made in this study to derive a general equation for all three data sets, however, this will be addressed in future analysis.

Plots of the three cases shown in Figs. 1-3 have a number of similarities. First, there are relatively low values at cloud top and base with a distinct peak near the bottom of the cloud. The mean, normalized flux at cloud top approaches zero and ranges from 0.3 to 0.5 at cloud base. The data from 25 November has a peak flux at a normalizedheight of 0.3, 26 November has a peak just above 0.1, and the peak is at 0.2 for 28 November. On 26 November, the peak in *imf* at a rather low level within the cloud may be partly the result of requiring a 300-beam minimum for good averages.

Cloud base on 26 November was slowly decreasing, even over the 25 min averaging period. The thresholding scheme may therefore haveeliminated the lower portion of the cloud. Cloud base on 25 and 28 November was much more stable over a given averaging period. Plotting the 26 November data without this thresholding produces a peak closer to 0.2.

A fourth day (not shown) was 22 November, which was not plotted because cloud base temperatures were much warmer than the -20°C threshold. Nevertheless, the normalized profiles from this day were very similar to those shown here, with a peak flux just below the 0.3 level.

We point out here that the relationship of Sassen (1987) is empirical and can be expected to be most accurate for the microphysical conditions under which it was obtained. New, more general techniques are being tested to derived *imc* and *imf* (Matrosov, et al., 1993). These incorporate radar reflectivity, Doppler velocity, and infrared radiometer data sets, and should improve the *imf* calculation.

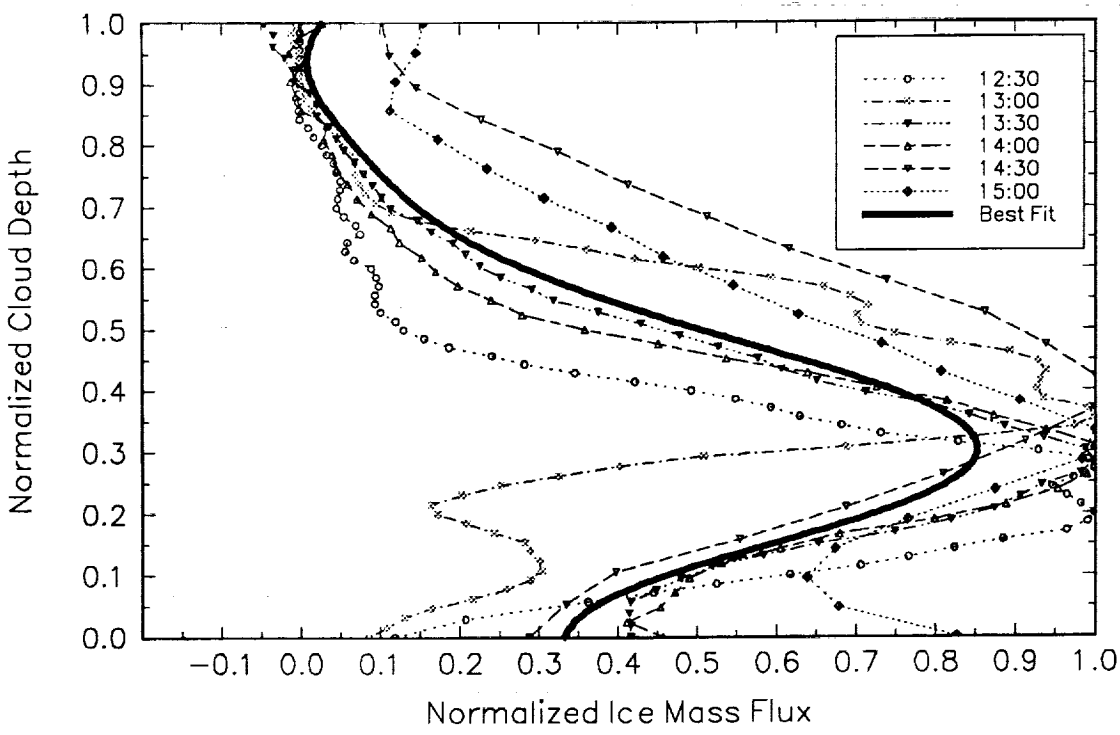

Figure 1. Normalized ice mass flux for November 25, 1991.

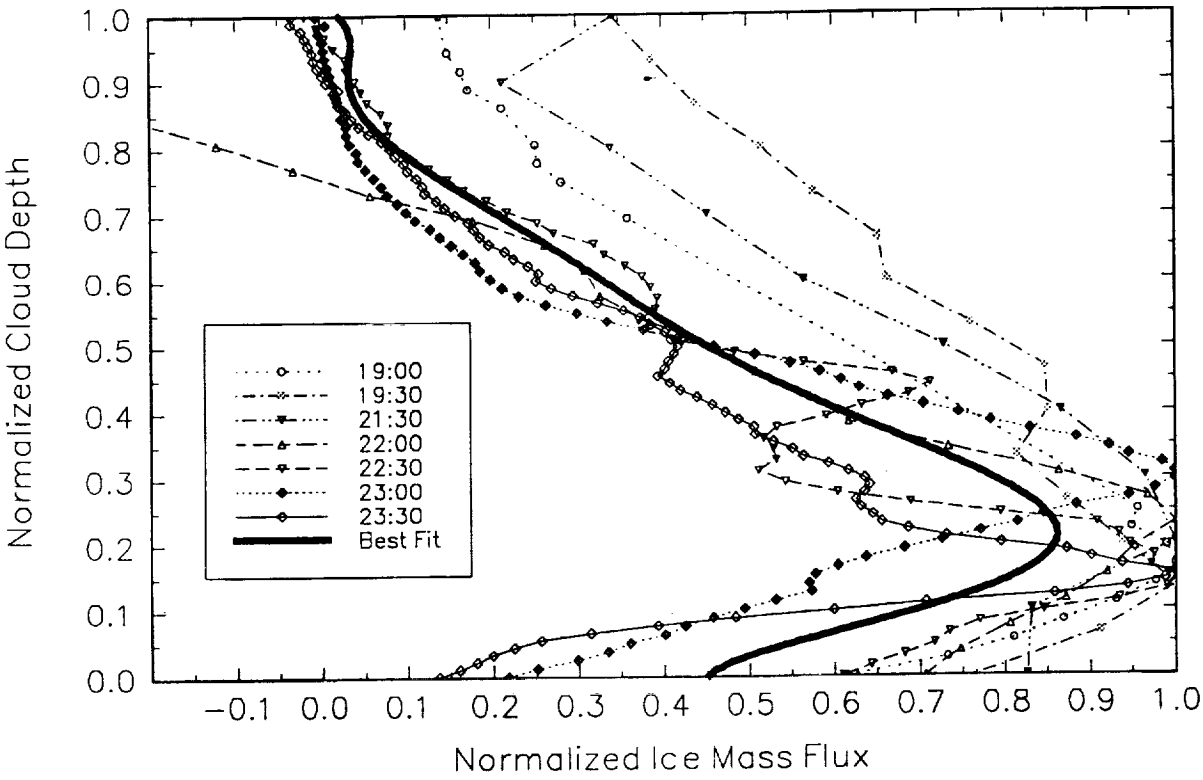

Figure 2. Normalized ice mass flux for November 28, 1991.

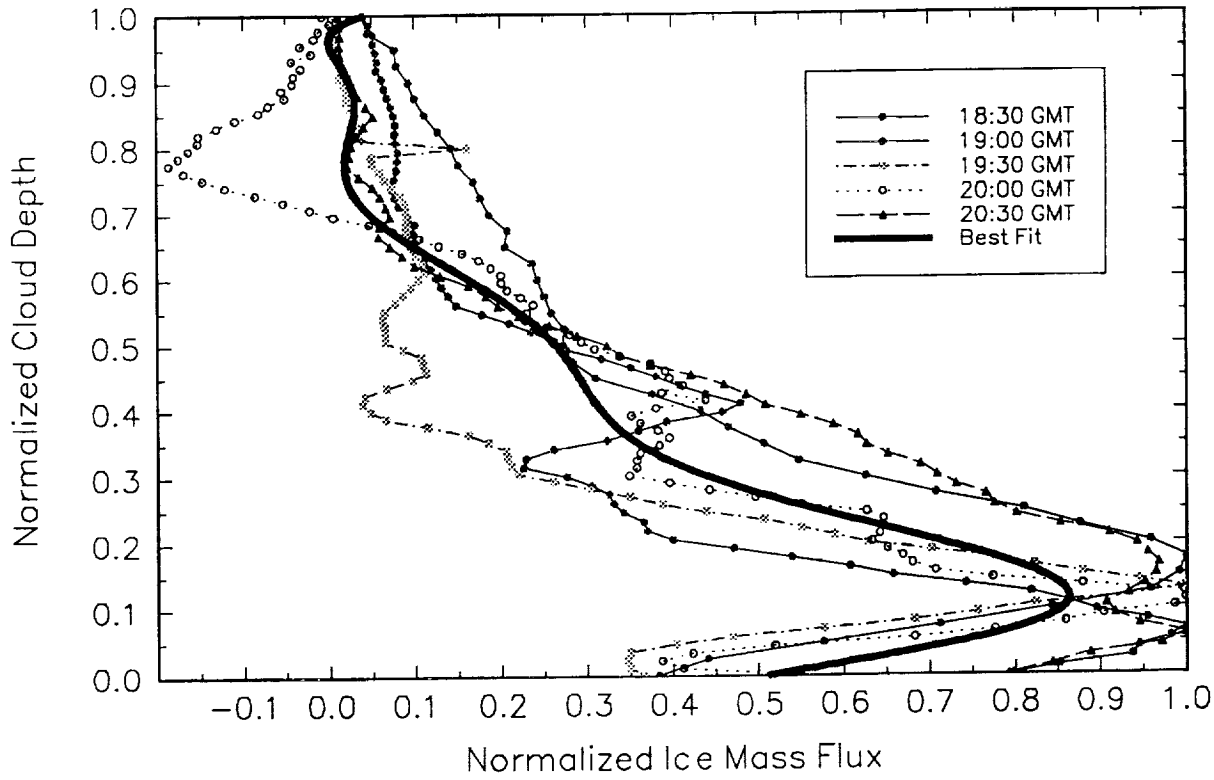

Figure 3 Normalized ice mass flux for November 26, 1991.

IV. Summary and Conclusions

The similarity of the three normalized *imf* data sets is encouraging. This description of cirrus clouds, if it proves generally applicable, could be valuable in improving the parameterization of cirrus clouds in GCMs. Modifications of this technique are being considered to determine better and simpler ways of characterizing cirrus clouds. Data sets from different locales, such as Porto Santo Island, Portugal, and Boulder, Colorado, will also be analyzed (using this technique) to determine the generality of these results.

V. References

Matrosov, S.Y., T. Uttal, J.B. Snider, and R.A. Kropfli, 1992: Estimation of ice cloud parameters from ground-based infrared radiometer and radar measurements, *J. Geophys Res.* **97**, 11567-11574.

Matrosov, S.Y., B.W. Orr, R.A. Kropfli, and J.B. Snider, 1993: Retrieval of vertical profiles of cirrus cloud microstructure parameters from Doppler radar and IR radiometer measurements. *J. Appl. Met.*, (in review).

Sassen, K., 1987: Ice cloud content from radar reflectivity, *J. Climate and Appl. Meteor.*, **26**, 1050-1053.

Uttal, T. and J.M. Intrieri, 1993: "Comparison of cloud boundaries measured with 8.6 mm radar and 10.6 μm lidar", Proc., Combined Optical-Microwave Earth and Atmosphere Sensing, March 22-25, Albuquerque, NM, 207-210.

543-47
197543
N94-29935

A COMPARISON OF SMALL AND LARGER MESOSCALE LATENT HEAT AND RADIATIVE FLUXES: DECEMBER 6 CASE STUDY

I. Gultepe and D. O'C. Starr
NASA, GSFC, Code 913
Greenbelt, MD 20771

A. J. Heymsfield
NCAR P.O. Box 3000
Boulder CO 80307

1. INTRODUCTION

Because of the small amounts of water vapor, the potential for rapid changes, and the very cold temperatures in the upper troposphere, moisture measuring instruments face several problems related to calibration and response. Calculations of eddy moisture fluxes are, therefore, subject to significant uncertainity.

The purpose of this study is to examine the importance of latent heat (moisture) fluxes due to small and larger mesoscale mesoscale circulations in comparison to radiative fluxes within cirrus. Scale separation is made at about 1 km because of significant changes in the structures within cirrus. Only observations at warmer than -40 C are used in this study.

The EG&G hygrometer that is used for measuring dewpoint temperature (T_d), is believed to be fairly accurate down to -40 C (Schanot, 1987). On the other hand, Lyman-Alpha (L-α) hygrometer measurements of moisture may include large drift errors. In order to compensate for these drift errors, the L-α hygrometer is often calibrated against the EG&G hygrometer (Jensen and Raga, 1991; Friehe et al., 1986). However, large errors ensue for T_d measurements at temperatures less than -40 C. The cryogenic hygrometer (Busen and Buck, 1993) frost point measurements may be used to calibrate L-α measurements at temperatures less than -40 C. In this study, however, measurements obtained by EG&G hygrometer and L-α measurements are used for the flux calculations.

2. AIRCRAFT MEASUREMENTS

Data for this case study were taken from the FIRE Cirrus II field project which took place over the Kansas region during November and December of 1991. Temperature, dewpoint, radiation and INS wind measurements from NCAR King Air for December 6 case were used in the calculations. Mixing ratio values are obtained from both EG&G and Lyman Alpha fast response hygrometers. Data sampling rate was 20Hz for the measurements used in flux calculations. The cirrus cloud formed on this day was related to an upper jet stream and short wave trough at about 300 mb. Time series of temperature and wind measurements at seven constant altitudes ranging from 6 to 9 km show that the layers close to cloud top had large w fluctuations (± 1 m s^{-1}). Broad band radiative fluxes were obtained from Eppley radiometers in both the shortwave and infrared range.

3. METHOD

This section describes the latent heat (moisture) and radiative flux calculations, and scale partition for the latent heat flux calculations.

a. Latent heat flux calculation

Mixing ratio values are calculated from both EG&G T_d and L-α hygrometer measurements. Mixing ratio q_{vE} from EG&G T_d measurements is obtained as

$$q_{vE} = \frac{\epsilon e(T_d)}{P - e(T_d)}, \tag{1}$$

where e is the saturated vapor pressure at the given dewpoint temperature, and P is the pressure.

Mixing ratio values from L-α measurements are obtained from the equations given by Buck (1976):

$$I = I_o exp(-s \sum \frac{k_i \rho_{vi}}{\rho_{vi}}), \tag{2}$$

$$V = ln(I), \tag{3}$$

where I is detector current, I_o is detector current with path length set zero, s the path length, k absorption coefficient, ρ_{vi} density of ith gas in path, and V is voltage. Vapor density then is calculated from the observed voltage (Schanot, 1987).

In our calculations, leg-averaged vapor mixing ratio values, calculated from EG&G bottom hygrometer measurements, are plotted versus constant altitude leg averaged L-α voltage (V) measurements (see Fig. 1). In this figure, the cross indicates mean values. The thin and thick lines are sounding values of the same parameters based on the L-α hygrometer q_v and EG&G q_v values, respectively. A regression line obtained from Fig. 1 is shown in Fig. 2 and it is given as

$$q_{vE} = 7.072 + 0.8036 V_{L-\alpha}. \tag{4}$$

Using perturbation theory, mixing ratio fluctuations from Eq. (4) are obtained as

$$q'_{vE} = 0.8036 V'_{L-\alpha}. \tag{5}$$

Using Eq. (5) and vertical velocity fluctuations w', time series of eddy latent heat fluxes are obtained from the following equation:

$$F = L_v w' q'_{vE} = L_v S w' V'_{L\alpha}, \tag{6}$$

where L_v is the latent heat of vaporization. S is the slope of regression line and it is equal to 0.8036 for December 6 case. Eq. (6) is used in this study to obtain time series and leg-averaged latent heat fluxes.

Scale separation within cirrus is made using a running-average technique. The calculated latent heat fluxes are thereby partitioned into those attributable to scales less than and greater than 1 km.

b. Radiative flux profiles

Average radiative fluxes of both IR and SW irradiances over constant altitude flight legs are obtained from the Eppley up and down looking radiometers. Radiative flux divergence for each layer is calculated from radiometer measurements.

4. RESULTS AND CONCLUSIONS

a. Comparisons of latent heat and radiative fluxes

Small and larger scale latent heat flux time series calculated over leg 1 and net radiative flux data are shown in Fig. 3 and Table 1, respectively. Mean values of latent heat fluxes (see Table 2) are found to be very small compared to radiative flux values. Although mean values are small, turbulent fluxes at individual points (see Fig. 3) are found to be comparable with net radiative fluxes (see Table 1) in any layer within cirrus. This shows that inhomogeneity within cirrus can be very important for trasferring heat and moisture in the horizontal and vertical. Heating rates corresponding to IR, SW, and IR+SW radiation are given in Fig. 4. Standard error of

IR and SW radiative fluxes are approximately ±5 and ±10 W m^{-2} (Gultepe and Starr, 1993), respectively.

Time series of latent heat fluxes (Fig. 3) show that small scale processes (scales less than 1 km) can have a significant contribution to mean latent heat fluxes (see Table 2). Table 2 shows the latent heat fluxes estimated for upward and downward directions in two different scales. The ratio R between small scale and large scale contributions is equal to $(w'q')_S/\ (w'q')_L$. Results show that small scale flux contribution is approximately 30%. Under the turbulent conditions which are indicated in legs 2 and 6, small scale contribution is about 70%.

b. Effects of moisture fluxes on ice crystal concentration

The typical values of mixing ratio and vertical velocity fluctuations are approximately 0.02 g m^{-3} and 0.20 m s^{-1}, respectively. Moisture flux rate then is obtained from Eq. (6) and it is about 0.004 g m^{-2} s^{-1}. Using Δt time period equal to 10 s, the transferred mass rate, ΔM_t, is estimated to be 0.04 g. If we assume that a layer just above the constant leg is saturated with respect to ice, using a mono-type particle size distribution with spherical crystal shape, and assuming that transferred moisture totally changes into ice, the number of ice crystals being formed is estimated as follows:

$$N_i[\frac{particles}{cm^2}] = \frac{\Delta t \times \Delta M_t \times 10^{-4}}{(4/3)\pi r_e^3 \rho_i} \tag{7}$$

where ρ_i is the ice crystal density. Using equivalent particle size r_e=10 μm and ρ_i=0.8 g cm^{-3}, N_i is estimated to be approximately 1.2×10^6 particles cm^{-2} for a 10 second time period. Even though this number may include large error (about %20-30), the results showed that small scale eddy moisture fluxes can play an important role in cirrus development.

ACKNOWLEDGEMENT

This work was supported by the NASA Office of Space Science and Applications under the direction of Dr. John T. Suttles. The first author during this work held a National Research Council Research Associateship at Climate and Radiation Branch of the NASA Goddard Space Flight Center in Greenbelt Maryland.

REFERENCES

Buck, A. L., 1976: The variable-path Lyman-alpha hygrometer and its operating characteristics. *Bull. Amer. Meteor. Soc.*, 57, 1113-1118.

Busen R., and A. L. Buck, 1993: The CR-1 cryogenic hygrometer on board the DLR falcon: installation, performance tests, and examples of measured data. *8th symposium on Meteor. Obser. and Instrumen.*,73rd AMS Annual Meeting, january 17-22.

Friehe, C. A., Grossman R. L. and Y. Pann, 1986: Calibration of an airborne Lyman-Alpha Hygrometer and measurement of water vapor flux using a thermoelectric hygrometer. *J. Atmos. Ocean. Tech.*, 3, 299-304.

Gultepe, I, and D. O'C. Starr, 1993: Dynamical structure and turbulence in cirrus clouds: Aircraftobservations during FIRE I. *J. Atmos. Sci.*, submitted.

Jensen, B. J., and G. B. Raga, 1993: Calibration of a lyman-α sensor to measure in-cloud temperature and clear-air dewpoint temperature. *J. Atmos. Ocean. Tech.*, 10, 1-26.

Schanot, A., 1987: An evaluation of the uses and limitations of a Lyman-Alpha hygrometer as an operational airborne humidity sensors. *6th symposium on Meteor. Obser. and Instrumen.*, january 12-16, New Orleans, La., 257-260.

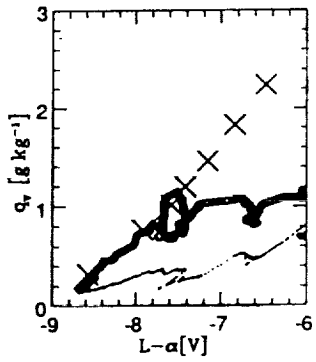

Fig. 1: Shows vapor mixing ratio versus L-α voltage. The crosses are for mean values over constant altitude flight legs. Other lines are for aircraft sounding values.

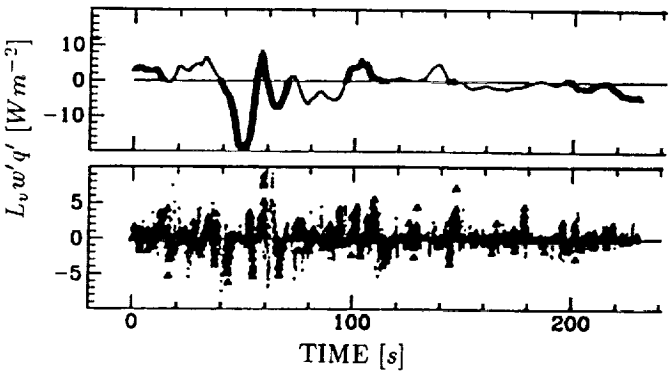

Fig. 3: Top and bottom panels shows time series of small and larger scale eddy latent heat fluxes along leg 1 (at 6.0 km) for December 6 case, respectively.

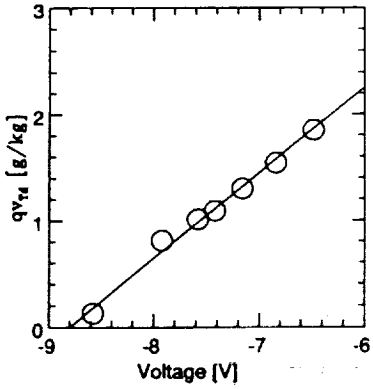

Fig. 2: Shows vapor mixing ratio versus voltage. The circles are for mean values at constant altitudes. The straight line is best fit for the mean values.

Z (km)	IR^u	IR^d	SW^u	SW^d	layer	IRnet	SWnet
6.0	286.3	240	10.9	153.4	1	-2.5	43.1
6.3	279.9	231.1	29.73	215.3	2	-32.1	16.4
6.6	275.0	194.1	63.02	278.6	3	3.5	4.1
6.9	264.6	188.2	73.93	280.0	4	-31.6	14.6
7.2	260.3	152.3	84.6	305.3	5	-23.3	95.7
7.5	256.3	125.0	118.1	434.5	6	-10.9	33.0
8.8	230.6	88.2	193.8	543.5			

Table 1: Averaged IR and SW irradiances (W m^{-2}) versus constant altitudes. Last two columns are gain or loss for each layer.

Table 2: Small and large scale eddy latent heat fluxes (F_S and F_L) for upward (+) and downward (-) directions. The R shows ratio between small and large scale fluxes. The F_{max} is the maximum individual flux value (W m^{-2}) on a leg.

Z (km)	F_L^+	sd	F_L^-	sd	F_S^+	sd	F_S^-	sd	R^+	R^-	F_{max}
6.0	2.4	1.9	3.2	3.9	0.8	1.1	0.8	1.0	0.34	0.24	20
6.3	1.4	1.4	0.9	1.0	0.9	1.5	0.6	1.0	0.64	0.73	8
6.6	1.8	1.3	2.1	3.1	0.3	0.4	0.2	0.3	0.14	0.10	-15
6.9	1.8	2.1	1.3	1.5	0.2	0.3	0.2	0.3	0.13	0.16	10
7.2	1.2	0.8	1.5	1.5	0.2	0.3	0.2	0.4	0.16	0.15	-8
7.5	2.7	5.1	1.4	1.3	1.4	4.0	1.0	3.5	0.53	0.73	20
8.8	6.1	8.7	1.2	1.2	0.3	0.5	0.3	0.4	0.06	0.26	20

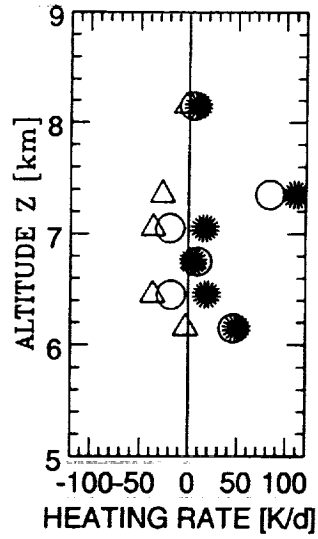

Fig. 4: Potential heating rates for IR (triangles), SW (stars), and IR+SW (circles) radiation.

544-47
N94-22336

IMPORTANCE OF AGGREGATION AND SMALL ICE CRYSTALS IN CIRRUS CLOUDS, BASED ON OBSERVATIONS AND AN ICE PARTICLE GROWTH MODEL

David L. Mitchell, Steven K. Chai, Yayi Dong, W. Patrick Arnott and John Hallett
Desert Research Institute, P.O. Box 60220, University of Nevada, Reno, NV 89506

Andrew J. Heymsfield
National Center for Atmospheric Research, Boulder, CO 80303

The 1 November 1986 FIRE I case study was used to test an ice particle growth model which predicts bimodal size spectra in cirrus clouds. The model was developed from an analytically based model which predicts the height evolution of monomodal ice particle size spectra from the measured ice water content (IWC). Size spectra from the monomodal model are represented by a gamma distribution,

$$N(D) = N_o D^{\nu} \exp(-\lambda D) \quad , \qquad (1)$$

where D = ice particle maximum dimension. The slope parameter, λ, and the parameter N_o are predicted from the IWC through the growth processes of vapor diffusion and aggregation. The model formulation is analytical, is computationally efficient, and well suited for incorporation into larger models. The monomodal model has been validated against two other cirrus cloud case studies as described in Mitchell (1993; 1991). From the monomodal size spectra, the size distributions which determine concentrations of ice particles < about 150 μm are predicted.

Ice particle size spectra measured by the DRI ice particle replicator on 21 Nov. 1991 during FIRE II indicate ice particles in cirrus with 10 μm < D < 150 μm conform to an exponential size distribution with approximately constant slope. Based on 21 size distributions, $\lambda = 226 \pm 35$ cm^{-1}. Size spectra from the 2D-C probe for 1 Nov. 1986 (during FIRE I) exhibited a similar constant slope value (about 250 cm^{-1}) for 50 μm < D < 150 μm. Assuming this result is general for most cirrus, this enables the component of the size distribution containing particles < 150 μm to be predicted from the size distribution containing larger particles, which is predicted by the growth processes of vapor diffusion and aggregation.

The height evolution of ice particle size spectra was measured during a Lagrangian spiral descent through a relatively uniform cirrus deck during FIRE I on 1 Nov. 1986. Cloud depth ranged from 9 km to about 5.1 km. Model predicted and measured size distributions were plotted and compared favorably, as shown in Fig. 1a-1b. Measured size distributions are indicated by the solid lines, and size spectra predicted by the ice particle growth model are indicated by the long dashed lines. The short-dashed lines are predicted for vapor deposition growth only (no aggregation). These spectra would occur if ice crystals did not combine to form aggregates, and remained as single ice crystals. The model assumes all ice particles are single ice crystals at cloud top (no aggregation), and thus there is no difference between the two predicted spectra at cloud top. The lower the level in the cloud, the more time there is for aggregation to occur as ice falls from cloud top, and the size spectra broaden to include the larger aggregates.

Since no theoretical method for predicting ν is known, ν was given a constant value of 5. This parameter controls the degree of bimodality (i.e. the magnitude of the secondary maximum) in the size distribution. The parameter ν varied between 3 at cloud base to 16 at cloud top. Since ν is underestimated in the model in the upper cloud, the observed bimodality is underestimated by the model predicted spectra above 7.4 km. Overall, however, the model predicted size spectra agree fairly well with the observed size spectra, especially at the smaller sizes. Since crystals < 150 μm may contribute significantly to size distribution area, the model appears well suited for predicting cirrus cloud radiative properties.

The ice water content was fairly constant throughout most of the cloud, indicating vapor deposition or sublimation did little to change ice particle sizes. This was confirmed by the model. The updraft calculated from the IWC was $\leq$ 10 cm s^{-1}, and should not significantly

affect ice particle size based on model results. Advection should not affect ice particle sizes since the sampling was conducted in a Lagrangian spiral descent. This leaves aggregation as the process most likely to account for the observed increase in ice particle size. These conditions made it possible to determine the mean cloud aggregation efficiency from the model and the field data. The mean aggregation efficiency was about 0.5±0.1 (depending slightly on what ice crystal mass-dimension relationship is used), which is typical of values calculated for frontal clouds. Ice particles descending over 3 km increased in mean size due to aggregation by about 40%.

Clear evidence of highly aggregated precipitation in cirrus was observed on replicator images of ice particles obtained during FIRE II on 5 Dec. 1991. Most particles > 100 μm were aggregates comprised of side planes and columns, as shown in Fig. 2. Side planes were always abundant in aggregates. Recent observations of single columns, bullets, and bullet rosettes in cirrus clouds by Matsuo et al. (1993) show no evidence of aggregation for these crystal types. Thus it is postulated that side planes are required for significant aggregation in cirrus clouds. They appear to act as the "glue" which bind other crystals like columns to an aggregate. Both side planes and bullet rosettes are spatial crystal habits believed to form from freezing haze or cloud droplets. Side planes can grow effectively at just above ice saturation, while comparable growth rates for bullet rosettes require higher supersaturations (Furukawa 1982).

Aggregation reduced the optical depth of the 1 Nov. 1986 cirrus cloud by about 20%, relative to the optical depth predicted for growth by vapor diffusion only. This is illustrated in Fig. 3, where the solid line gives the extinction coefficient for size spectra predicted by vapor diffusion and aggregation, while the dashed line is for diffusion growth only. Aggregation reduces the total surface area of a size distribution by combining many small crystals into fewer ice particles, thus reducing the extinction coefficient. Consequently, the single scatter albedo, ω_o, was significantly reduced in the near IR by aggregation growth. This is illustrated in Fig. 4, where ω_o is predicted with (solid line) and without (dashed line) aggregation at a wavelength of 2.2 μm. Calculations of the extinction and absorption coefficients were based on anomalous diffraction theory and the types of ice crystal habits observed by the 2D-C (spatial habits and columns), using the method described in Mitchell and Arnott (1993). The constant slope of the small particle end of the size distribution was used to extrapolate to zero size for these calculations.

Aggregation should also affect the phase function. As light passes through an ice crystal aggregate, multiple pairs of refraction events are likely and more side and back scattering should occur. Thus, the asymmetry factor might be lower in cirrus containing side planes if they are precursors for aggregation.

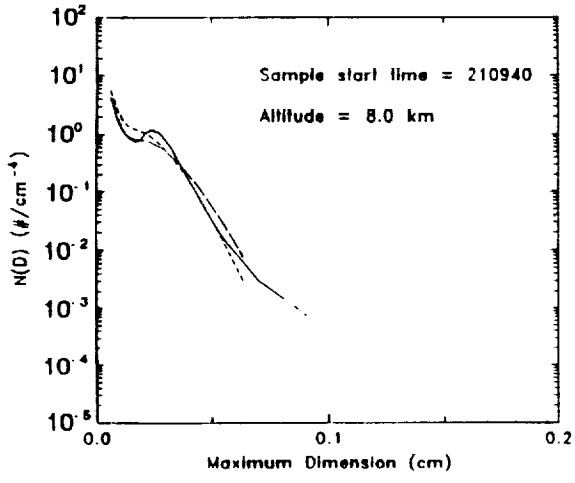

Fig. 1a. Comparison of size spectra from 1 Nov. case study (solid line) with model predicted spectra (long dashed line) and with spectra predicted without aggregation (short dashed line).

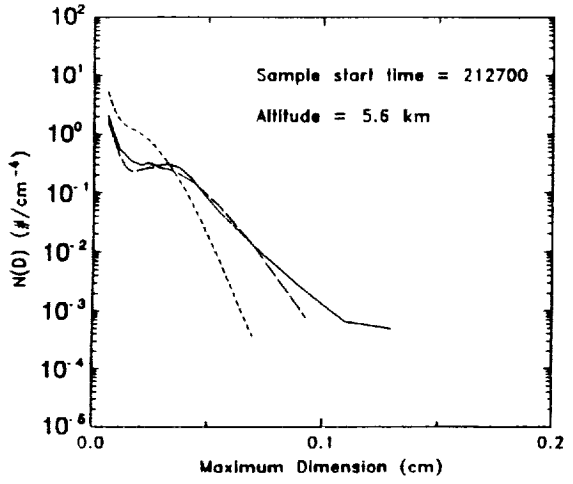

Fig. 1b. Same as Fig. 1 but at 5.6 km.

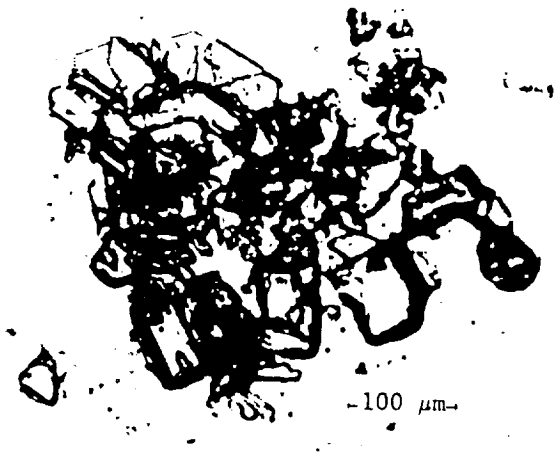

Fig. 2. A side plane/column aggregate from 5 Dec. 1991. Temperature was -40°C.

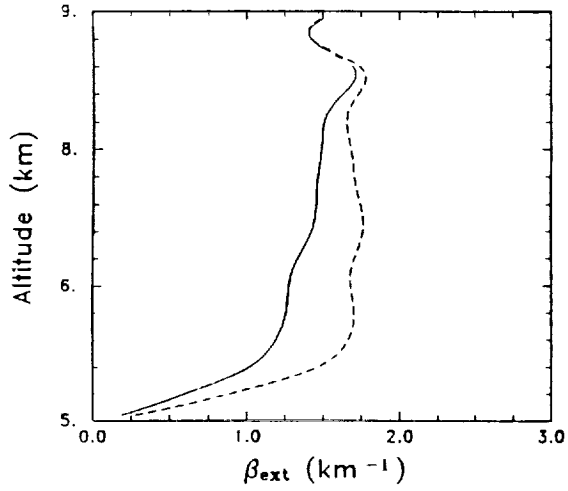

Fig. 3. Profile of the extinction coefficient for the 1 Nov. case study, predicted with (solid line) and without (dashed line) aggregation.

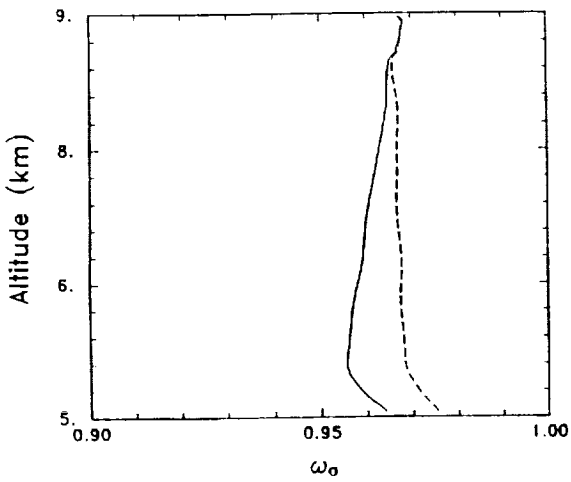

Fig. 4. Same as Fig. 3 except for the single scatter albedo.

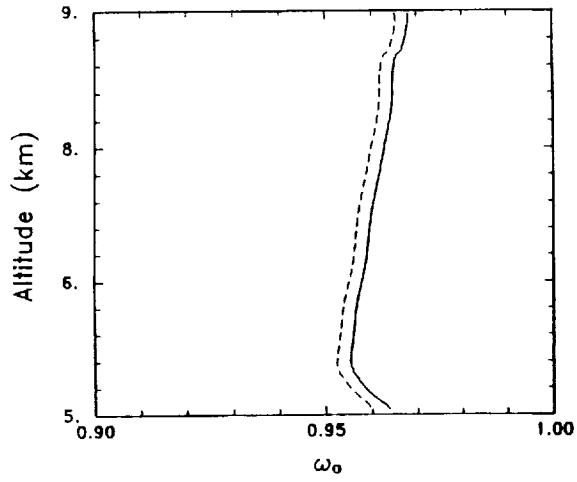

Fig. 5. Profile of the single scatter albedo calculated for all ice particles sizes (solid line), and for sizes > 150 μm (dashed line).

In light of all this, a few comments about anvil cirrus in the equatorial Pacific are in order. The vast majority of ice crystals measured by the DRI replicator during TOGA COARE were side planes. Sizes were small, concentrations were high and they generally appeared aggregated (although the slow speed of the replicator film may have resulted in "piling up" of ice crystals). Similar observations were reported in Takahashi and Kuhara (1993) for tropical cirrus in the western Pacific. Spatial or polycrystalline ice crystals form from frozen cloud or haze droplets, where bullet rosettes are favored at higher supersaturations and side planes dominate at lower supersaturations (Furukawa 1982). If the lower stratosphere contains higher CCN concentrations, such as H_2SO_4 aerosol, than the upper troposphere, then anvil cirrus subjected to stratospheric mixing may receive higher CCN fluxes than other types of cirrus. Homogeneous freezing nucleation rates (Sassen and Dodd 1988) may thus be relatively high, decreasing supersaturations and promoting side planes. The high area to mass ratio for side planes (which increases single scatter albedo (Mitchell and Arnott 1993)), a relatively low asymmetry parameter, and the relatively small sizes and high concentrations of side planes may conspire to produce cirrus which are more reflective in the tropics than in other regions where stratospheric air is not involved. This reasoning supports the theory of Ramanathan and Collins (1992), which emphasizes the high albedo observed from tropical cirrus. It may also help explain the FIRE II observations of 5 Dec. 1991, where cirrus evidently formed in the Mt. Pinatubo aerosol plume (Sassen 1992). The anomalously high CCN concentrations may have depressed supersaturations, explaining the dominance of side planes on that day. On the other hand, aggregation will act to diminish cirrus albedo. As the IWC increases and cirrus thicken, aggregation growth (which depends on IWC) accellerates. All of these factors should be considered when evaluating the albedo and greenhouse effect of tropical cirrus clouds.

Predicted ice particles larger than about 150 μm accounted for 89% of the optical depth in the 1 Nov. 1986 case study. The predicted influence of ice crystals < 150 μm on the single scatter albedo was weaker than the effect of aggregation, as shown in Fig. 5. This case study suggests that the discrepancy between reflectances predicted by radiative transfer models and measured reflectances is not due to extremely high concentrations of undetected ice crystals < 50 μm in length.

Acknowledgment: This research was funded by the NOAA Climate and Global Change Program under grant NA16RC0118-01 and by NASA grant NAG-1-1113.

References:

Furukawa, Y., 1982: Structures and formation mechanisms of snow polycrystals. J. Met. Soc. Japan, 60, 535-547.

Matsuo, T., H. Mizuno, M. Murakami, and Y. Yamada, 1993: Physical factors involved in cirrus cloud formation. Submitted to J. Atmos. Res.

Mitchell, D.L., 1991: Evolution of snow-size spectra in cyclonic storms. Part II: Deviations from the exponential form. J. Atmos. Sci., 48, 1885-1899.

Mitchell, D.L., 1993: A model predicting the evolution of ice particle size spectra and radiative properties of cirrus clouds. Part I: Microphysics. Accepted for publication in J. Atmos. Sci.

Mitchell, D.L. and W.P. Arnott, 1993: A model predicting the evolution of ice particle size spectra and radiative properties of cirrus clouds. Part II: Dependence of absorption and extinction on ice crystal morphology. Submitted to J. Atmos. Sci.

Ramanathan, V. and W. Collins, 1991: Thermodynamic regulation of ocean warming by cirrus clouds deduced from observations of the 1987 El Nino. Nature, 351, 27-32.

Sassen, K. and G. Dodd, 1988: Homogeneous nucleation rate for highly supercooled cirrus cloud droplets. J. Atmos. Sci., 45, 1357-1369.

Sassen, K., 1992: Evidence for liquid-phase cirrus cloud formation from volcanic aerosols: Climatic implications. Science, 257, 516-519.

Takahashi, T. and K. Kuhara, 1993: Precipitation mechanisms of cumulonimbus clouds at Pohnpei, Micronesia. Meteor. Soc. Japan, 71, 21-31.

545-47
N94-22337

Calibration of Radiation Codes in Climate Models: Comparison of Calculations with Observations from the SPECtral Radiation Experiment (SPECTRE)

R. G. Ellingson, W. J. Wiscombe, J. DeLuisi, H. Melfi, and W. Smith

Department of Meteorology
University of Maryland
College Park, MD 20742

Introduction

The primary goal of SPECTRE is to:

close the loopholes by which longwave radiation models have eluded incisive comparisons with measurements.

Likewise, the experimental approach was quite simple in concept, namely:

Accurately measure the zenith infrared radiance at high spectral resolution while simultaneously profiling the radiatively important atmospheric properties with conventional and remote sensing devices

The field phase of SPECTRE was carried out as part of FIRE Cirrus II, and detailed spectra of the downwelling radiance were obtained by several interferometers simultaneous to the measurement of the optical properties of the atmosphere. We are now well along in the process of analyzing the data and calibrating radiation codes so that they may be used more effectively in climate related studies. The calibration is being done with models ranging from the most detailed (line-by-line) to the broad-band parameterizations used in climate models. This paper summarizes our progress in the calibration for clear-sky conditions. When this stage is completed, we will move on to the calibration for cirrus conditions.

Line-by-line Studies

We have begun to compare clear-sky spectra of the downwelling radiance at the surface observed during SPECTRE with FASCOD3P and with narrow-and-broad band radiation models. The mean difference between the observed and FASCOD3P calculated radiance for 26 different spectra is shown in Fig. 1a. In general, the line-by-line model captures most of the features in the observed clear-sky spectra. There is a tendency for the model to underestimate the observed radiance in the window region between 800 to 1000 cm^{-1} and to overestimate it in portions of the 1200 to 1400 cm^{-1} region. The differences in many locations is the order or smaller than the estimated absolute accuracy of the observations (~1.5 units on Fig. 1), but we are not yet in the position to make firm conclusions concerning the spectral and absolute character of the differences because the final instrument calibration is not yet complete.

The differences between the observed and calculated spectra in the 800 to 1000 cm^{-1} region for the for the highest water vapor amounts seen during SPECTRE show that the FASCOD continuum yields better results than the one of Roberts et al. (1976). The data from the drier cases can not be use to support this conclusion at this time because the absolute error of the observations is larger than the radiance in the more transparent regions of the 800 to 1000 cm^{-1} region. As the instrument calibration is completed, it will be

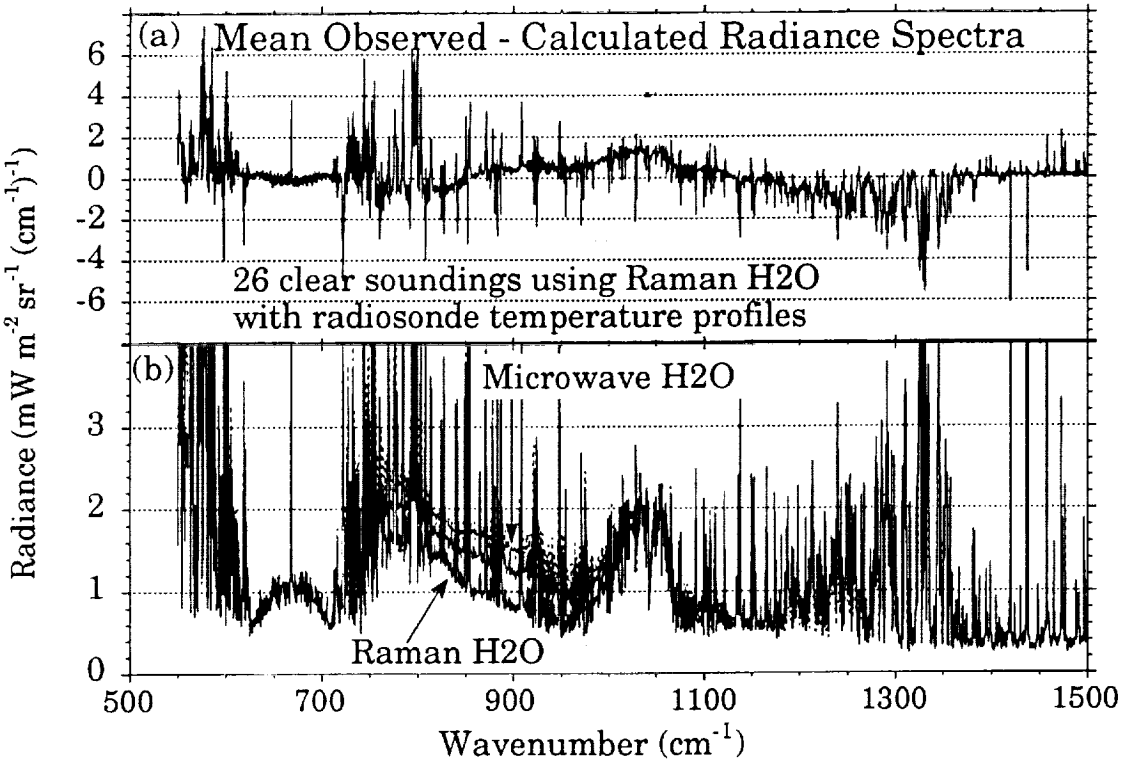

Fig. 1. Mean (a) and rms (b) AERI observed minus FASCOD3P calculated radiance spectra from SPECTRE. The calculations were performed using near simultaneous radiosonde temperature and Raman water vapor profiles with surface based trace gas data and the 1992 line compilation as input.

possible to use the high relative accuracy to check the spectral signatures of the differences and to put error bars on them. Nevertheless, the preliminary indications are that this model may be used to calibrate radiation codes used in climate models.

We recently completed 26 sets of comparisons of AERI observations with FASCOD calculations using near simultaneous water vapor profiles from radiosondes, Westwater's microwave radiometer and Melfi's Raman lidar. The spectral distribution of the rms differences (Fig. 1b) show that the Raman data yield a more consistent spectral pattern of differences between observations and calculations than occurs when the radiosonde or microwave data are used in the calculations. As the calibration of the AERI is finalized, it will be possible to use the high relative accuracy of the observations to check the spectral signatures of the differences between observations and calculations and to put better error bars on the absolute differences. The improved calibration data and CART site observations over larger water vapor amounts should allow more stringent tests of the continuum formulations than possible heretofore, particularly if a Raman lidar is used for profiling water vapor.

We have estimated the flux uncertainty of FASCOD relative to the observations in the 550 to 1500 cm^{-1} interval by using model calculations for the angular variations. The comparisons for 26 different spectra yield a mean (observed - calculated) flux uncertainty of the calculations of 0.4 ±0.2 W•m^{-2}. The data do not allow us to estimate the uncertainties in the 0 to 550 cm^{-1} region. However, since this portion of the spectrum is nearly opaque

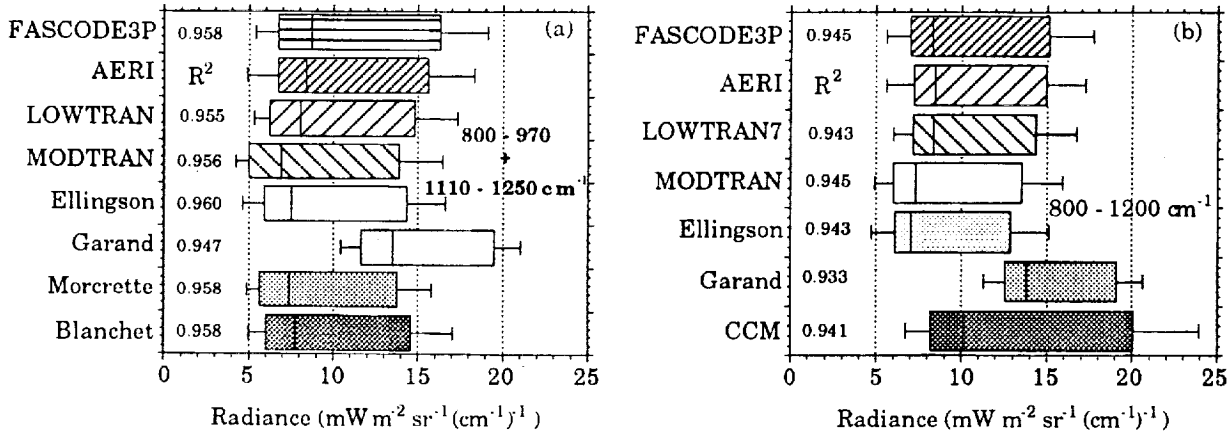

Fig. 2. Distributions of vertically downwelling radiance at the surface for 26 clear-sky cases as calculated by several different models and observed by the AERI during SPECTRE. The vertical lines in the boxes show the median values. The edges of the boxes mark the limits of ±25% of the population, and the lines extending from the boxes mark the minimum and maximum values. The fraction of the AERI variance explained by each model is shown in the column marked R^2.

for the conditions we observed during SPECTRE, the uncertainties in calculating the downward flux at the surface from this portion of the spectrum are relatively small. Since the uncertainties in the interferometer data are smaller than those associated with the pyrgeometers, we believe that the interferometer-based flux data will serve as a baseline calibration of the pyrgeometers for homogeneous clear or cloudy conditions.

A disturbing trend of the differences between the AERI "observed" and FASCOD fluxes is that differences become more negative as the total precipitable water (PW) increases, independent of the source of water vapor data. The calculated flux (integrated radiance for the 550 to 1500 cm^{-1} region) is greater than that observed for 6 of the 9 cases with PW > 1.4 cm. These differences appear to be correlated primarily with PW in the 1100 -1200 cm^{-1} region and with surface temperature in the 725 - 850 cm^{-1} region. These differences hint at potential problems in the continuum formulation - temperature dependence in the self-broadened term and the magnitude of the continuum coefficients in the foreign broadened regions. We will have to closely examine ARM observations at higher water vapor amounts and temperatures to see if these differences continue.

Calibration of Radiation Codes for Climate Models

Spectrally integrated observations have also been compared with calculations from models used in GCMs (including GLA, CCM1, CCC, NMC, RPN and ECMWF) and several detailed models (e.g., AFGL's MODTRAN and LOWTRAN7, and Ellingson's narrow band model). The study has concentrated on the semi-transparent 800 - 1200 cm^{-1} region first since ICRCCM indicated that this is the most suspect portion of the spectrum due to uncertainties associated with the water vapor continuum. Large differences have been found between some models and the observations, although the differences tend to be largely systematic (see Fig. 2). Interestingly, the fractional variance of the AERI observations explained by the different models is about the same. The latter result may largely be due to the small range of precipitable water sensed during SPECTRE. Clearly, some models have deficient parameterizations of the water vapor continuum, and these will

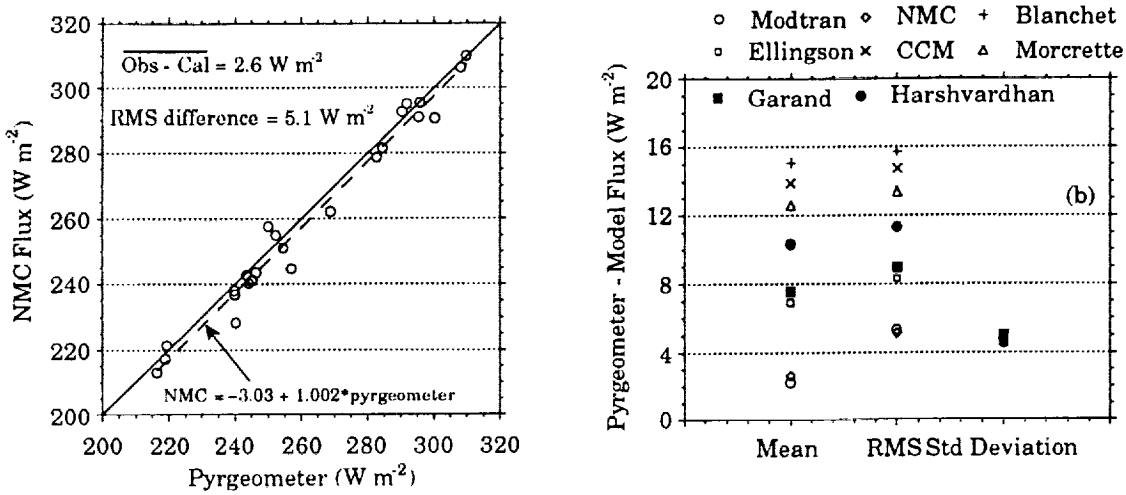

Fig. 3 Comparisons of model calculated with pyrgeometer observed clear-sky downward fluxes at the surface during SPECTRE. (a) NMC model; (b) Statistics from other models.

have to be changed in order for the models to yield correct radiances and fluxes over the full range of atmospheric conditions.

We've also begun to intercompare the model calculations with clear-sky pyrgeometer observations obtained during SPECTRE (Fig. 3). Overall, the results are quite impressive. For a 26 clear-sky set, the NMC model underestimates the observed fluxes by about 3 $W \cdot m^{-2}$ in the mean, and the rms difference is about 6 $W \cdot m^{-2}$. The other models have somewhat greater biases, but all models have about the same RMS error when the biases are removed - about 6 $W \cdot m^{-2}$. These comparisons are very consistent with the model-interferometer comparisons. Since the nominal accuracy usually ascribed to pyrgeometer data is about ±5%, the comparisons hint that the uncertainties in the pyrgeometer data may not be as large as thought heretofore when great care is exercised in the observations.

References

Roberts, R. E., J. E. A. Selby, and L. M. Biberman, 1976: Infrared continuum absorption by water vapor in the 8-12 μm window. *Appl. Opt.*, **15**, 2085-2090.

546-47
197546
4
N94-22238

SSH-2 Measurements of Cirrus at 18-28 μm from the King Air During FIRE II

Michael K. Griffin

Atmospheric Sciences Division
Phillips Laboratory, Geophysics Directorate
PL/GPAS
Hanscom AFB, MA 01731-3010

1. INTRODUCTION

In November of 1991, the First ISCCP (International Satellite Cloud Climatology Project) Regional Experiment (FIRE) Phase II cirrus study took place at Coffeyville Kansas. The field experiment incorporated instrumentation from surface, aircraft and satellite to attempt to define the optical, radiative and microphysical characteristics of these high altitude, predominantly ice clouds[1]. The NCAR King Air research aircraft was outfitted with a variety of radiative and microphysical instrumentation for the FIRE II project. Included for this project was the SSH-2, a 16-channel passive radiometer. The SSH-2 was originally designed as a space-qualified infrared (IR) temperature and water vapor sounder for deployment onboard the Defense Meteorological Satellite Program (DMSP) series of environmental satellites. For this experiment, only those channels associated with the water vapor profiling function have been examined although downwelling radiance measurements were taken at all channels during the project. With supporting information from the aircraft telemetry observations it may be possible to relate these SSH-2 measurements to cloud radiative and microphysical properties. The following sections will describe the spectral characteristics of the instrument, the calibration scheme used to convert the raw measured counts into calibrated radiances and the case studies that will be covered in this paper. This will be followed by a discussion of the results of this preliminary investigation and a description of future work to be done.

2. INSTRUMENT DESCRIPTION

In the early 1970s, DMSP developed an IR sensor, the SSH, to obtain atmospheric temperature and humidity information from space-based platforms. In 1978, a decision was made to break with the traditional IR sounding sensors and develop a suite of microwave sensors to perform the temperature and water vapor sounding tasks. With this change in direction, the lone remaining IR sounder (SSH-2 Serial #8) was placed in storage for a period of 12 years. In late 1990, the instrument was obtained by the Phillips Laboratory, Geophysics Directorate to be used for terrestrial applications, specifically, the FIRE II field project.

The SSH-2 employs 16 channels located: near the 15 μm CO_2 band, in the water vapor rotational band from 18 - 28 μm, in the IR window (11 - 13 μm) and at 3.7 μm (Table 1.). Prior to installation of the SSH-2 into the King Air some internal modifications were performed in the laboratory. Since the instrument is self calibrating and the cold space calibration is no longer feasible, a cold calibration source was added to the instrument. A portable personal computer was attached to serve as the controller and data acquisition system using software written to access and decode the data stream and to control the scanning mechanism of the SSH-2. With these modifications in place, the SSH-2 was pressure mounted directly to an upward-looking open viewport to avoid the problem of limitations in the spectral bandpass of the aircraft windows.

Measurements at each channel were made every second for a period of 128 seconds followed by a 32 second calibration sequence. Both internal warm and cold calibration sources are sampled during each calibration period for all 16 channels but the physical source temperatures are only measured every 15 minutes of operation. Aircraft telemetry data (ambient temperature, pressure, aircraft pitch, roll, etc.) was

accumulated and stored separately by NCAR RAF. The King Air also carried particle characterization instrumentation which provide *in-situ* measurements of cloud particle content, size, concentration and phase.

Calibration measurements were performed at intervals of approximately 2-3 minutes. The SSH-2 was designed to respond linearly to changes in the amount of radiation entering the system, therefore the conversion from instrument counts to radiant energy involves a simple linear regression of the instrument output to the energy input at each filter.

3. CASE STUDIES

During the intense observation period of 25-26 November 1991, the King Air flew three missions with two on 26 November. Flight 1 on the 26th was a clear air flight with little or no cloud cover over the central instrument site. The King Air took off at 1053 UTC from the Coffeyville, KS airport and gradually ascended to 8.5 km maintaining a relative ground position over the site (upward spiral). At 1143 UTC the King Air reached altitude and begun its descent back to Coffeyville again in a spiral over the site landing at 1237 UTC. The flight provided a unique opportunity to obtain background water vapor signals from the SSH-2 without contamination from cloud liquid water and ice particles. The lack of cloud moisture was confirmed by coincident radiosonde, raman lidar measurements and onboard particle measuring equipment during the course of the flight.

A plot of the calibrated downwelling radiance (or for this graph T_b) versus aircraft altitude for all 7 channels is shown in Figure 1a. The graph of each channel is denoted by its center wavenumber. As expected all seven channels display decreasing T_b with increasing altitude. Channel 16 (533 cm^{-1}) has the

Table 1. SSH-2 instrument channels, spectral bands and relative transmission characteristics. (CW = Center Wavenumber/Wavelength, FWHH = Full Width Half Height)

Channels	CW (cm^{-1})	FWHH (cm^{-1})	CW (μm)	FWHH (μm)	Spectral Bands	Relative Characteristics
1	668.3	2.3	14.963	0.051		Opaque
2	676.6	9.6	14.78	0.21		
3	695.5	10.1	14.378	0.209	CO_2	
4	707.4	9.1	14.136	0.182	Band	
5	731.2	9.7	13.676	0.181		
6	746.4	11.3	13.398	0.203		
7	796.5	10.9	12.555	0.172	Shoulder	
8	898.4	11.7	11.131	0.145	Window	Transparent
9	2657.7	274.6	3.763	0.39	Window	
10	355.5	14	28.129	1.108		Opaque
11	396.7	10	25.208	0.636		
12	409.3	12.4	24.432	0.74	Water	
13	419.8	19.9	23.821	1.13	Vapor	
14	440.6	18.3	22.696	0.943	Rotational	
15	496.6	14.2	20.137	0.576	Band	
16	533.2	14.4	18.755	0.507		Less Opaque

least decrease in T_b with height and Channel 10 (356 cm^{-1}) the largest change. Channel 10 is in a spectral region of high water vapor absorption and therefore its sampling volume would be limited to a region close to the aircraft. The two channels (497 and 533 cm^{-1}) have the smallest range of the SSH-2 channels due to their location in less absorbing regions of the water vapor rotational band. All channels display a quasi-constant change in T_b with altitude except for a small anomaly at approximately 4.3 km presumably due to the passage of the King Air under a thin contrail. Due to the dry atmospheric conditions that existed on the morning of 26 November 1991 the curves in Figure 2 should represent the minimum radiance or coldest T_b that each channel should measure at the respective altitude.

The King Air made its second flight of the day departing at 1812 and landing at 2128 UTC. During the hours between the end of the first flight and beginning of the second, cirrus began to form over the area. As the system approached, the cirrus shield grew from relatively thin scattered cirrus to broken and then overcast cirrostratus partially obscured in the later afternoon by a mid-level cloud deck. The King Air initially climbed to 8.5 km passing through the base of the cirrus layer at approximately 6 km. At 1951 the King Air began a descent to 6.2 km through the cirrus deck using a step-down racetrack pattern with 0.3 km increments. Upon reaching 6.2 km the King Air flew a spiral over the central site up to 8 km where at approximately 2107 UTC it began its descent to the landing at 2128 UTC. Throughout the flight the King Air was either inside the cirrus deck or just below; the King Air did not have a flight ceiling high enough to reach the top of the cirrus layer.

Figure 1b is a graph of Channel 13 (420 cm^{-1}) versus time (seconds UTC) for Flight 2. Compared to the earlier flight there is considerably more variability to the measurements due to the inhomogeneities of the cirrus in the field of view. Since the SSH-2 channels respond to both the opacity of the atmosphere with respect to water vapor and to the microphysical characteristics of the particles in the channel sampling volume it is difficult to isolate a single effect or contribution from a single channel measurement. However, with knowledge of the clear sky atmospheric radiance it may be possible to isolate the contribution from the cirrus. Figure 2 is a plot of the channel 13 T_b for both flights on 26 November as a function of aircraft altitude. Clearly the T_b for the clear flight is less than that for the cirrus flight at all altitudes. The data for Flight 2 is shown as a range of values measured over the course of the flight as a function of altitude. The mean values for each altitude are shown by a connected line.

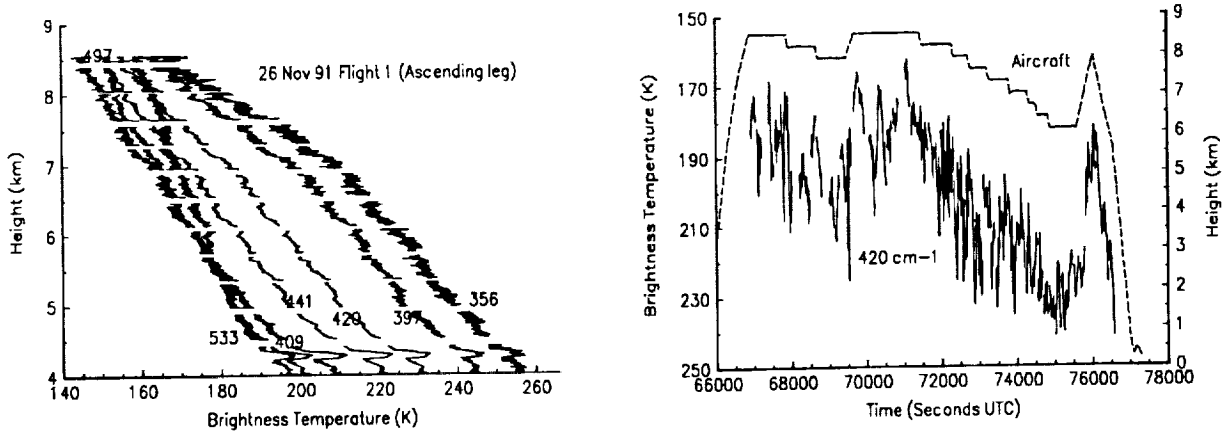

(a) (b)

Figure 1. SSH-2 measured Brightness Temperatures for Flights 1 and 2 on 26 November 1991. Measurements are for a) the ascending leg of Flight 1 (versus aircraft altitude) for each channel and b) for Flight 2, Ch 13 (420 cm^{-1}) as a function of time with aircraft altitude also shown (not meant to match T_b scale).

4. DISCUSSION

It is advantageous to be able to separate the background radiance from the cloud radiance either through a theoretical model or as in this case with actual measurements. The timeliness of the two flights make this case study unique in that the assumption of unchanging background from flight to flight has more validity because of the short time separation. However, the question remains what can be recovered from the cloud radiances? Utilizing the PL MODTRAN atmospheric transmission model[2] the theoretical background channel radiances can be obtained as well as radiances for specific instances of cirrus occurrence. Two cirrus models are available to MODTRAN (thin and standard cirrus) which differ only in the size of particles used in the cirrus parameterization (4 and 64 μm, respectively). The model was run for both clear and cirrus (at 6-9 km) cases for an aircraft altitude of 6 km (Figure 3). The slopes of the three curves vary measurably from clear to cloudy scenes. In theory, since both cirrus cloud model runs used the same cloud physical and extinction characteristics, the difference in the curves should be due to the microphysical characteristics of the models (i.e., particle size). If this assumption is true then it may be possible to estimate the cirrus particle sizes from measurements by computing the slope of the channel T_bs or ratioing two channels that most closely characterize the spectral change in T_b.

5. ACKNOWLEDGMENTS

Thanks to Dave Murcray, Frank Murcray, John Williams, Geoff Koenig and Andrew Heymsfield for their assistance in fielding this instrument. Funding for this project was provided by the Department of Energy Research and Development Division under Interagency Agreement # DE-AI06-91RL12348.

6. REFERENCES

1. D. O'C. Starr, "A cirrus cloud experiment: Intensive field observations planned for FIRE," *Bull. Amer. Meteoro. Soc.*, **67**, 119-124, 1987.

2. A. Berk, L. S. Bernstein and D. C. Robertson, "MODTRAN: A moderate resolution model for LOWTRAN 7," *Geophysics Laboratory Technical Report GL-TR-89-0122*, 42 pp., April 1989.

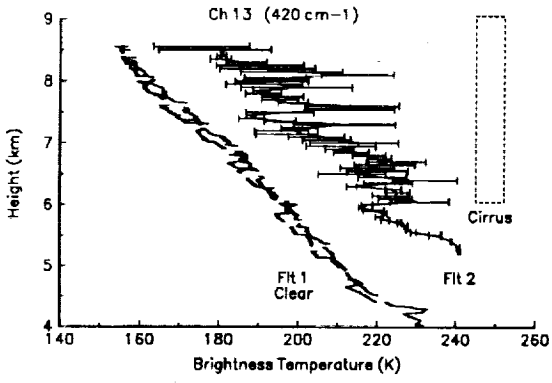

Figure 2. SSH-2 measurements for both clear and cirrus flights plotted together as a function of altitude for channel 13 (420 cm^{-1}).

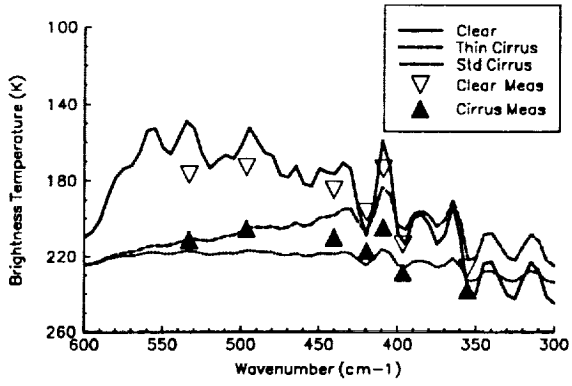

Figure 3. MODTRAN model estimations of the downwelling T_b at a 6 km altitude from a clear sky scene and from a 3 km cirrus layer at 6 km. The corresponding SSH-2 measurements are shown as triangles.

547-47
197547
N94-22339

Investigation of the Effects of the Macrophysical and Microphysical Properties of Cirrus Clouds on the Retrival of Optical Properties: Results for FIRE II

Paul W. Stackhouse, Jr. and Graeme L. Stephens
Department of Atmospheric Science, Colorado State Unisversity
Fort Collins, Colorado, 80521

Introduction

Due to the prevalence and persistence of cirrus cloudiness across the globe, cirrus clouds are believed to have an important effect on the climate. Stephens et al., (1990) among others have shown that the important factor determining how cirrus clouds modulate the climate is the balance between the albedo and emittance effect of the cloud systems. This factor was shown to depend in part upon the effective sizes of the cirrus cloud particles. Since effective sizes of cirrus cloud microphysical distributions are used as a basis of parameterizations in climate models, it is crucial that the relationships between effective sizes and radiative properties be clearly established. In this preliminary study, the retrieval of cirrus cloud effective sizes are examined using a two dimensional radiative transfer model for a cirrus cloud case sampled during FIRE Cirrus II. The purpose of this paper is to present preliminary results from the SHSG model demonstrating the sensitivity of the bispectral relationships of reflected radiances and thus the retrieval of effective sizes to phase function and dimensionality.

Two Dimensional Radiative Transfer Model

The Spherical Harmonic Spatial Grid (SHSG) method of radiative transfer developed by Evans (1993) is employed in this study. This method solves the two dimensional (2D) radiative transfer equation by approximating the radiance field in terms of a spherical harmonic expansion for the angular dependencies and a discrete grid for the spatial properties. The discretization of the radiative transfer equation in this way, along with the specified boundary conditions, results in a coupled linear system which is relatively sparse and is then solved iteratively using the conjugate gradient method. The advantage of SHSG for this study is that the transfer of radiation through arbitrary cloud inhomogeneities can be computed in an efficient manner. Additionally, since the radiance field at all grid points is expanded in terms of a spherical harmonic series, the radiances at any grid point or angle can be computed by summing over the truncated series . The summation of a truncated series introduces noise to the solution in the form of oscillations. In order to minimize these problems, the δ-M scaling method is used in order to damp the oscillations normally associated with truncating the Legendre series of the phase function and the Cesàro summation method (Dave and Armstrong, 1974) is adapted to two-dimensions to minimize the oscillations in the intensities. SHSG also has an independent pixel mode (I.P.) where the horizontal coupling of the radiation field is turned off, which simulates plane-parallel radiances. The 2D radiances produced from SHSG agree with Monte Carlo simulations to within 1% in the side scattering portion of the phase function, but can differ by at most 8% at the forward and backup scattering peaks. At this time the model is monochromatic and does not treat molecular scattering or absorption.

Estimation of the Cloud Field Optical Properties

For this study a 2D cloud field was obtained from a RHI scan by WPL's Ka-band radar for a cirrus cloud sampled on 26 November 1991 during the FIRE Cirrus II intensive field observation period (Taneil Uttal, personal communication). For the results shown here, an image was used which gave cloud reflectivities at 50 meter resolution and represented a rather homogeneous looking cirrus cloud characterized by a thick generating cell in the center. The cloud reflectivities were converted to ice water content using the empirical relation of Sassen (1987), $IWC = 0.037 Z_i^{0.696}$, where Z_i is the reflectivity factor of ice ($mm^6 \cdot m^{-3}$) and IWC is the ice water content ($g \cdot m^{-3}$). The estimated ice water contents were then used to scale the extinctions computed from a modified gamma distribution of equivalent area spheres with IWC of 0.0216 $g \cdot m^{-3}$ and an effective radius of 80 μm. Table 1 gives the optical properties of the cloud simulated in this study. The extinctions were computed at the two Landsat wavelengths 0.83 and 1.65 μm. The single scatter albedos and phase functions were assumed to remain constant across the cloud domain but varied with wavelength. The single scatter albedos were computed with Mie theory and the phase functions

were chosen to have asymmetry parameters consistent with the geometric optic computations of hexagonal ice crystals by Takano and Liou (1990 and personal communication). The asymmetry parameters for each wavelength were used as g_{eff} in the double Henyey-Greenstein function (DHG) to prescribe the phase function. The double HG has the form, $P(\cos\Theta) = b\ g_1 + (1-b)\ g_2$, where g_1, g_2 and b are constants related by $g_{eff} = b\ g_1 + (1-b)\ g_2$. Using the preceding assumptions, a cloud field was obtained which varied in extinction only, which means that the effective radius is held constant throughout the cloud.

Table 1: Cirrus cloud optical properties as a function of wavelength (λ) for the simulations presented in this paper.

λ (μm)	K_{ext} (km^{-1})	ω_0	b	g_1	g_2	g_{eff}
0.83	0.45863	0.9998	1.000	0.790	-0.600	0.79
			0.970	0.833	-0.600	0.79
			0.920	0.911	-0.600	0.79
1.65	0.46264	0.8940	1.000	0.810	-0.550	0.81
			0.970	0.852	-0.550	0.81
			0.920	0.928	-0.550	0.81

Results

Normalized nadir reflectances given by $R_\lambda = \frac{\pi L_\lambda}{\mu_0 F_{0_\lambda}}$ (Weilicki et al., 1990) were computed for the cloud fields described above using a grid of 110x29 which represented an area of approximately 11 km by 3 km. The solar zenith angle was 50°. The results are shown in the bispectral plot of reflectances at 0.83 and 1.65 μm as shown in Figure 1. For comparison, a series constant effective radius curves from 15 μm to 150 μm computed using the phase function with $b = 1$ (DHG1) and the independent pixel approximation of SHSG are plotted along with data in Fig. 1. As expected, the independent pixel results in the top panels of Fig. 1 give relationships which agree with the shapes of the effective radius curves and the reflectances from DHG1 lie on the 80 μm curve. However, it is also seen that the other forms of the phase function give reflectances that give underestimations of effective radii up to 35% for $\theta_0 = 50^0$ and over 80% for $\theta_0 = 10^0$. These underestimations decrease with increasing optical depth (optical depth increases from the origin along the curves). The sensitivity to the shape of the phase function is discussed by Wielicki *et al.* and is due to the magnitude of the phase function at a particular scattering geometry. In this case, the bispectral relationships at $\theta_0 = 10^0$ are much more sensitive than at $\theta_0 = 50^0$ because the forms of the phase function differed much more greatly in the backscatter portion ($\Theta = 170^0$) than in the sidescattered portion ($\Theta = 130^0$) of the phase function. The decreased sensitivity to the phase function shape as a function of optical depth is shown more clearly by Figure 2 which depicts the retrieved effective radius as a function of horizontal position throughout the cloud. The solid line gives the ideal retrieval for these cases since a distribution of 80 μm was assumed throughout the cloud. Referring to the I.P. retrieval lines shows that as optical depth increases the difference between the curves using DHG1 and DHG2 decreases dramatically. This sensitivity to the phase function in thinner clouds is due to the single scattering processes which dominate. As the cloud becomes thicker multiple scattering becomes more important and the individual shapes of the phase function become less important to the retrieval of effective radius.

Figure 1 also shows that unlike the independent pixel clouds, the 2D radiances for the upper cluster of points do not correspond in slope with the curves of effective radius. In fact, the thinner clouds give overestimations of effective radius up to a factor of 2 while the thicker clouds give underestimates of effective radius of 10-25% for $\theta_0 = 50^0$. The effect of the cloud geometry for this case is to change the fundamental relationship between the effective radii and the reflectances at the wavelengths shown for this preliminary study. This geometry effect can be better understood by referring again to Fig. 2. Note when comparing the 2D retrieval curves with the I.P. curves that the differences become greatest for the largest optical depth. Referring to the 3rd panel from the top and comparing it to the column optical depth in the bottom panel shows that at the front of the thickest part of the cloud (i.e., 4.5 km) there are underestimations of the effective radius while behind the cloud there are overestimations. This effect may be thought of as an "optical depth" shadowing phenomena because for this sun angle (50^0 where the sun comes from the left) radiances are enhanced in front of the cloud and decreased behind the cloud relative to the I.P. calculations. Note that for the higher sun angle shown in Fig. 1, this geometric effect is greatly reduced.

Lastly, figure 2 shows a large disagreement between the I.P. and curves and the ideal 80 μm line for the thinner clouds. This is due to the effects of the vertical inhomogeneities. Although this effect is not entirely understood at this time, it is clear that for thin clouds, as pictured in the top two panels of Fig. 2, the variation of optical along the vertical has a distinct effect on the reflected radiances as compared to an homogeneous cloud with an identical integrated optical depth. In cirrus which are dominated by thin clouds this process may play an extremely important role in the interpretation of the radiance fields.

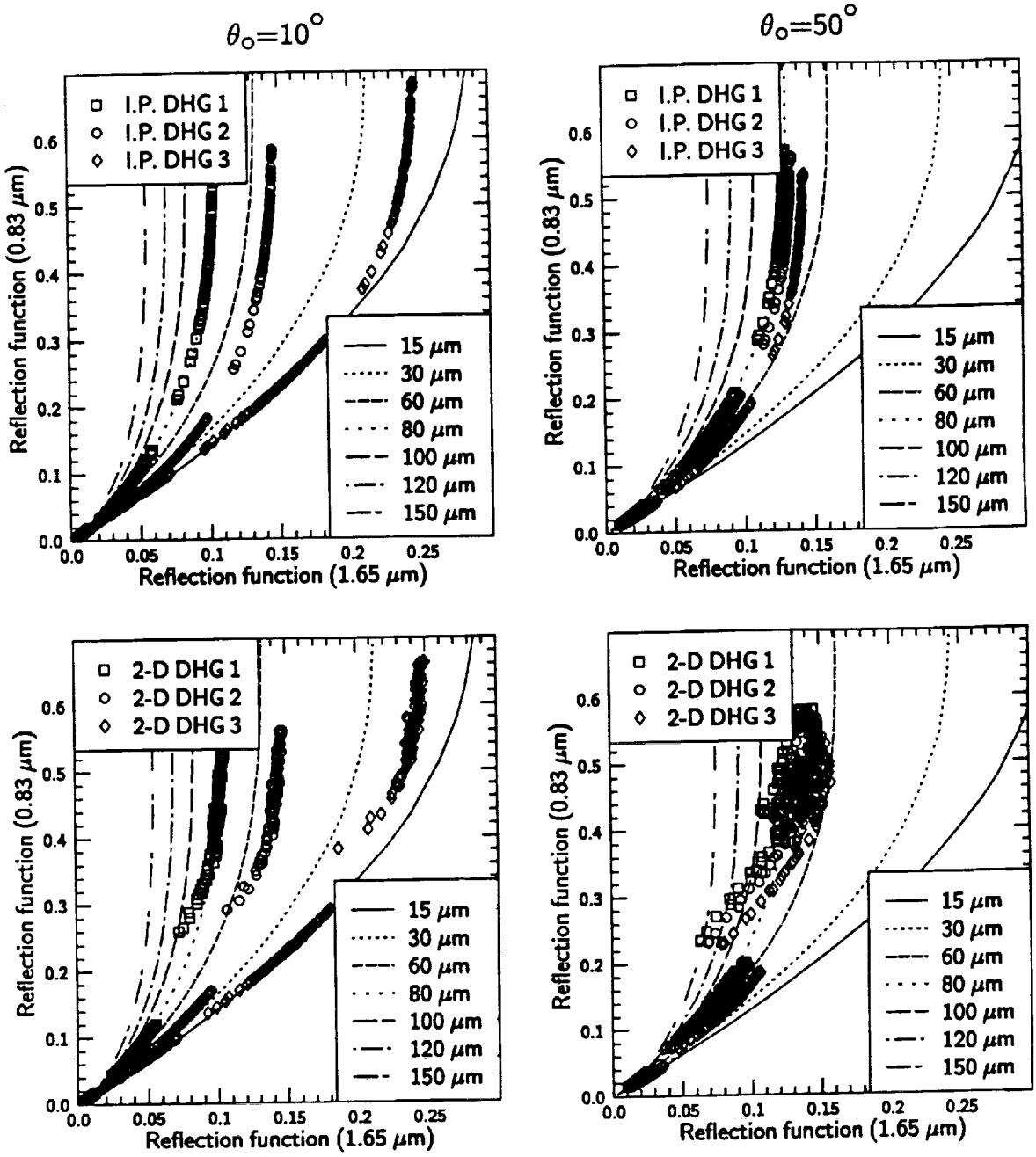

Figure 1: Bispectral plots of nadir reflectances for a simulated 2-D cirrus cloud field with variable exinction but constant effective radius ($r_e = 80\mu m$) with the optical properties shown in Table 1. The viewing angle is 0.0° and $\phi_o = 180°$. The top panels give I.P. results and the bottom panels give 2-D results. The solar zenith angle is labeled for each column.

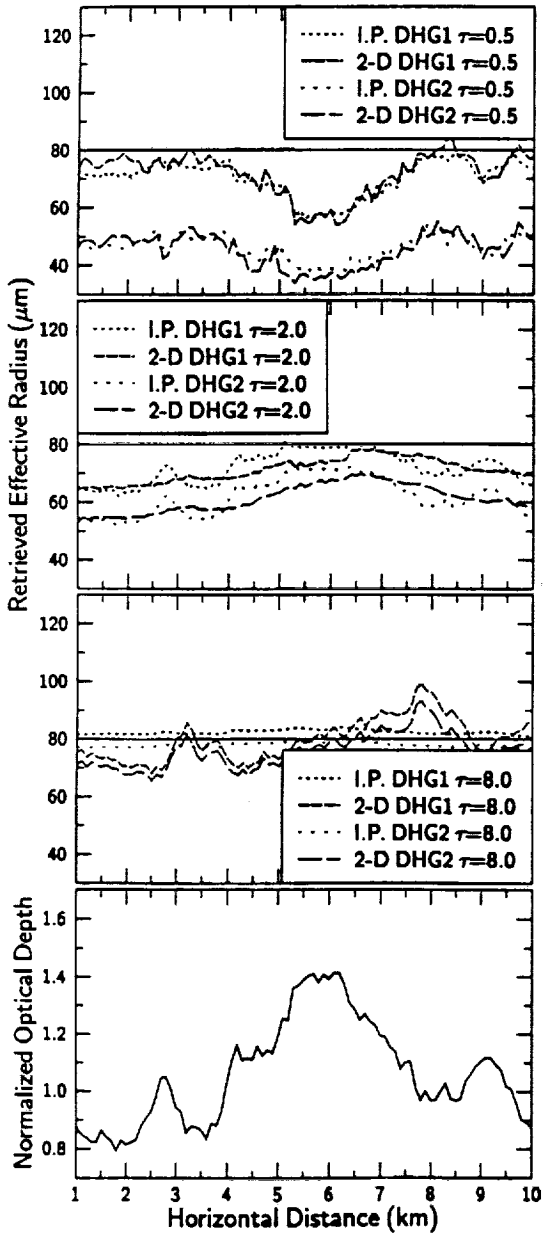

Figure 2: Retrieved effective radius as a function of horizontal position for the solar geometry of $\theta_o = 50.0°$, $\phi_o = 0.0°$ and a viewing angle of 0.0°. The top three panels represent 3 different optical depths and the bottom panel gives the integrated normalized optical depth throughout the cloud.

Conclusions

These results illustrate that retrieved cirrus effective radii contains significant biases not only due to the lack of understanding of ice scattering properties but also due to the inhomogeneities of the clouds systems. For cirrus clouds, which tend to be thinner, the sensitivities of the radiance fields to the shape of the phase function and to the vertical distribution of the optical depth may contribute greatly to biases in the retrieval of effective radius. Geometric biases may also play a role in very thick cirrus systems which sometimes occur in the tropics. Cirrus parameterizations based upon such retrieved effective radii will also produce biases in the radiative properties which may be important to the interpretation of climate simulations. This study shows that spectral changes in the radiance fields of cirrus clouds depend not only on the intrinsic microphysical properties of the clouds but also upon their spatial structure.

References

Dave J. V. and B. H. Armstrong, 1974: Smoothing of the intensity curve obtained from a solution of the spherical harmonics approximation to the transfer equation. *J. Atmos. Sci.*, **31**, 1934-1937.

Evans, K. F., 1993: Two-dimensional radiative transfer in cloudy atmosphere Part I: the spherical harmonic spatial grid method. (accepted *J. Atmos. Sci.).*

Sassen, K., 1987: Ice cloud content from radar reflectivity. *J. Clim. Appl. Meteor.*, **26**, 1050-1053.

Stackhouse, P.W., Jr. and G.L. Stephens, 1991: A theoretical and observational study of the radiative properties of cirrus: results from FIRE 1986. *J. Atmos. Sci.*, **48**, 2044-2059.

Stephens, S.-C. Tsay, P. W. Stackhouse, Jr., and P. J. Flatau, 1990: The relevance of the microphysical and radiative properties of cirrus clouds to climate and climatic feedback. *J. Atmos. Sci.*, **47**, 1742-1753.

Takano, Y. and K.-N. Liou, 1989: Solar radiative transfer in cirrus clouds. Part I: Single-scattering and optical properties of hexagonal ice crystals. *J. Atmos. Sci.*, **46**, 3-19.

Weilicki, B.A., J.T. Suttles, A.J. Heymsfield, R.M. Welch, J.D. Spinhirne, M-L.C. Wu, D.O'C. Starr, L. Parker and R.F. Arduini, 1990: The 27-28 October 1986 FIRE IFO Cirrus Case Study: Comparison of Radiative Transfer Theory with Observations by Satellite and Aircraft. *Mon. Wea. Rev.*, **118**, 2356-2376.

S48-47
197548
P 4

EXTINCTION EFFICIENCIES FROM DDA CALCULATIONS SOLVED FOR FINITE CIRCULAR CYLINDERS AND DISKS

Withrow, J. R., and Cox, S. K.
Department of Atmospheric Science
Colorado State University
Fort Collins, CO 80523

July 13, 1993

N94-22340

1.0 Introduction

One of the most commonly noted uncertainties with respect to the modelling of cirrus clouds and their effect upon the planetary radiation balance is the disputed validity of the use of Mie scattering results as an approximation to the scattering results of the hexagonal plates and columns found in cirrus clouds. This approximation has historically been a kind of default, a result of the lack of an appropriate analytical solution of Maxwell's equations to particles other than infinite cylinders and spheroids. Recently, however, the use of such approximate techniques as the Discrete Dipole Approximation has made scattering solutions on such particles a computationally intensive but feasible possibility. In this study, the Discrete Dipole Approximation (DDA) developed by Flatau (1992) is used to find such solutions for homogeneous, circular cylinders and disks. This can serve to not only assess the validity of the current radiative transfer schemes which are available for the study of cirrus but also to extend the current approximation of equivalent spheres to an approximation of second order, homogeneous finite circular cylinders and disks. The results will be presented in the form of a single variable, the extinction efficiency, Q_{ext}.

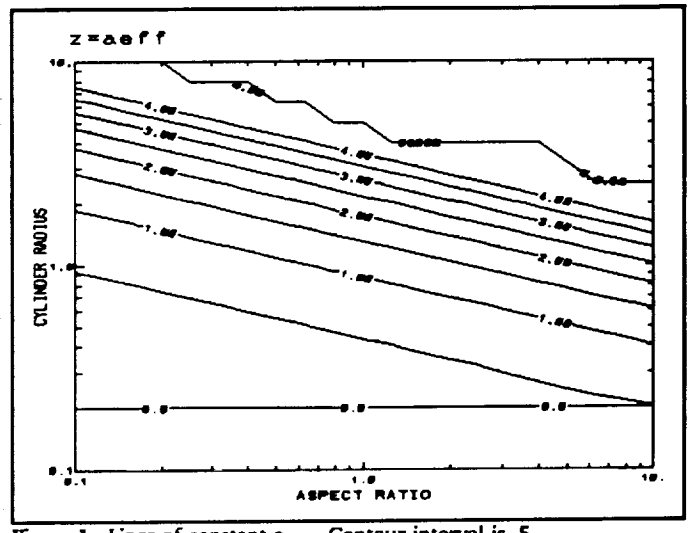

Figure 1. Lines of constant a_{eff}. Contour interval is .5.

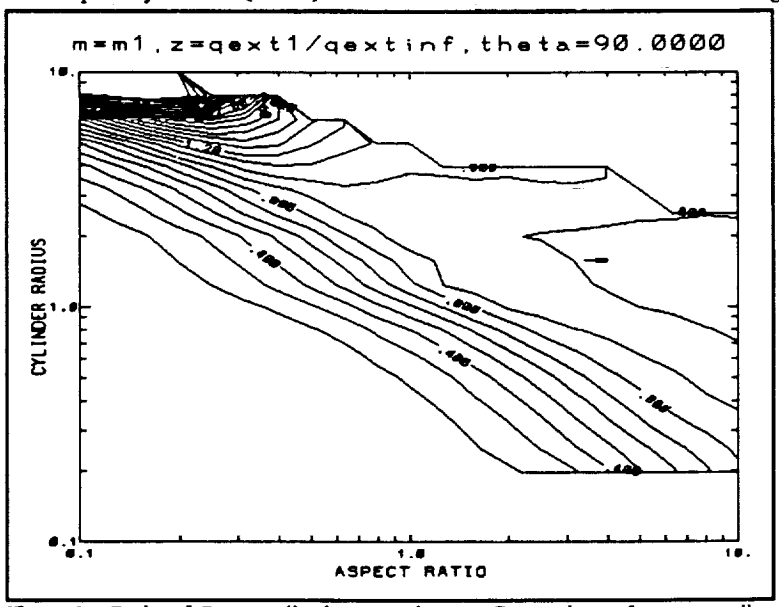

Figure 2. Ratio of Renormalized Q_{ext} values to Q_{ext} values of corresponding infinite cylinders. The contour interval is .1, m = 1.32 + 0i, and Θ=90.

Before proceeding, a few definitions and distinctions must be given. The first concerns the normalization of the extinction efficiency for nonspherical particles. Usually, Q_{ext} is normalized according to the following equation:

$$Q_{ext} = \frac{C_{ext}}{\pi a_{eff}^2}$$

where C_{ext} is the extinction cross section and a_{eff} is the (effective)

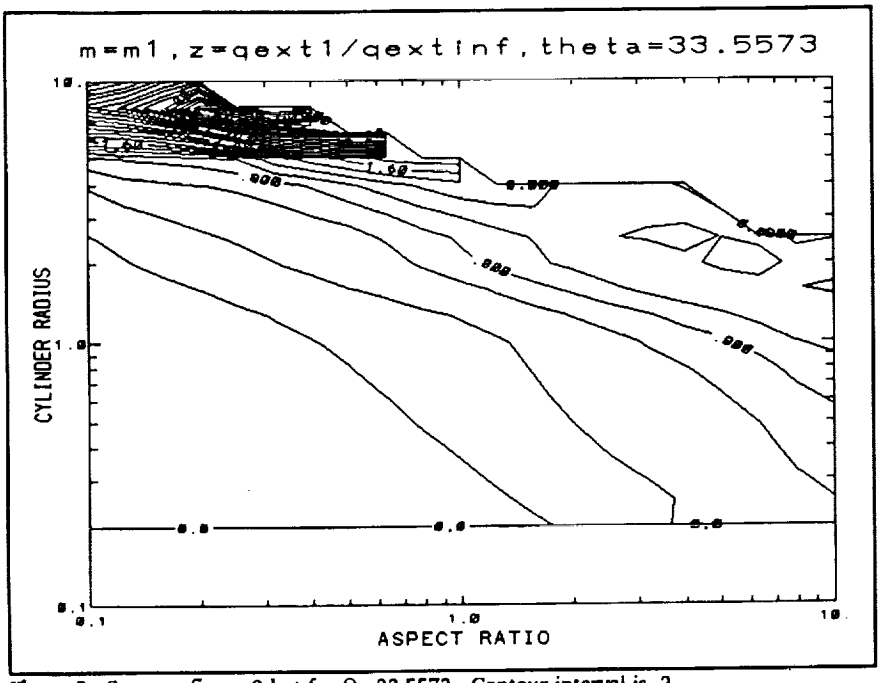

Figure 3. Same as figure 2 but for Θ=33.5573. Contour interval is .2.

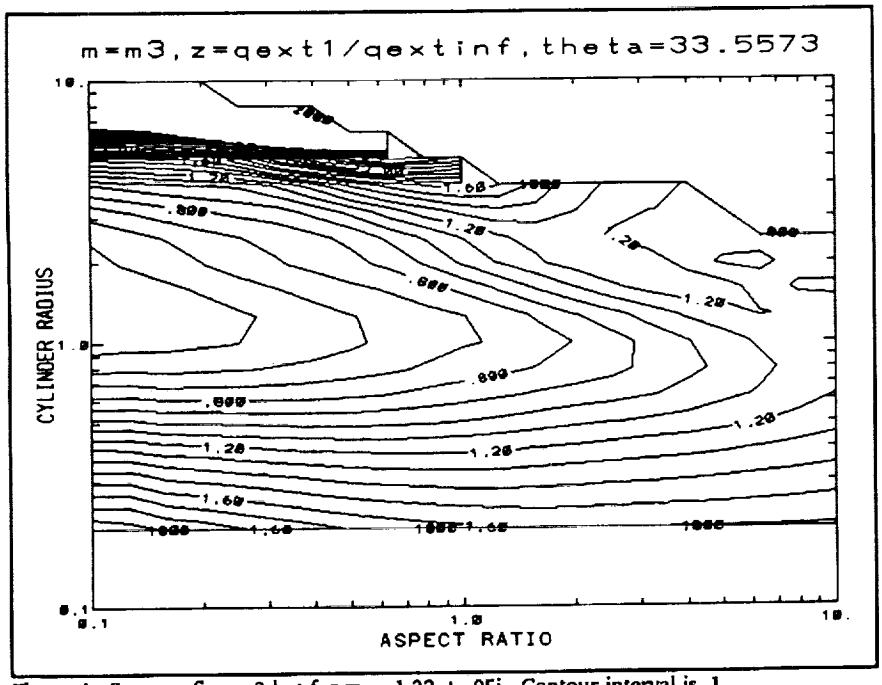

Figure 4. Same as figure 3 but for m = 1.32 + .05i. Contour interval is .1.

radius of the particle. This method is, of course, inappropriate for nonspherical particles and in the case of an infinite cylinder becomes inapplicable. For the infinite cylinder case, as defined in Bohren and Huffman (1983), the normalization becomes:

$$Q_{ext} = \frac{C_{ext}}{2r_{cyl}L}$$

where r_{cyl} is the cylinder radius and L is the cylinder length. Of course, this represents a normalization with respect to actual cross sectional area (with perpendicular incidence) instead of an "effective" cross sectional area.

All of the graphs shown in the analysis section are contour plots in which results are expressed in terms of cylinder radius and aspect ratio, β, where:

$$\beta = \frac{L}{2r_{cyl}}$$

It should also be noted that in all cases the wavelength of the incident radiation is taken to be 2π and that results will be given for two common refractive indices of ice. Since:

$$r_{cyl} = \sqrt[3]{\frac{2}{3\beta}}\, a_{eff}$$

and all the axes are logarithmic, lines of constant a_{eff} will be linear with a slope of -1/3 (see Figure 1). Also, the top and bottom lines in Figure 1 reveal the region of the available data. These appear in all of the plots.

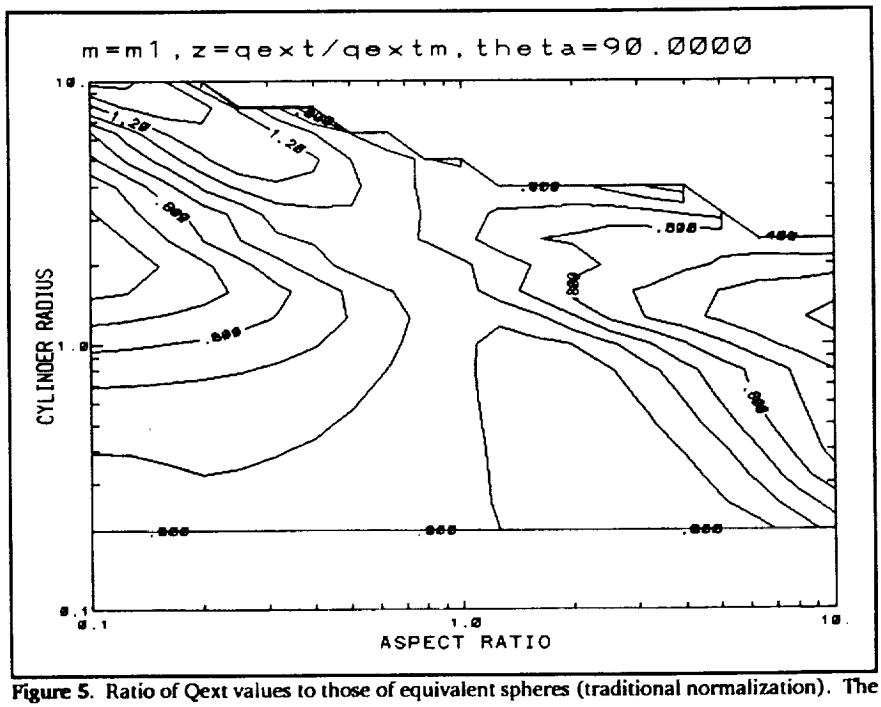

Figure 5. Ratio of Qext values to those of equivalent spheres (traditional normalization). The contour interval is .1, m = 1.32 + 0i, and Θ=90.

2.0 Analysis

It is most appropriate to begin the analysis with a look at the Q_{ext1} values. With the aforementioned renormalization we will be able to address the degree to which finite cylinders behave like infinite cylinders. Figures 2 through 4 display ratios of extinction efficiency for finite cylinders and infinite cylinders of the same radius. Here m_1 equals 1.32 + 0i and the angle of incidence (Θ) is expressed with respect to the cylinder axis. Note first that a "plateau" of infinite cylinder behavior is visible in Figure 2 in a region where r_{cyl} is between .4 and 3 and where β is between about .6 and 10, revealing that, in some cases at this incidence angle, the behavior of finite cylinders can approach that of their infinite counterparts very quickly, sometimes with aspect ratios as low as one or less. The region of this approach shows a strong but apparently monotonic dependence on r_{cyl}, appearing at lower values of β as r_{cyl} increases. There is also a dependence upon incidence angle, with the oblique incidence case showing a more complex approach to infinitum. Along these lines, resonance peaks are present near r_{cyl}=2, revealing most likely a Struve-function-type approach to infinitum instead of a purely monotonic approach. The peak found in the region of r_{cyl}=10 is very strong and is most strongly observed as θ approaches 0. More on this in a moment. Extending this to a case of strong absorption (m_3 = 1.32 + 0.05i), the same basic structure is observed in Figure 4, where it becomes apparent that the approach to infinitum and its dependence upon r_{cyl} is in fact not monotonic, but that in regions below r_{cyl} = 1.0 a strong dependence on r_{cyl} starts to become visible. A quick glance at figure 7 reveals this to be a region of mostly "Mie-type" behavior, which in the realm of extinction-per-unit-length apparently translates to a high dependence on r_{cyl} and a relatively low dependence on cylinder length.

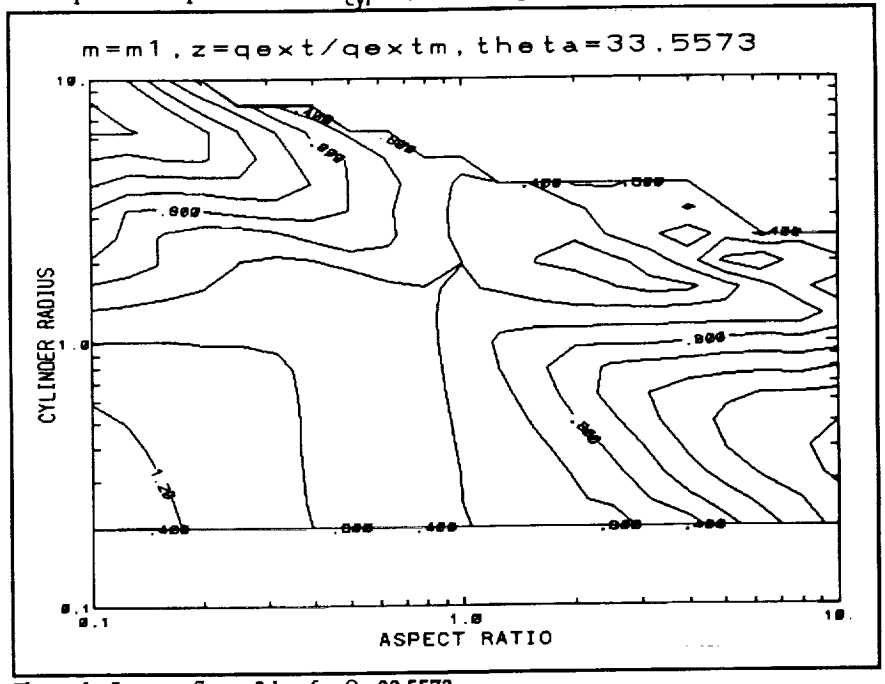

Figure 6. Same as figure 5 but for Θ=33.5573.

Figures 5 through 7 show ratios of traditionally normalized Q_{ext} values with respect to those of

equivalent spheres. Here, in the same region around $r_{cyl}=10$, efficiencies which are much less than that of spheres are observed. A quick glance at figure 1 reveals that the $r_{cyl}=10$ resonance displayed in figures 2 through 4 occurs in a region in which a_{eff} is close to 4, where the Mie extinction profiles reach a maximum. Apparently the strong resonances in figures 2 through 4 are due to the disks behaving to some extent as Mie particles, behavior which translates into a large amount of extinction per unit length in the case of thin disks. In contrast, however, the peaks near $r_{cyl}=2$ are reiterated here, revealing that neither spherical nor infinite cylinder theory can explain their existence, and that they are most likely resonances associated with characteristic distances in the particle. What is most observable is a large degree of remarkable agreement between finite cylinders and spheres for a large range of aspect ratios, cylinder radii, incidence angles, and refractive indices. As would be expected, the region of agreement is centered around $\beta=1$ and improves slightly with the addition of absorption.

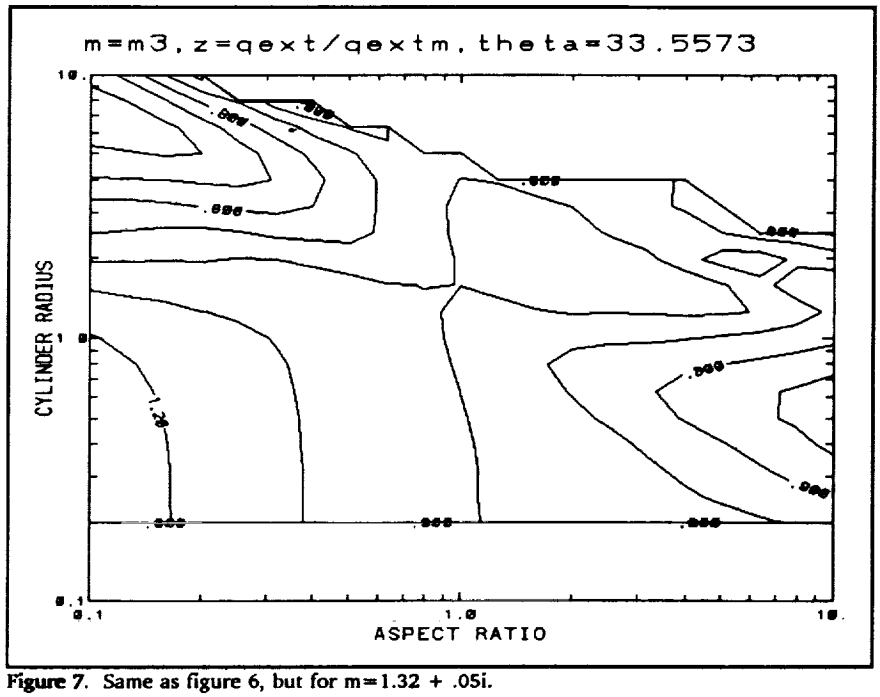

Figure 7. Same as figure 6, but for m=1.32 + .05i.

3.0 Conclusion

The agreement of extinction efficiencies between finite cylinders and spheres is remarkable especially at aspect ratios close to 1. This agreement subsides as β increases and the particle begins to behave like an infinite cylinder. This agreement also subsides as β becomes much less than 1. This agreement region shows a high sensitivity to incidence angle and a weak dependence on absorption. Infinite cylinder behavior is observed for nonabsorbing cylinders at normal incidence in some cases even when β is less than 1, but this agreement becomes more complex as incidence angles become oblique.

Acknowledgements

This research has been supported by The Office of Naval Research under Contract No. NOOO14-91-J-1422, P00002, National Aeronautics and Space Administration under Grant NAG 1-1146, and The Department of Energy, Contract No. DE-FG02-90ER60970. Acknowledgement is also made to the National Center for Atmospheric Research, which is sponsored by the National Science Foundation, for the computing time used in this research.

References

Bohren, C. F., and Huffman, D. R., Absorption and Scattering of Light by Small Particles, Wiley & Sons, 1983.

Flatau, P. J., Scattering by Irregular Particles in Anomalous Diffraction and Discrete Dipole Approximations, Colorado State University, Department of Atmospheric Science Paper Number 517, 140 pp.

549-47
197549
p-4

Surface-Induced Brightness Temperature Variations and Their Effects on Detecting Thin Cirrus Clouds Using IR Emission Channels in the 8-12 μm Region

N94-22341

Bo-Cai Gao, and W. J. Wiscombe
Climate & Radiation Branch, Code 913, NASA Goddard Space Flight Center
Greenbelt, MD 20771

Abstract

A method for detecting cirrus clouds in terms of brightness temperature differences between narrow bands at 8, 11, and 12 μm has been proposed by Ackerman et al. (1990). In this method, the variation of emissivity with wavelength for different surface targets was not taken into consideration. Based on state-of-the-art laboratory measurements of reflectance spectra of terrestrial materials by Salisbury and D'Aria (1992), we have found that the brightness temperature differences between the 8 and 11 μm bands for soils, rocks and minerals, and dry vegetation can vary between approximately -8 K and +8 K due solely to surface emissivity variations. We conclude that although the method of Ackerman et al. is useful for detecting cirrus clouds over areas covered by green vegetation, water, and ice, it is less effective for detecting cirrus clouds over areas covered by bare soils, rocks and minerals, and dry vegetation. In addition, we recommend that in future the variation of surface emissivity with wavelength should be taken into account in algorithms for retrieving surface temperatures and low-level atmospheric temperature and water vapor profiles.

1. Introduction

Thin cirrus clouds partially scatter solar radiation back to space and partially prevent the escape to space of the longwave emission originating from the surface and lower atmosphere. They are difficult to detect in images taken from current satellite platforms. The NASA FIRE Cirrus Program (Starr, 1987) was designed to improve our understudying of physical and radiative properties of cirrus clouds and their effects on the climate system.

Ackerman et al. (1990) developed a method for detecting thin cirrus clouds using three narrow channels at 8 (8.3-8.4), 11 (11.06-11.25), and 12 (11.93-12.06) μm. The method, referred to as the '8-11-12 μm method' hereinafter, was based on the analysis of data acquired with the Cloud and Aerosol Lidar (CALS) (Spinhirne and Hart, 1990) and the High-spectral resolution Interferometer Sounder (HIS) (Revercomb et al., 1988) on board an ER-2 aircraft over areas covered by vegetation and water in Wisconsin during the first FIRE Cirrus Field Experiment in October 1986. Figure 1 illustrates the method (Ackerman et al., 1990). Basically, the cloud-free regions have negative brightness temperature differences between the 8 and 11 μm channels (Δ BT (8 – 11)) while the areas covered by cirrus clouds have positive brightness temperature differences (> 1 K). The additional use of brightness temperature differences between the 11 and 12 μm channels, Δ BT (11 – 12), is for the purpose of separating the cirrus clouds from the low level water clouds. When applying the 8-11-12 μm method to a similarly measured data set but over a different geographic location, the method failed to detect thin cirrus clouds (S. A. Ackerman, personal communication, 1992).

During their development of the 8-11-12 μm method, Ackerman et al. (1990) carefully considered the absorption and scattering properties of water and ice particles, and the absorption and emission effects of atmospheric water vapor. The variation of surface emissivity with wavelength was not taken into consideration, however.

Recently, Salisbury and D'Aria (1992) have made state-of-the-art laboratory measurements of reflectance spectra of terrestrial materials between 2 and 14 μm. We have studied surface-induced brightness temperature variations in the 8-14 μm region using these spectra. Some of our findings relevant to remote sensing of cirrus clouds are presented in this paper.

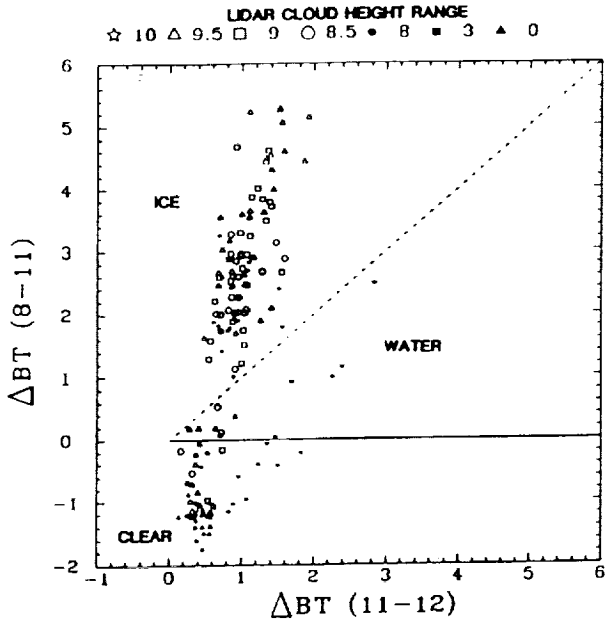

Fig. 1: Scatter diagram of Δ BT (8 – 11) versus Δ BT (11 – 12) (Ackerman et al., 1990). Each symbol represents a range in cloud altitude determined with the Cloud and Aerosol Lidar (CALS) (Spinhirne and Hart, 1990).

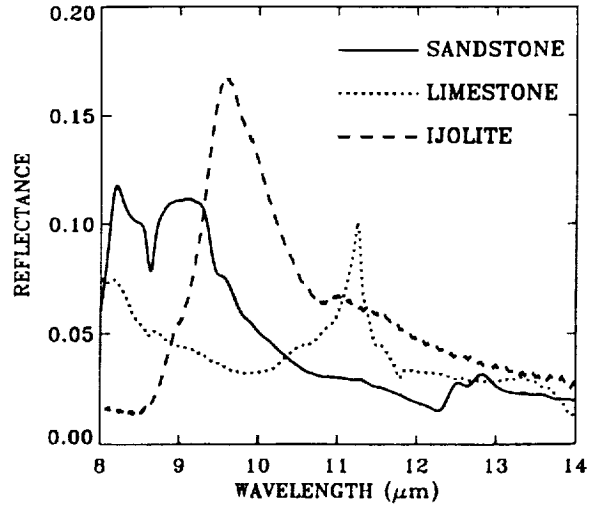

Fig. 2: Examples of reflectance spectra of three types of soils (Salisbury and D'Aria, 1992).

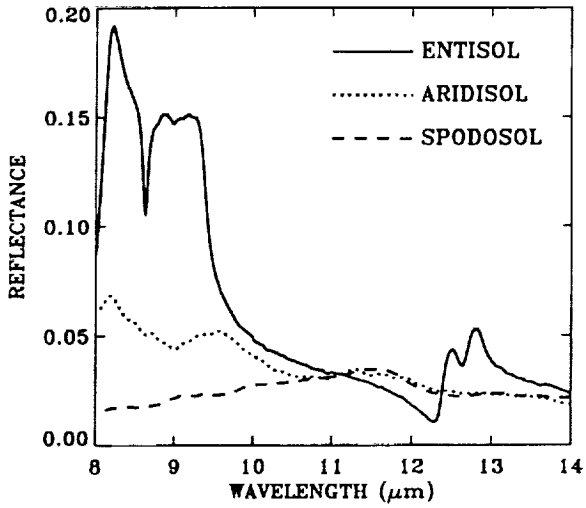

Fig. 3: Examples of reflectance spectra of three types of soils (Salisbury and D'Aria, 1992).

2. Surface Reflectance Spectra

Directional hemispherical reflectance spectra of a variety of rocks and minerals, soils, green and dead vegetation, water and ice have been made and summarized by Salisbury and D'Aria (1992). They were measured using Fourier transform spectrometers with integration sphere attachments. Figure 2 shows examples of reflectance spectra of three types of rocks; various absorption features due to vibrational band transitions can be seen. The reflectances in the 11 (11.06-11.25) μm region for ijolite and limestone are greater than those in the 8 (8.3-8.4) μm region, while the converse is true for sandstone. Figure 3 shows examples of reflectance spectra of three types of soils; various absorption features can be seen. Figure 4 shows sample reflectance spectra of green and dry vegetation. The green vegetation has nearly a constant reflectance value (0.02) in the 8–14 μm region, while the dry vegetation has several absorption bands.

Figure 5 shows sample reflectance spectra of sea water and sea ice (rough surface); the reflectances are small (between approximately 0.01 and 0.04). The reflectance minimum for sea water is located near 11 μm, that for sea ice near 10.3 μm. The emissivity is defined as one minus reflectance. It is easy to see from Figures 2, 3, 4, and 5 that the emissivities for soils, rocks and minerals, and dry vegetation in the 8-14 μm region vary significantly with wavelength. The emissivities for green vegetation, water, and ice do not vary much with wavelength and are generally greater than 0.96.

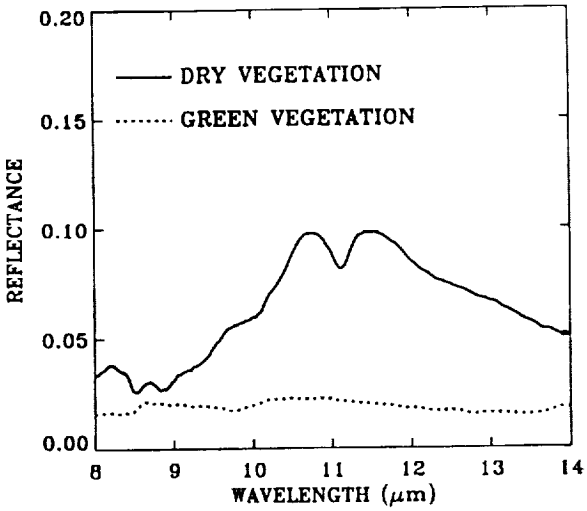

Fig. 4: Examples of reflectance spectra of dry and green vegetation (Salisbury and D'Aria, 1992).

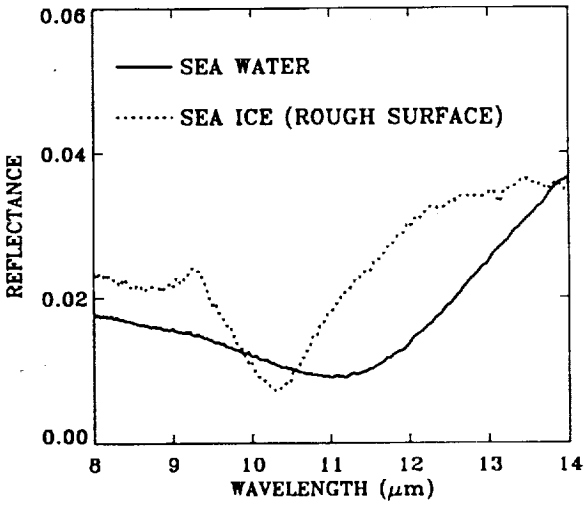

Fig. 5: Examples of reflectance spectra of sea water and ice (Salisbury and D'Aria, 1992).

3. Sensitivity of Brightness Temperature to Emissivity

The brightness temperature of a surface is a function of both its kinetic temperature and emissivity. We have studied the sensitivity of the Planck function to changes in temperatures for surface temperatures of 270, 280, 290, and 300 K. From these sensitivities, we have derived the sensitivities of brightness temperatures to emissivities. The results show that, for kinetic temperatures between 270 and 300 K, an error of 0.01 in assumed surface emissivity results in errors

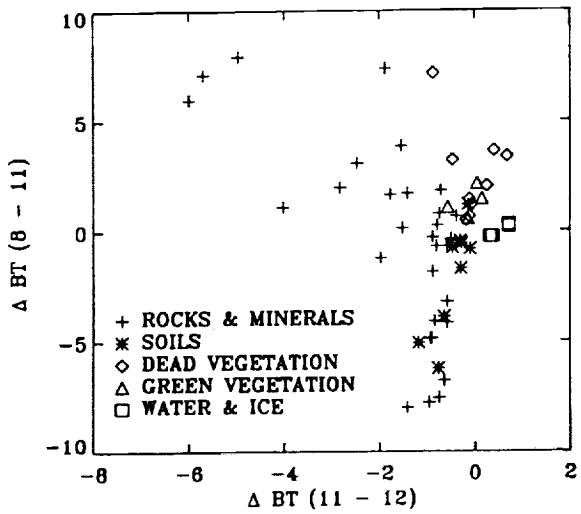

Fig. 6: Scatter diagram of surface-induced Δ BT (8 – 11) versus Δ BT (11 – 12) for rocks and minerals, soils, dead and green vegetation, and water and ice (rough surface).

of approximately 0.48 K in surface temperature at 8.35 μm, 0.63 K at 11.155 μm, and 0.67 K at 11.995 μm.

4. Results

Based on the sensitivity of brightness temperatures to surface emissivity described in Section 3 and using the reflectance data from Salisbury and D'Aria (1992), we have quantified the surface-induced brightness temperature variations in the 8, 11, and 12 μm region for soils, rocks and minerals, green and dry vegetation, and water and ice. Figure 6 shows the scatter diagram of the Δ BT (8 – 11) versus Δ BT (11 – 12). The surface-induced Δ BT (8 – 11) can vary between approximately –8 K and 8 K for rocks and minerals, 0.5 to 7 K for dead vegetation, –6 and 1 K for soils. These differences are greater than the Δ BT (8 – 11) in Figure 1.

The large differences in the surface-induced Δ BT (8 – 11) are sufficient to cause confusion when using the 8-11-12 μm method for detecting cirrus clouds. For example, if the measurements were made from high-altitude aircraft or satellite platforms over areas covered by dead vegetation but no cirrus clouds, the straight forward application of the 8-11-12 μm method would misidentify the areas as being covered by cirrus clouds. On the other hand, if the same

measurements were made over areas covered by bare soils with a –4 K surface-induced Δ BT (8 – 11) and also covered by very thin cirrus clouds with a 1 K cirrus-induced Δ BT (8 – 11), the application of the 8-11-12 μm method would identify the areas as being clear.

5. Discussion

Because of the traditional lack of reliable IR emissivity measurements (Salisbury and D'Aria, 1992) of terrestrial materials, algorithms developed for retrieving atmospheric temperatures and surface temperatures from satellite IR emission channels typically assume constant values of emissivity (about 0.96) in the 8–14 μm spectral region. As a result, errors of 10 K or greater in the derived surface temperatures from current satellite IR emission measurements exist (Wu and Chang, 1991).

6. Summary

We have studied surface-induced brightness temperature variations in the 8-12 μm spectral region using laboratory measurements of emissivity of terrestrial materials (Salisbury and D'Aria, 1992). It is found that the brightness temperature differences between the 8 and 11 μm bands for soils, rocks and minerals, and dry vegetation can vary between approximately –8 K and 8 K. We conclude that although the 8-11-12 μm method of Ackerman et al. (1990) is useful for detecting cirrus clouds over areas covered by green vegetation, water, and ice, the technique is less effective for detecting cirrus clouds over areas covered by bare soils, rocks and minerals, and dry vegetation. We suggest that the variation of surface emissivity with wavelength should also be taken into account in algorithms for retrieving surface temperatures and low-level atmospheric temperature and water vapor profiles.

7. Acknowledgments

The authors are grateful to J. W. Salisbury at the Department of Earth and Planetary Sciences, Johns Hopkins University for providing the emissivity spectra of terrestrial materials in digital form. This research was partially supported by the NASA FIRE Project Office through a grant to the NASA Goddard Space Flight Center.

8. References

Ackerman, S. , W. L. Smith, J. Spinhirne, and H. Revercomb, The 27-28 October FIRE IFO cirrus case study: Spectral properties of cirrus clouds in the 8-12 μm window, *Mon. Wea. Rev., 118,* 2377-2388, 1990.

Revercomb, H., H. Buijs, H. Howell, D. LaPorte, W. L. Smith, and L. Sromovsky, Radiometric calibration of IR Fourier transform spectrometer: Solution to a problem with the High-spectral resolution Interferometer Sounder, *Appl. Opt.*, 27, 3210-3218, 1988.

Salisbury, J. , and D. D'Aria, Emissivity of terrestrial materials in the 8-14 μm atmospheric window, *Remote Sens. Env., 42,* 83-106, 1992.

Spinhirne, J. , and W. Hart, The 27-28 October 1986 FIRE cirrus case study: ER-2 lidar and spectral radiometer cirrus observations, *Mon. Wea. Rev., 118,* 2329-2343, 1990.

Starr, D., A cirrus cloud experiment: Intensive field observations planned for FIRE, *Bull. Amer. Meteor. Soc., 67,* 119-124, 1987.

Wu, M.-L., and L. Chang, Differences in global data sets of atmospheric and surface parameters and their impact on outgoing longwave radiation and surface downward flux calculations, *J. Geophys. Res., 96,* 9227-9262, 1991.

S50-47
197550
p. 4

Remote Sensing Estimates of Cirrus Particle Size for Tropical and Midlatitude Cirrus : Hexagonal Crystals and Ice Spheres.

Bruce A. Wielicki and Patrick Minnis
Atmospheric Sciences Division
NASA Langley Research Center
Hampton, VA 23681-0001

N94-22342

Robert Arduini and Lindsay Parker
Lockheed Engineering and Sciences Corp.
Hampton, VA 23666

Si-Chee Tsay
Universities Space Research Association
NASA Goddard Space Flight Center
Greenbelt MD 20771

Yoshihide Takano and Kuo-Nan Liou
Department of Meteorology, University of Utah
Salt Lake City, Utah

1. INTRODUCTION

A large discrepancy exists in current estimates of a mean cirrus particle size appropriate for calculations of the effects of these ice clouds on solar and thermal infrared radiative fluxes. For spheres with large size parameter ($x = 2\pi r/\lambda > 30$, where r is particle radius), and moderate absorption ($n^I x < 1$, where n^I is the imaginary index of refraction for ice), the optimal effective particle radius (Hansen and Travis, 1974) is given by:

$$r_e = \int r^3 n(r) dr \,/\, \int r^2 n(r) dr .$$

For the remote sensing of cirrus particle size at wavelengths of 0.83, 1.65, and 2.21μm, a 50μm ice sphere would have a size parameter of about 200, and values of $n^I x$ of 0, 0.045, and 0.06, satisfying the above conditions.

However, while r_e is a well-defined parameter for spheres, this cross-section area-weighted particle radius can only be extended to non-spherical particles by defining some equivalent sphere, typically an equivalent volume or equivalent cross-section area sphere. Using equivalent volume spheres, values of r_e obtained over Lake Michigan on October 28, 1986, during FIRE phase I varied from 200μm (King Air 2D imaging probes) to 60μm (Landsat reflectances at 0.83, 1.65, and 2.2μm, Wielicki et al., 1990), to 25μm (HIS spectrometer thermal emission between 8 and 12μm, Ackerman et al., 1990). Three major uncertainties were identified in this comparison: small ice particles missed by the 2D-C aircraft probes, uncertain ice refractive index, and uncertainties in the single scatter albedos and scattering phase functions used in the radiative calculations.

Since the first FIRE cirrus results, advances have been made in all three areas. The present paper reports on improvements in the radiative modeling of ice particles at 0.83, 1.65 and 2.21 μm wavelengths appropriate for comparisons to Landsat Thematic Mapper data. The paper also includes new results for Landsat observations of ice clouds in the eastern and western tropical Pacific.

2. RADIATIVE MODEL

Radiative transfer calculations used to predict Landsat spectral radiances are performed as outlined in Wielicki et al., 1990 with two exceptions. First, the finite difference radiative transfer method has been replaced by a discrete ordinate method, hereafter termed DISORT (Stamnes et al., 1988; Tsay et al., 1991). The overall accuracy of these two methods,

however, are similar. Second, a hexagonal ice crystal model (Takano and Liou, 1989) is used in the present study for both the single scatter albedo (ω), and scattering phase function (Φ) used in the DISORT calculations. In the earlier study by Wielicki et al., (1990) Mie spheres were used to determine ω, while Φ was taken from laboratory measurements of ice crystals by Volkovitskiy et al. 1980, hereafter denoted as VPP. The VPP phase function was only available for $\lambda = 0.63\mu m$, but was used for all three channels, in the absence of better information. The present study uses phase functions derived for randomly oriented hexagons of width 2a and length L (see Table 1) determined using ray tracing at $\lambda = 0.55$, 1.6, and 2.2μm (Takano and Liou, 1989). Figure 1 shows the hexagonal phase functions for L/2a = 120/60 at all three wavelengths. The figure demonstrates the importance of absorption in reducing the amount of side scattered radiation, as the average imaginary index of refraction for ice increases with wavelength. Table 1 summarizes the radiative modeling differences between the two studies.

TABLE 1. Radiative Modeling Changes

Radiative Model	Scattering Phase Function	Single Scatter Albedo
Current Results:		
Discrete Ordinate	Hexagons, ray tracing: 2a/L = 20/20, 50/40, 120/60, 300/100, 750/160 $\mu m/\mu m$; λ = 0.55, 1.6, 2.2 μm	Hexagons, ray tracing: 2a/L = 20/20, 50/40, 120/60, 300/100, 750/160 $\mu m/\mu m$; 0.83, 1.56 - 1.8, 2.10 - 2.35 μm
Wielicki et al., 1990:		
Finite Difference	Laboratory: 20 μm plates: λ = 0.6 μm only	Mie : r_e = 4, 8, 16, 32, 64, 128μm 0.83, 1.56 - 1.8, 2.10 - 2.35 μm

Figure 2 compares the new hexagonal crystal results for the Landsat 0.83 μm and 1.65 μm channels with the previous VPP/Mie sphere results at a solar zenith angle of 45°. Calculations were performed at 0.83μm extinction optical depths of 0.1, 0.2, 0.5, 1, 2, 3.5, 5, 10, 20, and 50 and are marked by symbols in Figure 2. Takano and Liou (1989) and others have shown that particle absorption efficiency Q_{abs} scales with particle volume. In order to compare with the earlier Mie sphere estimates of Q_{abs}, (which for large particles with $2\pi r/\lambda >> 1$ determines ω) we have given the radius of an equivalent volume sphere for each hexagonal crystal size. Figure 2 shows that for large optical depths the new calculations give results similar to an equivalent volume sphere. At smaller optical depths, however, the changes in the hexagonal scattering phase function with λ (Figure 1) cause larger deviations from the earlier results, so that the hexagonal crystal r_{vol} is as much as a factor of 2 smaller than the VPP/Mie sphere results. In summary, at large optical depths the single scatter albedo dominates the result, and equivalent volume spheres give reasonable results, while at optical depths less than about 10, the λ dependence of the scattering phase function plays a large role.

3. RESULTS

Figure 3 compares the hexagonal crystal predictions for Landsat reflectances at 0.83μm and 1.65μm with Landsat observations. Landsat observations are shown at full spatial resolution of 30 meters, and are uniformly sampled over a set of independent Landsat cloud scenes. Each Landsat scene is a 60 km by 60 km region. The observations are divided into three sets by geographic regions. Figure 3a gives results for 14 Landsat (60 km)^2 scenes taken from the western tropical Pacific near the TOGA/COARE region (13S - 13N, 150E-175E). Figure 3b gives results for 6 scenes from the Eastern Pacific (0N - 13N, 95W-135W). Figure 3c gives results for 5 scenes for northern mid latitudes (30N - 60N, 60W-130W).

Figure 3 shows several interesting characteristics. For all 25 regions, greater than 98% of the observations fall between the 50/40 and 300/100 hexagonal crystal results (r_{vol} between 23 and 78 μm). The median value agrees well with the 120/60 crystal size (r_{vol} = 41 μm). The Eastern Pacific results appear to be bimodal (but no single scene shows both modes). The mid latitude cases and most of the optically thin tropical cirrus (0.83 μm reflectance below 0.2) show a smaller size range of about 50/40 to 120/60. For all data, however, very few observations are found with particle sizes smaller than 50/40. In fact, the

small number of observations following the 20/20 results for the mid latitude cirrus in Figure 3b are supercooled water droplets from the 10/28/86 case in Wielicki et al. (1990).

4. CAVEATS

The great complexity of ice crystal shapes in clouds indicates that even hexagonal crystal interpretations of remotely sensed particle size must be viewed with caution. In particular, studies of the dependence of the scattering phase function on particle shape and imaginary index of refraction are especially important. Final resolution of these issues will require consistency of aircraft, and various remotely sensed particle estimates including near-infrared and thermal infrared radiance techniques, as well as new techniques using multiple wavelength active lidar and radar systems. It should also be noted that the particle sizes inferred from Figure 3 would represent a vertical average over the entire cloud depth for optically thin cloud, while the sizes would represent the microphysical conditions nearer cloud top (optical depth 3-6) for optically thick cloud.

Even with these difficulties, the current results suggest that there might be strong similarities in mid latitude and tropical ice microphysics, at least for optically thin cirrus. Additional cases of mid latitude ice clouds with larger optical depths are needed.

5. REFERENCES

Ackerman, S. A., W. L. Smith, J. D. Spinhirne, and H. E. Revercomb, 1990: The 27-28 October 1986 FIRE IFO Cirrus Case Study: Spectral Properties of Cirrus Clouds in the 8-12μm Window. *MWR*, **118**, 2377-2388.

Hansen, J. E. and L. D. Travis, 1974: Light scattering in planetary atmospheres, *Space Sci. Rev.*, **16**, 527-610.

Stamnes, K., S. C. Tsay, W. Wiscombe, and K. Jayaweera, 1988: Numerically stable algorithm for discrete-ordinate-method radiative transfer in multiple scattering and emitting layered media. *App. Optics*, **24**, 2502-2509.

Takano, Y. and K- N. Liou, 1989, Solar Radiative Transfer in Cirrus Clouds. Part I: Single Scattering and Optical Properties of Hexagonal Ice Crystals. *Jour. Atmos. Sci.* **46**, 3-19.

Tsay, S.-C., G. L. Stephens, and T. J. Greenwald, 1991: An investigation of aerosol microstructure on visual air quality. *Atmos. Environ.*, **25A**, 1039-1053.

Volkovitskiy, O. A., L. N. Pavlova, and A. G. Petrushin, 1980: Scattering of light by ice crystals. *Izv. Atmos. Ocean. Phys.*, **16**, 98-102.

Wielicki, B. A., J. T. Suttles, A. J. Heymsfield, R. M. Welch, J. D. Spinhirne, M-L. C. Wu, S. K. Cox, D. O'C. Starr, L. Parker, and R. F. Arduini, 1990: The 27-28 October 1986, FIRE IFO Cirrus Case Study: Comparison of Radiative Transfer Theory with Observations by Satellite and Aircraft. *MWR*, **118**, 2356-2376.

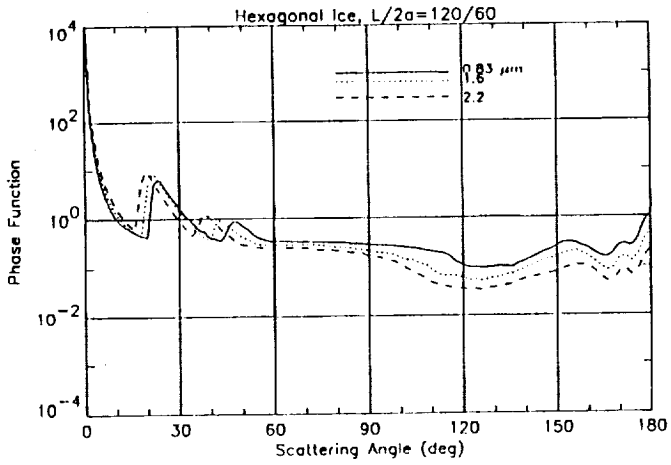

Figure 1

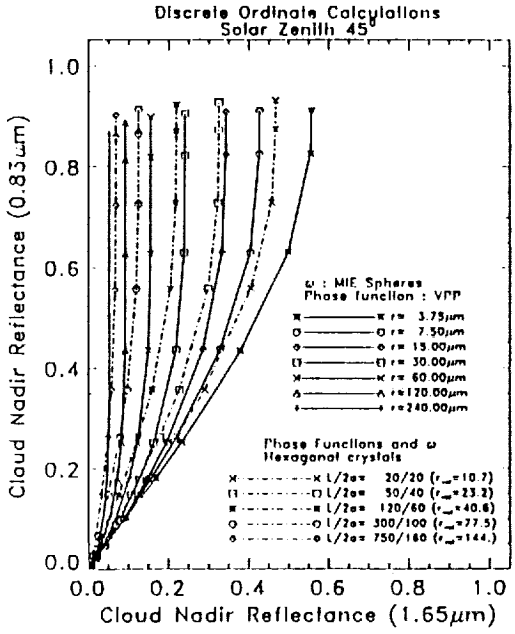

Figure 2

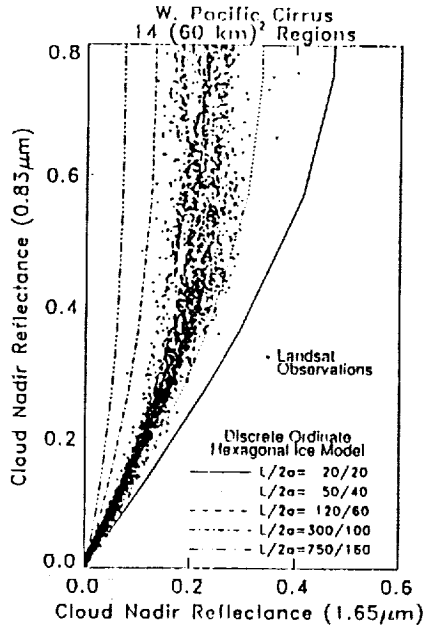

Figure 3a

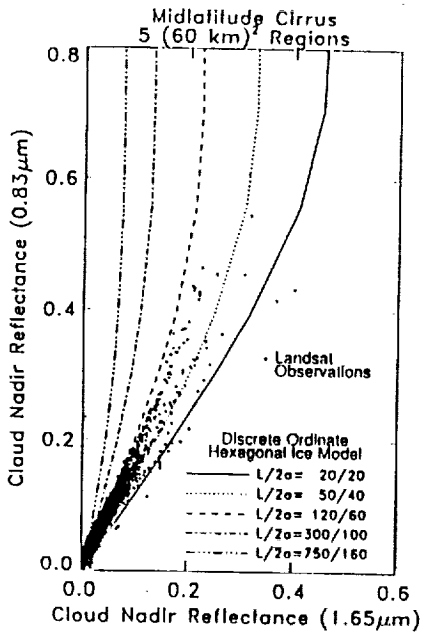

Figure 3c

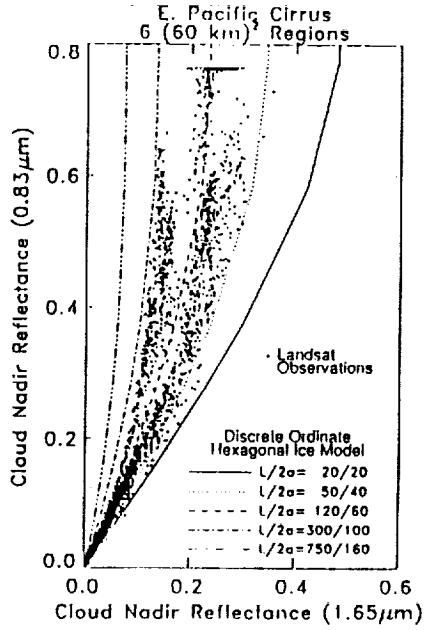

Figure 3b

S51-47
197551
p. 4

ARE TROPICAL CIRRUS BRIGHTER THAN MID-LATITUDE CIRRUS?

N94-22343

David L. Mitchell, W. Patrick Arnott,
Yayi Dong and John Hallett
Desert Research Institute
P.O. Box 60220
University of Nevada, Reno
Reno, Nevada 89506

Kenneth Sassen
Meteorology, 819 WBB
University of Utah
Salt Lake City, UT 84112

Recent measurements during FIRE II, in the tropics and elsewhere support an emerging hypothesis about the role of stratospheric mixing in determining the microphysical and radiative properties of cirrus clouds. This is only a working hypothesis, and may change as new measurements become available. We will begin by reviewing the conditions under which certain types of ice crystals form.

BACKGROUND

Polycrystalline ice crystals, or spatial crystal habits, often form from freezing cloud or haze droplets, with rosettes or side planes (also called crossed plate crystals) forming at $T < -20°C$ (Hallett and Mason 1964; Magono and Aburakawa 1968). Side planes grow well at low supersaturations relative to ice ($\leq 10\%$), while bullet or column rosettes require higher supersaturations to grow, and may dominate at higher supersaturations (Furukawa 1982; Furukawa and Kobayashi 1978). Side planes grow at lower supersaturations since their growth is driven by the surface kinetics of the ice lattice (grain boundary dislocations) in addition to the vapor gradient, while the two-dimensional growth mechanism of rosettes is only driven by the vapor gradient. In other words, the condensation coefficient (the probability of an impinging water molecule incorporating into the ice lattice) for side planes should be greater at low supersaturations than for crystals which grow by the two dimensional nucleation mechanism, such as columns, plates and rosettes.

Takahashi and Kuhara (1993) sent specially developed radiosondes into cumulonimbus clouds over Pohnpei, Micronesia. High concentrations of side plane ice crystals were reported near the tropopause, around -63°C. Flights in cirrus with the DRI replicator during TOGA COARE did not get near the tops of anvil cirrus. The replicator was mounted on an aircraft wing, with a 3 mm x 8 mm intake slot for ice crystals. The ice particles impacted the formvar coated replicator film at aircraft speeds, so that mid-to-large size ice crystals tended to be shattered. The data has yet to be quantified, although preliminary inspections indicate high concentrations of planar type ice crystals dominated. Although difficult to describe, the "best guess" at this time is that the crystals are mostly fragments of side planes.

HYPOTHESIS

Evidence of side planes dominating in anvil cirrus suggests that supersaturations with respect to ice were low. Since water vapor densities tend to be lowest in the upper troposphere relative to lower levels, little moisture is available for condensation. Modest changes in the demand for moisture by growing ice crystals, due to changes in ice crystal concentrations, could thus

affect supersaturations. In the tropics, the tropopause is generally around 16 km (Rosen and Hofmann 1975), and cumulonimbus clouds often penetrate into the stratosphere up to 18 or 20 km (Ramanathan and Collins 1991). Between 16 and 20 km in the tropics, there is generally a four fold increase in the mixing ratio (number of particles per milligram of air) of aerosol particles > 0.3 μm diameter (Rosen and Hofmann 1975). These are ideal although large CCN sizes. Aerosol mixing ratios in both the middle and upper troposphere are low relative to the lower stratosphere in the tropics. Thus, relatively high CCN concentrations may be entrained into cumulonimbus tops and cirrus anvils, which may nucleate haze droplets which freeze to form ice crystals (Sassen and Dodd 1988). Nucleation rates of these polycrystals should be relatively high, and the competition for vapor should drive down the supersaturation. This could produce a rapid transition in crystal habit from rosettes to side planes (a few rosettes were observed in the replicator film from TOGA COARE).

The above scenario should produce anvil cirrus with relative high albedos for the following reasons: (1) entrainment of stratospheric CCN results in high concentrations of small ice crystals, which yields more ice surface area per unit volume of cloudy air for a given ice water content (IWC). This results in greater optical depth and albedo. (2) Side planes are very complex in structure, and appear to promote ice crystal aggregation in cirrus (Mitchell et al. 1993, these preprints). Side plane crystals and aggregates containing them are expected to produce greater side- and backscatter than other crystal types, since multiple pairs of refraction events are likely as light passes through these particles. (3) Although not quantified yet, it appears that side planes may have relatively high projected area to mass ratios. The amount of energy scattered per unit mass would then be relatively high, promoting greater cloud averaged single scatter albedos in the near IR. The near IR accounts for about 15% of the solar irradiance at cirrus levels.

As shown in Mitchell et al. (1993, these preprints), aggregation may be an important growth process in cirrus when side planes are present. Aggregation acts to reduce the surface area of the size distribution and thus reduces optical depth and cloud averaged single scatter albedo. An increase in IWC will increase the aggregation rate (Mitchell 1991), so that the relation between optical depth and IWC may not be linear. If side planes allow significant aggregation to occur in cirrus, it must be shown that the radiative effects of aggregation are secondary to the effects mentioned above which would enhance albedo.

On a final note, a somewhat bizarre observation made during TOGA COARE may have relevance here. Scientists flying through cirrus in the vicinity of -40°C observed substantial amounts of liquid water impacting the aircraft windshield. Similar observations have been made by pilots and scientist observers of aircraft icing while flying through cirrus at temperatures colder than -40°C. As discussed in Sassen (1992), such observations could be the result of liquid haze droplets which form below water saturation. They can exist at such temperatures due to their high solute concentrations which lowers their freezing point. Since these haze droplets should be less than about 4 μm in diameter, depending on CCN mass and relative humidity, it would take high concentrations of these haze droplets to produce the amounts of liquid observed on the aircraft windshield. As noted above, higher concentrations of large CCN may arise due to mixing with stratospheric air. Clearly, more information is needed to draw any conclusions, and it is hoped that aerosol and cloud particle measurements are available during these flight periods to evaluate this question further.

In general, this reasoning would suggest that tropical anvil cirrus, due to their mixing with stratospheric air, would be exhibit greater albedos than cirrus which did not encounter such mixing, such as most mid-latitude cirrus. However, injections of stratospheric air into mid-latitude cirrus can occur along the jet stream at tropospheric folds. CCN fluxes under these conditions can be particularly high if the stratosphere is affected by recent volcanic eruptions. This may have occurred during the FIRE II case study of 5-6 December 1991.

FIRE II CASE STUDY OF 5-6 DEC. 1991

As discussed in Sassen (1992), cirrus formed in association with a strong jet stream out of the subtropics on these days. A surge of volcanic aerosols from the Mount Pinatubo eruption accompanied the jet stream and was believed to mix with cloudy cirrus air through injections of stratospheric air along the jet stream. We will show how the ice crystals were complex planar shapes on that day, and tended to be highly aggregated. The complex shapes appear most similar to side planes, and appear polycrystalline. Linear depolarization ratios, obtained from the polarization diversity lidar, give an indication of how complex the ice particle shapes are, with higher ratios for greater complexity. The periods of greatest lidar backscatter and linear depolarization ratio corresponded to periods of high ice particle concentration when side plane habits were most dominate. Lower depolarization ratios were obtained during periods where columns were abundant in side plane/column aggregates.

More analysis needs to be done to achieve a more comprehensive understanding of the microphysics and associated radiative properties on these days before any firm conclusions can be drawn. However, the observations for this period are consistent with the hypothesis stated above. High aerosol particle concentrations from the stratosphere coincided with relatively high concentrations of planar polycrystals, which are expected to dominate under such conditions. Side planes and aggregates thereof tended to exhibit greater backscatter, owing to relatively high concentrations and complex shapes.

CLIMATE IMPLICATIONS

In the western Pacific, deep convection produces cumulonimbus-cirrus anvil cloud systems which can grow up to 10^6 km^2 in a day or less, with cirrus sometimes several hundreds of km away from their convective source (Houze and Betts 1981). Due to their spatial extent, the radiative properties of these systems are dominated by the anvils and stratiform cirrus. The albedo of these cloud systems can be as high as 60%-80% (Harrison et al. 1991). These cloud systems have been proposed by Ramanathan and Collins (1991) to act as a thermostat in regulating sea surface temperatures in the tropics, as well as enhancing the Hadley and Walker circulations. Key to understanding this phenomena is to understand why the albedo from these cloud systems is so high. The hypothesis presented here is one possible explanation for the observed high albedo of tropical cirrus. This hypothesis also implies that the albedo of tropical cirrus may be influenced by volcanic eruptions which penetrate into the stratosphere.

Major volcanic eruptions have been estimated to reduce global surface temperatures by about 1°C or less (Ardanuy and Kyle 1986). The possibility that increased aerosol loading of the stratosphere may increase albedo in tropical and some mid-latitude cirrus suggests another mechanism by which volcanoes can affect climate.

Acknowledgment: This research was funded by the NOAA Climate and Global Change Program under grant NA16RC0118-01 and by NASA grant NAG-1-1113. Both agencies are thanked for their support.

REFERENCES

Ardanuy, P.E., and H.L. Kyle, 1986: Observed pertubations of the Earth's radiation budget: A response to the El Chichon Stratospheric aerosol layer? J. **Clim. Appl. Meteorol.**, **25**, 505.

Furukawa, Y., 1982: Structures and formation mechanisms of snow polycrystals. J. **Met. Soc. Japan**, **60**, 535-547.

Furakawa, Y., and T. Kobayashi, 1978: On growth mechanism of polycrystalline snow crystals with a specific grain boundary. J. **Crystal Growth**, **45**, 57-65.

Hallett, J. and B.J. Mason, 1964: Experimental studies on the crystallization of supercooled water. J. **Atmos. Sci.**, **21**, 671-682.

Harrison, E.F., P. Minnis, B.R. Barkstrom, V. Ramanathan, R.D. Cess, and G.G. Gibson, 1991: Seasonal variation of cloud radiative forcing derived from the Earth Radiation Budget Experiment. J. **Geophys. Res.**, **18**, 687-703.

Houze, R.A., Jr., and A.K. Betts, 1981: Convection in GATE. **Review of Geophysical and Space Physics**, **19**, 541-576.

Mitchell, D.L., 1991: Evolution of snow-size spectra in cyclonic storms. Part II: Deviations from the exponential form. J. **Atmos. Sci.**, **48**, 1885-1899.

Mitchell, D.L., S.K. Chai, Y. Dong, W.P. Arnott, A.J. Heymsfield and J. Hallett, 1993: Importance of aggregation and small ice crystals in cirrus clouds, based on observations and an ice particle growth model. **FIRE Cirrus Conference**, Breckenridge, Colorado, June 1993 (these preprints).

Magono, C. and H. Aburakawa, 1968: Experimental studies of snow crystals of plane type with spatial branches. J. **Fac. Sci.**, Hokkaido University, Ser. VII, 3, 85-97.

Ramanathan, V. and W. Collins, 1991: Thermodynamic regulation of ocean warming by cirrus clouds deduced from observations of the 1987 El Nino. **Nature**, **351**, 27-32.

Rosen, J.M. and D.J. Hofmann, 1975: Stratospheric aerosol measurements II: The worldwide distribution. J. **Atmos. Sci.**, **32**, 1457-1462.

Sassen, K. and G. Dodd, 1988: Homogeneous nucleation rate for highly supercooled cirrus cloud droplets. J. **Atmos. Sci.**, **45**, 1357-1369.

Sassen, K., 1992: Evidence for liquid-phase cirrus cloud formation from volcanic aerosols: Climatic implications. **Science**, **257**, 516-519.

Takahashi, T. and K. Kuhara, 1993: Precipitation mechanisms of cumulonimbus clouds at Pohnpei, Micronesia. **Meteor. Soc. Japan**, **71**, 21-31.

S52-47
197552
P-3
N94-22344

An Overview of the Radiation Component of the NASA TOGA-COARE Experiment

Thomas Ackerman
Department of Meteorology
The Pennsylvania State University
University Park, PA, 16802

John T. Suttles
NASA, Code YSC
Washington, D. C. 20546

During January and February, 1993, the Physical Climate Branch of NASA sponsored an aircraft program in support of the Tropical Ocean - Global Atmosphere (TOGA) Coupled Ocean-Atmosphere Response Experiment (COARE). The NASA program was integrated with and contributed directly to the COARE objectives, but had as its primary foci measurements of convection and precipitation related to the Tropical Rainfall Measurement Mission (TRMM) and measurements of the physical and radiative properties of tropical cirrus related to the International Satellite Cloud Climatology Project (ISCCP) and the First ISCCP Regional Experiment (FIRE). This brief overview will concentrate on the measurements associated with FIRE and ISCCP.

The NASA program involved two aircraft, the ER-2 used as a remote sensing platform, and the DC-8 used as a combined remote sensing and *in situ* platform. A list of the instrumentation payload for the two aircraft is given in Table 1. The primary instruments for the radiation component were the Radiation Measurement System (RAMS), the two lidar systems (CLS and VIRL), the microphysical measurement system (MMP), and the imaging radiometer (MAS).

The principal objectives of the radiation component of the experiment were to

1. measure the clear sky flux profile in the convective tropics;
2. measure the physical properties and flux divergence of cirriform cloud over a range of optical thicknesses;
3. measure the physical properties and flux divergence of anvil outflow cirrus;
4. overfly the Pilot Radiation Observation Experiment (PROBE) site at Kavieng, Papua New Guinea, with cirrus present; and
5. measure cirrus properties and radiative characteristics coincident with satellite overpasses.

The variety of flight requirements posed by the various components of the experiment and the limitations of the available resources necessitated careful flight planning and optimization of every opportunity to acquire data. Although data collection was essentially continuous on all flights, data of particular utility with regard to the radiation objectives were acquired in three basic modes: (i) dedicated radiation missions, (ii) radiation legs or segments during missions primarily devoted to other experiment components, and (iii) measurements during transit from the aircraft base, located in Townsville, Australia, and the COARE Intensive Flux Array (IFA) centered at about 1.75 °S and 156 °E. A brief summary of the primary radiation flights is given in Table 2. During all these flights the ER-2 and DC-8 were operated in tight coordination in a stacked pattern. Flight 1 was carried out in coordination with a NOAA P3 flying in the boundary layer so a detailed flux profile can be constructed for that mission.

ER-2 INSTRUMENTATION FOR TOGA-COARE		
Instrument	**PI**	**Data Parameters**
Cloud Lidar System	Spinhirne/GSFC	Cloud structure, boundaries and density
MODIS Airborne Simulator (MAS)	King/GSFC	Passive multi-channel radiometric data
Advanced Microwave Precipitation Radiometer (AMPR)	Spencer/MSFC Hood/MSFC	High resolution, multifrequency sampling of tropical rain systems
Millimeter Imaging Radiometer (MIR)	Adler/GSFC Racette/GSFC	Cloud structure, rainfall, water vapor profiling, cirrus cloud ice content and particle size distribution
Radiation Measurement System (RAMS)	Valero/ARC	Radiation fields, infrared fluxes, brightness tempertures
Lightning Instrument Package (LIP)	Blakeslee/MSFC	Components of electrical field and air conductivity

DC-8 INSTRUMENTATION FOR TOGA-COARE		
Instrument	**PI**	**Data Parameters**
Visible and Near IR Lidar (VIRL)	Spinhirne/GSFC	Cirrus radiation characteristics, structure and boundaries
Airborne Rain Mapping Radar (ARMAR)	Li/JPL	Vertical profile of rainfall in convective systems
Microphysical Measurement Package (MMP)	Pueschel/ARC Heymsfield/NCAR Hallett/DRI	Water budget of clouds, portion of condensate transported to anvil
Advanced Microwave Moisture Sounder (AMMS)	Wang/GSFC	Water vapor, retrieval and microwave precipitation signatures
Electronically Scanned Microwave Radiometer (ESMR)	Wang/GSFC Wilheit/Texas A&M	Two dimensional view of rainfall features in conjunction with AMMS/AMMR
Airborne Multichannel Microwave Radiometer (AMMR)	Wang/GSFC	Dual polarized microwave signatures of precipitation
Radiation Measurement System (RAMS)	Valero/ARC	Upward & downward radiative flux, ambient temperature
Dropwinsonde	(Facility)	Temperature, moisture, wind speed, pressure
Lightning Instrument Package (LIP)	Blakeslee/MSFC	Components of electrical field, lightning characteristics and location

Table 1: Instrument payloads for the NASA aircraft.

DATE	FLIGHT No.	DESCRIPTION
Jan. 11-12	1	Clear sky over IFA
Jan. 17-18	2	Thin cirrus in transit to IFA
Jan. 18-19	3	Thin cirrus in transit to IFA
Jan. 25-26	4	Kavieng overflight -- thin to moderate cirrus
Jan. 31-Feb. 1	5	Thin to moderate outflow cirrus to south of the IFA
Feb. 8-9	8	Cirrus outflow from tropical cyclone Oliver
Feb. 20-21	11	Moderate to thick cirrus outflow south of IFA
Feb. 23-24	13	Kavieng overflight -- thick cirrus and convection

Table 2. Summary of radiation-related missions. Dates are UTC.

Flights 4 and 13 were overflights of the PROBE site at Kavieng. The primary purpose for this site, which was sponsored by the DOE Atmospheric Radiation Measurement (ARM) program, was measurement of the surface radiation budget and atmospheric quantities that influence that budget. Surface radiation measurements consisted of broad-band solar and infrared upwelling and downwelling fluxes, total/diffuse/direct spectral solar fluxes, direct/diffuse broad-band fluxes, near-infrared spectral irradiance, thermal infrared (window channel) nadir radiance, and thermal infrared spectral irradiance. Ground-based remote sensing measurements of integrated water vapor and liquid water path, cloud base and cloud structure, and atmospheric optical depth as a function of wavelength were also taken. Meteorological measurements included CLASS radiosondes of temperature, dewpoint, and winds four times a day, wind and virtual temperature profiles acquired with a 915 MHz profiler and radio acoustic sounding system (RASS), and surface temperature, dewpoint, pressure, winds, and precipitation. Whole sky images were acquired with a CCD.

Preliminary analysis of the data is extremely encouraging. The instruments performed reliably and the data quality is very good. These data indicate that most of the experiment objectives were met. At least three complete flux profiles were obtained, one in the clear sky over the IFA and two over the PROBE site. A wide variety of measurements of flux divergence in cirrus of varying optical thicknesses are available. In some of these cases, the cirrus was relatively fresh (i.e., still attached to its convective source), while in others the cirrus was well detached from any convection. Excellent observations of cirrus structure utilizing the lidars are also available. In addition, cloud microphysical measurements were made in conjunction with the radiation measurements in a number of cirrus decks.

To date, data processing has been limited by the participation of several of the investigators in a subsequent campaign and commitments to analysis of the data from previous campaigns such as the FIRE Cirrus II experiment in Kansas. The expectation is that much of the initial data processing will be complete by the end of this year in time for presentations at meetings in the beginning of the 1994.

In summary, the radiation component of the NASA TOGA COARE experiment appears to have been very successful. We anticipate a significant improvement in our quantitative understanding of tropical cirrus to result from these data.

Acknowledgments. A successful field program is always the result of the effort and hard work of a great number of people. I would like to take this opportunity to express my appreciation to the members of the air and ground crews of the NASA ER-2 and DC-8. Without their able participation and co-operation, none of these data would be available. The various staff members of the FIRE Project Office provided invaluable support both prior to and during the deployment, as did the staff of the TOGA COARE Project Office. And last, but certainly not least, the contributions of Drs. John Theon and Ramesh Kakar of NASA headquarters should be recognized. Their continued support of this field program throughout the planning and implementation phases was absolutely vital.

omit to END

AUTHOR INDEX

PRECEDING PAGE BLANK NOT FILMED

REPORT DOCUMENTATION PAGE

Form Approved
OMB No. 0704-0188

Public reporting burden for this collection of information is estimated to average 1 hour per response, including the time for reviewing instructions, searching existing data sources, gathering and maintaining the data needed, and completing and reviewing the collection of information. Send comments regarding this burden estimate or any other aspect of this collection of information, including suggestions for reducing this burden, to Washington Headquarters Services, Directorate for Information Operations and Reports, 1215 Jefferson Davis Highway, Suite 1204, Arlington, VA 22202-4302, and to the Office of Management and Budget, Paperwork Reduction Project (0704-0188), Washington, DC 20503.

1. AGENCY USE ONLY *(Leave blank)*	2. REPORT DATE	3. REPORT TYPE AND DATES COVERED
	December 1993	Conference Publication

4. TITLE AND SUBTITLE
FIRE Cirrus Science Results 1993

5. FUNDING NUMBERS
WU 460-42-90-70

6. AUTHOR(S)
David S. McDougal, Editor

7. PERFORMING ORGANIZATION NAME(S) AND ADDRESS(ES)
NASA Langley Research Center
Hampton, VA 23681-0001

8. PERFORMING ORGANIZATION REPORT NUMBER
L-17365

9. SPONSORING/MONITORING AGENCY NAME(S) AND ADDRESS(ES)
National Aeronautics and Space Administration
Washington, DC 20546-0001

10. SPONSORING/MONITORING AGENCY REPORT NUMBER
NASA CP-3238

11. SUPPLEMENTARY NOTES
Cosponsored the National Science Foundation, the National Oceanic and Atmospheric Administration, the Dept. of Energy, and the Office of Naval Research.

12a. DISTRIBUTION/AVAILABILITY STATEMENT
Unclassified–Unlimited

Subject Category 47

12b. DISTRIBUTION CODE

13. ABSTRACT *(Maximum 200 words)*

FIRE (First ISCCP Regional Experiment) is a U.S. cloud-radiation research program that seeks to improve our basic understanding and parameterizations of cirrus and marine stratocumulus cloud systems and ISCCP data products. The FIRE Cirrus Science Conference was held in Breckenridge, CO, June 14–17, 1993, to present results of cirrus research for the second phase of FIRE (1989-present) and to refine cirrus research goals and priorities for the next phase of FIRE (1994-future).

This Conference Publication contains the text of short papers presented at the conference. The papers describe research analyses of data collected at the Cirrus Intensive Field Observations-II field experiment conducted in Kansas, November 13–December 7, 1991.

14. SUBJECT TERMS	15. NUMBER OF PAGES
FIRE; ISCCP; Cirrus; Cloud-radiation; Field experiment	225
	16. PRICE CODE A10

17. SECURITY CLASSIFICATION OF REPORT	18. SECURITY CLASSIFICATION OF THIS PAGE	19. SECURITY CLASSIFICATION OF ABSTRACT	20. LIMITATION OF ABSTRACT
Unclassified	Unclassified	Unclassified	